Orographic enhancement of mid-latitude cyclone precipitation.

María del Socorro Medina Valles

A dissertation submitted in partial fulfillment
of the requirements for the degree of

Doctor of Philosophy

University of Washington

2005

Program Authorized to Offer Degree: Atmospheric Sciences

University of Washington
Graduate School

This is to certify that I have examined this copy of a doctoral dissertation by

María del Socorro Medina Valles

and have found that it is complete and satisfactory in all respects,
and that any and all revisions required by the final
examining committee have been made.

Chair of the Supervisory Committee:

_____

Robert A. Houze, Jr.

Reading Committee:

_____

Robert A. Houze, Jr.

_____

Bradley F. Smull

_____

Clifford F. Mass

Date: _____

University of Washington

Abstract

Orographic enhancement of mid-latitude cyclone precipitation.

María del Socorro Medina Valles

Chair of the Supervisory Committee:
Professor Robert A. Houze, Jr.
Atmospheric Sciences

As mid-latitude cyclones move across mountain ranges, the distribution of precipitation is altered. The windward slopes experience enhancement of precipitation, which is determined by dynamical and microphysical factors. Detailed radar observations collected near the European Alps and the Oregon Cascade Mountains reveal that the windward terrain-modified flows have characteristics that are repeated from storm to storm and from mountain range to mountain range. These flow patterns and their precipitation formation mechanisms are synthesized in conceptual models of orographic enhancement of precipitation.

In Type A pattern, low static stability low-level air rises easily as it encounters the first peaks of the terrain. Lifting of moist low-level air produces high liquid water contents over these peaks, which favor growth of pre-existing precipitation by riming and coalescence. If the upstream flow is potentially unstable, convective cells will be triggered in the upslope ascent. These cells produce pockets of especially high liquid water content where the coalescence and riming processes are accentuated. A mesoscale model simulation suggests that subsequent peaks may also be subjected to this kind of precipitation enhancement.

Type B pattern exhibits a shear layer on the windward slopes. The combination of

high shear and static stability produces conditions that support dynamical instability manifested in the form of Kevin-Helmholtz billows and turbulent overturning cells. Aggregation of ice particles falling from the baroclinic system into the layer of cells is aided by the turbulent motions. The strong updrafts produce pockets of high liquid water content, which favor riming and coalescence. Idealized numerical simulations indicate that a shear layer may develop on the windward side of a mountain as a result of strong static stability and/or surface friction.

During mid-latitude cyclone passage over a mountain range, windward precipitation is enhanced by small-scale updrafts regardless of the character of the low-level flow. In Type A (Type B) storms static (dynamic) instability is responsible for the updraft generation. The updrafts produced in both scenarios are strong enough to activate accretion growth processes (coalescence, aggregation, and riming), which are capable of producing large particles that fallout rapidly on the windward side of the terrain.

TABLE OF CONTENTS

LIST OF FIGURES

vii

viii

LIST OF TABLES

ACKNOWLEDGMENTS

Chapter 1

INTRODUCTION

1.1 Orographic enhancement of precipitation

The presence of a mountain range has a profound effect on the local weather and climate of a region. It has a particularly strong effect on the distribution of precipitation, where an enhancement on the windward slope is often observed. There are different ways in which the orography can enhance the precipitation on the windward slope. This study focuses on the windward precipitation enhancement that occurs when a baroclinic mid-latitude system interacts with orography. The magnitude of this enhancement has been documented in several studies. For example, Hobbs et al. (1975) observed an occluded frontal system as it moved from the Pacific Ocean over the Washington Cascade Mountain Range. They found that the frontal precipitation over the windward slopes of the Cascade Range exceeded that observed over the low-lying Puget Sound Basin by a factor of two or three (Fig. 1.1). Neiman et al. (2002) conducted an observational study of orographic precipitation over the coastal mountains of California. They reported a case where a warm sector passage was accompanied by an eightfold increase in the rainfall between a coastal site (at an elevation of 11 m) and a site located on the windward slope (at an elevation of 1021 m). These sites were located only 35 km apart.

The windward enhancement of precipitation seems to occur systematically. For example, it was observed over the Oregon Cascade Mountains during IMPROVE-2 (Stoelinga et al. 2003), a field project that collected data during November-December 2001, a period when $\sim$16 troughs made their way from the Pacific Ocean to the coast

of Oregon and Washington. The enhancement of precipitation as these systems moved over the Oregon Cascade Mountains is exemplified in Fig. 1.2. Salem (at an elevation of 64 m), located in the lowlands of the Willamette valley (Fig. 1.3), consistently measured less precipitation than Little Meadows (at an elevation of 1219 m), a station located on the windward slopes (Fig. 1.3). The precipitation accumulated during IMPROVE-2 in Salem was ∼26 cm (10.2 in.) compared to 77 cm (30.5 in.) in Little Meadows (Fig. 1.2), consistent with the findings of Hobbs et al. (1975).

Long-term climatologies clearly show the impact that individual systems like the one studied by Hobbs et al. (1975) have on the precipitation distribution. The climatological distribution of precipitation during December, January and February over Washington and Oregon shows a maximum over the western side of the Washington Olympic Mountains and the Oregon Coastal Range, a local minimum over Puget Sound and the Willamette Valley, a secondary maximum over the western side of the Cascade Mountains and a dramatic decrease over the eastern side of the Cascades (Fig. 1.4). In this study, we will investigate the mechanisms that produce precipitation enhancement on the west slopes of the Cascades and on the southern slopes of the European Alps (Fig. 1.5)[1]. The Mediterranean side of the Alps is a region where heavy precipitation and flooding events are frequent during the autumn season. These events tend to occur when deep, elongated baroclinic troughs move over the region producing strong moist southerly or southeasterly low-level flow, i.e., flow quasi-perpendicular to the southern side of the Alps. Using 20 years of daily rain-gauge data, Frei and Schär (1998) constructed a high-resolution precipitation climatology for the Alpine region. They found that during autumn the precipitation has a maximum on the southern slopes of the Alps (Fig. 1.6). The doubling or tripling

---

[1]Several studies have investigated precipitation over coastal mountains (e.g., Yu and Smull [2000], Colle and Mass [1996], Colle et al. [1999], Doyle [1997], Neiman et al. [2002], James and Houze [2005]). Most of the data used in this study was collected in mountains near the Mediterranean Sea or the Pacific Ocean but sufficiently inland not to be considered as coastal ranges, therefore our focus will be on inland mountain ranges.

of the precipitation observed from the lowlands to the windward slopes occurs in a relatively short distance (40 km), which suggests that as a baroclinic systems move over the windward slopes and the flow interacts with the orography, a large fraction of the atmosphere's moisture is quickly converted to precipitation.

1.2 Controlling factors of orographic precipitation

The observations mentioned above illustrate the magnitude and persistence of the windward enhancement of orographic precipitation in mountain ranges exposed to repeated passage of mid-latitude systems. Understanding the mechanisms that produce this enhancement is not simple, as they depend on both airflow dynamics and cloud microphysics. The dynamic aspects depend on the upstream characteristics of the flow and on the terrain configuration, which together determine the ways in which the flow interacts with the terrain, while the microphysical aspects determine how much and how quickly cloud water is converted into precipitation and how fast precipitation falls (Smith et al. 2005).

1.2.1 Dynamic aspects (numerical simulations)

Given that many factors govern airflow-terrain interactions, numerical simulations have aided in understanding the problem by providing a framework where the roles of the orography and different aspects of the upstream flow may be evaluated via sensitivity studies.

Dry, statically stable flow over an isolated peak

Many studies have focused on the behavior of statically stable flow on the leeward side of a mountain (e.g., Durran and Klemp 1983). In this study we are interested on the windward enhancement of precipitation, therefore our main focus is going to be on the flow upwind of the mountain. For dry, statically stable flow over simple

terrain (and neglecting surface friction and rotational effects), it has been recognized that the significant parameters in determining the interaction between the flow and the terrain are the cross-mountain wind speed U_0, the dry Brunt-Väisälä frequency of the upstream flow N_d ($N_d{}^2 = [g\ d\,ln\,\theta/dz]$, where θ is the potential temperature, g the gravitational acceleration, and z is the vertical coordinate) and the maximum terrain height h (Pierrehumbert and Wyman 1985). The ratio $U_0/(N_dh)$ has been used extensively in studies of stratified flow over orography as a way to characterize the flow-terrain interaction. The ratio $U_0/(N_dh)$ represents the relative importance of the upstream velocity U_0 to the perturbation velocity (N_dh) (Ding et al. 2003) and gives a measure of the importance of nonlinear effects in the flow (Smolarkiewicz and Rotunno 1989)[2]. According to Baines (1995) this ratio (or in some cases its inverse) has been inappropriately termed "Froude number" (Fr), as Fr denotes a fluid speed divided by a wave speed. In this dissertation, we will avoid using of the term "Froude number" in the context of stable flow interacting with terrain. We will follow Baines (1995) in calling the flow parameter $U_0/(N_dh)$ "Nhu" and we will denote it with the Greek letter ν or ν_d, where the subscript d is used to denote dry flow.

Smolarkiewicz and Rotunno (1989, 1990) illustrated the usefulness of the non-dimensional parameter ν_d under the idealized conditions described before. They used a numerical model to study the interaction of dry, statically stable flow with a three-dimensional (3D) bell-shaped obstacle. They found that when ν_d is relatively large (e.g., ν_d =2.2), the low-level flow on the windward side rises over the terrain, as shown by their streamline patterns in Fig. 1.7a,b. Conversely, when ν_d is relatively small (e.g., ν_d =0.33), the low-level flow on the windward side can exhibit "upstream block-

---

[2]Smolarkiewicz and Rotunno (1989) found that the linear theory described by Smith (1980, 1988) gives a qualitatively consistent flow representation when $U_0/(N_dh)$ is approximately greater than 0.5, however as $U_0/(N_dh)$ goes below this value linear theory ceases to be valid and windward flow stagnation and reversal occur. For extremely low $U_0/(N_dh)$ values (e.g., less than 0.1), Smolarkiewicz and Rotunno (1990) point out that the flow tends toward 2D potential flow behavior (i.e., it is constrained to move in horizontal planes). However such small values are not typically observed in the atmosphere.

ing" and reverse direction (Fig. 1.7c,d). According to the AMS glossary, upstream blocking is defined as "the retardation of stable, low-level, forced upslope flow on the windward side of a mountain or mountain barrier". Pierrhumbert and Wyman (1985), Smolarkiewicz and Rotunno (1990) and others evaluated the occurrence of upstream blocking in numerical simulations by setting up an upstream cross-barrier flow approaching a barrier with wind speed U_0 and tracking the minimum windward surface wind speed in the cross-mountain direction (U_{min}). If U_{min} is zero, then the flow has suffered stagnation and blocking. If U_{min} is in the opposite direction from the upstream flow, then upstream blocking and flow reversal of the low-level flow have occurred. If $U_{min} < U_0$, the low-level flow is partially blocked, with the degree of blocking related to the ratio of U_{min} to U_0 (Colle, 2004). In Fig. 1.7c,d the stagnation points are indicated with black dots. Following Pierrehumbert and Wyman (1985), in this study we will describe the flow pattern depicted in Fig. 1.7a,b as a "flow-over" regime and the pattern in Fig. 1.7c,d as a "flow-around" regime.

Given the dependence of the flow pattern on U_0, N_d, and h, the studies by Smolarkiewicz and Rotunno suggest that there are several means by which a flow-over configuration can transition to flow-around: by sufficiently decreasing the upstream wind speed, by increasing the stability, or by increasing the mountain height. Sheppard (1956) estimated the critical ν_d value (ν_{dc}) at which windward flow stagnation and regime transition occurs. He proposed that the critical condition occurred when the kinetic energy of the flow was equal to the potential energy required for it to rise over the mountain, which implies that $\nu_{dc} = 1$. Smith (1989) pointed out that Sheppard's argument neglected the pressure difference term, which could be as large as the kinetic energy terms. Numerical and experimental studies for 3D hills suggest that $\nu_{dc} = 0.91\text{-}0.95$ (Smith and Grönas 1993, Baines and Smith 1993). However, ν_{dc} also depends on the shape of the obstacle, i.e., on the three-dimensionality of the problem.

When the Earth's rotation is considered, Pierrhumbert and Wyman (1985) found

that the Rossby number ($R_o = U/(fa)$, where a is the mountain half-width and f is the Coriolis parameter), as well as ν_d, needs to be considered to determine the character of stable flow over orography. They found that rotation limits the extension of the upstream blocking, which reaches a maximum distance from the mountain crest given by the Rossby radius of deformation ($L_R = N_d h / f$).

Moist, statically stable flow over an isolated peak

In studying the interaction of statically stable flow with orography, it is necessary to consider that when near-saturated air is forced to ascend a barrier its temperature decreases and as a result saturation and condensation may occur. This process is accompanied by the release of latent heat of condensation. This heating decreases the effective stability of the atmosphere, which in turn has an impact on the flow dynamics. According to Durran and Klemp (1982) when the atmosphere is saturated, the effective Brunt-Väisälä frequency is given by:

$$N_m^2 = \left[\frac{g}{T}(\frac{dT}{dz} + \Gamma_m)(1 + \frac{Lq_s}{RT}) - \frac{g}{1 + q_w}\frac{dq_w}{dz} \right] \qquad (1.1)$$

where T is the temperature, q_w is the total water mixing ratio, q_s is the saturation mixing ratio, L is the latent heating of vaporization, R is the ideal gas constant for dry air and Γ_m is the saturated adiabatic lapse rate. Jiang (2003) used the Advanced Regional Prediction System (ARPS) mesoscale numerical model with a bulk microphysical parameterization scheme (BMP, Lin et al. 1983) to explore the response of near-saturated, stable 3D flow interacting with an isolated Gaussian-shaped circular mountain. He suggested that when moisture is included, the windward flow response may be represented by the flow parameter $\nu_m = U_0/(N_m h)$. Using numerical simulations, Jiang (2003) showed that diabatic heating from condensation may cause the flow to transition from a flow-around to a flow-over regime. For example, for a case with relative humidity (RH) = 95 %, $T_0 = 270$ K and N_d =0.011 s^{-1}, Jiang found

that the release of latent heat of condensation would cause the low-level flow to rise twice as much as dry air would[3].

Obviously, the type of interaction that the flow has with the terrain will have an impact on the distribution and amount of precipitation. A mesoscale numerical simulation of flow over regime ($\nu_d = 1.14$, $\nu_m = 2.08$) conducted by Jiang (2003) produced maximum surface precipitation rates on the windward slope (Fig. 1.8a). A vertical cross section through the domain center shows that there are two areas of maximum precipitation growth, represented by snow mixing ratio (the only type of precipitation produced, as the surface temperature in all his simulations was 270 K). One area was located over the windward slope of the mountain associated with stable ascent with another area over the lee side due to gravity wave lifting (Fig. 1.8c), an interpretation that is confirmed by the vertical velocity distribution (Fig. 1.8d)[4]. By comparing the horizontal (Fig. 1.8a) and vertical (Fig. 1.8c) distribution of precipitation, it is clear that the snow produced by gravity wave lifting did not reach the surface of the obstacle.

A corresponding simulation of the flow-around regime ($\nu_d = 0.30$, $\nu_m = 0.56$) shows that the precipitation rates are maximized in an arc-shaped band upstream of the obstacle, with a local maximum on the windward slope (Fig. 1.9a). A vertical cross-section through the domain center shows that in this case there are three areas of maximum snow mixing ratio: the absolute maximum is shallow and located upstream from the peak, creating the arc-shaped precipitation band (Fig. 1.9c). A local maximum is located over the windward slope, which was produced through upslope ascent. A third local maximum occurs over the downwind side due to gravity wave lifting (Fig. 1.9c). These interpretations are consistent with the vertical velocity pattern (Fig. 1.9d). The vertical velocity updraft responsible for the upstream maximum

---

[3]Jiang (2003) actually used $\nu_m{}^{-1}$ to characterize the flow.

[4]The simulations shown in Fig. 1.8 in panels (a-b) were conducted with $h = 800$ m, while those in panels (c-d) used $h = 1000$ m.

precipitation rate is elevated and detached from the ground (Fig. 1.9d). Jiang (2003) interpreted the upstream precipitation maximum and its associated updraft as the result of convergence between incoming and reversed flows, a picture that is consistent with the surface wind field (not shown, but qualitatively similar to Fig. 1.7c).

Jiang compared the mesoscal numerical simulations presented in Figs. 1.8a and 1.9a with precipitation patterns predicted by an "upslope or slab model" of orographic precipitation (Smith 1979). The upslope model of orographic precipitation poses that stable flow impinging on a mountain will be forced to ascend over the orography and will produce vertical motions proportional to the horizontal wind speed and the slope of the terrain. Assuming that the flow is saturated, that the water vapor condenses as soon as the flow starts to ascend and that the condensed water turns into precipitation and falls out instantaneously, the precipitation is calculated as the product of the upslope component of the wind, the vapor mixing ratio and the layer mean air density. For the flow-over regime, the upslope model produces a precipitation pattern with spatial distribution relatively similar to the precipitation pattern predicted by the more sophisticated mesoscale model (cf. panels [b] and [a] of Fig. 1.8). However, the precipitation rates are overestimated and the maximum occurs at lower elevations compared with the mesoscale model, which reflects the fact that in the upslope model the moisture condenses and falls out instantaneously[5]. For the flow-around case, the upslope model produces a precipitation distribution that is similar to that of the flow-over regime (cf. Figs. 1.8b with 1.9b), indicating that during flow around regime the upslope model representation of the precipitation is not appropriate.

---

[5]In recent work, Smith and his colleagues have developed more sophisticated models of upslope precipitation by parameterizing microphysical processes using timescales to delay precipitation formation and fallout (Smith and Barstad 2004).

Moist flow over elongated barriers

The numerical simulations described above used a relatively simple representation of the orography. Several numerical studies have been conducted using more complex orography, in particular an elongated barrier, which could be viewed as a simplified representation of actual mountain ranges (e.g., the Pyrenees, the Andes, and the Alps). This type of terrain was used by Buzzi et al. (1998) and Rotunno and Ferretti (2001) who conducted mesoscale numerical simulations of the "Piedmont flood". This flood occurred in the region of that name (around 45°N, 7.5°E in Fig. 1.5) in November 1994 as a baroclinic trough moved towards the Alps producing southerly flow upstream of the terrain and rain accumulations as high as 300 mm over a 24 h period at some stations (Rotunno and Ferretti 2001). The methodology of these studies consisted of comparing a control Piedmont flood simulation with experiments where the flow characteristics varied.

Buzzi et al. (1998) used a numerical model and the actual Alpine orography to explore the role of the condensational latent heating on flow regime. They compared a Piedmont flood control simulation with an experiment where the temperature tendencies due to condensation were eliminated. Their control experiment showed a low-level easterly flow over the Po Valley that rose over the Alpine terrain in the Piedmont region. In a simulation in which the temperature tendencies associated with condensation were eliminated (with the formation and fall of precipitation still occurring), the low-level easterly flow simulated south of the western Alps did not rise over the terrain in the Piedmont region, but instead was diverted around the Alps and turned toward the south. Hence, in the control experiment, there was a flow-over regime in the Piedmont region, in contrast to the case with no condensation where a flow-around regime developed at low levels in the same region. The experiments of Buzzi et al. (1998) also illustrate that for an elongated mountain range, inhomogeneities in flow regime appear: for a range oriented in a west-east fashion, flow may

be blocked on the eastern side of the range but rise over the terrain over the western side. Therefore when the orography is more complicated than an isolated peak, the flow regime exhibits considerable spatial variability.

This idea was clarified further by Rotunno and Ferretti (2001). They suggested that an east-west moisture gradient was responsible for the observed flow and precipitation maximum over the Piedmont region. Upstream of the western Alps, the flow was nearly saturated; therefore its effective stability was N_m. The upstream flow was drier near the eastern end of the Alps, hence its effective stability was N_d. The reduced stability values on the western side of the Alps allowed the airflow to go up and over the barrier, while the more stable air to the east flowed around the barrier, in an easterly manner. Over the western Alps, the moist southerly flow converged with and rose over the easterly flow and then over the terrain producing large precipitation amounts over the Piedmont region.

1.2.2 Observational evidence of "flow-over" and "flow-around" regimes and their precipitation distribution

Numerical simulations are useful in understanding the role that different parameters play in determining orographic precipitation by simplifying the characteristics defining the actual flow and terrain and by enabling sensitivity studies. However, this simplicity and other restrictions inherent to models produce a picture that lacks some of the physics and complexities of the actual atmosphere. For example, it has been documented that the precipitation amounts forecast by operational mesoscale models tend to have problems over complex orography (Colle et al. 1999, Colle and Mass 1999). In this section we will review relevant observational results regarding flow-over and flow-around regimes. One particular aspect that is often lacking in simple numerical simulations of orographic precipitation is the preexisting mid-latitude cloud associated with a baroclinic system passing over the mountain range. In this thesis, we will present evidence that suggests that the hydrometeor field that exists

in a mid-latitude system, prior to its passage over the range, plays an important role in accelerating the microphysical growth mechanisms that lead to the windward enhancement of precipitation when such a system moves over a mountain range.

One of the clearest examples of the flow-over regime behavior was observed during the Big Thompson river flash flood, which occurred in northern Colorado in 1976 (Caracena et al. 1979). Upstream soundings and Doppler acoustic echo-sounder data documented strong cross-barrier flow at low-levels. The lifting of potentially unstable air over the eastern slopes of the Front Range resulted in 48 h rain accumulations of 280-300 mm[6], which caused extensive damage in the region. A large percentage of rain accumulated in the 48 h period was recorded during a time interval of a few hours. This case is an example of a case in which the flow dynamics, thermodynamics (and microphysics, sec. 1.2.3) acted in tandem to produce extreme orographic enhancement of precipitation.

Flow-around and upstream blocking has been studied in mountain ranges all around the world, e.g., over the Western Ghat mountains in India (Grossman and Durran, 1984), over the Olympic mountains in western Washington and Vancouver Island (Overland and Bond, 1995; Colle and Mass 1996); adjacent to the coastal ranges of Oregon and California (Yu and Smull, 2000) and over the Wasatch range of Utah (Cox et al. 2005). Marwitz (1987) analyzed statically stable storms over the Sierra Nevada and found that the cross-barrier winds were at times profoundly blocked at low levels, however they increased very rapidly with height, exceeding 20 $\mathrm{m\,s^{-1}}$ over the crest. A low-level jet frequently characterized the along-barrier flow. A similar flow behavior was observed during a strongly stable Alpine case during 21 October 1999. Bousquet and Smull (2003b) profoundly blocked low-level flow and strong cross-barrier wind at higher levels.

A few observational studies have analyzed and contrasted flow regimes. Peterson

---

[6]This measurement was outside the region of most severe flooding, as no rain gauges were located in this area.

et al. (1991) identified, contrasted and documented two case studies belonging to flow-over and flow-around regimes. They referred to them as "coupled" and "decoupled" regimes, respectively, to indicate similar (or dissimilar) directions between the flow at crest level and the low-level flow. Their cases were observed in the Yampa Valley, in northern Colorado. Peterson and colleagues lacked detailed information of the flow structure in the vertical, however, since the Yampa Valley is narrow and they had a relatively large number of surface stations located on the floor and walls of the valley, they tried to infer a 3D picture of the flow. They suggested the conceptual model shown in Fig. 1.10. For cases with high ν, the flow nearly at all levels is able to rise over the terrain and the precipitation enhancement occurs on the steepest windward slopes (Fig. 1.10a). In contrast when ν is small, the low-level flow is decoupled from the flow above. The low-level flow does not rise over the terrain, instead it is either stagnant or reversed (i.e., moving away from the mountain). The blocked air (shown in the Fig. 1.10 by the shaded area) alters the location of maximum precipitation by forcing orographic uplift upstream of the mountain, as the airflow at higher levels rises over the layer of blocked air as well as over the mountain. This horizontally-extended modification experienced by the upstream flow is known as the "effective mountain effect". Most of the observations available to Peterson et al. (1991) were collected at the surface and were complemented by limited aircraft information collected at a fixed altitude. Therefore, their picture of the flow and precipitation vertical structure was very limited. Our study will present detailed vertical structure observations, which will test some of the ideas put forward in the conceptual model of Peterson et al. (1991). The observational data presented in this study provides unprecedented details of terrain-modified flow, as well as the microphysical processes responsible for precipitation enhancement.

Houze et al. (2001) constructed a two-season climatology of airflow and precipitation data south of the Alps, in the Lago Maggiore region (Fig. 1.11) using Monte Lema radar during autumn seasons of 1998/99. A composite of radar data was con-

structed according to the thermodynamic and wind characteristics of the upstream flow, as measured from a sounding launched at Milan[7] (Fig. 1.11). In particular, they grouped radar-derived airflow and precipitation[8] according to ν_m. They found that cases with $\nu_m > 1$ were characterized by cross-barrier flow in the entire low-level layer, i.e., conforming to a flow-over regime. The cases with $\nu_m < 1$ exhibited cross-barrier flow at around 2 km but terrain-parallel flow at 0.5 km, i.e., flow-around behavior, or what Peterson et al. (1991) called decoupled flow. In terms of precipitation, the flow-over composite showed precipitation maximum over and just upwind of the lower windward slopes. The flow-around case was characterized by a weak precipitation echo maximum over the lower windward slopes and some enhancement $\sim$80 km upstream of the radar or some 140 km upstream of the mountain crest.

In a study of winter precipitation over California's coastal mountains, Neiman et al. (2002) identified unblocked (flow-over) and blocked (flow-around) regimes using wind profiler data[9]. They calculated vertical profiles of correlation coefficient between upstream cross-barrier wind and rain rate on the windward slopes. They provided observational evidence that when the low-level flow is unblocked, the rain rate at a windward slope site is highly correlated with the low-level cross-barrier flow measured just upstream at a coastal location. The correlation between the windward rain rate and the cross-barrier upstream flow remained high from the surface up to an altitude near to the rain rate site's elevation. The correlation coefficient decreased very sharply with height above this level. Therefore the flow at the very lowest levels (below 2 km for the coastal mountains of California) is fundamental in producing orographic enhancement of precipitation for unblocked cases. On the other hand, for blocked

---

[7]Houze et al. (2001) used the mean values in the 925-700 mb layer to characterize the flow.

[8]Only events with southerly and southeasterly upstream flow were included, which were found to account from most of the orographic enhancement of precipitation in the region (Houze et al. 2001).

[9]The thermodynamic data available to Neiman et al. (2002) was very limited, so they were not be able to infer stability characteristics.

cases, the correlation coefficient between near surface cross-barrier upstream flow and windward rain rate was almost zero. This correlation coefficient increased just above mountaintop, which Neiman et al. attributed to upslope precipitation that occurred when the flow at higher levels rose over the low-level blocked flow and over the terrain.

James and Houze (2005) conducted a climatolgical study of orographic precipitation over the California coastal mountains using radar-derived fields. They saw evidence of both flow-over and flow-around patterns. An indication of a flow-over regime appeared in the form of precipitation maxima over the first major terrain peaks. The possibility of recurring blocked flows during the 2.5 year of observed data was suggested by precipitation enhancement upstream of the terrain and offshore, although they mention that this pattern could also be the result of enhanced frontogenesis in the coastal zone.

1.2.3 Cloud microphysical processes and small-scale motions

Secs. 1.1 and 1.2.2 have described the orographic enhancement of precipitation associated with mid-latitude system passage over orography. These discussions suggest that regardless of the nature of the terrain-modified low-level flow, a large faction of the atmosphere's water vapor is converted into precipitating particles that fall out on the windward side of the mountain. When a midlatitude baroclinic cloud system passes over a mountain range, these processes rearrange the precipitation production of the baroclinic system so that the windward-side precipitation is enhanced while that on the lee side is reduced or even eliminated.

The growth rate and fallspeed of precipitation particles are controlled by microphysical processes. There are seven basic types of microphysical processes or pathways that may contribute to the conversion of water vapor into precipitation: nucleation of cloud droplets and ice, vapor diffusion, accretion or collection, breakup of drops, sedimentation, ice concentration enhancement and melting (Houze 1993). The accretion or collection processes may be subdivided in three categories: coalescence (growth of

cloud droplets or raindrops by collecting other cloud droplets or raindrops), aggregation (growth of ice particles by collecting other ice particles), and riming (growth of ice particles by collecting supercooled cloud liquid droplets, which freeze on contact).

A limited amount of existing observations of particle types in orographic precipitation suggest that the accretion processes may be important in precipitation enhancement. For example, in cool season storms over western U. S. mountain ranges, Hobbs (1975) and Marwitz (1987) found a maximum in liquid water content (LWC) over the windward slopes. Using a simple model of airflow over an idealized version of the Cascade Mountains, Hobbs et al. (1973) found that such LWC distribution implies that rimed particles are more likely to reach the ground on the windward slopes while unrimed particles fall out predominantly on the lee slopes. Indeed, particle samples collected at ground level on the windward slopes of the Cascades showed evidence of particle growth by riming and aggregation (Hobbs 1975). By analyzing crystals during orographic precipitation storms with flow-over and flow-around regimes, Peterson et al. (1991) found that in both cases dendrites with some aggregation and light riming were present. This study was conducted in Colorado, at higher altitudes, where the lower moisture content of the air may have reduced the cloud liquid water content and hence the potential for riming. In the flow-over regime Big Thompson flood, Caracena (1979) suggested that the precipitation grew mainly through coalescence.

Coalescence and riming may produce particles big enough to fall out rapidly since these accretion processes tend to create large/heavy particles. The production of heavier, more rapidly falling particles contributes to precipitation enhancement by providing the means for the condensed water to fall out quickly once cloud drops have been produced by orographic lifting. Aggregation, too, may hasten the fallout of condensed water. Aggregation produces snowflakes particles that are large and constitute large targets for riming. The large rimed aggregates will turn into large, rapidly falling drops when they melt.

The size/weight of a hydrometeor determines its fallspeed and hence how far

downstream it will be advected before reaching the ground. A simple calculation illustrates that under uniform horizontal wind speeds of 15 $\mathrm{m\,s^{-1}}$, a particle released at an altitude of 3 km will be advected $\sim$4.5 km downstream before reaching the ground if its terminal fall speed is that of rain (10 $\mathrm{m\,s^{-1}}$). Snow, on the other hand, with smaller terminal fall speed (1 $\mathrm{m\,s^{-1}}$) can be advected as much as 45 km downstream before reaching the ground. This difference in the advection distance has a potential impact on whether a hydrometeor falls on the windward or leeward side. If, as suggested by previous studies, the accretion processes are a key factor in the windward enhancement of precipitation, it is important to understand how are they invigorated when a cloud system encounters a mountain range.

Smith (1979) suggested that small-scale cellularity may play a role in accelerating the growth of hydrometeors by producing localized areas of strong updrafts. These updrafts are potential mechanisms to invigorate the accretion microphysical processes. Kirshbaum and Durran (2004) conducted 2D and 3D mesoscale simulations (horizontal resolution = 0.5 km, vertical resolution = 0.1 km) of unstable flow over terrain using warm-rain microphysics. They showed that under certain conditions small-scale embedded convection, cellular in form, forms on the windward slope of the terrain. Kirshbaum and Durran showed that when small-scale cellularity is activated, the maximum precipitation rate, the precipitation accumulation, and the precipitation efficiency all increase compared to cases without such cells. According to their simulations, the increased hydrometeor growth and precipitation accumulation associated with the updrafts is not compensated by the decreased growth and precipitation that occurs in the downdrafts, at the edge of the cells. These simulations suggest that small-scale cellularity may constitute a mechanism of efficiently removing moisture from the airflow as it rises over an obstacle. In this study we will show observational evidence of small-scale cells and of their role in the enhancement of orographic precipitation via accretion processes.

1.3   Objective and methods of this research

This study analyzes detailed observational information collected during the passage of baroclinic systems over mountain ranges. The vertical structure of cross-barrier flow and precipitation on the windward sides of mountain ranges in cases with some similarities to canonical flow-over and flow-around regimes is documented. The objective is to better understand how the airflow within a pre-existing baroclinic storm is modified by the orography and how this interaction invigorates the cloud microphysical processes of the storm to enhance windward precipitation. This understanding will be synthesized in empirical conceptual models of the processes that produce windward orographic enhancement of mid-latitude precipitation. This study benefits particularly from specialized radar measurements, including polarimetric Doppler radar data, airborne Doppler radar, and vertically pointing Doppler radar. These data provide continuous and simultaneous information on the terrain-modified flow and on the precipitation. Information on particle type may be inferred from polarimetric radar data, which gives information on microphysical growth mechanisms. Vertically pointing radar provides higher temporal and vertical resolution information on precipitation and air motions and is used to deduce particle growth mechanisms. The aircraft radar provides information in regions obscured from the view of the ground-based scanning radars. The data used were collected in field campaigns conducted over two mountainous regions: the Mesoscale Alpine Program (MAP) held over the European Alps from 7 September to 15 November 1999 (Bougeault et al. 2001) and the second phase of the Improvement of Microphysical PaRametrizations through Observational Verification Experiment (IMPROVE- 2) held over the Oregon Cascade Mountains from 26 November - 21 December 2001 (Stoelinga et al. 2003). The study also benefits from high-resolution numerical model simulations. Both idealized and storm-based simulations are used as a consistency test of specific aspects of the empirical conceptual models of orographic enhancement of precipitation obtained from

the specialized field datasets.
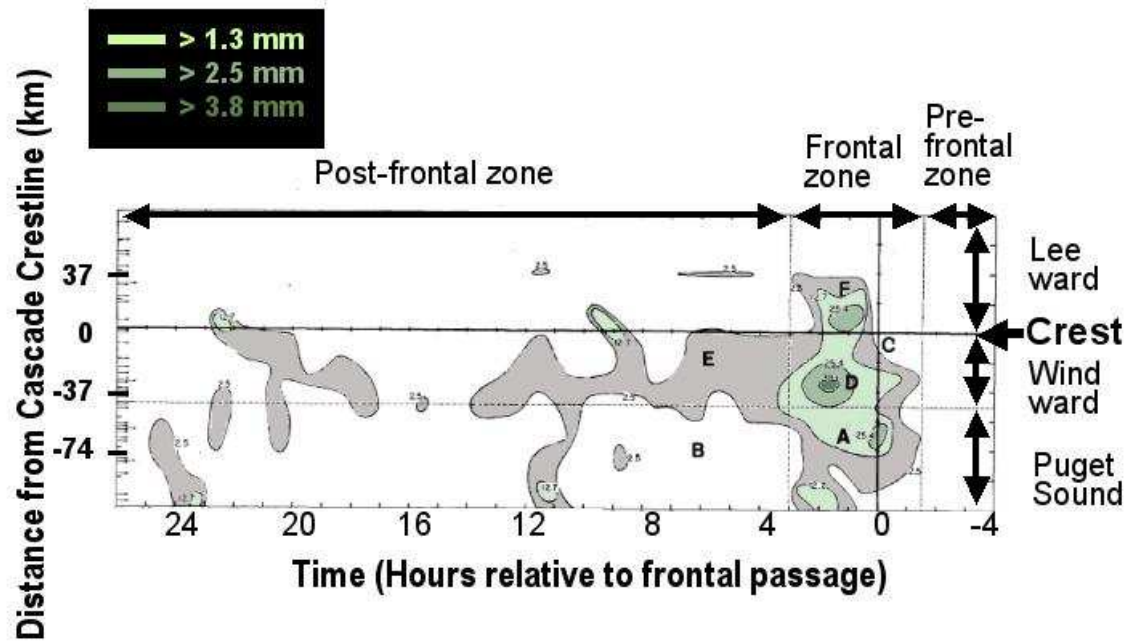
Figure 1.1: Mean hourly precipitation with respect to the orography (ordinate axis) and to the position of the front (abscissa axis). From Hobbs et al. (1975).
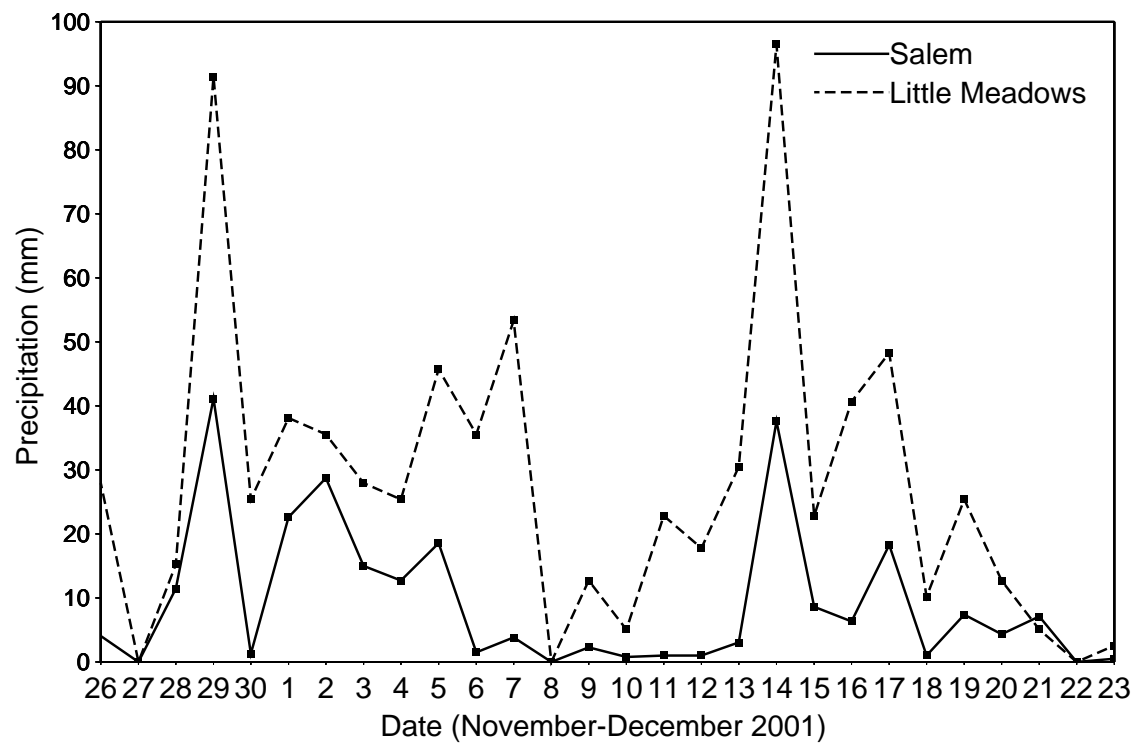
Figure 1.2: IMPROVE-2 time series of daily precipitation measured by Salem (solid line) and Little Meadows (dashed line) rain gauges. From Houze and Medina (2005).
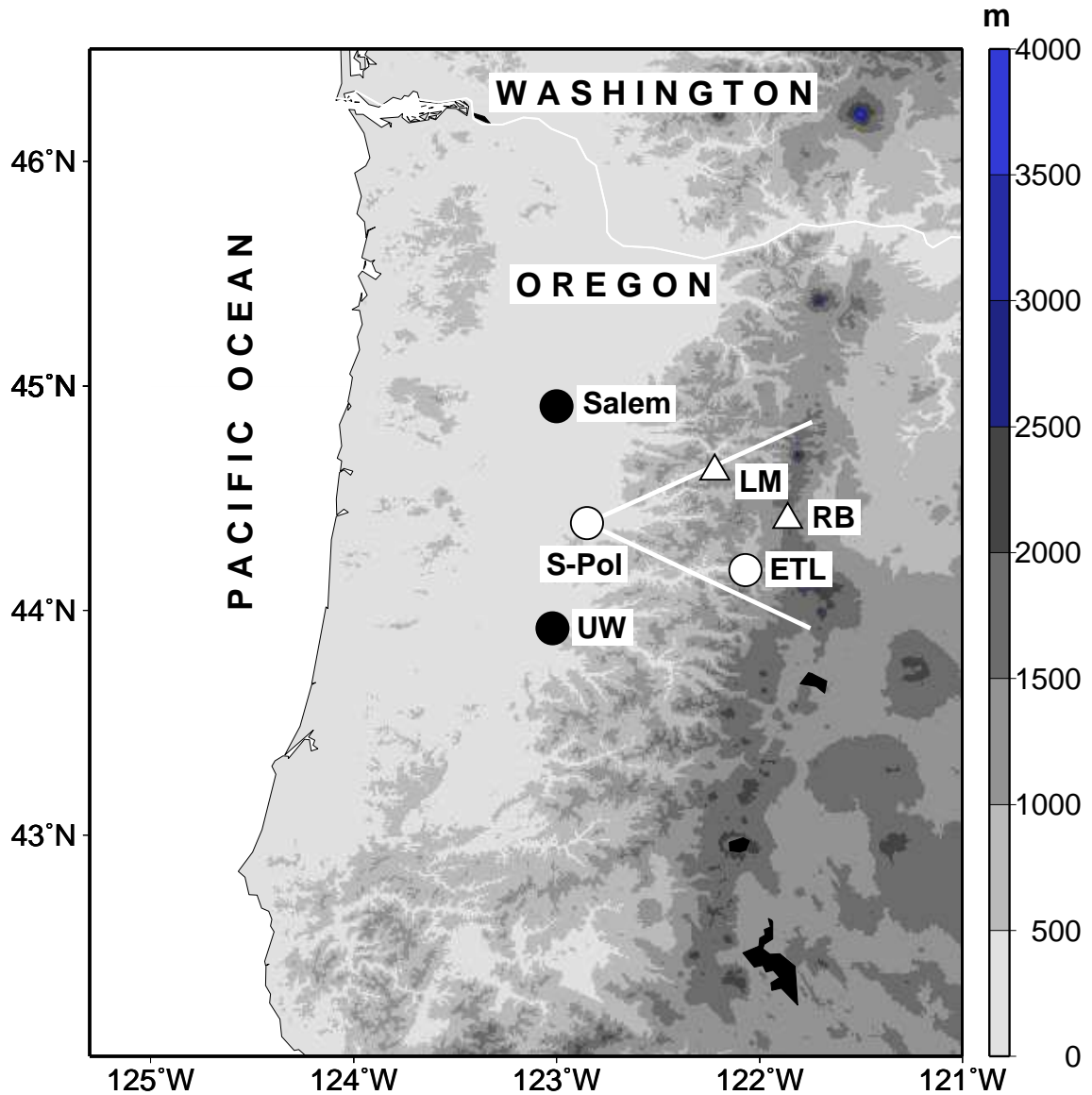
Figure 1.3: IMPROVE-2 observational area. Western Oregon orography and the location of the observations relevant to this study. "S-Pol" marks the location of the polarimetric scanning Doppler radar. The white lines bound the eastward-looking sector scanned regularly duing the 13-14 December 2001 case. "ETL" marks the location of a vertically pointing radar and a wind profiler. "Salem" and "UW" denote upper-air sounding locations. Observations collected at Little Meadows ("LM") and Ray Benson SnoPark ("RB") are discussed in the text.
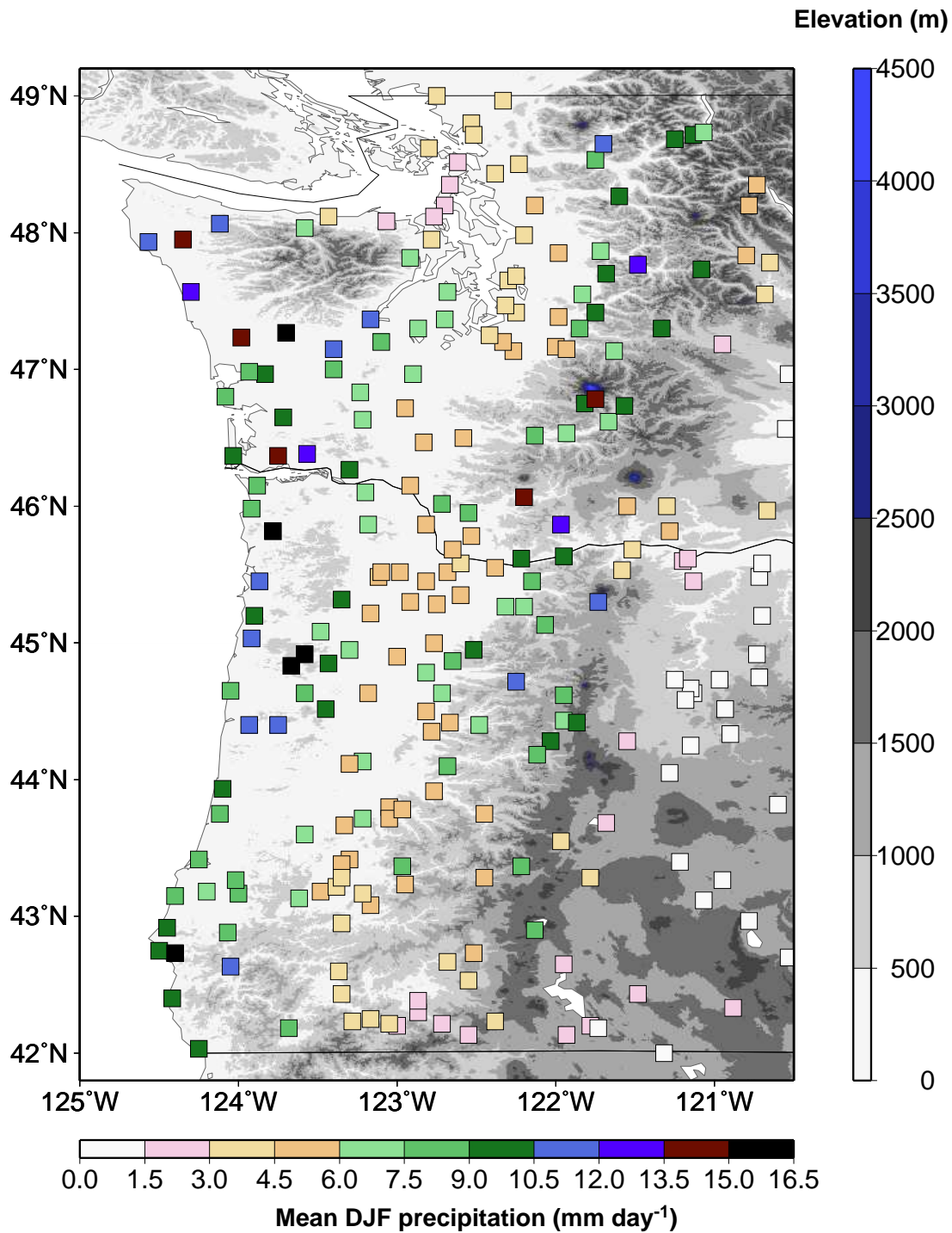
Figure 1.4: Orography and climatological precipitation for December, January, and February in western Washington and Oregon. Precipiation data from 1961-1990 historic normals provided by NCDC-NOAA.
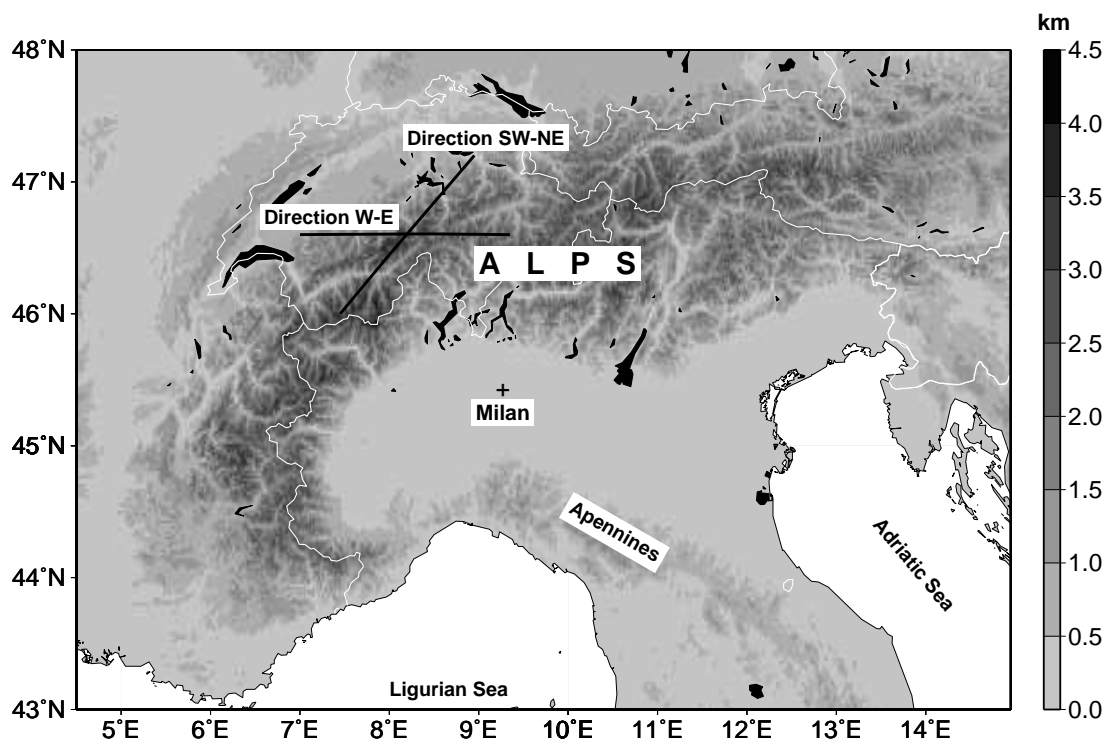
Figure 1.5: Orography and geographic features around the Alps. Direction lines are discussed in the text.
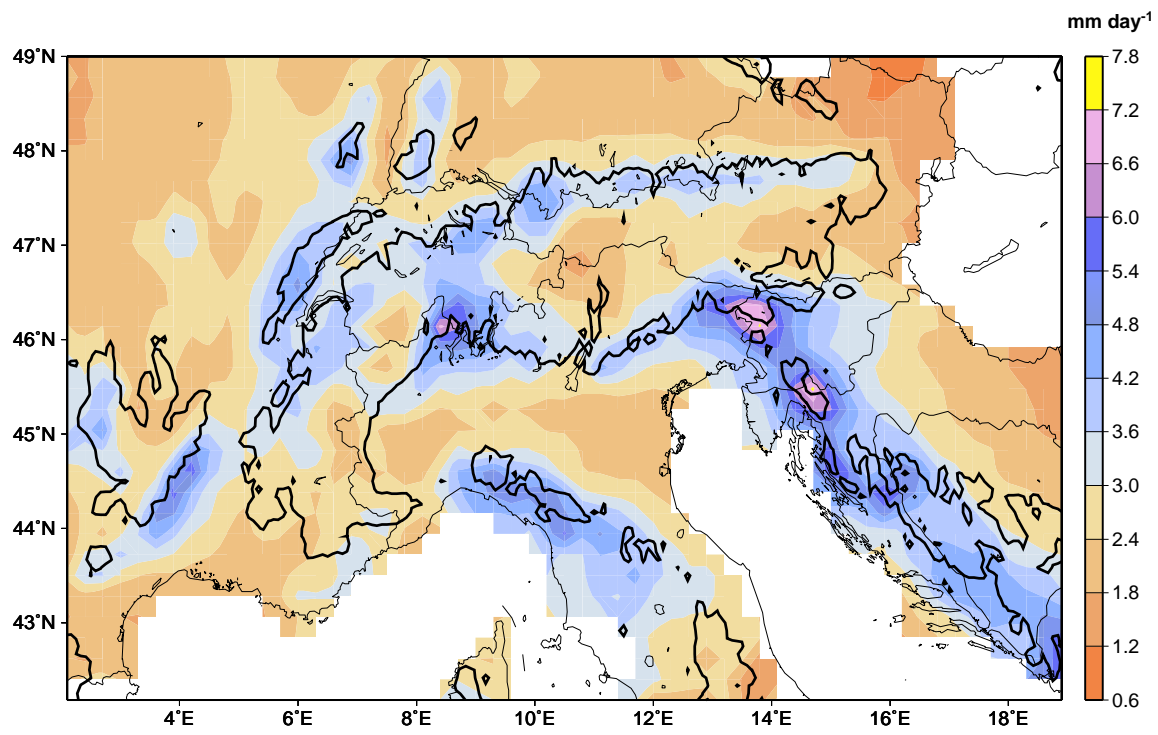
Figure 1.6: September-November climatological precipitation and 800 m orographic contour From Frei and Schär (1998).
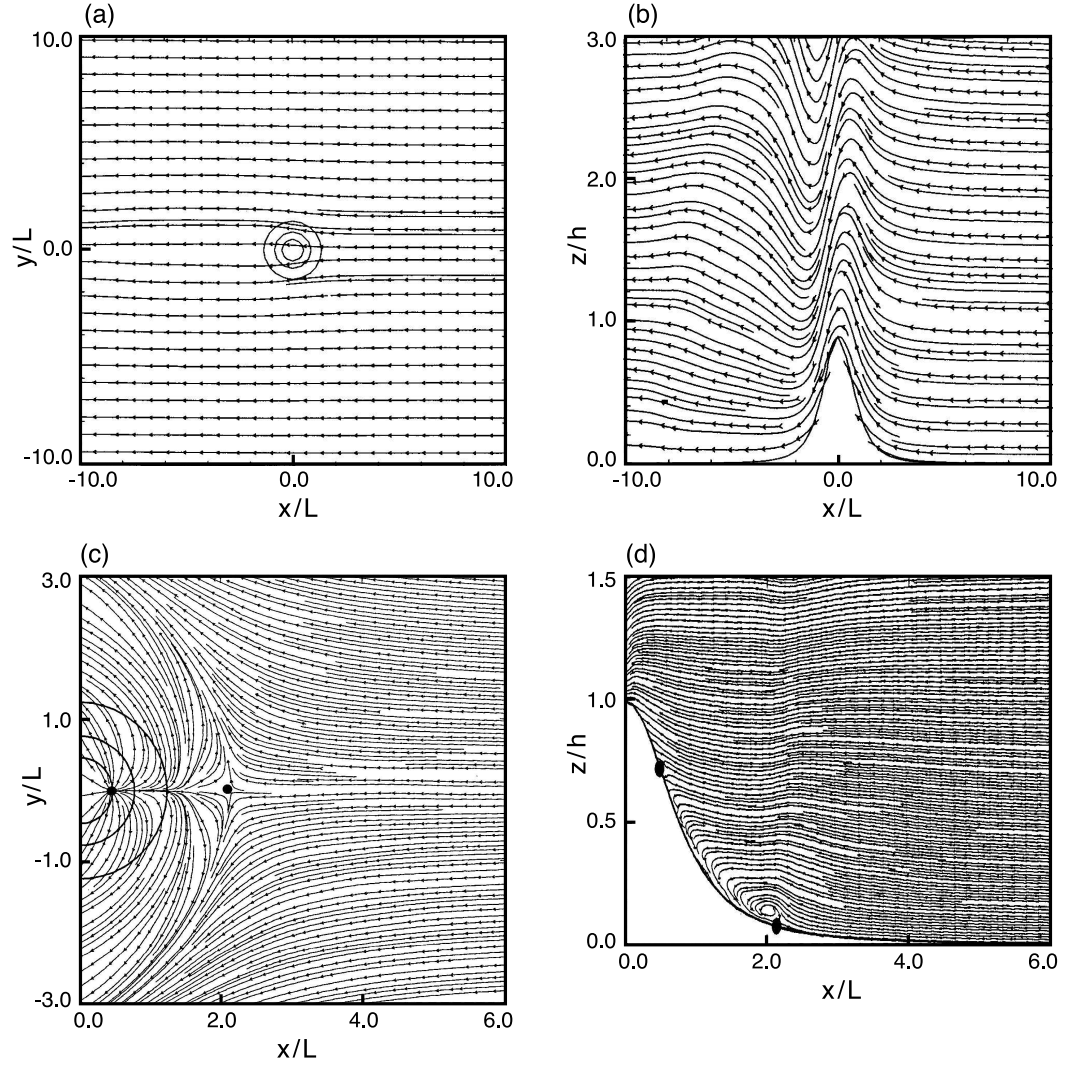
Figure 1.7: Smolarkiewicz and Rotunno (1998, 1990) numerical simulations of stream-lines (a,c) at the lower surface and (b,d) in a vertical cross section trough the center plane for (a)-(b) $\nu_d = 2.2$, and (c)-(d) $\nu_d = 0.33$. Concentric contours in (a) and (c) indicate lines of constant obstacle height with contour interval 0.25 h. The black dots in (c)-(d) indicate the location of the stagnation points. The upstream flow is from the right to left. Note that the horizontal and vertical domains, as well as the density of the streamlines are different between (a)-(b) and (c)-(d)
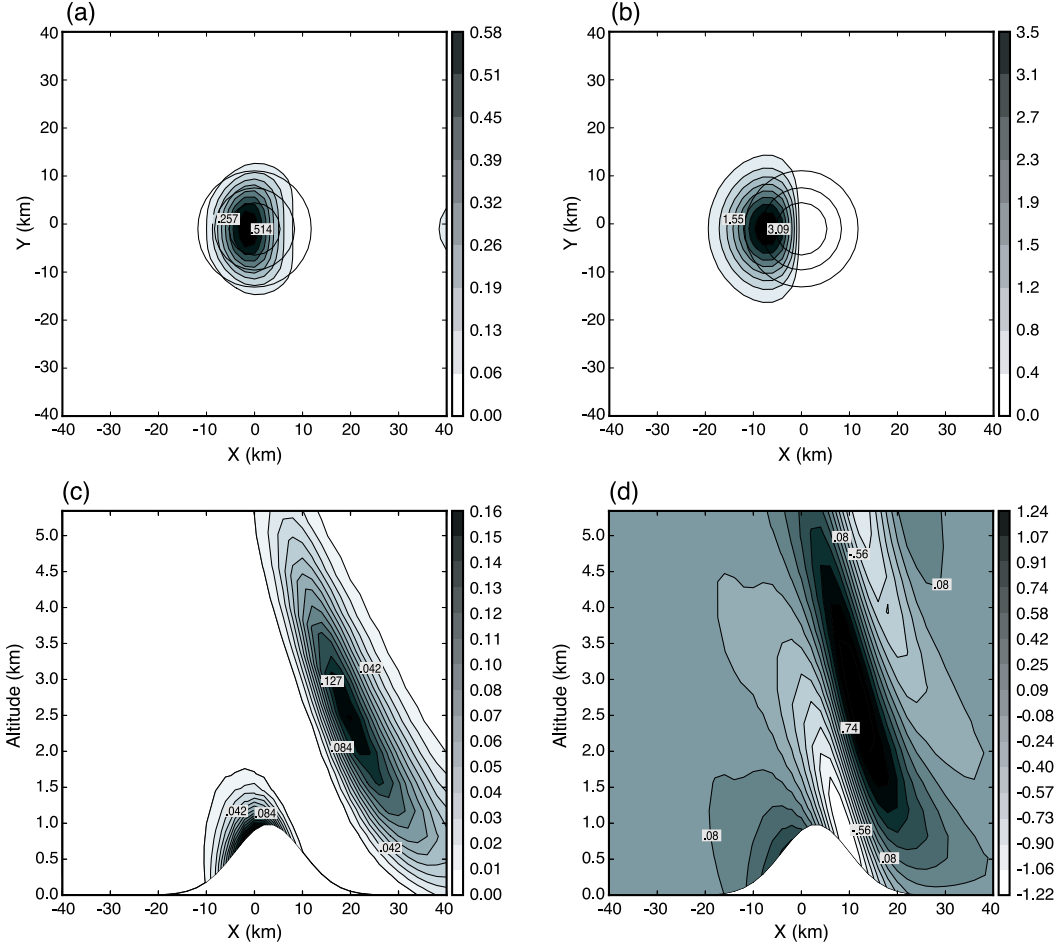
Figure 1.8: Adapted from Jiang's (2003) simulations of flow-over regime conducted with a mesoscale model with BMP in (a), (c), and (d); and a simple upslope model in (b). Panels (a)-(b) show precipitation rates (mm h^{-1}); (c) snow mixing ratio (g kg^{-1}); (d) vertical velocity (m s^{-1}). The simulations in (a) and (b) were conducted using ν_d = 1.14, ν_m = 2.08 (N_d = 0.011 s^{-1}, U=10 m s^{-1}, T_0 = 270 K, RH = 95% and h = 800 m). The parameters used in the simulation shown in (c)-(d) are identical to those used for the simulations shown in (a)-(b), except for the obstacle height which used h =1000 m. Concentric contours in (a-b) indicate lines of constant obstacle height with contour interval 0.25 h. The upstream flow is from the left to right.
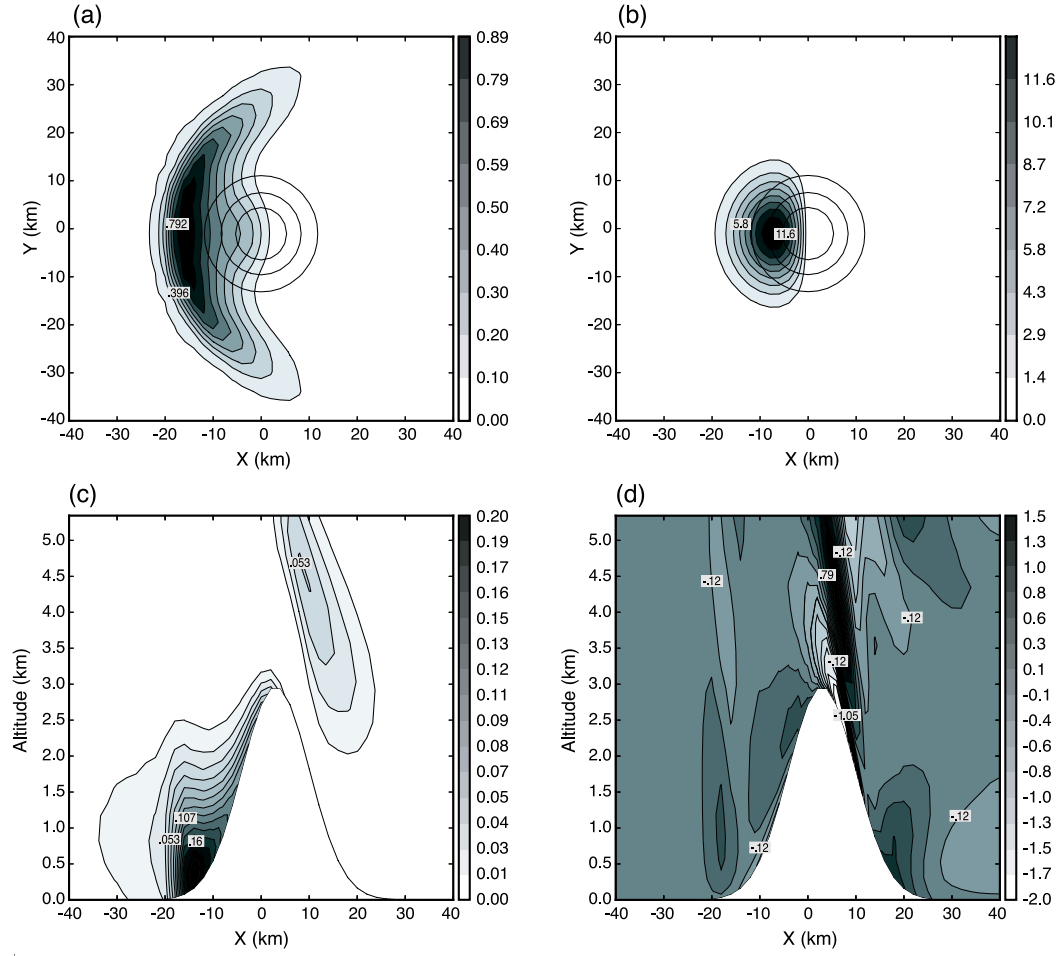
Figure 1.9: Adapted from Jiang's (2003) simulations of flow-around regime conducted with a mesoscale model with BMP in (a), (c), and (d); and a simple upslope model in (b). Panels (a)-(b) show precipitation rates (mm h^{-1}); (c) snow mixing ratio (g kg^{-1}); (d) vertical velocity (m s^{-1}). The simulations were conducted using $\nu_d = 0.30$, $\nu_m = 0.56$ ($N_d = 0.011$ s^{-1}, $U=10$ m s^{-1}, $T_0 = 270$ K, $RH = 95\%$ and $h = 3000$ m). Concentric contours in (a-b) indicate lines of constant obstacle height with contour interval 0.25 h. The upstream flow is from the left to right.
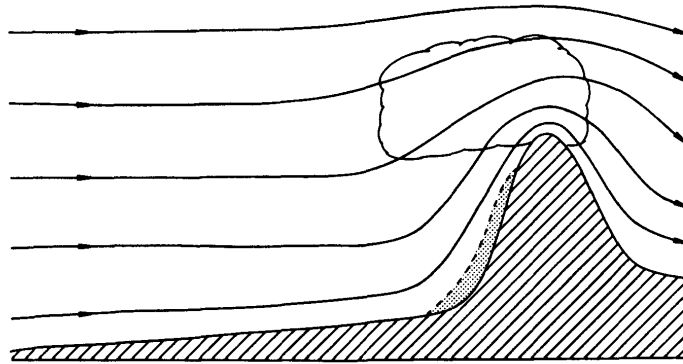
(a)
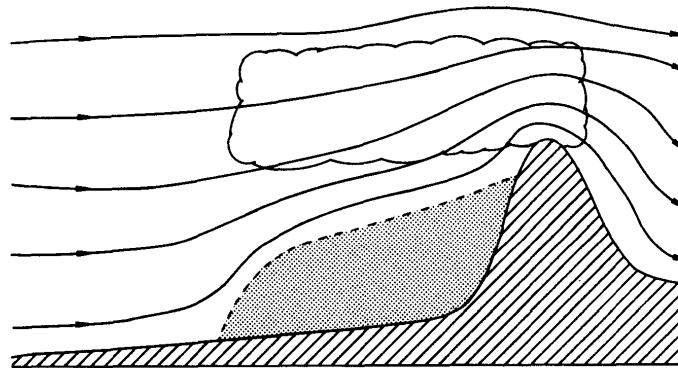
(b)

Figure 1.10: Conceptual model by Peterson et al. (1991) for low-level (a) flow-over and (b) flow-around regime. The shaded area denotes blocked flow.
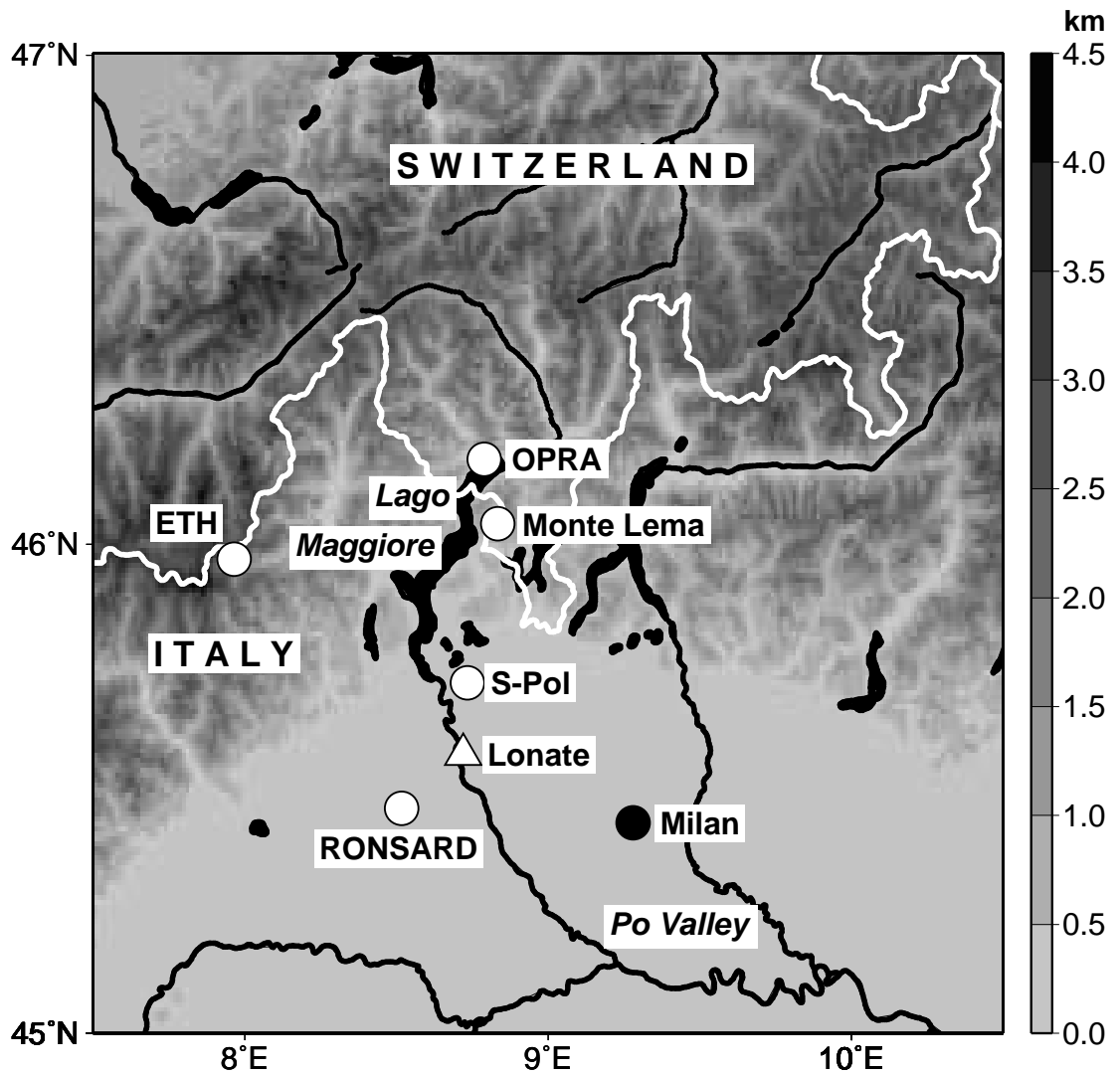
Figure 1.11: MAP observational area. The orography around Lago Maggiore is shown with the location of the observations relevant to this study. "S-Pol" marks the location of the polarimetric scanning Doppler radar. "Monte Lema" and "RONSARD" show the locations of scanning Doppler radars. "ETH" and "OPRA" mark the locations of vertically pointing radars. "Lonate" marks the locations of a wind profiler. "Milan" denotes the location of the upper-air sounding.

Chapter 2

DATA

This study uses data collected over the European Alps during MAP and over the Oregon Cascade Range during IMPROVE-2. Together, these projects documented ~30 major precipitation events, most of them associated with the passage of baroclinic systems over major mountain ranges. Similar instruments were deployed in each project, in similar positions relative to the mountains, to determine the mechanisms responsible for the orographic enhancement of precipitation. Parallel datasets allow an evaluation of the repeatability of the terrain-modified airflow and microphysical growth mechanisms in different geographical locations.

2.1 Ground-based radar data

Figures 1.11 and 1.3 show the observational areas for MAP and IMPROVE-2, respectively and the location of the ground-based observational facilities used in this study relative to the terrain. In Fig. 1.11 the Alps encircle the region of the Lago Maggiore in northern Italy. The Alpine crest is ~4 km (unless otherwise indicated all the altitudes in this study are MSL). In Fig. 1.3 the Cascades run approximately north-south through the experimental area. The crest is ~2 km.

The characteristics of the radars used in this study are listed in Table 2.1. The National Center for Atmospheric Research (NCAR) S-band dual-polarimetric radar (S-Pol) was deployed during MAP (Fig. 1.11) and IMPROVE-2 (Fig. 1.3) to simultaneously map the precipitation and airflow over the windward mountain slopes with high spatial and temporal resolution. Besides measuring reflectivity and radial velocity, a polarimetric radar transmits and receives both horizontally and vertically

polarized radiation. These measurements are influenced by the size, shape, thermodynamic phase, bulk density, and spatial orientation of the scattering hydrometeors and therefore they are useful in remotely identifying hydrometeor characteristics. Some of the relevant parameters obtained from dual-polarimetric radar measurements are: reflectivity (dBZ), differential reflectivity (ZDR), linear depolarization ratio (LDR), specific differential propagation phase (K_{DP}), and correlation coefficient between returns at horizontal and vertical polarization (ρ_{HV}). The definitions of these polarimetric variables are given in Appendix A. By analyzing the signal that a hydrometeor produces on several polarimetric variables, it is possible to infer information regarding particle type. Based on this principle, algorithms capable of identifying particle type have been developed. To classify a particular pixel, some algorithms use set thresholds (Zeng et al. 2001). The PID algorithm used in this study is based on a fuzzy logic approach, where there is a smooth transition in polarimetric observation boundaries among precipitation types (Vivekanandan et al. 1999). This algorithm determines the degree to which a particular observation belongs to each particle type and assigns the observation to the particle type that has the largest value. A detailed description of this algorithm is provided in Appendix A. Data from a radar scanning over mountainous terrain is subject to contamination by echoes from the terrain, which are often called ground clutter. Ground clutter was removed from the S-Pol data set by the process described in Appendix B.

In MAP, the S-Pol scanning sequence consisted of azimuthal sector scans manually adjusted to cover the region of heaviest orographic precipitation. The S-Pol scans alternated plan position indicator (PPI) and range-height indicator (RHI) sectors[1]. When precipitation was occurring close to or over the experimental area, the S-Pol radar scanning sequence in IMPROVE-2 normally consisted of:

---

[1]A PPI is the horizontal projection of radar data obtained while scanning the antenna in azimuth while holding the elevation angle constant. An RHI is a vertical cross section of radar data obtained when scanning the antenna in elevation while holding the azimuth constant.

i. Surveillance PPI scans collected at 0.5, 1.5, and 2.4 degrees of elevation.

ii. An eastward-looking sector consisting of 60 RHI scans at 1 deg azimuth intervals.

iii. A westward-looking RHI.

This cycle of PPIs and RHIs required $\sim$11 min to complete.

In addition to the S-Pol radar, vertically pointing (VP) radar data is also used in this study. During MAP two VP radars collected data over the southern slopes of the Alps: the University of Washington (UW) S-band Orographic Precipitation Radar (OPRA; Yuter and Houze 2003) and the Swiss Federal Institute of Technoplogy (ETH) X-band radar (Fig. 1.11). These VP radars measured reflectivity and radial velocity with high temporal resolution (1 s for OPRA, 30 s for ETH) and high vertical resolution (150 m for OPRA, 50 m for ETH). During IMPROVE-2, the National Oceanic and Atmospheric Administration (NOAA)/Environmental Technology Laboratory (ETL) S-band vertically pointing radar (White et al. 2000) was deployed near the Cascade crest (Fig. 1.3) to provide precipitation and air motion information with high resolution in time (3-8 s). The ETL radar alternately emitted single, vertically oriented rays with pulse lengths of 300 ns (range resolution of 45 m, maximum range $\sim$3.8 km) and 700 ns (range resolution of 105 m, maximum range 9.8 km). In this study we make use of the 700 ns data because its maximum range gives information in the layer extending well above the 0°C level.

2.2 Aircraft data

During MAP and IMPROVE-2, the NOAA WP-3D research aircraft equipped with a fore-aft scanning X-band (3.2 cm wavelength) tail-mounted Doppler provided detailed vector airflow information at key times and at locations obscured from the view of the ground-based S-pol radar (Jorgensen et al. 1996, Bousquet and Chong 1998,

Chong and Cosma 2000). The analysis technique applied to the P-3 airborne radar observations to obtain 3D airflow and precipitation structures is described by Bousquet and Smull (2003a,b). The P-3 also provided flight level data of meteorological parameters. During IMPROVE-2, ice-particle images from the Knollenberg Particle Measuring System (PMS) probes on the P-3 aircraft were also obtained.

2.3   Sounding data

During MAP, upper-air soundings were collected four times a day (0000, 0600, 1200 and 1800 UTC) at Milan (Fig. 1.11). During IMPROVE-2, operational and special upper-air sounding were collected at Salem, as well as at a University of Washington (UW) mobile sounding site at the foot of the mountain range (Fig. 1.3).

2.4   Wind profiler data

During MAP, the flow inside the Po Valley was sampled at every 15 min by a French UHF/VHF (ultra high frequency/very high frequency) wind profiler located at Lonate, Italy (Fig. 1.11). This profiler collected data with vertical resolution of 144 m (with a maximum range of $\sim$6 km) and 375 m (with a maximum range of $\sim$16 km). Collocated with the ETL VP radar in IMPROVE-2 was a NOAA/ETL wind profiler (Fig. 1.3) that provided a vertical profile of the winds every 60 minutes. The vertical resolution of this wind profiler is 58 m (with maximum range of $\sim$2.8 km) and 100 m (with a maximum range of $\sim$4.4 km).

Table 2.1: Characteristics of radars

Radar	Altitude (km)	λ^a (cm)	Peak power (kW)	Beam width (°)	v^b (m s^{-1})
NCAR S-Pol^c	0.280^d 0.475^e	10.6	400	0.92	[-22.4,22.4]
NOAA-ETL^f	0.512	10.4	0.360	2.5	[-10.5,10.5]^g
ETH^h	1.3	3.2	90	2.4	[-32.0,32.0]
UW OPRA^f	0.382	10	60^i, 35^j	4.3	[-25.0,25.0]

^{a} Wavelength

^{b} Nyquist interval

^{c} S-band Doppler and polarimetric

^{d} MAP

^{e} IMPROVE-2

^{f} S-band vertically-pointing Doppler

^{g} For 700 ns pulse length

^{h} X-band vertically-pointing Doppler

^{i} Maximum

^{j} Minimum

Chapter 3

CROSS-BARRIER FLOW AND STABILITY IN OROGRAPHICALLY MODIFIED STORMS

Most of the observations presented in this thesis were made as mid-latitude troughs approached a mountain range. In this chapter we present an overview of the large-scale characteristics during these storms. In addition, the mesoscale aspects of the terrain-modified cross-barrier flow will be documented, as well as the thermodynamic and kinematic characteristics upwind of the mountain ranges.

3.1 Synoptic conditions of mid-latitude systems approaching mountain ranges

Data collected during four MAP and two IMPROVE-2 mid-latitude storms have been used to study the processes responsible for orographic enhancement of precipitation. The first MAP storm relevant to this study occurred during 20 September 1999 (MAP Intensive Observing Period [IOP] 2b), when a mid-latitude system moved over northern Italy (Fig. 3.1a). The ECMWF model forecast for 1200 UTC on that day indicated a deep trough positioned over Western Europe extending south to northern Africa (Fig. 3.1b). At 850 mb the flow was southerly toward the southern flank of the Alps (Fig. 3.1c). MAP IOP3 (25-26 September 1999) and IOP5 (3 October 1999), like IOP2b, occurred ahead of baroclinic troughs (Figs. 3.2 and 3.3, respectively). On 21 October 1999 (MAP IOP8) another mid-latitude cyclone located over Western Europe (Fig. 3.4a) produced large precipitation accumulations in northern Italy. The ECMWF model showed a baroclinic trough approaching the Alps (Fig. 3.4b) and southerly flow was observed at 850 mb over the Ligurian Sea, upstream of the Alps and the Apennines (Fig. 3.4c). IOPs 2b and 8 have been widely studied

by the MAP community (e.g., Medina and Houze 2003a, Rotunno and Ferretti 2003, Bousquet and Smull 2003a,b, Steiner et al. 2003, Smith et al. 2003, Yuter and Houze 2003, Georgis et al. 2003, Asencio et al. 2003).

One of the two IMPROVE-2 cases of interest occurred during 13-14 December 2001 (Case 11) as a frontal system (Fig. 3.5a) and upper-level trough (Fig. 3.5b) passed over the Pacific Northwest and IMPROVE-2 experimental domain. As a result, westerly winds were observed at 850 mb over the Oregon coast (Fig. 3.5c). A detailed synoptic and mesoscale description of this case using observations and MM5 output is given by Garvert et al. (2005). A similar event occurred over the IMPROVE-2 network on 28 November 2001 (Case 1). The synoptic conditions (Fig. 3.6) generally resembled those for the 13-14 December case upstream of the experimental domain.

In summary, each of these six events occurred when a baroclinic system impinged upon an orograhic barrier. In each case, the far upstream wind direction around 850 mb was oriented quasi-perpendicular to the mountain range. As these systems passed over the respective mountain range, the cross-barrier flow and precipitation patterns exhibited characteristic and repeatable features that will be described in detail in secs. 3.2, 4.1.1, and 4.2.1.

3.2   Observation of distinctive cross-barrier flow patterns

Our analysis suggests the existence of two distinct configurations by which the terrain-modified flow affects precipitation in a baroclinic cloud system. The first configuration, represented by the MAP cases IOP2b, IOP3, and IOP5, is called Type A. The second configuration, represented by MAP IOP8 and Cases 1 and 11 of IMPROVE-2, is called Type B.

3.2.1   Type A cross-barrier flow pattern

By constructing time average radar fields during the heaviest precipitation periods of orographic storms, Medina and Houze (2003a) found that during MAP IOP2b the

low-level flow (from 0.5 to 2.0 km) in the Lago Maggiore (LM) region (Fig. 1.11) was preferentially south-easterly (i.e., perpendicular to the local orography). They found that during this event the entire lower layer of air rose over the terrain. Fig. 3.7a shows a vertical cross section of S-Pol radar radial velocity averaged over 3 h during IOP2b, from 0700 through 1000 UTC 20 September 1999, a period when the precipitation was intense. The cross section extends from the radar, located at the lower right corner of the panel, toward the range crest, in a direction quasi-perpendicular to the local orography and parallel to the low-level flow (red line in Fig. 3.8). The flow was positive everywhere (yellow, red and blue contours) denoting flow away from the radar or from right to left. A low-level jet rose abruptly as the airflow encountered the first large peak of the orography. This jet transported low-level moisture to higher levels (sec. 4.1.1). Mean radar fields have been constructed for MAP storms IOP3 (0000- 0300 UTC 26 September 1999) and IOP5 (1100-1400 UTC 3 October 1999), during periods of heavy precipitation. Vertical cross sections of S-Pol radar data mean radial velocity for IOP3 (Fig. 3.7b) and IOP5 (Fig. 3.7c), extending from the radar toward the range crest in a direction roughly parallel to the low-level flow (blue and green lines in Fig. 3.8), also exhibit a low-level cross-barrier jet rising over the first peak of the terrain. During IOP3 there was a jet at higher levels (around 3 km altitude), however the Type A classification is due to the jet observed just above the surface (Fig. 3.7b). The low-level air rose over the terrain suggesting a "flow-over" or unblocked flow regime. This structure will be referred to as Type A.

In summary, a low-level jet rising abruptly over the first major peaks of the terrain characterized the cross-barrier flow in Type A cases.

3.2.2   Type B cross-barrier flow pattern

A dramatically different cross-barrier flow signal appears in another set of cases: MAP IOP8, and IMPROVE-2 Cases 1 and 11. The top row of Fig. 3.9 shows mean radial velocity fields for MAP IOP8 (panel a), IMPROVE-2 Case 11 (panel b) and Case 1

(panel c). As before, the cross sections extend from the radar, located over the plains, toward the range crest. The cross sections show mean radar fields during periods of heavy precipitation. Fig. 3.9a shows a 3-hour mean vertical cross section of S-Pol radar collected from 0800 to 1100 UTC 21 October 1999, during MAP IOP8. The cross section extends from the S-Pol radar, located at the lower right-hand corner of the panel, across the Alps in a direction approximately perpendicular to the local orography (white line in Fig. 3.8). The positive (yellow, red and purple) contours denote flow away from the radar, whereas negative (green) contours show flow toward the radar. The white contour denotes radial velocities ~ 0 m s^{-1}. At ranges close to the radar near 1.0 km altitude there is a layer of strong wind shear (~ 18 m s^{-1} km^{-1}). This layer sloped upward with distance toward the Alpine crest. Above this layer the airflow was strong and directed away from the radar, i.e., ascending the terrain in a cross-barrier direction, while the radial component of the flow at lower levels was weak and directed toward the radar (i.e. away from the higher terrain). The NOAA P-3 aircraft collected radar data within the cross section shown in Fig. 3.9a between 0917-0952 UTC 21 October 1999. Fig. 3.10a shows the flow component in the plane of the cross section as derived from airborne Doppler radar data. Airborne radar provided information is some regions that were obscured from the view of the ground-based radar. The full extent of the shear layer is not evident from the ground-based radar because blockage of the beam by the terrain and decreasing resolution (i.e., beam broadening) at more distant ranges. The airborne radar shows that the shear layer was not only present over the lower Alpine slopes, but also extended over the higher terrain (cf. Figs. 3.9a and 3.10a). The airborne radar data show weak and reversed (downslope) flow within the Alpine valleys (Fig. 3.10a), which has been documented by Steiner et al. (2003) and Bousquet and Smull (2003b).

In the IMPROVE-2 cross sections, the S-Pol radar is located in the lower left corner of the panels and they extend from west to east (white line in Fig. 3.11). Fig. 3.9b shows a vertical cross section of 3 h mean S-Pol radar radial velocity collected

from 2300 UTC 13 to 0200 UTC 14 December 2001 (Case 11), an IMPROVE-2 case in which widespread heavy rainfall accumulations occurred. The cross section extends from the S-Pol radar across the Oregon Cascade Range, in a direction perpendicular to the orography. The radial velocities are positive everywhere, corresponding to flow directed away from the radar, thus indicating flow toward the barrier at all levels. At the lowest level where data were available, the flow was 10 ms^{-1}. However, airborne radar data, available very close to the surface, measured cross-barrier flow as low as 4 ms^{-1} (Fig. 3.10b). As opposed to low-level flow away from the terrian observed during IOP8, flow in the IMPROVE-2 cases was directed toward the terrain at all levels during Case 11. The weak flow at low levels was bounded above by a layer of strong shear separating it from strong cross barrier flow aloft (Fig. 3.9b). The shear layer is seen to extend almost to the crest of the mountain range, even subject to the limitations of the ground-based radar discussed above. The P-3 collected radar data over an area encompassing the region shown in Fig. 3.9b, but a malfunction of airborne radar prevented sampling along this particular section. Fig. 3.10b thus shows P-3 cross-barrier flow along a west-east section located ~40 km north of that shown in Fig. 3.9b (red line in Fig. 3.11). In order to span a broad cross-barrier distance, this display was constructed from a composite of airborne radar data collected over a ~45 min period centered at 0000 UTC 14 December 2001. Although the times and locations of data shown in Figs. 3.9b and 3.10b are somewhat different, the general features depicted are similar, confirming that many flow features were ubiquitous along this relatively 2D segment of the Cascade range. The reach of airborne radar coverage into the leeside region captures downward-sloping flow contours (Fig. 3.10b) consistent with the presence of a terrain-induced gravity wave, which has been documented by Garvert et al. (2006). Further evidence of strong downslope winds are consistent with a well developed mountain wave in central Oregon was provided by reports of damaging winds during his interval (NOAA Storm Data, 2001; http://www7.ncdc.gov/SerialPublications/).

Figure 3.9c shows a vertical cross section of S-Pol radar data collected from 1600 to 1900 UTC 28 November 2001 (Case 1), during the first event of IMPROVE-2. The location of this cross section relative to the terrain is identical to that in Fig. 3.9b. The flow direction was everywhere away from the radar, indicating cross-barrier flow. The mean radial velocity exhibited weak low-level flow and a sheared layer sloping upward over the terrain, similar to the structure observed during MAP IOP8 and during Case 11 of IMPROVE-2 (Figs. 3.9a,b). There were no aircraft Doppler radar data collected in this case, however the available ground-based measurements exhibit strong similarity to those cases previously discussed.

In summary in Type B cases the cross-barrier flow was weak at low-levels (below $\sim$1 km). At crest level the cross-barrier flow was strong and away from the radar. In between was a layer of highly sheared-flow, which sloped upward with distance toward the crest.

3.3 Characteristics of the flow upwind of the terrain

This section describes flow characteristics upwind of the mountains during cases exhibiting Type A and Type B airflow patterns. For the MAP cases, Milan soundings were used (Fig. 1.5). UW soundings were used for IMPROVE-2 Cases (Fig. 1.3). The soundings collected during Type A storms are shown in Fig. 3.12. At low-levels they were characterized by potential instability and display moist-unstable layers (e.g., between 900 and 650 mb in Fig. 3.12a). This structure is also reflected in the vertical profiles of squared moist Brunt-Väisälä frequency[1] ($N_m{}^2$; Fig. 3.13d) which is negative at $\sim$1-1.5 km (above the lowest layer where a temperature inversion existed) implying potentially unstable atmospheres. $N_d{}^2$ was positive for Type A cases (Fig. 3.13c). For the purposes of this study, $N_m{}^2$ will be considered to be the relevant measure

---

[1]The resolution of the original sounding was decreased slightly and interpolated to a regular grid. A running mean filter (averaging vertical points over a 2 km-wide layer) was then applied to the temperature data. $N_m{}^2$ was calculated following Durran and Klemp (1982).

of the stability. This choice is consistent with the fact that we are considering cases where deep cloud layers and heavy precipitation were occurring over the windward slopes of the terrain. We assume that even if the upwind airflow was sub-saturated (Fig. 3.13b) it reached saturation by the time it moved over the windward slopes, as it was producing heavy rainfall. This is also consistent with the observed convective nature of the radar reflectivity during these cases, which suggested that instability was released over the terrain (Fig. 3.7d-f discussed in sec. 4.1.1).

The wind structure of Type A cases consisted of a jet at ~0.5 km (IOP3 and IOP5 had an additional jet ~2 km as seen in Fig. 3.14a). The winds veered with height between 0.5 and 1.5 km with the wind direction remaining fairly constant above this level (Fig. 3.14b). In the LM region (Fig. 1.5), it is difficult to define a single characteristic terrain orientation since the Alpine range curves. Since the wind direction at ~1 km for Type A cases was ~180° (Fig. 3.14b), a west-east (W-E) oriented orography was assumed to calculate the components of the wind perpendicular and parallel to the terrain (Fig. 1.5). The cross-barrier component of the winds exhibited a low-level jet between the surface and 1 km (Fig. 3.14c), documenting the low-level jet seen in Fig. 3.7a-c before it reached the windward slopes and rose over the terrain. The along-barrier component had a jet at ~0.5 km (Fig. 3.14d) as the flow at that level was southeasterly (Fig. 3.14b).

Figure 3.15 shows the soundings collected during Type B storms, which show stable layers at low levels (e.g., the inversion between 900 and 800 mb in Fig. 3.15a). The vertical profiles of squared Brunt-Väisälä frequency indicated that the air was statically stable when subsaturated ($N_d{}^2$; Fig. 3.16c), a characteristic that was also observed for Type A soundings (Fig. 3.13c). However a distinction existed with respect to saturated flow ($N_m{}^2$; Fig. 3.16d). The soundings corresponding to Type B cases exhibited mostly positive $N_m{}^2$ values, denoting absolute stability (Fig. 3.16d). The air was particularly stable around 1.5 km for IOP8 and Case 1 (black and red dots, respectively). Slightly negative $N_m{}^2$ values occurred in a thin layer during Case

11 (blue dots in Fig. 3.16d). Type B cases occurred under colder (cf. Figs. 3.13a and 3.16a) and higher relative humidity (cf. Figs. 3.13b and 3.16b) conditions. Additional sounding characteristics, such as the lifting convection level (LCL), the level of free convection (LFC), the surface temperature and the 0°C level, are given in Table 3.1.

The wind structure for Type B IOP8 had weak wind speeds below ~0.8 km, noticeably increasing in the layer immediately above (black dots in Fig. 3.17a). The wind direction veered by ~180° between the lowest level and ~0.8 km (black dots in Fig. 3.17b). For the additional Type B soundings the wind speed increased by ~40 m s^{-1} from the surface up to 2.5 km (red and blue dots in Fig. 3.17a). For IOP8 the winds ~1 km were southeasterlies (Fig. 3.14b), therefore a southwest-northeast (SW-NE) oriented orography was assumed to calculate the components of the wind perpendicular and parallel to the terrain for this case (Fig. 1.5). For the IMPROVE-2 cases, the orography orientation was assumed to be north-south (N-S). The cross-barrier wind for Type B cases have a negative component (i.e., away from the terrain) below ~0.5 km (Fig. 3.17c). The cross-barrier flow increased with height to reach 25 m s^{-1} at ~1.5 km (Fig. 3.17d), forming the shear layer observed in the radar structures (Figs. 3.9a-c and 3.10a-b). The magnitude of the along-barrier component had a local maximum at low levels (below ~1.5 km, Fig. 3.17d)[2]. The cross-barrier wind and moist stability were averaged over the lowest 3 km to calculate flow parameter ν_m, Rossby radius of deformation (L_R) and Rossby number (Ro) (see Table 3.1). For Type A storms IOP2b and 3, $\nu_m > 1$. For Type A storm IOP5, ν_m was not calculated since $N_m{}^2 < 0$. For Type B storms IOP8, $\nu_m < 1$. Type B Cases 1 and 11 had $\nu_m > 1$ despite having moderate to large values of stability as a result of their strong cross-barrier winds (Table 3.1). The distance from the sounding site to the mountain crest was ~140 km for MAP and ~100 km for IMPROVE-2. Table

---

[2]During IOP8, Bousquet and Smull (2003a) documented the existence of an along-barrier jet. For Cases 1 and 11, the flow near the Oregon coast (i.e., far upstream) had a large along-barrier component. Garvert et al. (2006) concluded that a clearly defined barrier jet was absent during Case 11.

3.1 shows that Type A storms sounding were collected more than a L_R away from the mountain crest, i.e., sufficiently away to be consider not perturbed by the terrain and representative of the upstream conditions. On the other hand Type B soundings were collected within a L_R from the mountain and were probably affected by its presence.

Summarizing, Type A low-level upstream atmosphere consisted of neutral or potentially unstable stratification and embodied a cross-barrier jet. When the low-level jet reached the first major rise of the terrain, it abruptly ascended over the barrier. For Type B cases, the low-level flow upwind of the mountain range consisted of mostly stable air and weak (or even negative, i.e., away from the mountain) cross-barrier flow. The flow $\sim$2.0-2.5 km altitude rose gradually over the low-level, stable flow (and the terrain). A shear layer formed above the low-level air, which also sloped upward in concert with the terrain.

Table 3.1: Sounding-derived parameters for selected MAP and IMPROVE-2 storms

Experiment	MAP[†]				IMPROVE-2[‡]	
Storm	IOP2b	IOP3	IOP5	IOP8	Case 1	Case 11
Time (UTC)	0900	0000	1200	0600	1726	2356
Date (dd/mm)	20/09	26/09	03/10	21/10	28/11	13/12
Type	A	A	A	B	B	B
$T_s{}^a$ (°C)	18.5	20.5	21.8	7.2	10.5	10.6
$q_s{}^b$ (g kg^{-1})	12	13	10	5	6	7
$Z_0{}^c$ (km)	3.5	3.8	3.3	2.9	2.6	2.0
LCL^d (km)	0.4	0.5	0.8	0.5	0.6	0.2
LFC^e (km)	2.1	1.3	1.0	0.5	NA	1.2
$N_m{}^{2*,f}$ (10^{-4} s^{-2})	0.03	0.03	-0.41	1.60	0.71	0.37
$U_\perp{}^{*,g}$ (m s^{-1})	14.1	8.3	9.1	11.6	21.5	22.5
$L_R{}^h$ (km)	54	54	NA	392	160	116
Ro^i	3.2	1.9	2.1	2.6	6.7	7.0
$\nu_m{}^j$	2.6	1.5	NA	0.3	1.3	1.9

[†] Mean crest height in experimental domain (h) = 3.1 km, mean mountain half-width in experimental domain (a) = 44 km ; [‡] h = 1.9 km, a = 32 km

[*] Variables vertically averaged over the lowest 3 km; [a] Surface temperature; [b] Surface mixing ratio; [c] Zero degree level; [d] Lift condensation level; [e] Level of free convection; [f] Moist squared Brunt-Väisälä frequency; [g] Cross-barrier wind; [h] Rossby radius of deformation: $L_R = \frac{N_m h}{f}$; f = Corolis parameter; [i] Rossby number: $Ro = \frac{U_\perp}{fa}$; [j] Moist flow parameter: $\nu_m = \frac{U_\perp}{N_m h}$
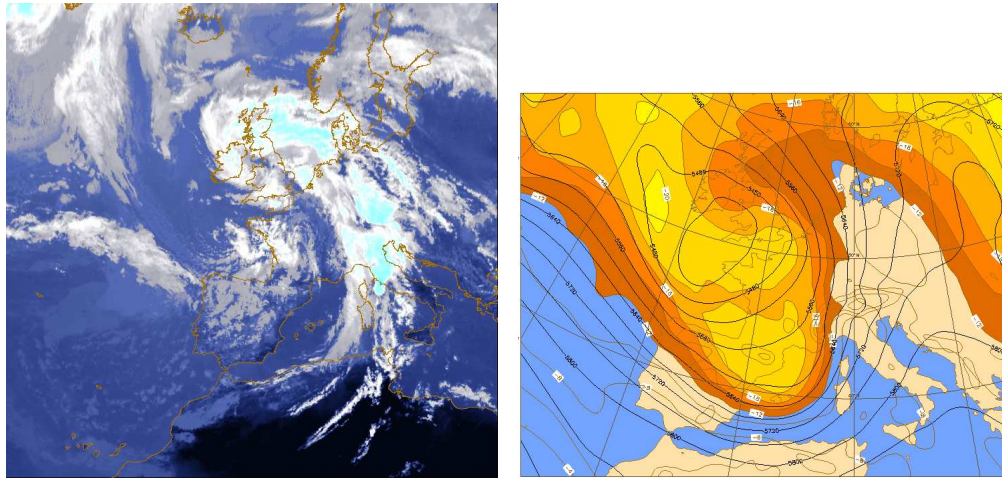
(a)

(b)
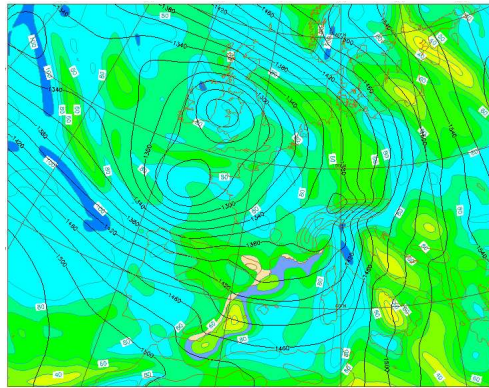
(c)

Figure 3.1: (a) Infrared satellite image at 1200 UTC 20 September 1999. (b) 500 mb geopotential height (black contours, 40 m interval) and air temperature (color shading, 2°C interval), (c) 850 mb geopotential height (black contours, 20 m interval) and relative humidity (color shading, 10% interval) from 12h ECMWF forecast valid at 1200 UTC 20 September 1999.
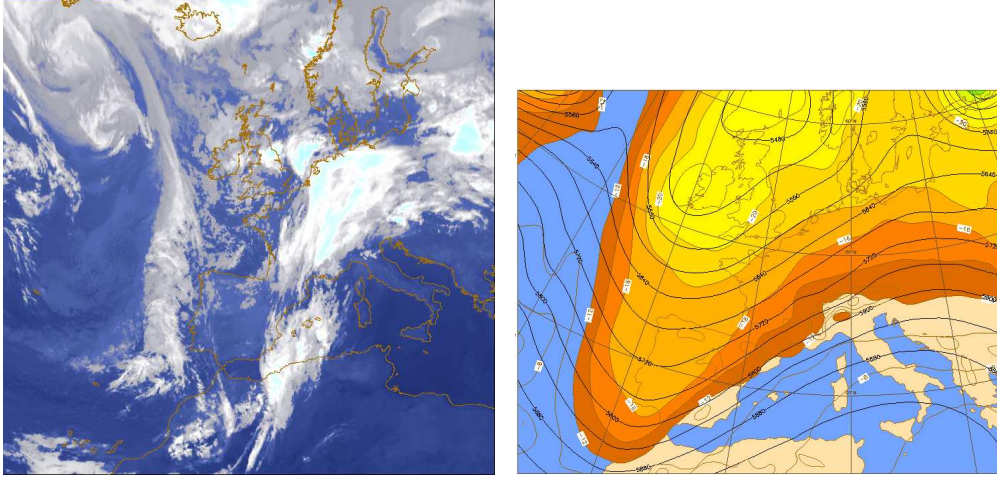
(a)

(b)
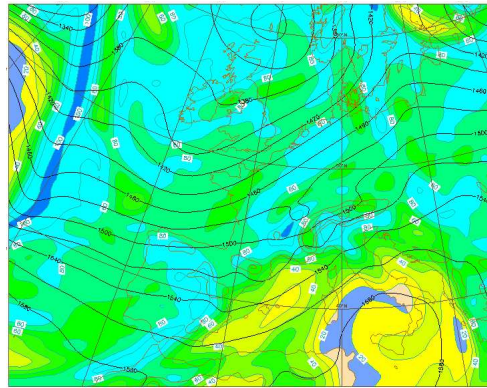
(c)

Figure 3.2: (a) Infrared satellite image at 0100 UTC 26 September 1999. (b) 500 mb geopotential height (black contours, 40 m interval) and air temperature (color shading, 2°C interval), (c) 850 mb geopotential height (black contours, 20 m interval) and relative humidity (color shading, 10% interval) from 36h ECMWF forecast valid at 1200 UTC 25 September 1999.
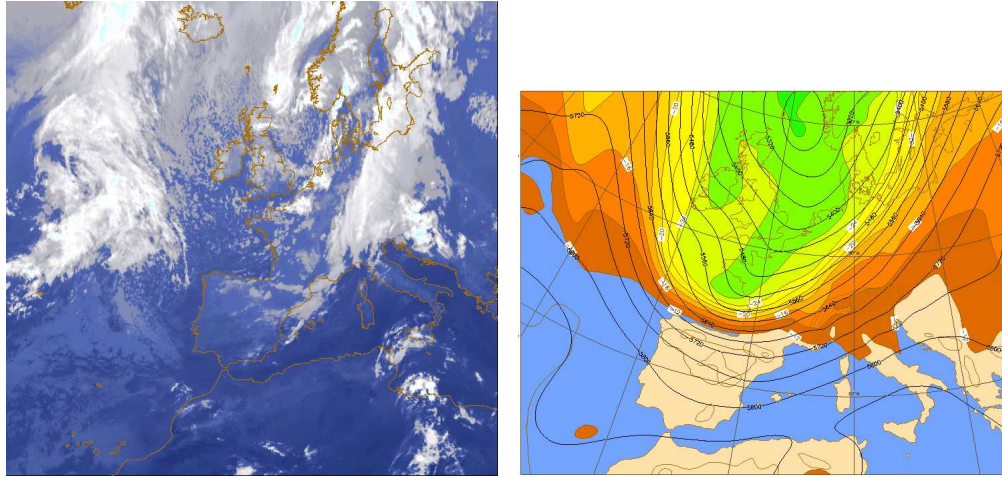
<div align="center">(a)</div>

<div align="center">(b)</div>
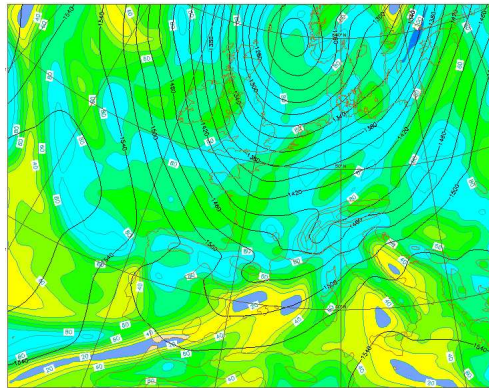
<div align="center">(c)</div>

Figure 3.3: (a) Infrared satellite image at 2100 UTC 3 October 1999. (b) 500 mb geopotential height (black contours, 40 m interval) and air temperature (color shading, 2°C interval), (c) 850 mb geopotential height (black contours, 20 m interval) and relative humidity (color shading, 10% interval) from 12h ECMWF forecast valid at 1200 UTC 3 October 1999.

48
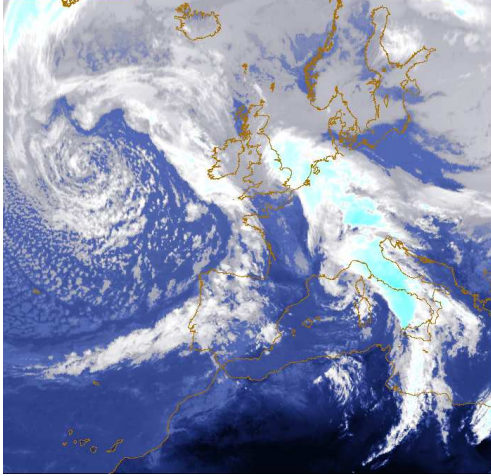
(a)
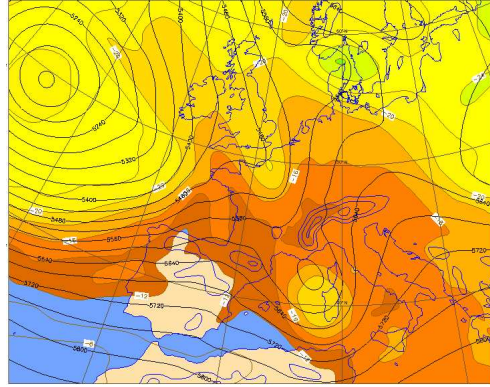
(b)
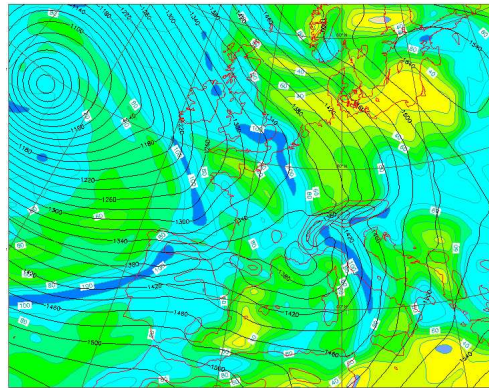
(c)

Figure 3.4: (a) Infrared satellite image at 1200 UTC 21 October 1999. (b) 500 mb geopotential height (black contours, 40 m interval) and air temperature (color shading, 2°C interval), (c) 850 mb geopotential height (black contours, 20 m interval) and relative humidity (color shading, 10% interval) from 12h ECMWF forecast valid at 1200 UTC 21 October 1999.
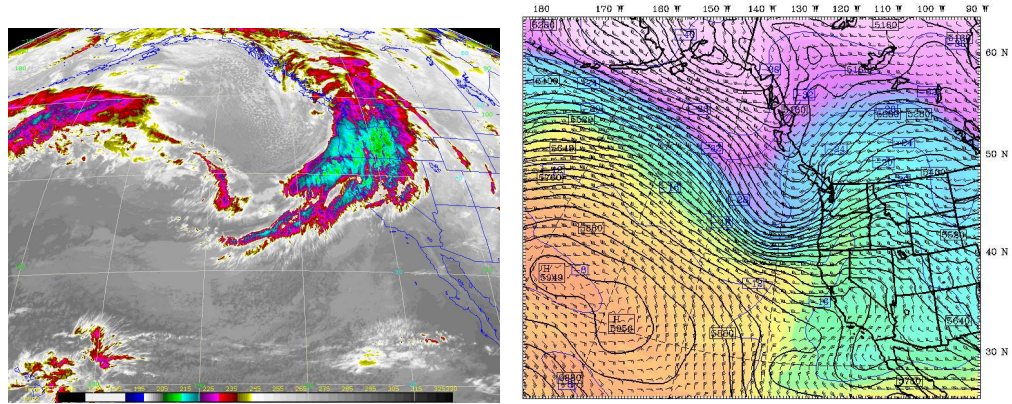
(a)

(b)
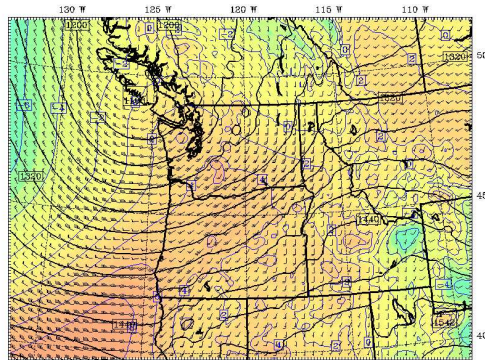
(c)

Figure 3.5: (a) Infrared satellite image at 0000 UTC 14 December 2001. (b) MM5 500 mb geopotential height (black contours, 30 m interval), air temperature (color shading and blue contours, 4°C interval), and winds from initailized UW operational 36-km run. (c) MM5 850 mb geopotential height (black contours, 30 m interval), air temperature (color shading and blue contours, 2°C interval) and winds from initialized UW operational 12-km run. MM5 output valid at 0000 UTC 14 December 2001.
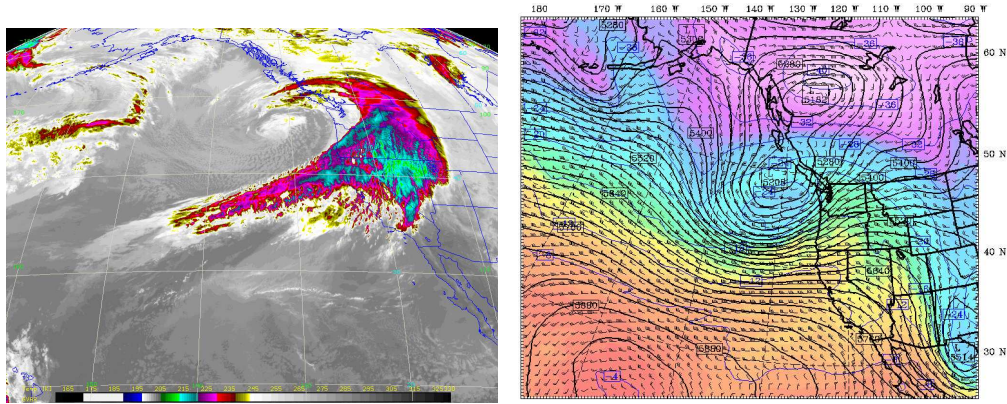
(a)

(b)
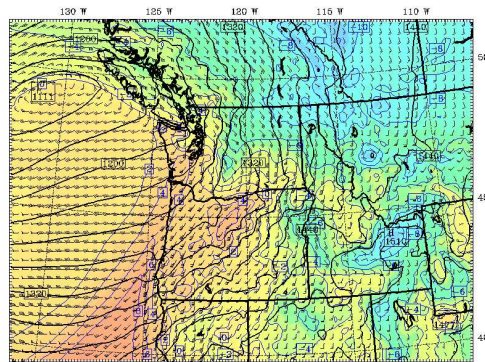
(c)

Figure 3.6: (a) Infrared satellite image at 1800 UTC 28 November 2001. (b) MM5 500 mb geopotential height (black contours, 30 m interval), air temperature (color shading and blue contours, 4°C interval), and winds from 6h UW operational 36-km run. (c) MM5 850 mb geopotential height (black contours, 30 m interval), air temperature (color shading and blue contours, 2°C interval) and winds from 6h UW operational 12-km run. MM5 output valid at 1800 UTC 28 November 2001.
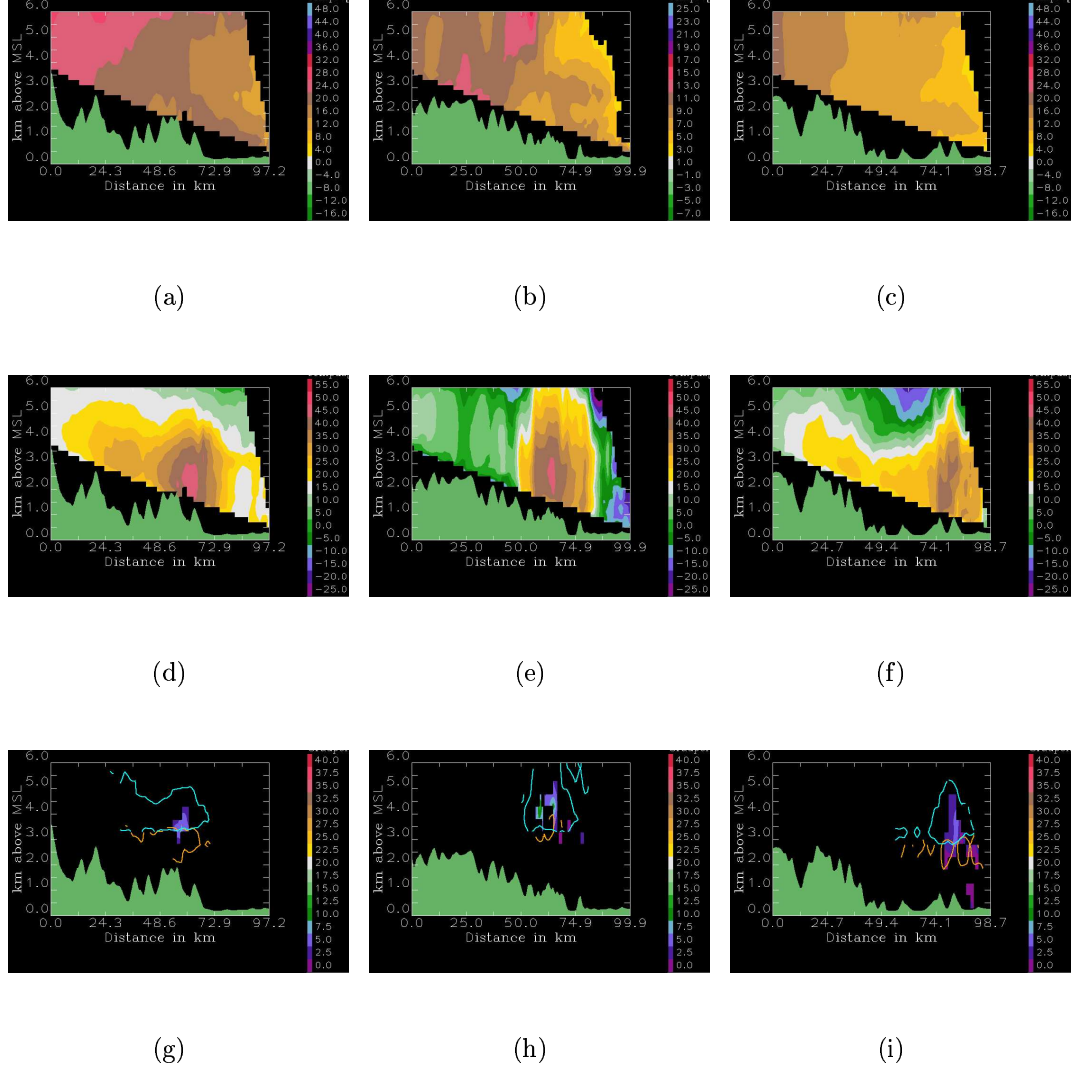
Figure 3.7: Vertical cross section of S-Pol radar data extending from the radar site (on the bottom RHS of each panel) toward the mountain crest. The fields in the panels have been either averaged or accumulated for IOP2b (0700-1000 UTC 20 September 1999, first column), IOP3 (0000-0300 UTC 26 September 1999, second column), and IOP5 (1100-1400 UTC 3 October 1999, third column). The top row shows mean radial velocity ($\mathrm{m\,s^{-1}}$; Positive contours denote flow away from the radar, i.e., from right to left), the middle one shows reflectivity (dBZ), and the bottom one shows accumulated frequency of occurence of particle types (%). Particle types shown are: dry snow (cyan contour of 45%, 30%, and 20%, from left to right), wet snow (orange contour of 30%, 5%, and 8%, from left to right) and graupel (color shading). Orography shown in green shading. The locations of the cross sections are indicated in Fig. 3.8.
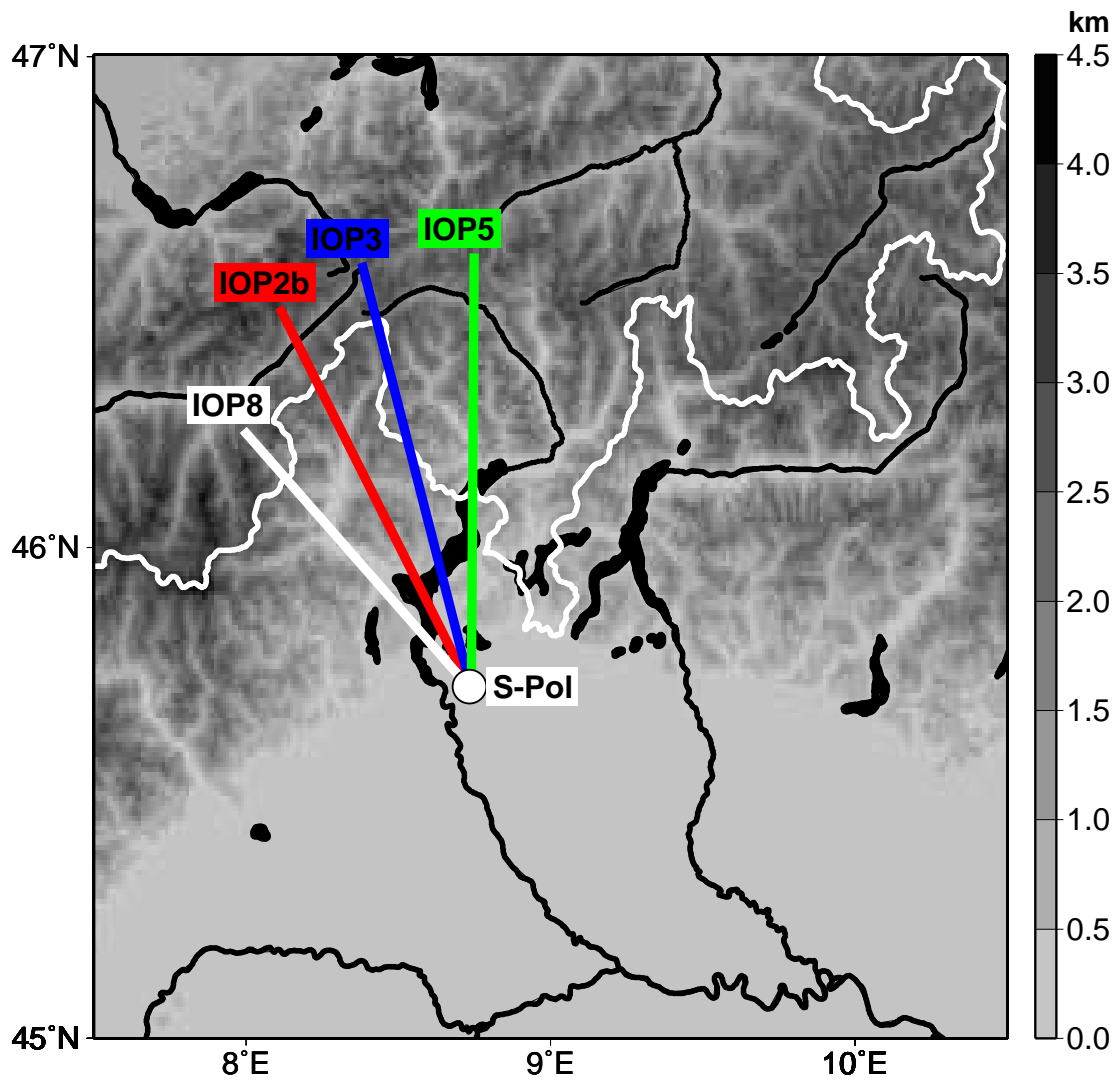
Figure 3.8: Location of vertical cross sections in relation to orography for MAP storms.
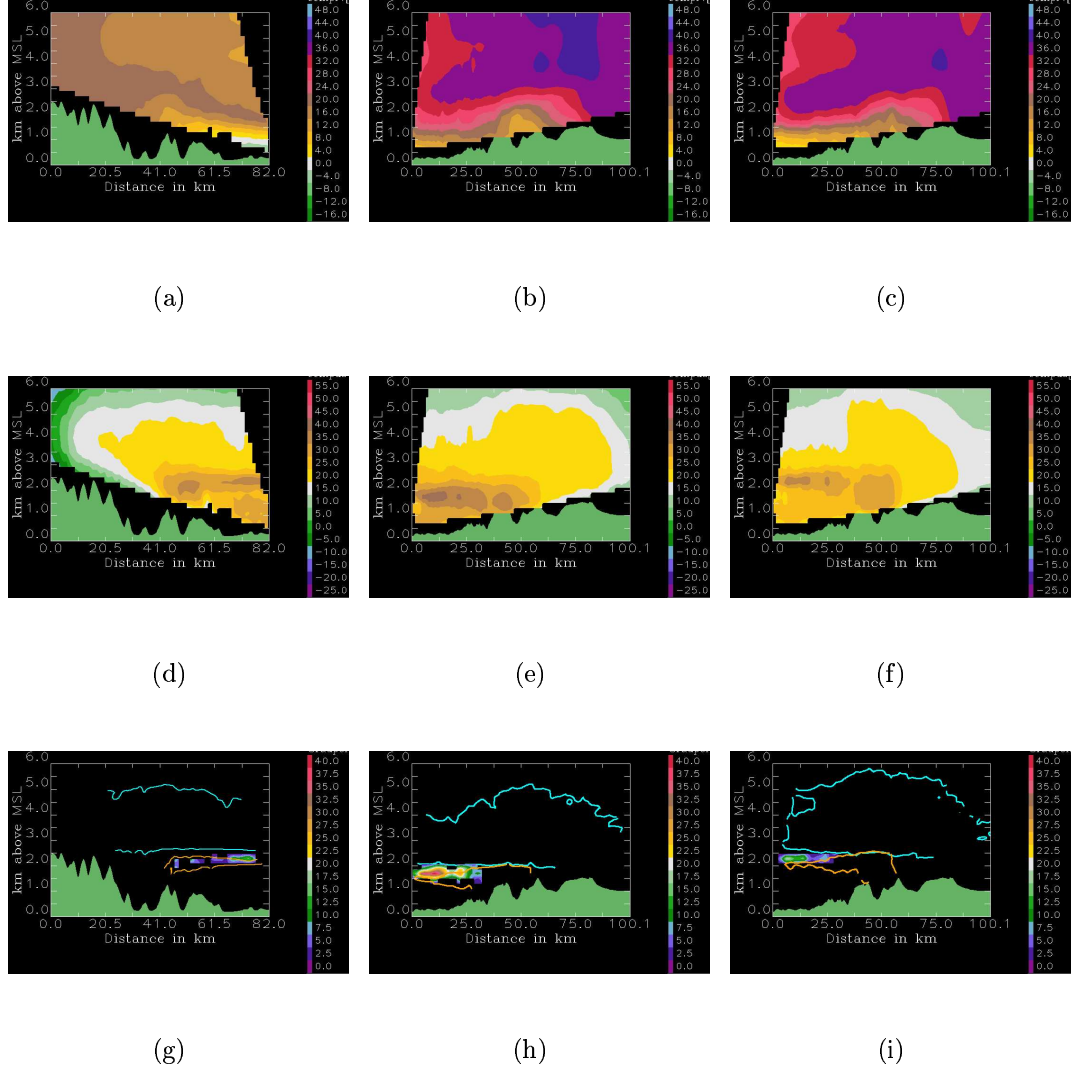
Figure 3.9: Vertical cross section of S-Pol radar data extending from the radar site (on the bottom RHS of the panels in first column, on the bottom LHS of the rest of the panels) toward the mountain crest. The fields in the panels have been either averaged or accumulated for IOP8 (0800-1100 UTC 21 October 1999, first column), Case 11 (2300 UTC 13 December to 0200 UTC 14 December 2001, second column), and Case 1 (1600-1900 UTC 28 November 2001, third column). The variables shown are as in Fig. 3.7. Particle types shown are: dry snow (cyan contour of 70%, 70%, and 45%, from left to right), wet snow (orange contour of 60%, 40%, and 35%, from left to right) and graupel and/or dry aggregates (color shading). Orography shown in green shading. The locations of the cross sections are indicated by white lines in Figs. 3.8 and 3.11.

(a)

(b)

(c)

(d)
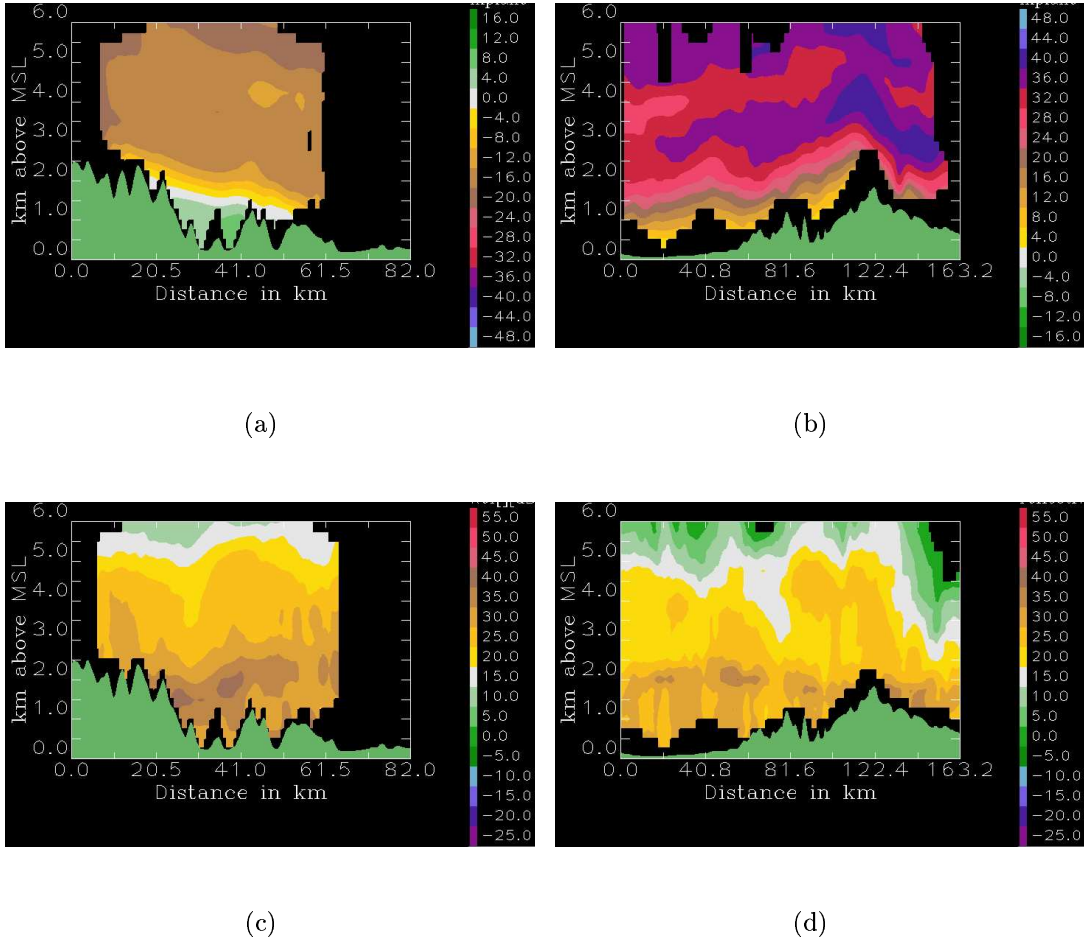
Figure 3.10: Vertical cross section of P-3 airborne radar analysis for IOP8 from data collected around 0952 UTC 21 October 1999 (first column) and Case 11 from data collected over a 45 min period centered at 0000 UTC 14 December 2001 (second column). The top row shows wind velocity in the direction of the cross section ($\mathrm{m\,s^{-1}}$; Positive values denote flow from left to right), the bottom row shows reflectivity (dBZ). Orography shown in green shading. The locations of the cross sections are indicated in Figs. 3.8 (white line) and 3.11 (red line). From Medina et al. (2005)
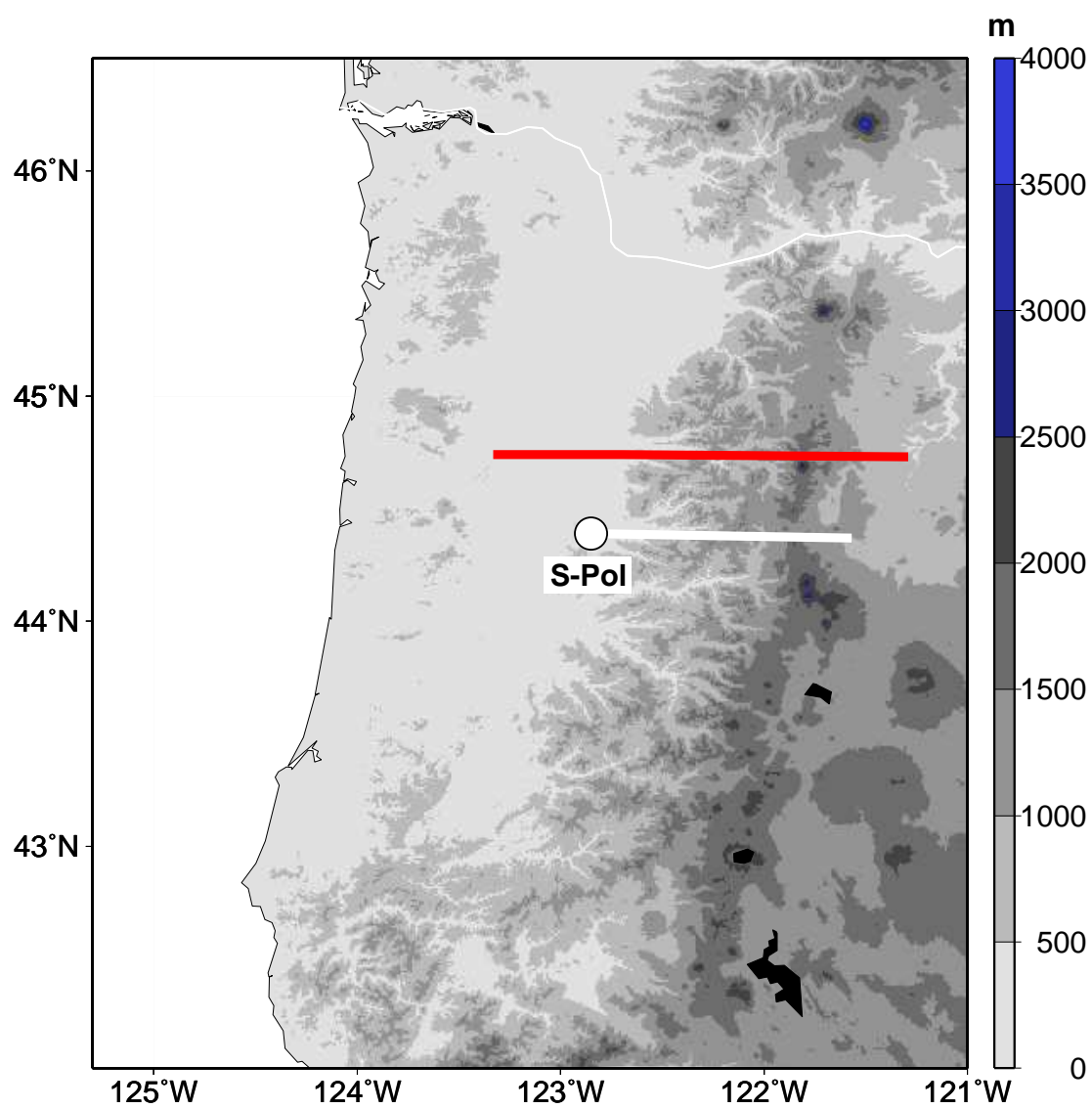
Figure 3.11: Location of vertical cross sections in relation to orography for IMPROVE-2 storms.

(a)

(b)

(c)
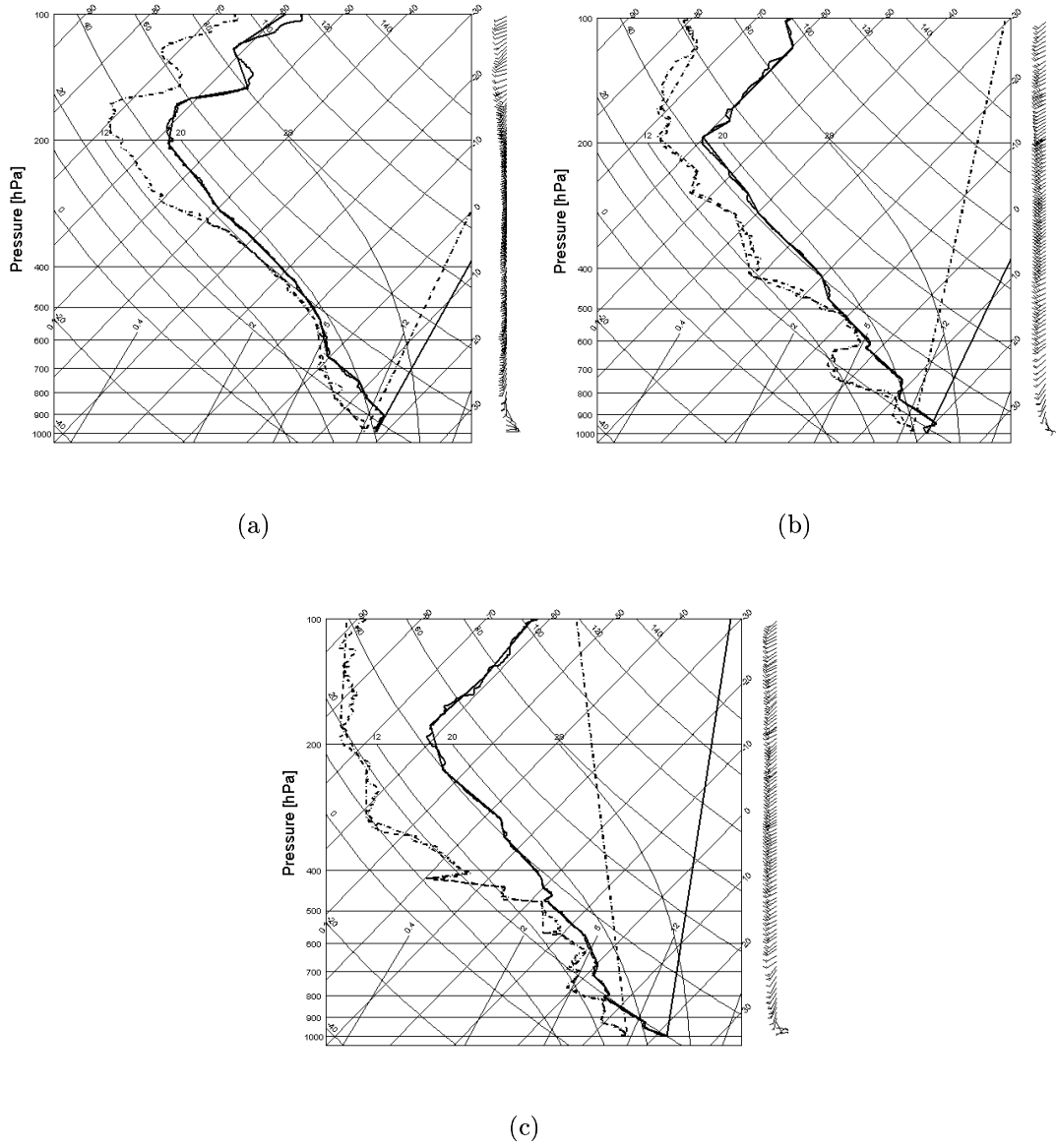
Figure 3.12: Wind vectors and skew T-log p diagram of temperature (solid line) and dew-point temperature (dashed line) from Milan soundings collected during (a) IOP2b (0900 UTC 20 September 1999), (b) IOP3 (0000 UTC 26 September 1999), and (c) IOP5 (1200 UTC 3 October 1999). Temperature, moist and dry adiabat are in °C , saturation mixing ratio lines are in g kg^{-1}.
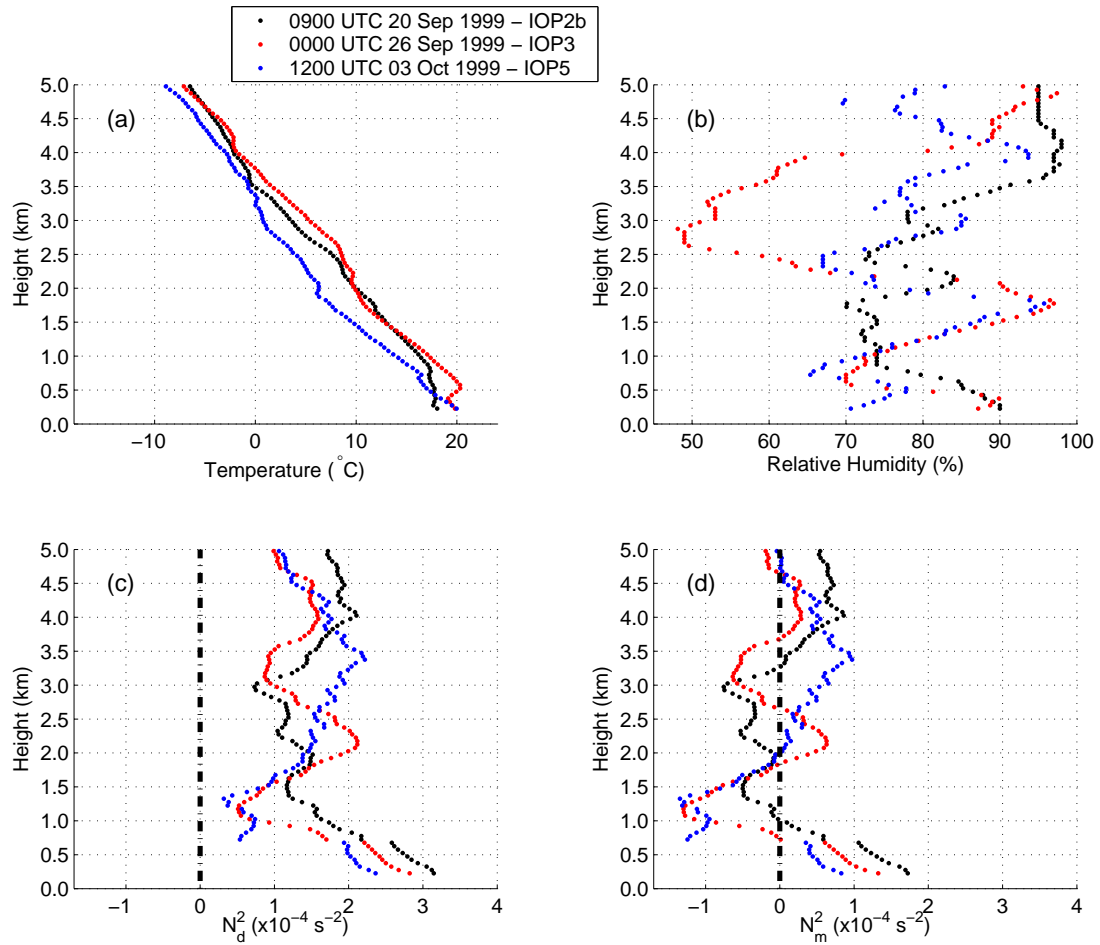
Figure 3.13: Vertical profiles of (a) temperature, (b) relative humidity, (c) squared dry Brunt-Väisälä frequency, and (d) squared moist Brunt-Väisälä frequency for Type A storms.

58
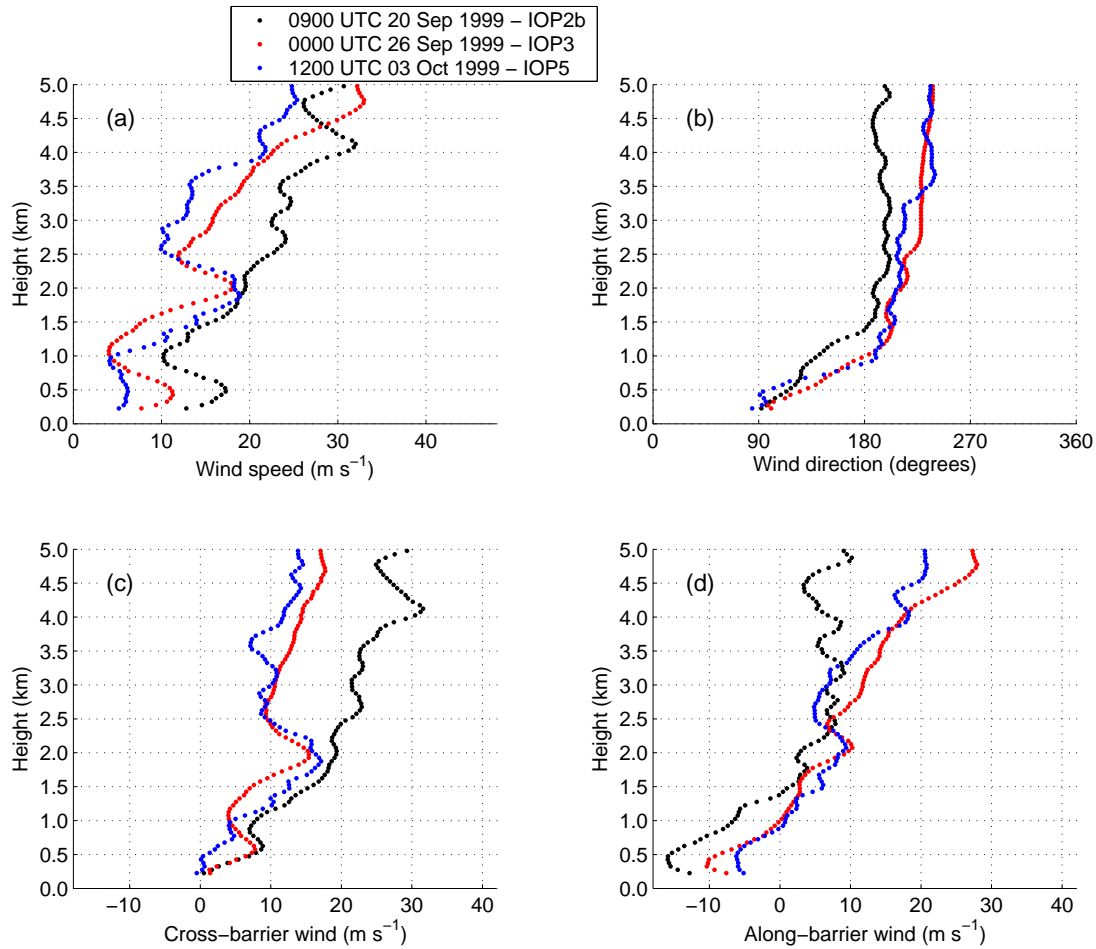
Figure 3.14: Vertical profiles of (a) wind speed, (b) wind direction, (c) cross-barrier and (d) along-barrier wind component for Type A storms. The orientation of the orography used to calculate the wind components is indicated by the W-E line in Fig. 1.5.

(a)

(b)
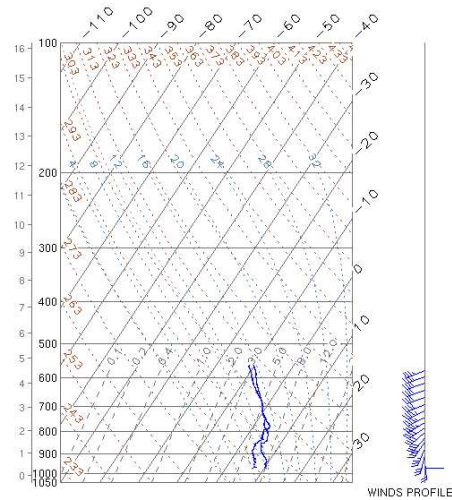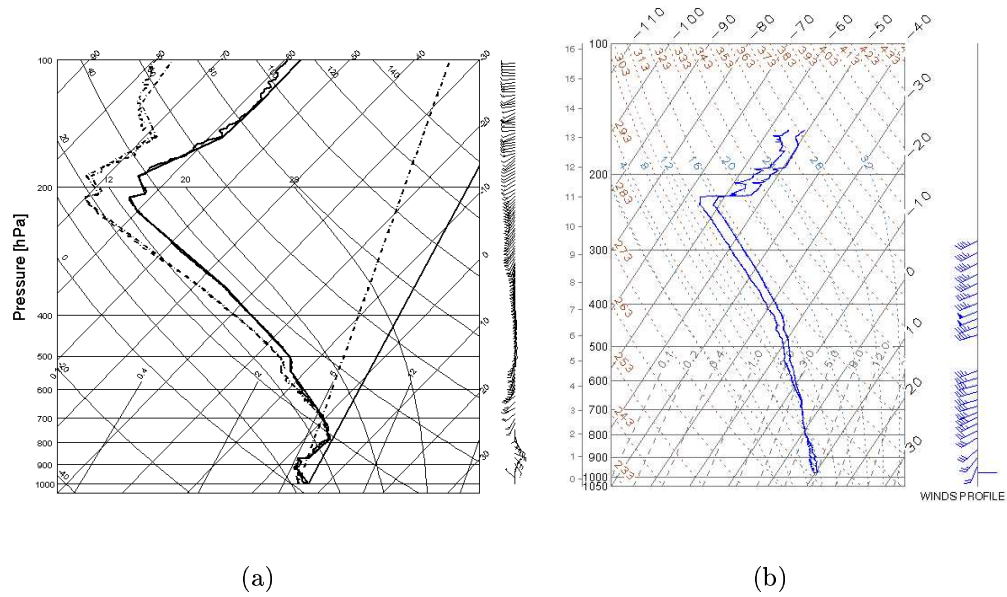
(c)

Figure 3.15: Wind vectors and skew T-log p diagram (a) as in Fig. 3.12 but for IOP8 (0600 UTC 21 October 1999). Panels (b)-(c) shown temperature and dew point temperature from UW soundings collected during (b) Case 11 (2356 UTC 13 December 2001), and (c) Case 1 (1726 UTC 28 November 2001). Temperature and dry adiabat are in °C, moist adiabats are in K, and saturation mixing ratio lines are in g kg^{-1}. The vertical coordinate is (b) and (c) is labeled in km (leftmost scale) and hPa (second scale from the left).
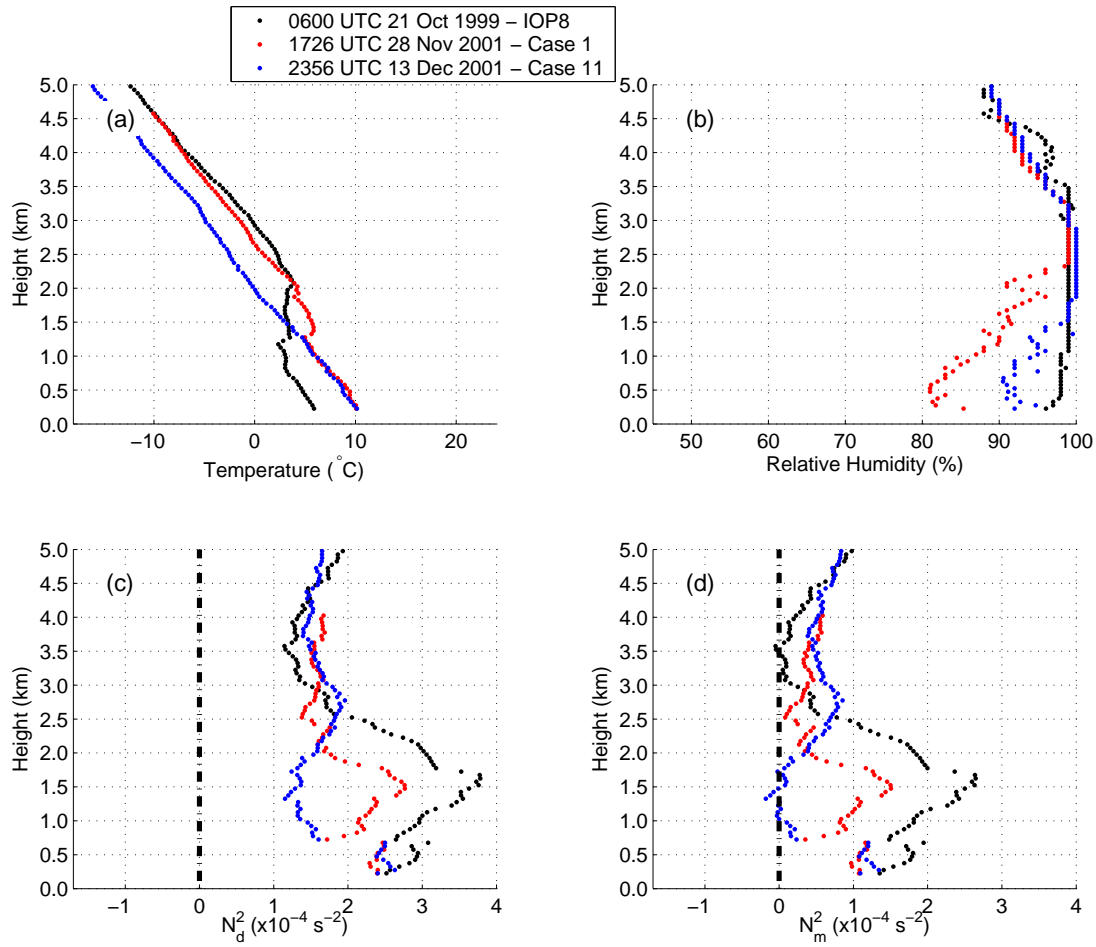
Figure 3.16: Vertical profiles of (a) temperature, (b) relative humidity, (c) squared dry Brunt-Väisälä frequency, and (d) squared moist Brunt-Väisälä frequency for Type B storms.
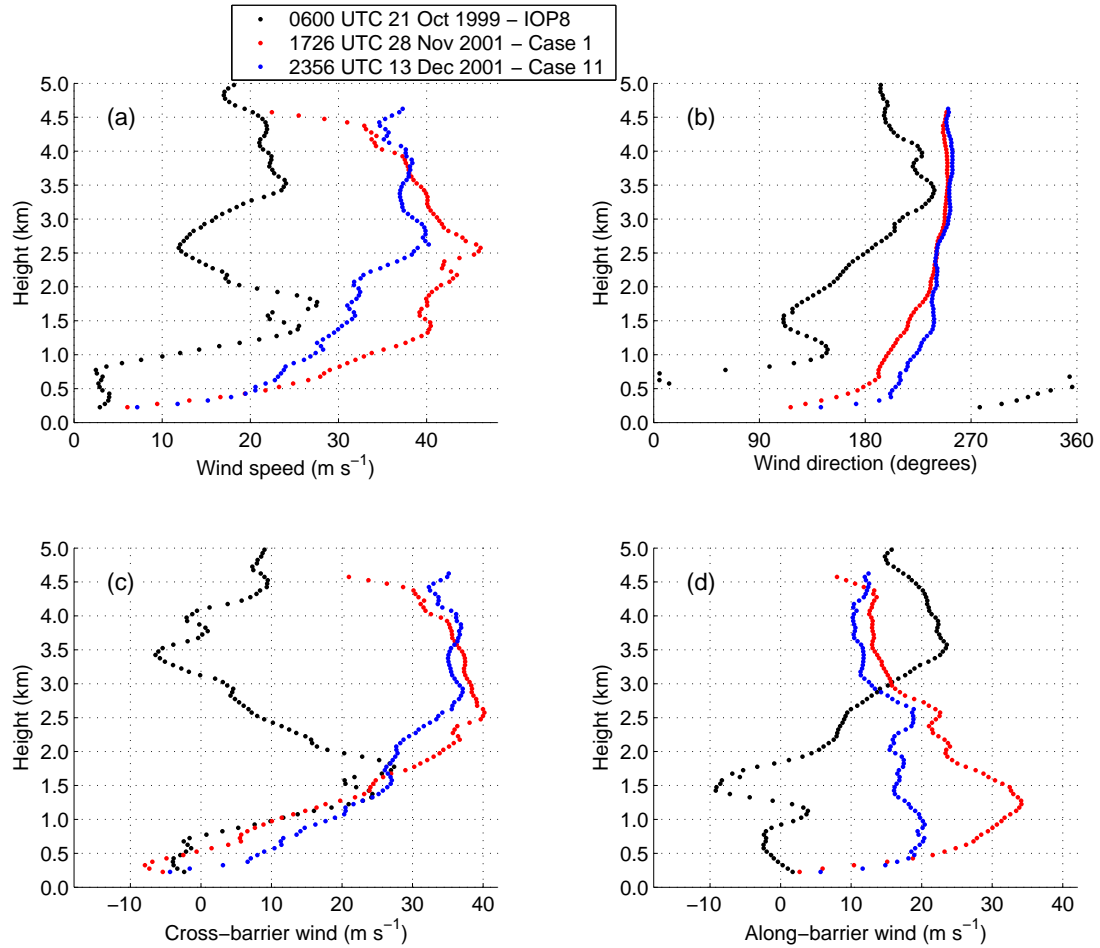
Figure 3.17: Vertical profiles of (a) wind speed, (b) wind direction, (c) cross-barrier and (d) along-barrier wind component for Type B storms. The orientation of the orography used to calculate the wind components is indicated by the SW-NE line in Fig. 1.5 for IOP8. A N-S orientation of the Cascades was assumed for Cases 1 and 11.

Chapter 4

FINE-SCALE AIR MOTIONS AND MICROPHYSICAL PROCESSES OF PRECIPITATION GROWTH

The previous chapter documented two types of terrain-modified flows, which were termed Type A and B patterns. These flow patterns characterize the mesoscale flow fields that modify the structure of a baroclinic cloud system passing over a mountain range. The thermodynamic and kinematic characteristics of the upstream air for both flow patterns were also described. This chapter now examines the small-scale convective and turbulent air motions that affect the precipitation growth and fallout over the windward slope. The microphysical processes of particle growth, which are facilitated by these smaller-scale air motions are also described. The small-scale air motions and microphysics differ between the Type A and B storms; therefore, the discussion will continue to be organized around those two archetypes. The MAP and IMPROVE 2 datasets are well suited for examining the fine-scale air motions and microphysics in the storms sampled in these projects. The vertically pointing (VP) radars (see sec. 2.1) collected data continuously with high vertical and temporal resolution. The time resolutions of a few seconds easily allowed updrafts ∼1 km to be identified. The particle-identification capability of the S-Pol radar and in situ sampling of ice particle images allowed the associated microphysics to be documented.

4.1 Precipitation processes in Type A terrain-modified flow pattern

4.1.1 Precipitation processes indicated by polarimetric radar

The small-scale air motions and microphysical growth mechanisms during IOP2b were described by Medina and Houze (2003a). Their results, outlined below, are

applicable to other cases with a Type A flow pattern (Medina and Houze 2003b). Mean reflectivity cross-sections for IOP2b, 3 and 5 (Type A cases) show a convective-like echo structure over the first major peak of the terrain (Fig. 3.7d-f, respectively). A core of high reflectivity in a similar location in relation to the terrain was observed in a climatological study of heavy precipitation over the coastal mountains of California (James and Houze 2005). Our Type A cases were characterized by potentially unstable upstream flow (Fig. 3.13d), hence convective cells were triggered when the LFC was reached. For IOP2b, 3, and 5 LFC was between 1-2 km (Table 3.1), i.e., similar to the elevation of the first peaks of the terrain. A reflectivity maximum below the 0°C level suggests that coalescence may have been important in the orographic enhancement of precipitation, as Caracena et al. (1979) suggested in their study of the Big Thompson flood in the Rocky Mountains.

Figures 3.7g-i show contours of frequency of occurrence of particle types. The particles were classified by applying the particle identification (PID) algorithm of Vivekanandan (1999) to S-Pol radar data. A description of the algorithm is given in Appendix A. The contours indicate regions of maximum occurrence of three types of hydrometeors identified by the polarimetric radar PID: graupel, wet snow and dry snow. Graupel (shaded contours in Fig. 3.7g-i) occurred intermittently (evident by the low frequency of occurrence) above the first major mountain peak, directly above the reflectivity maximum (Fig. 3.7d-f), and at the downwind location where the radial velocity jet reached its maximum altitude (Fig. 3.7a-c). The graupel was embedded in a broad and persistent layer of dry snow (cyan contour), which was melting and falling into a layer of wet snow (orange contour). The maximum graupel occurrence directly over the precipitation maximum seen in the reflectivity suggest that riming of ice particles just above the 0°C level and their subsequent fallout and melting were another factor, besides coalescence, contributing to the reflectivity maximum at lower levels. As the baroclinic system (with its background field of pre-existing stratiform precipitation) advanced over the mountain slopes, the precipitation growth processes

64

were accelerated in the manner described below. The low-level radial velocity jet (Fig. 3.7a-c) transported moisture to higher levels, helping saturate the air and condense cloud liquid water. The orographically generated cloud liquid water was both collected by raindrops below the 0°C level and accreted by ice particles above. The accretion of supercooled cloud liquid water by ice particles led to the maximum of graupel occurrence over the first peak of the terrain (Fig. 3.7g-i).

4.1.2 Convective air motions indicated by vertically pointing radar and implication for microphysical enhancement

During MAP, two VP radars collected high-resolution data of precipitation and air motion (OPRA and ETH in Fig. 1.11). Figure 4.1 shows a 60 min time series of OPRA reflectivity (top row) and radial velocity (bottom row) for Type A storms[1]. The reflectivity had a bright band and fallstreaks during IOP2b (Fig. 4.1a) and convective cells for IOP3 and 5 (Fig. 4.1b,c, respectively). The radial velocity showed a few deep and isolated updrafts during IOP2b, IOP3, and IOP5 (Fig. 4.1d-f, respectively), suggesting that the existing potential instability was released when the air was lifted over the mountains and that the slight instability of the upstream flow reaching the windward slopes favored the occurrence of embedded convective cells[2]. Yuter and Houze (2003) used OPRA radar data and a 1D parcel model with parametrized microphysics to show that during IOP2b riming and graupel formation could be expected above the 0°C level, while warm coalescence enhanced rain formation below the 0°C level. These results are consistent with the polarimetric radar inferences of particle growth processes.

---

[1]Except for IOP5, the time periods shown in Fig. 4.1 are within the 3 h mean displayed in Fig. 3.7. Due to the highly convective nature of IOP5, the echo over the OPRA site was either weak or shallow during the time interval shown in Fig. 3.7 and it did not show any updrafts.

[2]The radial velocity has not been converted to air velocity by subtracting the particle fall speed, so the updrafts in Fig. 4.1 are an underestimation of the air vertical velocity.

4.2 Precipitation processes in Type B terrain-modified flow pattern

4.2.1 Precipitation processes indicated by polarimetric radar

Type B cases had a dramatically different reflectivity structure from that observed in Type A cases. Mean S-Pol radar reflectivity cross sections for Type B cases exhibited a well-defined bright band over the lower windward slopes of the terrain, characterizing the precipitation as stratiform (Fig. 3.9d-f). The bright band is also shown in the P-3 reflectivity data collected during IOP8 and Case 11 (Fig. 3.10c-d). The P-3 data shows additional details in the reflectivity patterns, which have some degree of repeatability. In Fig. 3.10c-d the peak reflectivities defining the bright band fell to lower height immediately adjacent to steep terrain. Marwitz (1983, 1987) noted a similar dip in the 0°C isotherm close to the windward slopes of the Sierra Nevada, and suggested that this effect was associated with increased melting and diabatic cooling resulting from high precipitation rates over the windward slopes. If stably stratified air at the top of the shear layer is forced to ascend the barrier, adiabatic ascent may also contribute to localized cooling (Mass and Ferber 1990). During MAP IOP8, pre-existing cool air trapped inside the Po Valley was eroded from the south (Bousquet and Smull 2003b), leaving lower temperatures to the north, which could produce the dip in the bright band seen in Fig. 3.10c. However, such an effect on the temperature field was not noted during IMPROVE-2 Case 11, where the lowering of the bright band adjacent to the terrain is also observed, suggesting that local adiabatic and diabatic effects may be enough to produce the cooling adjacent to the terrain.

Figure 3.10d shows an elevated (3.5-5.0 km altitude) secondary maximum of reflectivity at 90-120 km ranges and spill-over of precipitation into the lee of the Cascades in the form of a plume with values > 25 dBZ. This plume was probably the result of hydrometeors being transported to lower levels by the downslope flow associated with a gravity wave described in Chapter 3 (Fig. 3.10b). The secondary reflectivity maximum observed at altitudes ~3.5-5.0 km could have been dynamically produced

(Garvert et al. 2006). It is consistent with the gravity wave response produced in numerical simulations of stable flow over a mountain. As described in Chapter 1, under these conditions an area of precipitation is formed at low levels on the lee side of the mountain. The area of large vertical velocity and increased snow mixing ratio tilts upstream with increasing height (Figs. 1.8c and 1.9c from Jiang [2003]). The precipitation particle production associated with the gravity wave lifting may extend to elevations of 5 km or higher. Depending on the wave tilt, the precipitation perturbation may extend to the mountain crest (Jiang 2003) or even over the windward slope (Colle 2004). Alternatively, the secondary reflectivity maximum could have been produced by microphysical processes. The temperatures at the 4-4.5 km level (approximately -13.0 to $-10.5°C$, blue line in 3.16 a) would have favored growth and aggregation of dendrites (Hobbs 1974; Houze 1993). Aggregates formed at these altitudes could have been large enough to produce high reflectivity, which is proportional to the 6th power of the particle dimension.

The distribution of accumulated frequency of occurrence of radar-identified hydrometeors observed during Type B cases is shown in the bottom row in Fig. 3.9. A persistent layer of dry snow is seen above the $0°C$ level (cyan contour). Immediately below the snow there is an intermittent layer of graupel (color shading), which transitions below the $0°C$ level into a layer of wet snow (orange contour). Since the patterns shown in Fig. 3.9g-i resulted from accumulating data over three-hour intervals, the details of the precipitation processes operating at any given time are obscured in favor of illustrating persistent effects. To analyze the vertical structure with more detail, S-Pol radar data at a single time is examined. Fig. 4.2a shows that the hydrometeors types identified by the PID algorithm tend to form horizontal layers, consisting of (from bottom to top): light rain (light orange shading), wet snow (intermediate blue shading), graupel (intermediate green shading) and dry snow (cyan or light blue shading). As described in Appendix A, the particle types are determined primary by the reflectivity (Fig. 4.2b), differential reflectivity (Fig. 4.2c) and temperature values,

with the other polarimetric variables listed in Table A.1 playing a smaller role. The layer of dry snow is associated with low reflectivity (10 to 35 dBZ, Fig. 4.2b) and low ZDR (-1.0 to 1.4 dB, Fig. 4.2c). Wet snow is defined mainly by high reflectivity values (20 to 50 dBZ) and high ZDR (> 0.3 dB). The moderate values of both reflectivity (13 to 40) and differential reflectivity (-0.3 to $\sim$2.4) below the bright band are classified as light rain. High reflectivity (33 to 55 dBZ) and low ZDR (-0.3 to $\sim$1.9 dB) values are interpreted as graupel (roughly enclosed by the horizontal black lines).

The horizontal layering of the graupel signature as well as in situ aircraft data (both discussed in sec. 4.2.4) suggest that in this case the "graupel" category of the PID algorithm was triggered by either graupel or large aggregates. This is understandable considering that the PID algorithm grew out of investigations of convective storms (especially hailstorms) in which the microphysical processes in the ice regions are dominating by riming, with aggregation playing little if any role. However, in frontal systems both aggregation and riming play important roles. Since the ZDR values associated with the graupel or large aggregates category are small (Fig. 4.2c), we conclude that the melting of these particles had either not yet begun or had not yet made the particles appear wet to the radar. Although the reflectivity bright band has traditionally been identified with the layer of melting, in this case the bright band is very wide (Fig. 4.2b, enclosed by the horizontal black lines) and does not seem to give a very precise indication of the level at which melting occurs. The ZDR field seems to indicate the melting level more precisely. Figure 4.2c shows that the ZDR values throughout most of the depth of the reflectivity bright band in Fig. 4.2b were small, near zero. The vertical profile of ZDR has a very large and sudden jump at $\sim$1.7 km, which is probably the level at which the largest aggregates begin to melt, changing their apparent dielectric constant, which magnifies the ZDR signal due to their typical horizontally-oblate orientation.

The aircraft data discussed in sec. 4.2.4 indicate that aggregates were ubiquitous

above the 0°C level. Many were apparently rimed. Graupel images were not obvious but could not be ruled out. It is possible that the large dry aggregates (including rimed ones) dominated the high reflectivity values seen in the layer above the 0°C level (Fig. 4.2a) but retained a low value of ZDR (Fig. 4.2c, in the layer above the sharp jump) as long as they remained dry, with low dielectric constant. To our knowledge, the polarimetric characteristics of large rimed aggregates have not been studied specifically, however it seems possible that their polarimetric signals in reflectivity and differential reflectivity is similar to that of small graupel. To account for these possibilities, in cases were the graupel signature exhibited an extensive horizontal layering, we will rename the "graupel" category as "graupel and/or dry aggregates". To be consistent with this nomenclature, the "wet snow" category will be called "melting aggregates". However, making use of the contextual information of the hydrometeor signals, this amendment to the "graupel" category will not be made when the hydrometeor appears as a quasi-circular contour on top of a reflectivity maximum above the first peak of the terrain in more unstable Type A events (e.g., 3.7g-i).

4.2.2 Turbulent air motions indicated by vertically pointing radar and implication for microphysical enhancement

VP radars located over the windward slopes provided detailed temporal and vertical resolution in the precipitation layer. The location of the radars in relationship with the orography is shown in Figs. 1.11 (ETH) and 1.3 (ETL). Fig. 4.3a-c shows a distinct bright band located around 2 km for Type B cases. It also shows fine-scale variability in the form of spikes above and below the bright band and some evidence of a secondary maximum of reflectivity around 4-5 km altitude. The bottom row of Fig. 4.3 shows the radial Doppler velocities in the vertical direction. The radial velocities have not been converted to vertical air velocity by subtracting the particle fall speed. Places where the particles are moving unequivocally upward are shown

by positive values (yellow and red contours). Intermittent updraft cells occurred in the layer between 2-4 km (Fig. 4.3d-f) i.e., above the melting level. There is some indication that the temporal variability above and below the 0°C level is similar, suggesting that the updrafts extended below the melting level but were masked by the large fall velocities of the melted raindrops. The mean size of the updrafts is estimated by averaging the radial velocity over a vertical layer where the updrafts are well defined (Fig. 4.4). By assuming that the cells were being advected with the low level wind, typical sizes of updraft cells are estimated to be ~4-5 km (Table 4.1).

An early indication of this type of vertical velocity structure was provided by the Cascade Project (Hobbs 1975). In that field program, a vertically pointing Doppler radar was deployed near the crest of the Cascade Mountains of Washington (Weiss and Hobbs, 1975). As an occluded front passed over the Washington Cascades, the VP radar recorded updrafts ~2 $\mathrm{m\,s^{-1}}$ above the melting layer (between 2 and 3 km altitude) for a period of 2 h (Hobbs et al. 1974). This radar had rather low time resolution and did not distinguish individual cells. The comparable magnitude, duration, altitude range, and location within the frontal system were strikingly similar to the cases described in this study. The similarity of the reflectivity and Doppler velocity structure seen in the three cases shown in Fig. 4.3 suggests that the dynamical and microphysical structures seen in the baroclinic systems passing over mountain ranges have a repeatable behavior from one frontal system to another and from one mountain range to another.

One possible explanation of the updrafts seen in Fig. 4.3 is that the shallow layer of weak potential instability observed in the upstream flow (Fig. 3.16d) was released as the air ascended the Cascade Mountains, forming a shallow layer of buoyant cells. However, apart from some weak instability at the lowest levels, the upstream air was stable during Case 11. During Case 1 and IOP8, the atmosphere was stable at all altitudes, ruling out the possibility of buoyant instability playing a role in producing the updraft cells. The updraft cells were therefore more likely a manifestation of

some form of turbulence, induced either by the strong shear in this layer or by the flow of the stable air over the rough lower boundary formed by the windward slope terrain, or both. Hobbs et al. (1974) suggested that the updrafts they observed by vertically pointing radar were a manifestation of turbulence associated with the wind shear in the frontal system passing over the Cascades. Alternatively, idealized simulations have shown that in some instances stable flow over a lower rough boundary creates a non-stationary response in the vertical velocity field (D. Durran, personal communication).

To indicate how the radial velocity updraft cells in the Type B frontal systems related both to the prevailing wind shear and to the microphysical processes, Figs. 4.5 and 4.6 compare data obtained from several sources during the IMPROVE storms. The period between the vertical lines corresponds to the time period shown in Fig. 3.9. Panels (a) of Figs. 4.5 and 4.6 display data from the McKenzie Bridge wind profiler (ETL site in Fig. 1.3). These data show how the wind shear between the 3.0 km altitude and the surface varied in time during the passage of the storm over the windward side of the terrain. The radial velocity measured by the VP radar (ETL in Fig. 1.3) is shown in the (b) panels of Figs. 4.5 and 4.6. Radial velocity updrafts of 0-6 m s^{-1} are indicated in black. Throughout the passage of the main rainband of the frontal system in each storm, the vertically pointing radar showed the intermittent upward radial velocities seen also in Fig. 4.3e,f. Comparison of the (a) and (b) panels in Figs. 4.5 and 4.6 indicate that the radial velocity updrafts tended to occur during periods of large shear.

When the Richardson number [$Ri = N_m{}^2/(du/dz)^2$], where N_m is the moist Brunt-Väisälä frequency] is less than 0.25, shear-induced turbulence can develop (Houze 1993, p. 60). The wind shear, calculated from the data shown in Fig. 3.17a, was very large for Type B cases, particularly at low levels (Fig. 4.7a). Type B cases had low-level layers with moist Ri values below 0.25 (Fig. 4.7b), consistent with the

occurrence of shear-induced turbulence[3].

Panels (c) of Figs. 4.5 and 4.6 indicate the maximum magnitudes of the radial velocity updrafts in the 2-3 km layer as a function of time in the regions where the reflectivity exceeded a threshold value of −2 dBZ. Since the maximum values regularly reached magnitudes of several meters per second, with 2 m s^{-1} being typical, the updraft velocities were sufficient to produce large supercooled cloud liquid water contents and hence riming. Baschek et al. (2002, 2003) sampled ice particles near the top of a mountain within view of a VP radar and found that the degree of riming increases as the radial velocity updrafts (in which the particles are embedded) become more intense. The highly variable vertical velocities also would favor aggregation. Through the turbulent cascade of energy, variability in the vertical velocities field in the 4 km scale would be passed down to smaller scales, and particles would be driven into each other by the highly variable smaller-scale air motions. Moreover, these turbulent air motions were in a layer where the temperature would also favor aggregation (Hobbs 1974; Houze 1993).

Panels (d) of Figs. 4.5 and 4.6 show the time-height variability of the frequency of occurrence of dry aggregates and/or graupel according to the S-Pol polarimetric particle identification algorithm. These signals registered when the shear was strong (panels (a)), the frequency of occurrence of radial velocity updrafts was greatest (panels (b)), and the intensity of the drafts was highest (panels (d)). The lag time between the occurrence of dry aggregates and/or graupel and the stronger updrafts seen in the IMPROVE-2 cases can be reconciled by considering that the S-Pol radar, which measured particle types, was located upstream of the vertically pointing radar, which measured the updrafts. This coincidence of key dynamical and microphysical variables observed by three different instruments (the wind profiler, the vertically pointing radar, and the polarimetric scanning S-Pol radar) suggests that the highly

---

[3]Running mean filters were applied to the $N_m{}^2$ and wind speed profiles to reduce the noise in the Richardson number calculation.

turbulent air motions above (and probably also below) the melting layer were promoting both aggregation and riming of ice particles. The turbulence in this layer could thus account for the maxima of dry aggregates and/or graupel in this layer. The persistence of this layer of turbulence provided an environment in which ice particles could aggregate to form larger particles that would be larger targets for riming by collection of supercooled cloud liquid water drops. The turbulence also created pockets of high liquid water contents within which the large aggregates could grow by riming and thus increase their fallspeeds. Turbulence not driven by buoyancy could thus have been a crucial component of the windward- side orographic enhancement of the precipitation in these storms by providing mechanisms by which particles would be more likely to aggregate and more able to grow by riming, thus facilitating the fallout of precipitation particles on the lower windward slopes before being advected up to and over the crest of the mountain range.

4.2.3 Scanning radar observations of Kevin-Helmholtz instability

Evidence of Kevin-Helmholtz (KH) instability was observed by the ground based S-Pol radar at near ranges from the radar during MAP IOP8 and IMPROVE-2 Cases 1 and 11. The dynamical instability appears as radial velocity perturbations at altitudes between 1-2 km and with horizontal sizes of 2-4 km [Panels (b) in Figs. 4.8, 4.9, and 4.10]. Early observations of Kevin-Helmholtz instability where made during clear air turbulence (CAT) (e.g., Atlas et al. 1970, Browning 1971, and Browning and Watkins 1970). Observations of KH billows embedded in precipitation have been made in southern Britain by Chapman and Browning (1997, 1999). Chapman and Browning (1999) documented billows with typical sizes of 5 km in the horizontal and 1 km in the vertical evident in the radial velocity field (Fig. 4.11a). They observed these features also in the wind shear field (Fig. 4.11c), which exhibits a "braided" or shear splitting structure characteristic of KH instability billows.

Our observations also display a braided structure in the shear field[4]. [panels (c) of Figs. 4.8, 4.9, and 4.10 as well as in the spectral width of the radial velocity field (panels (d) of Figs. 4.8, 4.9, and 4.10), which is the square root of the second spectral moment about the mean velocity[5]. At close ranges from the radar, where the billows are well resolved, they are located below the melting layer (indicated by the bright band in the reflectivity data of panels (a) of Figs. 4.8, 4.9, and 4.10). As the shear layer ascends over the terrain (Fig. 3.10a,b), the billows probably also rise, as supported by the presence of turbulence in the VP radars (located on the windward slopes, Figs. 1.11 and 1.3) in the layer of 2-4 km (bottom row in Fig. 4.3).

The KH instability signal can only be observed at near ranges from the radar probably due to the rapid decrease of vertical resolution of the radar beam with distance. While the S-Pol radar beam (with a width of 1°) is 0.35 km wide at a distance of 20 km from the radar, its width is 0.9 km at 50 km from S-Pol. On the other hand, Chapman and Browning's observations were made with the Chilbolton radar, which has unusually narrow beam (0.28°). Therefore the vertical resolution is higher than that of the S-Pol radar and hence the billows are well resolved at farther ranges. Chapman and Browning reported that they were able to resolve quantitative information of the billows out to 50 km range from the radar. According to Chapman and Browning (1999), it is necessary that radar observations are made in a direction quasi-perpendicular to the billow axes for them to be evident in radial velocity data. This means that only particular vertical cross-sections (RHI's) can reveal the presence

---

[4]Taking into consideration that the billows were observed at close ranges from the radar and at low elevation angles, the shear was calculated as the difference in the radial velocities between gates adjacent in elevation divided by the vertical distance separating the gates.

[5]The spectral width of the radial velocity (σ) is defined by:

$$\sigma^2 = \frac{\int_{-\infty}^{\infty} \left(V - \overline{V}\right)^2 S(V)\, dV}{\int_{-\infty}^{\infty} S(V)\, dV}$$

where $\overline{V}$ is the mean Doppler velocity and $S(V)$ is the power spectrum in the interval $S(V)\, dV$ (Battan 1973).

of the billows and hence that they may be difficult to identify in a quasi-horizontal cross-section (PPI). Moreover, Newsom and Banta (2003) have found that KH waves do not form in extensive horizontal layers that cover and entire region, but in smaller patches. According to Newsom and Banta (2003), the understanding of the physical characteristics, causes and effects of shear-flow instability is still an active area of research, investigated in recent field experiments (e.g., the Cooperative Atmosphere-Surface Exchange Study conducted in south central Kansas in 1999 [CASES-99]).

4.2.4   Ice particles, liquid water content, and vertical air motions along the aircraft
           flight track

The evidence presented so far suggests that Type B storms are characterized by a layer above the 0°C level where the growth of graupel and/or dry aggregates is facilitated by the occurrence of mechanically induced turbulent updraft motions in the shear layer that develops as the frontal systems advance over the windward slopes of the terrain. In this section, we present aircraft data collected in this layer.

Figure 4.12 shows the only flight track segment in which ice particles were collected in the layer of interest in any of the Type B cases described herein. This track was flown by the NOAA WP-3D aircraft during the 13-14 December 2001 IMPROVE-2 storm (Case 11). In Fig. 4.12 the track is overlaid on radar data showing that the aircraft was in the main precipitation layer during this time. Figure 4.13a shows the altitude as a function of time along with other key variables during part of the flight shown in Fig. 4.12. In this sub-segment, the altitude decreased from slightly above 2.5 to 2 km (grey line). The air temperature (blue line) increased from about −3.0°C to about 1°C during the time shown; i.e., the aircraft crossed the 0°C level and encountered precipitation particles falling from just above that level, where the turbulent motions were indicated by the vertically pointing radar (Figs. 4.3e and 4.5b,c). The vertical velocity trace (red line) indicates that the aircraft entered a region of increased turbulence around 0125 UTC 14 December 2001 when it descended

to an altitude close to 2.1 km. Magnitudes of vertical air velocities of 1 m s^{-1} were common and occasionally reached 4 m s^{-1} during the time interval between 0125-0130 UTC 14 December 2001. For this time period, cloud liquid water contents (black line in Fig. 4.13a) measured by the Johnson-Williams probe ranged from 0.1-0.6 g m^{-3}. After 0130 UTC 14 December 2001, the turbulence signal in the vertical velocity measurements decreased and so did the liquid water contents. Figure 4.13b shows the same data as panel (a) but with a 5-point running mean filter applied to the time series (except for the pressure altitude variable, which was not filtered). This trace suggests an association between cloud liquid water content and vertical velocity. Whenever the cloud liquid water content exceeded 0.4 g m^{-3}, the vertical velocity was over 1 m s^{-1}, suggesting that the turbulent updrafts were producing pockets of moderate cloud liquid water content that would have been available for riming. In Fig. 4.13c, a 2-min segment of panel (b) was expanded. Besides the correlation between cloud liquid water and vertical velocity, an anticorrelation of these variables with the air temperature was observed. This behavior indicates that the turbulence was mechanical rather than buoyant in nature.

The S-Pol radar indicated that reflectivity values associated with the polarimetrically inferred graupel and/or dry aggregates were as large as 45 dBZ (Fig. 4.2b). To determine if this rather high reflectivity was consistent with the inferred particle types, we examined the Particle Measuring System probe data collected by the NOAA WP-3D from 0126-0127 UTC 14 December 2001, a period when the aircraft was flying at an elevation of 2 km and in subzero temperatures (Fig. 4.13). Figure 4.14a shows the 2DP probe particle number density spectrum. The reflectivity associated with this distribution was calculated following Vivekanandan et al. (1994) (Fig. 4.14b). The density values used to calculate the reflectivity correspond to observed values (Locatelli and Hobbs 1974). The curves in Fig. 4.14b indicate the reflectivity produced by the distribution in (a) assuming different densities of ice particles. The total reflectivity produced by the distribution fluctuates between 25 and 55 dBZ,

depending on the degree of riming. This calculation indicates that if the observed particles had densities between those of "graupel-like snow of lump type" and "conical graupel" they would have produced reflectivity values of $\sim$45 dBZ, corresponding to the radar-observed reflectivity at this level. Ice particle images seen on the Particle Measuring System probes (Fig. 4.15) frequently appeared to be aggregates, as inferred from the predominant characteristic of irregular shapes with open gaps. Since the open gaps were often filled in and somewhat blobby in appearance, we further infer that the aggregates were frequently rimed. Occasionally, the images were completely filled in with smoother edges and could be inferred to be graupel. Thus, the ice particle images collected on board the aircraft were consistent with the presence of rimed aggregates and/or graupel falling out of the layer of turbulent air motions seen in the vertically pointing radar data. These ice particle samples furthermore appear to be consistent with the particle types indicated by the S-Pol polarimetric variables and also with the heavy rimed aggregates of graupel-like snow collected at Ray Benson SnoPark (Woods et al. 2005), a ground-based observational site located at an elevation of 1454 m (Fig. 1.3).

4.3 Conceptual models of orographic precipitation

4.3.1 Type A flow pattern

Figure 4.16 presents a conceptual model of the mechanisms for orographic enhancement of precipitation during storms with low-level terrain-modified flow of Type A, which was proposed by Medina and Houze (2003). The figure represents a vertical cross section perpendicular to a barrier, extending from the lowlands to the crest. As a baroclinic system and its associated cloud move over the windward slopes of the terrain, they provide a background field of stratiform precipitation. When the low-level air reaches the first peak of the terrain, it rises over it easily because the upstream flow has low stability and strong cross-barrier component. The lifting of

the moisture-laden low-level flow produces high liquid water contents over the first peaks of the terrain. High water content favors growth of pre-existing frontal precipitation by coalescence below the 0°C level and by riming above. The rapid fallout of graupel and coalescence-produced raindrops favor locally enhanced precipitation over the first major peaks of terrain encountered by the upstream flow. If, in addition, the upstream flow is potentially unstable, convective cells will be triggered in the sudden upslope ascent. These cells produce pockets of especially high concentrations of cloud liquid water. The embedded buoyant convective cells thus accentuate the coalescence and riming processes that occur in the flow-over regime.

4.3.2   Type B flow pattern

A highly simplified picture of the mechanism of orographic enhancement of widespread frontal precipitation during storms with low-level terrain-modified flow of Type B, which was proposed by Houze and Medina (2005), is summarized in Fig. 4.17. The figure represents a vertical cross section perpendicular to a barrier, extending from the lowlands to the crest, when a widespread, deep, stable precipitating cloud of a frontal system is passing over the windward slope of the mountain range. As a large-scale precipitating cloud system reaches the windward slopes, the cross-barrier flow component at the lowest levels (below ~ 1 km) is either weak (e.g., IMPROVE-2 Cases 1 and 11) or blocked (e.g. MAP IOP8).

The flow layer above the weak low-level air is strong and able to cross the mountain barrier. A sheared layer is thus formed above the low-level flow. Reasons for the formation of this shear layer will be explored by idealized modeling in the next chapter. The layer of shear is observed to slope upward, following the general slope of the terrain. The combination of high shear and stability in this layer produces conditions that support turbulent cells (Ri < 0.25). Transient oscillations triggered by flow of stable air over the rough lower boundary may also contribute to the formation of the turbulent cells; however, such a process is not yet well described theoretically.

The updraft cells located in the stable sheared layer atop the low-level air operate within the deep broad precipitating cloud of the large-scale baroclinic system. The widespread deep cloud is producing snow in response to the dynamics of the baroclinic frontal disturbance that is moving over the mountain range. As the frontal system traverses the mountain range, additional lifting owing to the ascent over the mountain range produces condensate exceeding that produced by the baroclinic system dynamics alone. The layer of cells that form in the sheared layer are embedded in the larger cloud system, and they act to concentrate the additional condensate produced by orographic lifting into pockets of high liquid water content associated with the small scale updraft cells. Aggregation of the ice particles falling from the broader deep frontal cloud into the layer of cells is aided by the turbulent air motions associated with the cells. The aggregate snowflakes are large targets for riming by collection and accretion of supercooled cloud drops when they find themselves within the cellular pockets of high cloud liquid water content. The aggregates and other ice particles thus acquire greater mass and fall out quickly. In this way the additional condensate produced by orographic lifting can quickly reach the ground on the lower windward slopes. Without the aid of the cells, the condensate may be carried farther downstream, falling out higher up on the ridge or even on the leeside (as demonstrated by Hobbs et al. 1973). Since the sloped shear layer may cross the 0°C level, the microphysical processes of growth enhancement vary. Below the 0°C level, the accretion may take the form of coalescence, as the melted snow from above falls through the cells of enhanced liquid water content.

Idealized simulations of moist orographic flow suggest that when small-scale cells are embedded in a large stratiform cloud, the precipitation rates, amounts and efficiency all increase considerably (Kirshbaum and Durran 2004). For Type B cases, our empirical conceptual model of orographic enhancement of precipitation suggests that riming, aggregation, and coalescence engendered by the turbulence in the shear layer all contribute to the production of heavy particles that fall out more quickly

over the windward slopes than they would in the absence of the cells.

Table 4.1: Parameters used in calculating mean size of updraft cells

Storm	Mean updraft duration[a] (s)	Mean wind speed[b] ($m s^{-1}$)	Mean updraft size (km)
IOP8	420	11.6	4.9
Case 1	190	21.1	4.0
Case 11	200	22.5	4.5

[a] From Fig. 4.4

[b] From Table 3.1
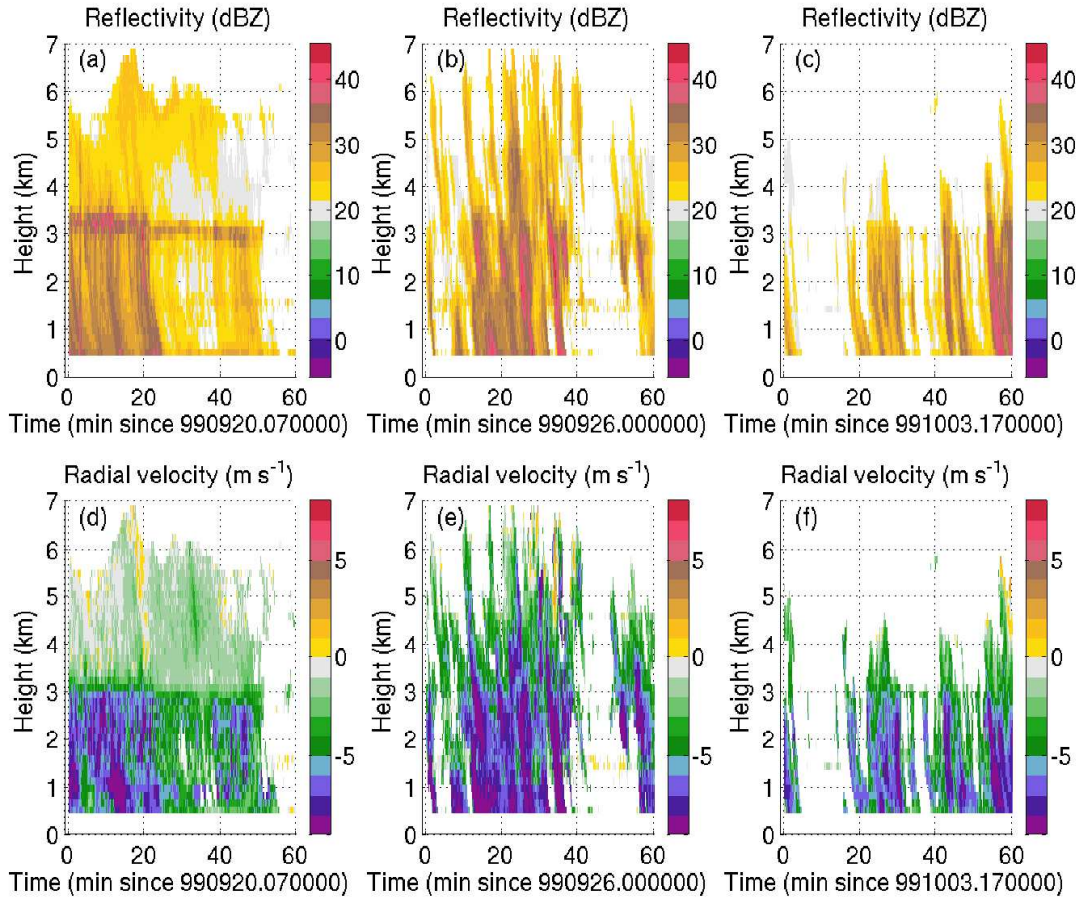
Figure 4.1: Data from OPRA vertically-pointing radar (see location in Fig. 1.11) collected during IOP2b (first column), IOP3 (second column), and IOP5 (third column). The top row shows reflectivity (dBZ), the bottom row radial velocity ($m s^{-1}$) with positive (negative) values denoting flow away (toward) the radar.

(a)

(b)

(c)
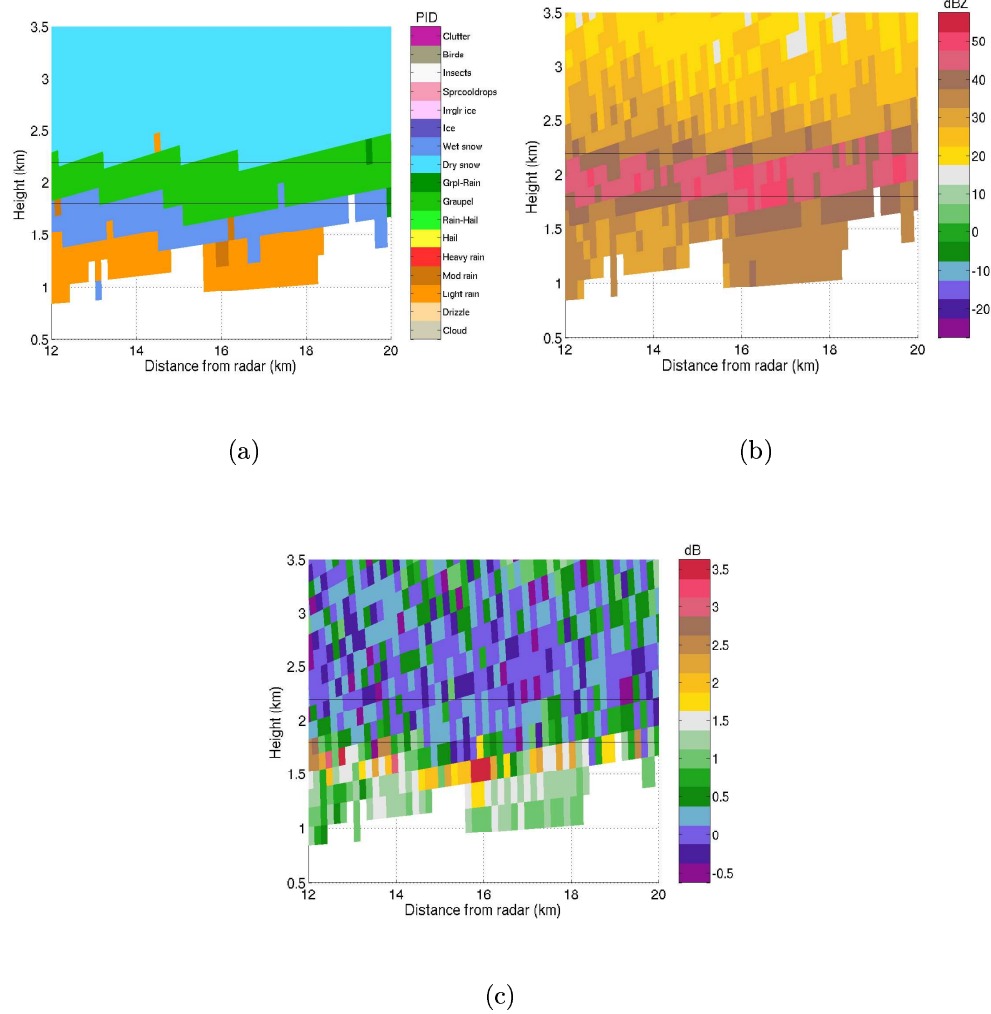
Figure 4.2: S-Pol radar RHI collected at 2353 UTC 13 December 2001 for an azimuth of 92° showing (a) particle classification from PID algorithm. (b) Reflectivity, and (c) differential reflectivity. The horizontal lines are discussed in the text.
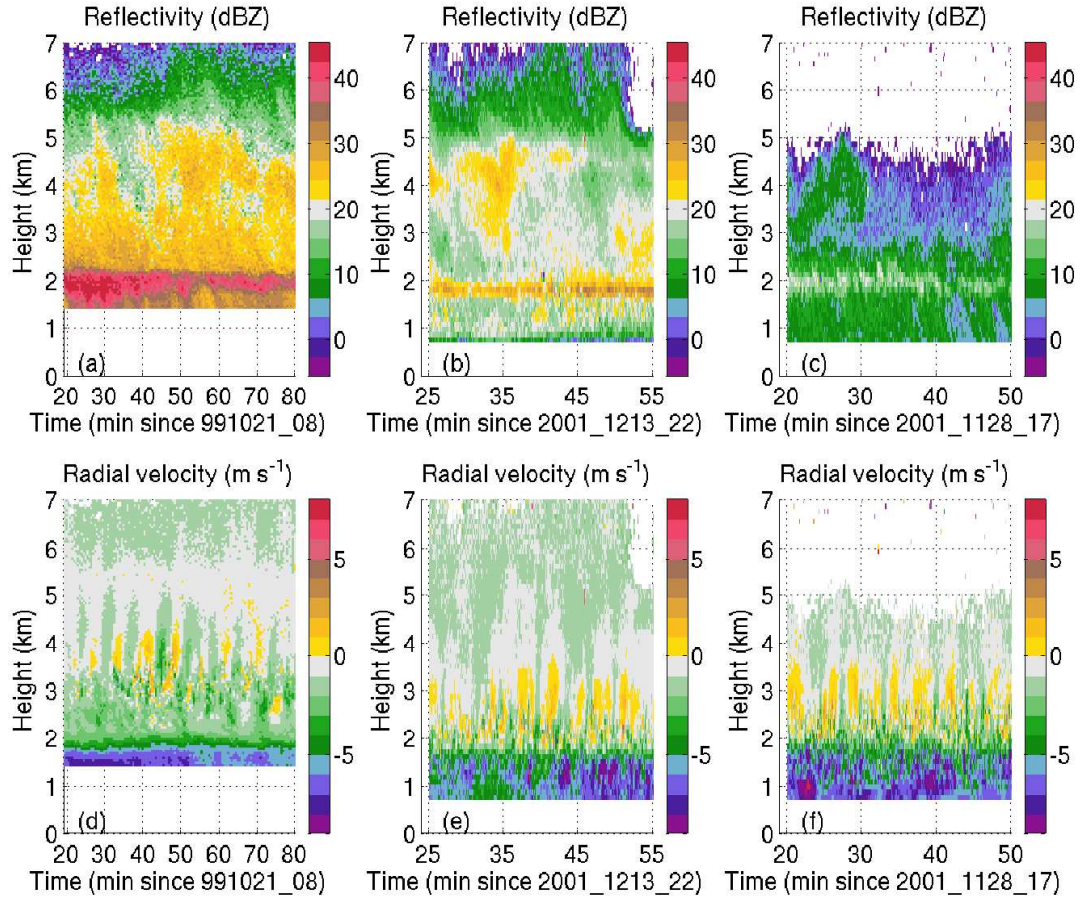
Figure 4.3: Data from vertically-pointing radars collected during IOP8 (first column), Case 11 (second column), and Case 1 (third column). For IOP8, data from the ETH radar (see location in Fig. 1.11) is used, while Cases 11 and 1 present ETL radar (see location in Fig. 1.3) data. The top row shows reflectivity (dBZ), the bottom row radial velocity ($\mathrm{m\,s^{-1}}$) with positive (negative) values denoting flow away (toward) the radar.
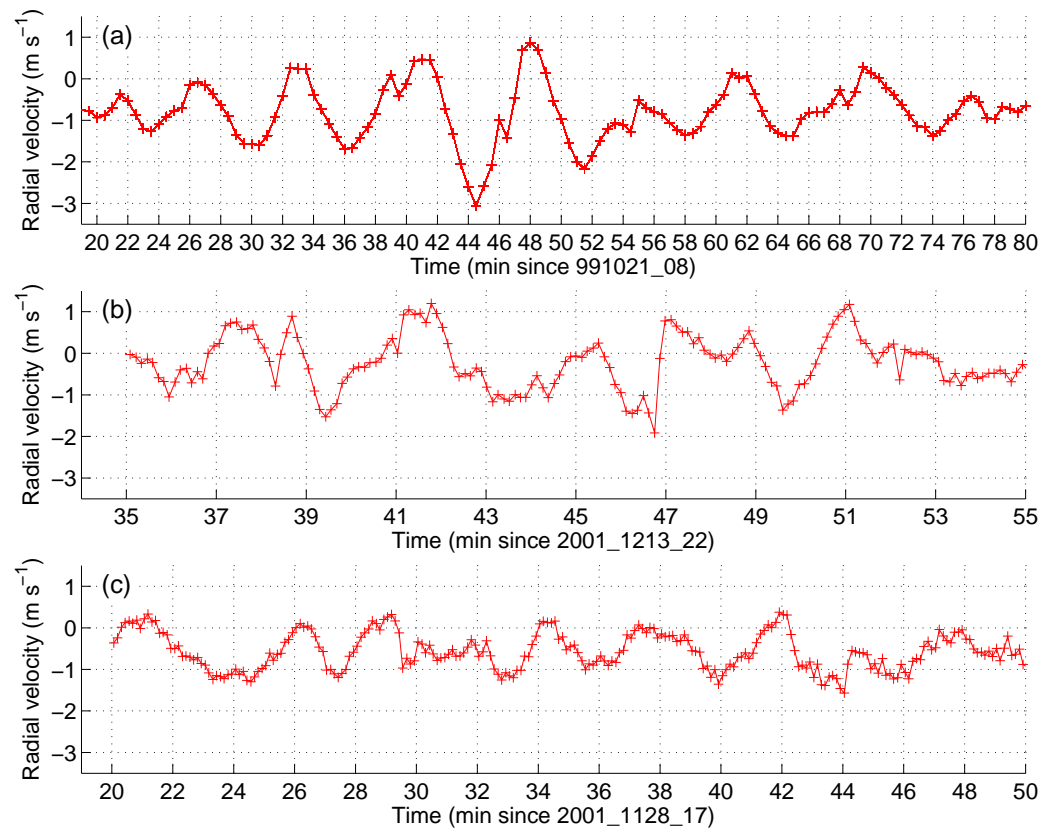
Figure 4.4: Vertically averaged radial velocity data from vertically-pointing radar during (a) IOP8 (averaged from 3.5 to 4.5 km), (b) Case 11 (averaged from 2.7 to 3.2 km), and (c) Case 1 (averaged from 3.0 to 4.0 km).
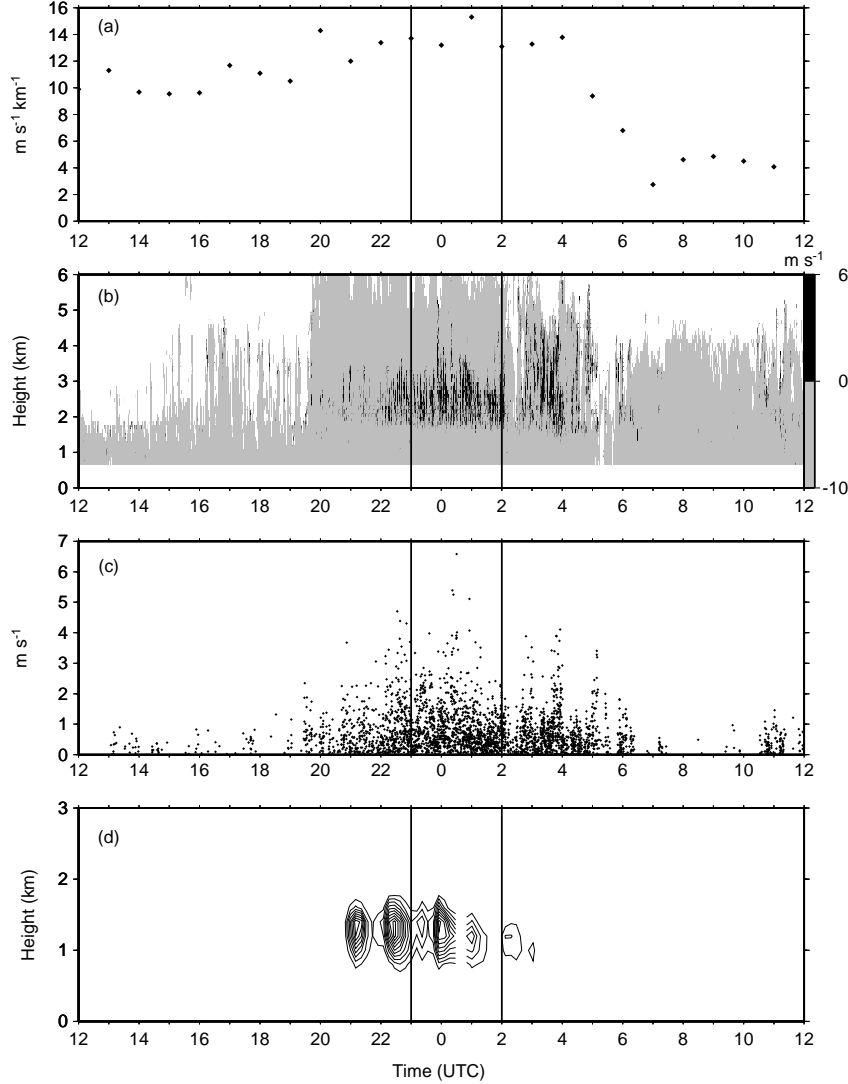
Figure 4.5: Time series during Case 11 (13-14 December 2001) storm of (a) vertical wind shear between 3 km and the lowest available level (0.66 km), according to vertical wind profiler data (ETL in Fig. 1.3), (b) radial velocity from the vertically pointing radar (ETL in Fig. 1.3), (c) maximum value of radial velocity in the 2-3 km layer from data in (b), and (d) frequency of occurrence of dry aggregates and/or graupel according to the PID algorithm applied to S-Pol radar data collected in an eastward-looking sector from 10-60 km ranges (outer contour interval is 2%, each contour incrementing by 2%). The period between the vertical lines corresponds to the time interval averaged or accumulated in the second column of Fig. RADAR-TYPE-B). From Houze and Medina (2005).
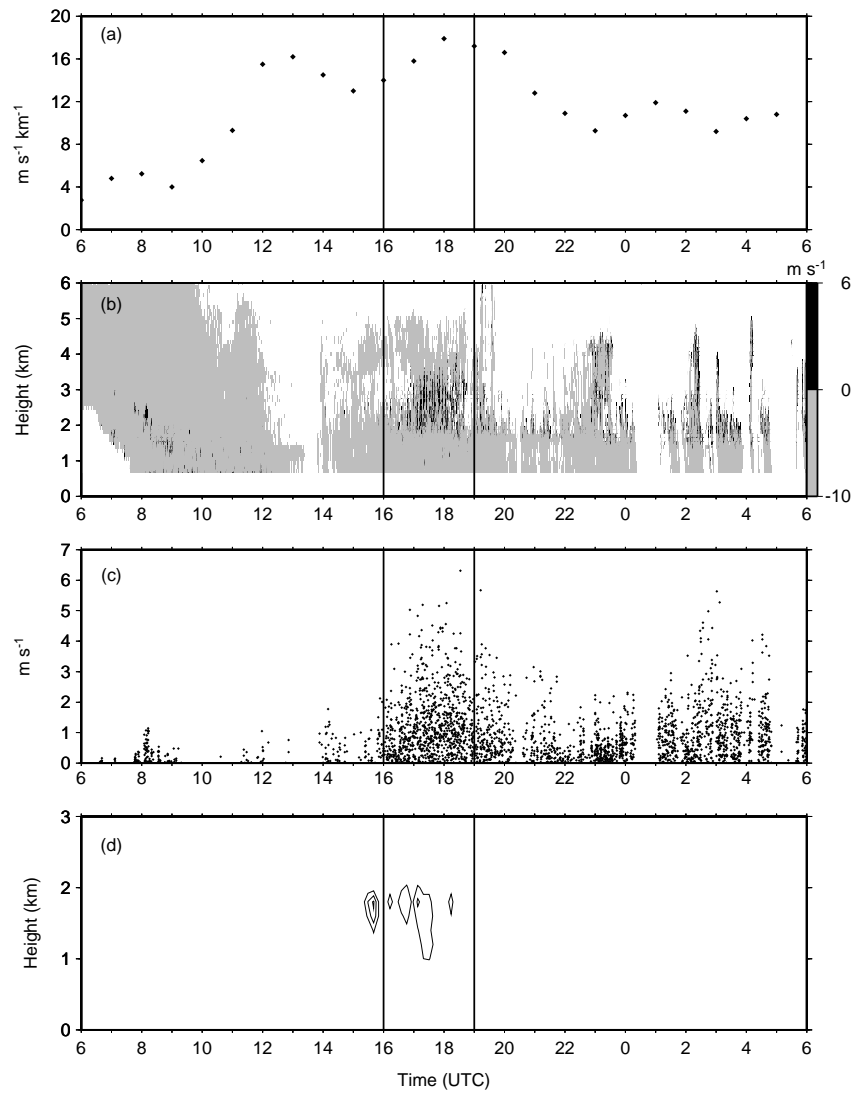
Figure 4.6: As in Fig. 4.5 but for the 28-29 November 2001 storm. The period between the vertical lines corresponds to the time interval averaged or accumulated in the third column of Fig. 3.9). From Houze and Medina (2005).
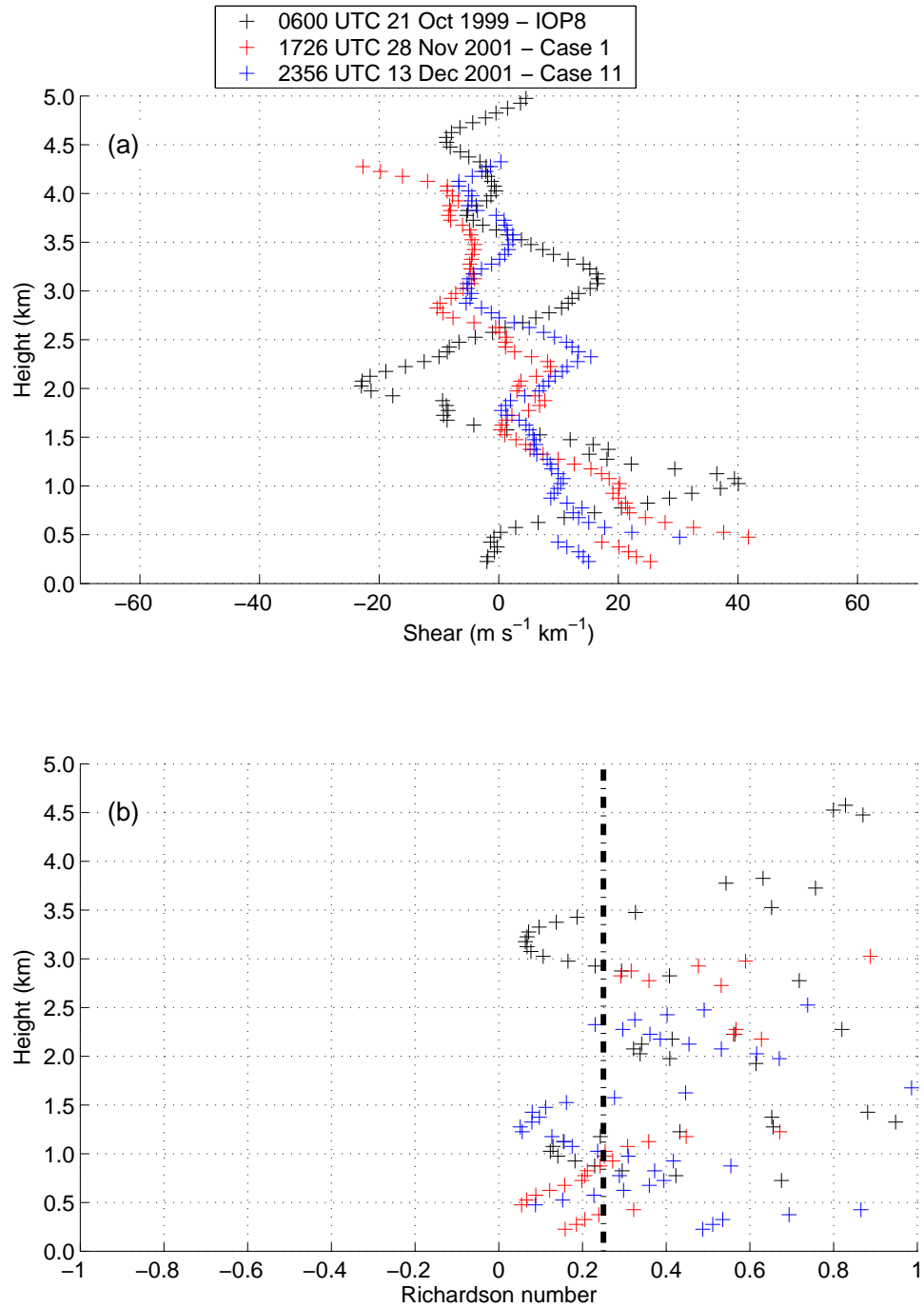
Figure 4.7: (a) Vertical wind shear for Type B storms calculated from the data shown in Fig. 3.17a. (b) Richardson number (calculated using moist Brunt-Väisälä frequency).
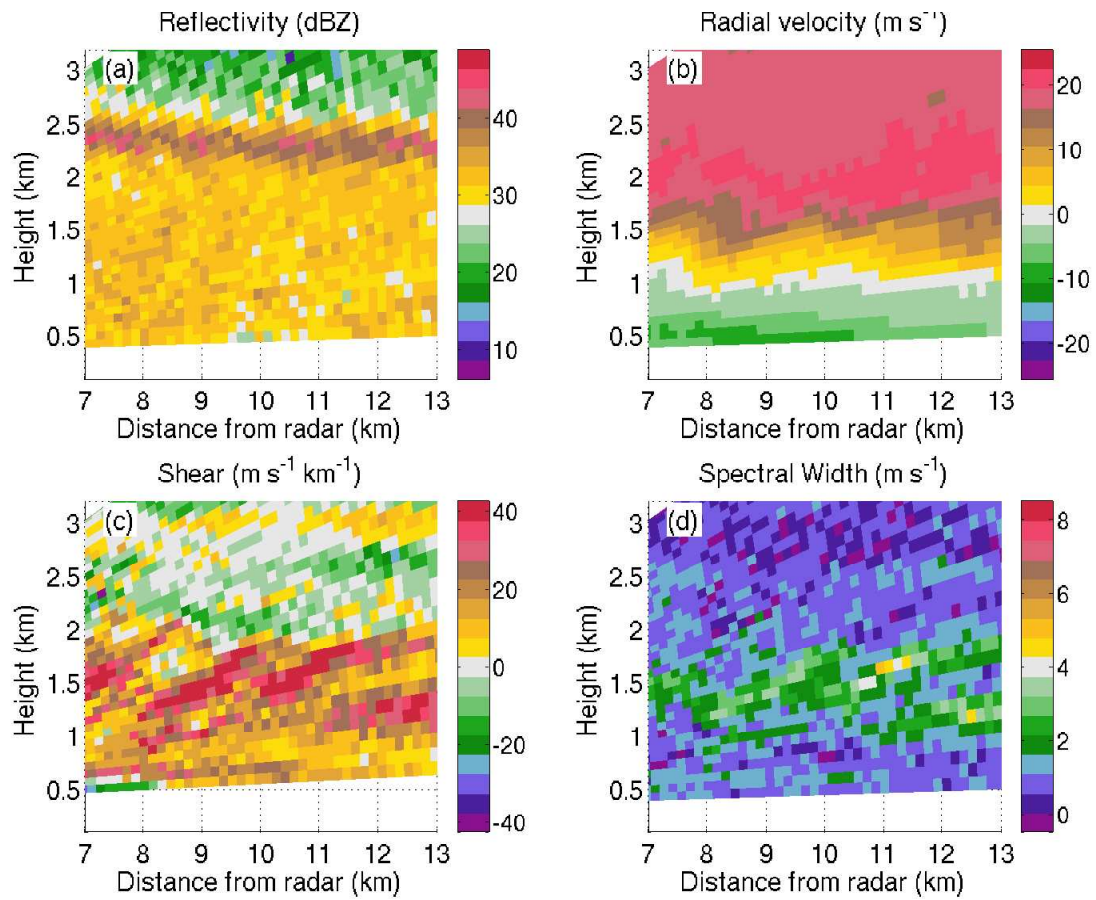
Figure 4.8: S-Pol radar RHI collected at 0857 UTC 21 October 1999 for an azimuth of 317.5° showing (a) reflectivity (dBZ), (b) radial velocity ($\mathrm{m\,s^{-1}}$), vertical wind shear ($\mathrm{m\,s^{-1}\,km^{-1}}$), and spectral width ($\mathrm{m\,s^{-1}}$).
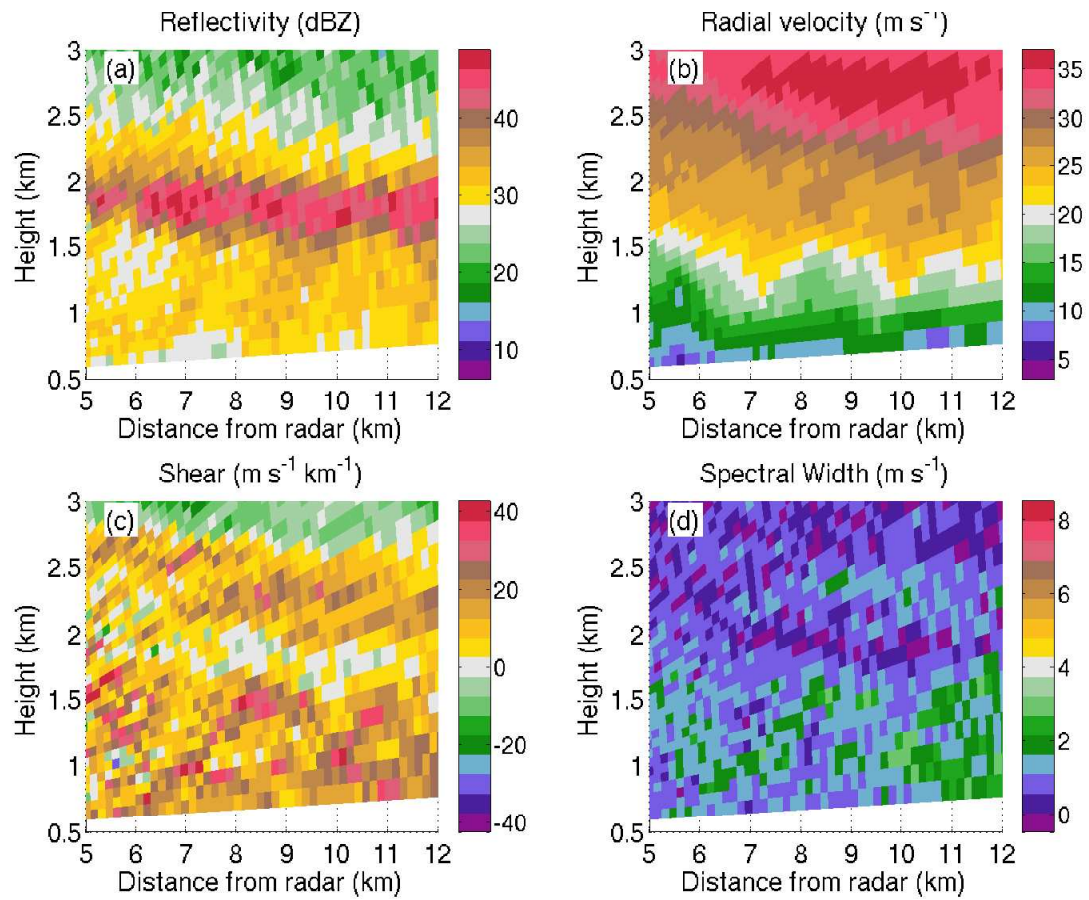
Figure 4.9: S-Pol radar RHI collected at 0025 UTC 14 December 2001 for an azimuth of 90.0° showing (a) reflectivity (dBZ), (b) radial velocity ($m\,s^{-1}$), vertical wind shear ($m\,s^{-1}\,km^{-1}$), and spectral width ($m\,s^{-1}$).
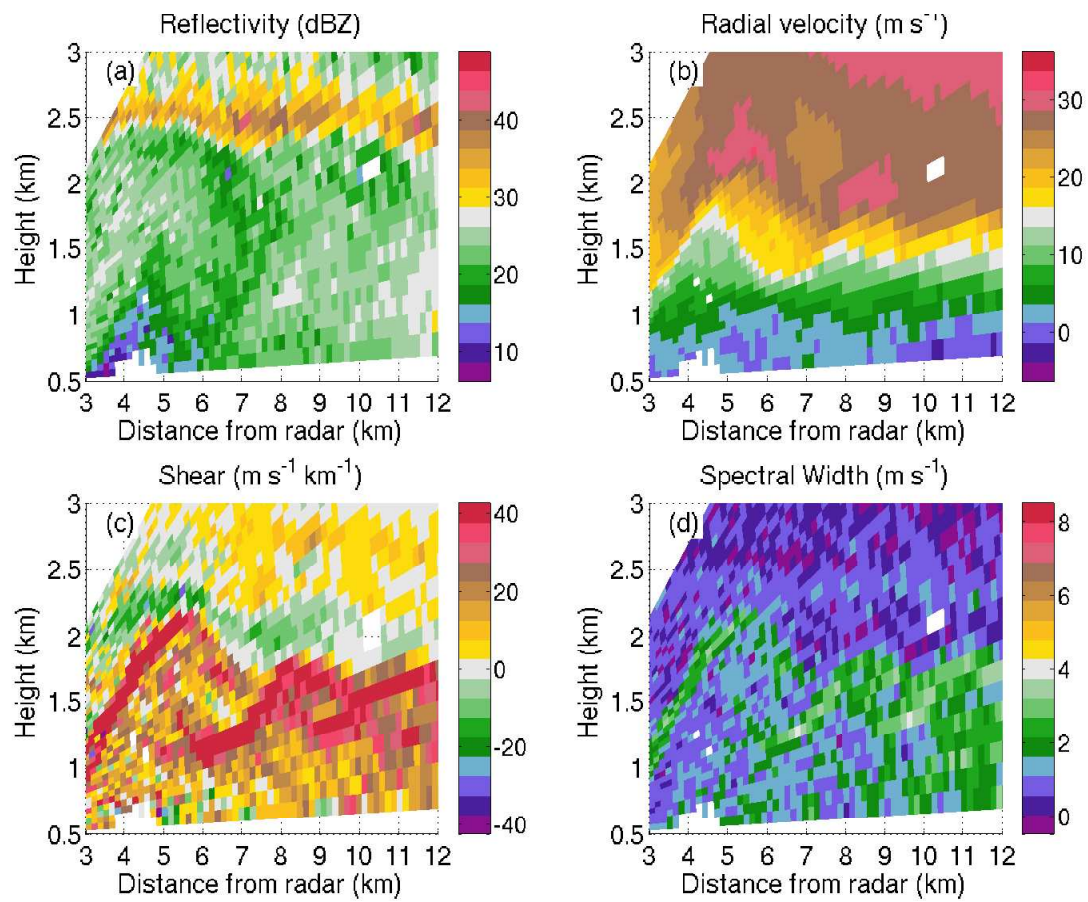
Figure 4.10: S-Pol radar RHI collected at 1500 UTC 28 November 2001 for an azimuth of 90.0° showing (a) reflectivity (dBZ), (b) radial velocity ($\mathrm{m\,s^{-1}}$), vertical wind shear ($\mathrm{m\,s^{-1}\,km^{-1}}$), and spectral width ($\mathrm{m\,s^{-1}}$).
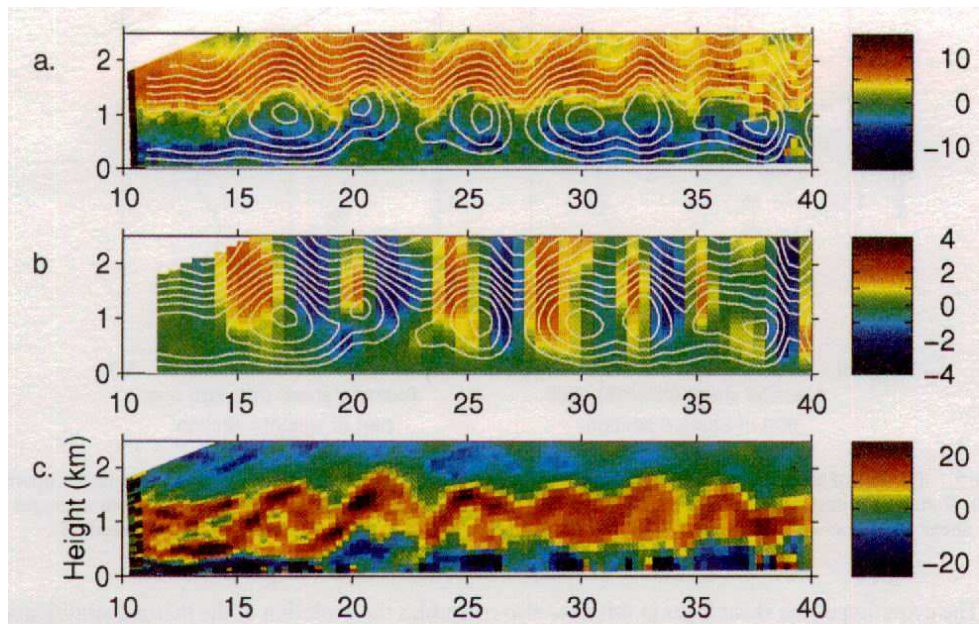
Figure 4.11: Vertical RHI collected by Chilbolton radar at 2220 UTC 6 September 1995 for an azimuth of 90.0° showing (a) radial velocity ($\mathrm{m\,s^{-1}}$, blue to the left and red toward the right). Superimposed are contours of mass-streamfunction projected onto the plane of the RHI. (b) Vertical velocity ($\mathrm{m\,s^{-1}}$), and (c) vertical wind shear ($\mathrm{m\,s^{-1}\,km^{-1}}$). The horizontal scale denotes distance (in km) from the Chilbolton radar. From Chapman and Browning (1997).
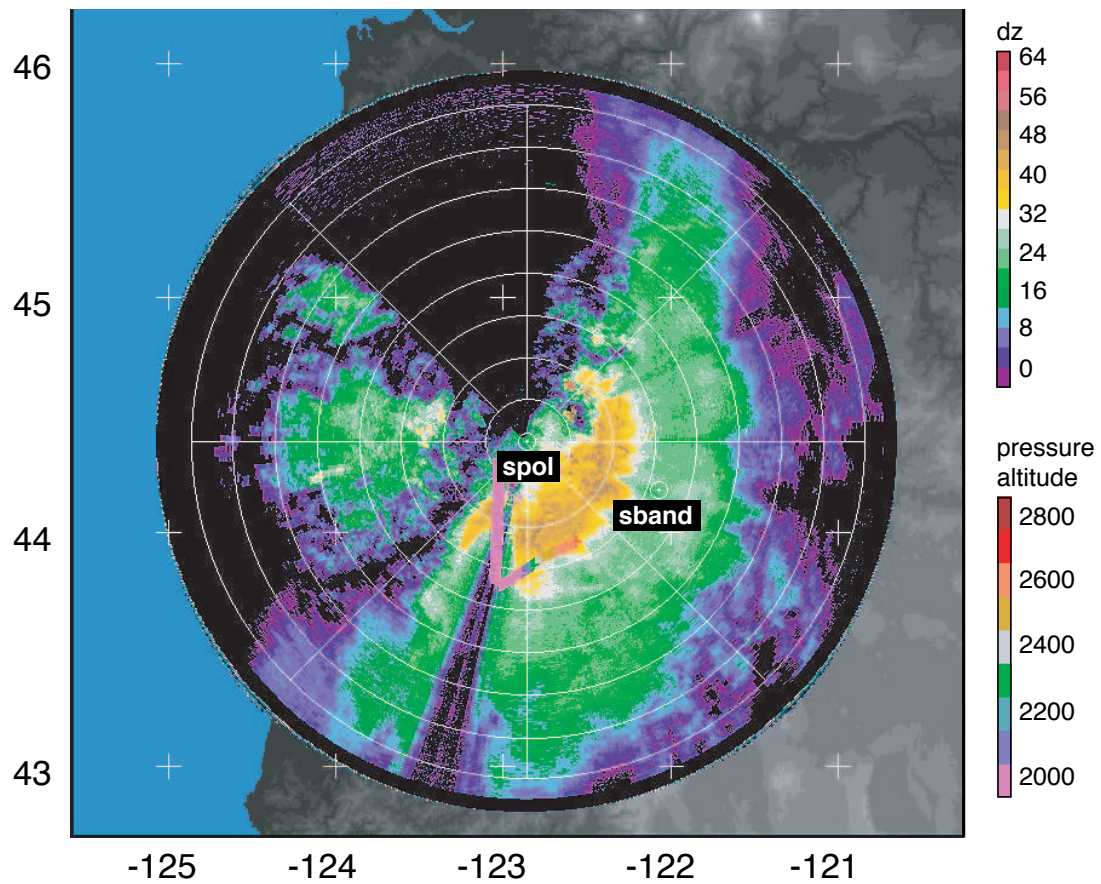
Figure 4.12: 1.5° elevation PPI of S-Pol reflectivity at 0106 UTC 14 December 2001. The WP-3D flight track from 0120-0135 UTC 14 December 2001 is shown with color-coded pressure altitude (m). The range ring spacing is 20 km. From Houze and Medina (2005).
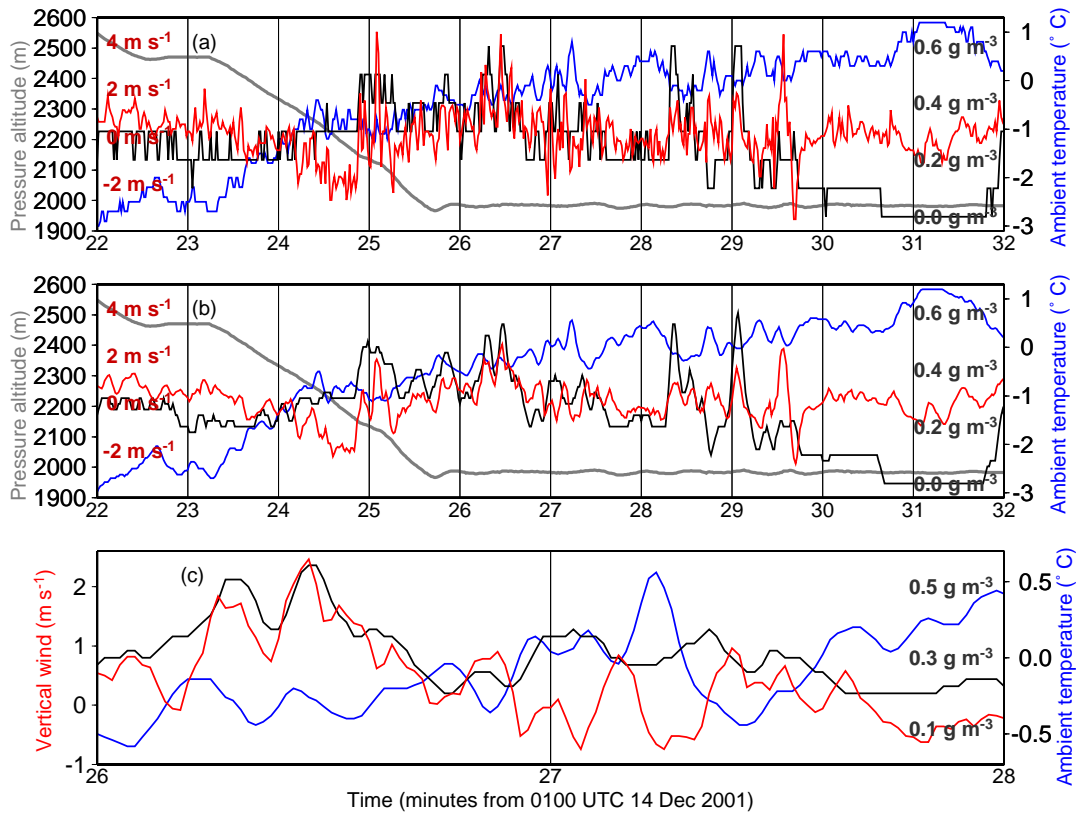
Figure 4.13: WP-3D flight track data collected during a segment of the flight shown in Fig. 4.12. (a) Pressure alitude (gray line), air temperature (blue line), vertical wind (red line), and cloud liquid water (black line). (b) As in (a) but with a 5-point running average filter applied to all variables except pressure altitude. (c) As in (b) zooming in over a 2-min segment. From Houze and Medina (2005).
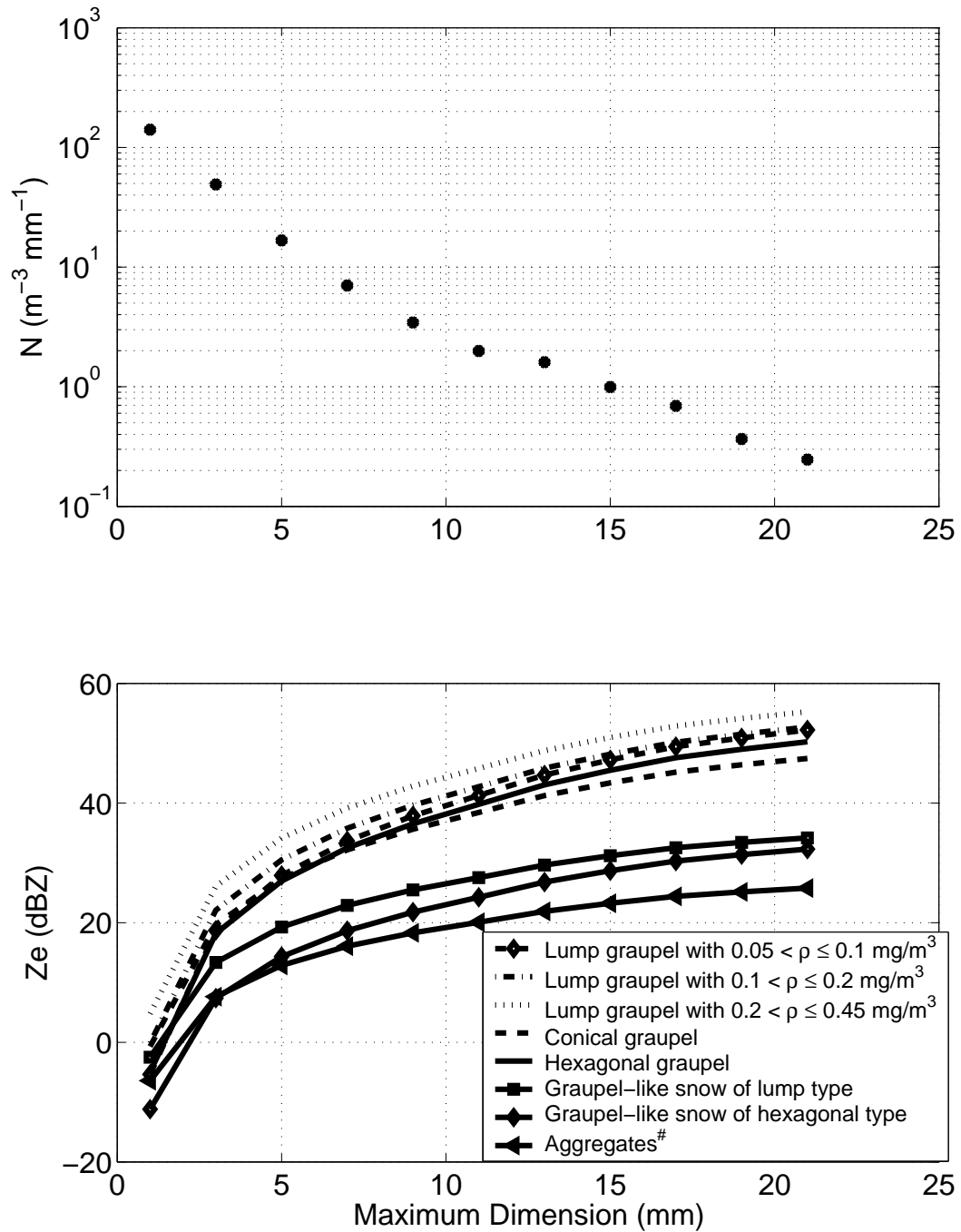
Figure 4.14: (a) Particle number density spectrum from WP-3D 2DP PMS probe from 0126-0127 14 December 2001. (b) Reflectivity produced by the spectrum in (a) for different densities of rimed particles. The densities used are from Locatelli and Hobss (1974). From Houze and Medina (2005). #The full description of this category is: aggregates of densely rimed radiating assemblages of dendrites or dendrites.
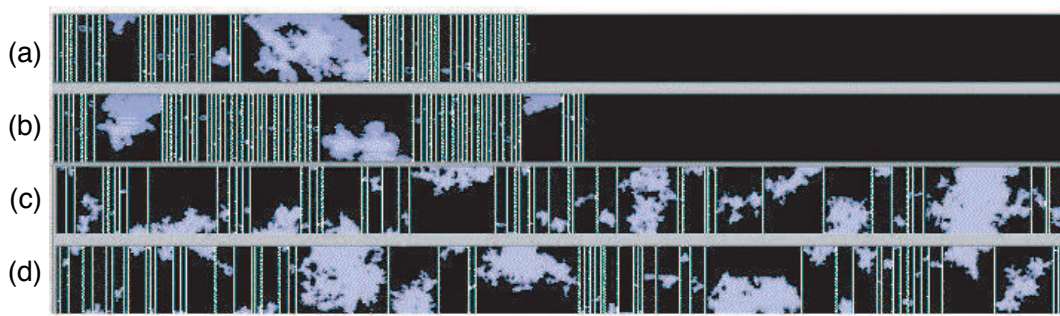
Figure 4.15: Ice particle imagery taken with PMS probes on the WP-3D aircraft at an altitude of 2 km ($\sim$60 km to the south of the S-Pol radar). Data collected at 0126 UTC 14 December 2001 with (a)-(b) 2DC probe (width = 1.6 mm) and (c)-(d) 2DP probe (width = 9.6 mm). From Houze and Medina (2005).

(a)
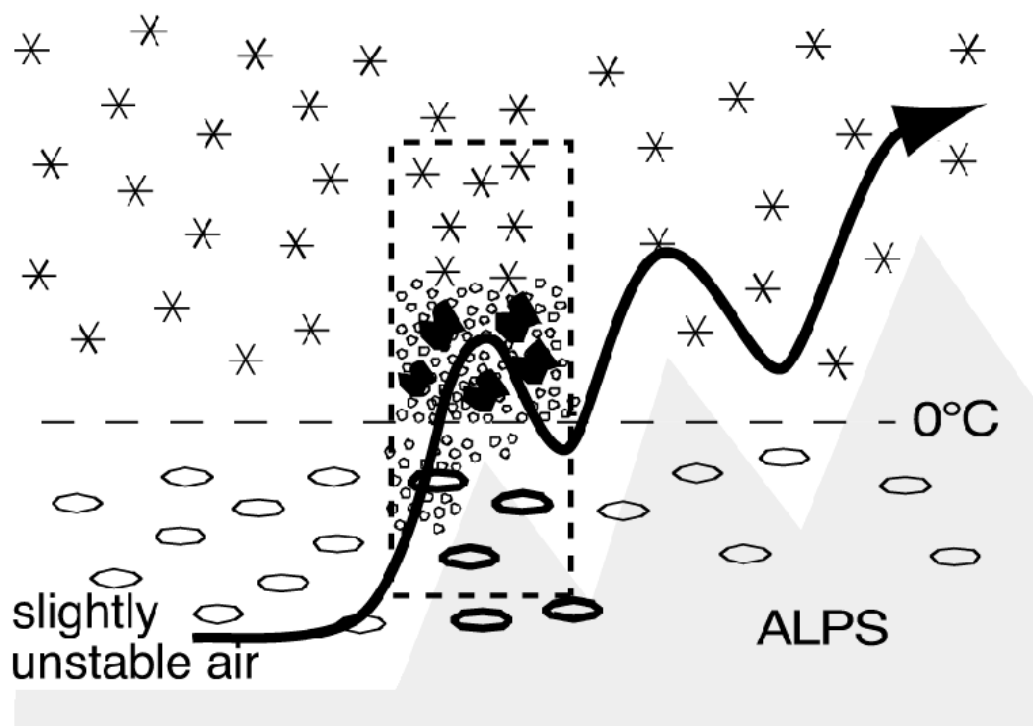
(b)

Figure 4.16: (a) Conceptual model of the dynamical and microphysical mechanism responsible for the orographic enhancement of precipitation during storms with low-level flow rising over the terrain (Type A). (b) Key for hydrometeors. From Medina and Houze (2003a).

* Widespread snow associated with large-scale baroclinic system
∘ Rain
Overturning cell
Region of enhanced growth by coalescence
Region of enhanced growth by riming and aggregation
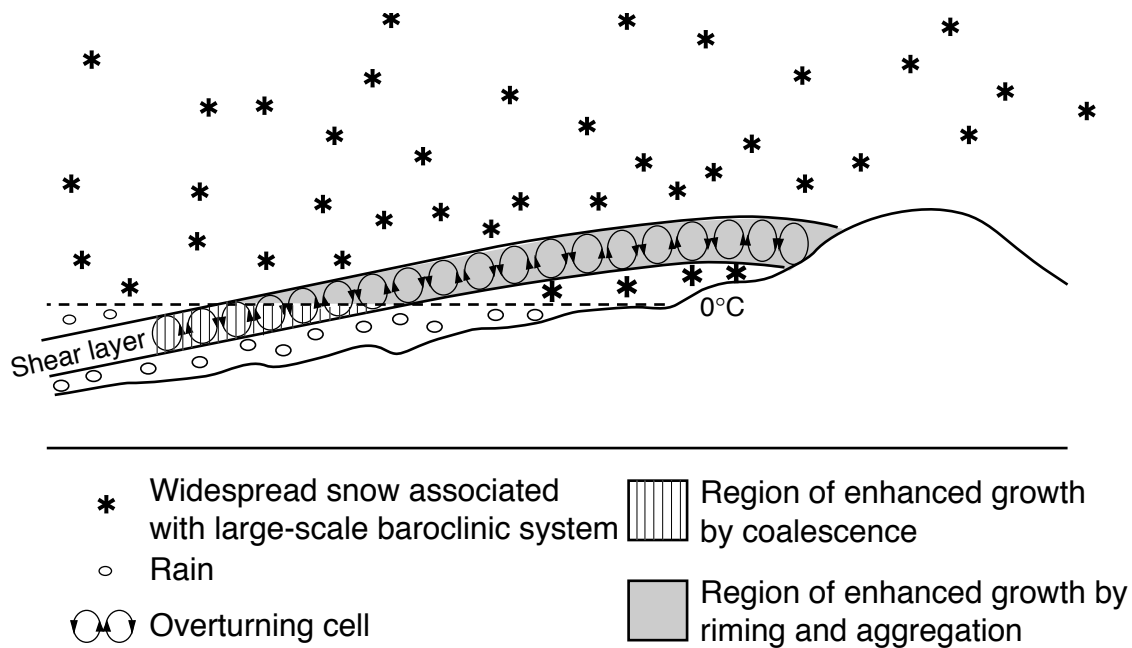
Figure 4.17: Conceptual model of the dynamical and microphysical mechanism responsible for the orographic enhancement of precipitation during storms characterized by a shear layer on the windward slopes (Type B). From Houze and Medina (2005).

Chapter 5

NUMERICAL SIMULATIONS OF SHEAR LAYER DEVELOPMENT IN TERRAIN MODIFIED CROSS-BARRIER FLOW

The observations of orographic storms over different geographic regions described in Chapter 3 and 4 suggest that the airflow pattern on the windward slope of the terrain exhibits certain key similarities, which indicate recurring dynamical mechanisms. In this chapter, we will explore possible mechanisms that contribute to the formation of the shear layer observed during Type B storms. A variety of mechanisms may contribute to the existence and maintenance of stably stratified airflow and associated shear impinging upon mountain barriers. In particular, it is possible that the observed shear layer is the manifestation of pre-existing baroclinic shear. This chapter explores the role of steep terrain in the development of the observed cross-barrier pattern. We will use two-dimensional (2D) numerical simulations conducted with the Weather Research and Forecasting (WRF) model to examine how the shear layer separating low-level weak flow from upper-level unblocked flow develops as a baroclinic system passes over a mountain barrier. Idealized numerical simulations are used here to study how flow with varying degrees of stabilities and shear responds to the terrain. The use of an idealized model allows us to focus in this chapter solely upon the terrain-airflow interaction. In the next chapter, realistic 3D mesoscale model simulations are presented to analyze terrain-airflow interaction in the detailed representation of precipitation, hydrometeor types and microphysical processes.

5.1 Model description and experimental approach

A suite of 2D idealized simulations was conducted in collaboration with Matthias Steiner from Princeton University; the outcome of this collaboration was presented in Medina et al. (2005). In this chapter we summarize the results from that work. The simulations were conducted with the non-hydrostatic WRF model (Michalakes et al. 2001; Skamarock et al. 2001) version 1.3 formulated in Eulerian mass coordinates. The simulations used the Lin et al. (1983) hydrometeor scheme, which included prognostic equations for cloud, rain, snow, and graupel. Fifth- and third-order momentum and scalar advection schemes were used in the horizontal and vertical, respectively. The calculations were made assuming both a frictionless "free-slip" land surface and a more realistic treatment assuming a non-dimensional surface drag coefficient $C_d = 0.01$. Turbulent processes above the surface are neglected. The horizontal domain covered 400 grid points at 2 km spacing, with open lateral boundary conditions applied at the upstream and downstream ends of the domain. A stretched terrain-following vertical coordinate was used, composed of 120 layers with an approximate vertical resolution of 250 m. Rayleigh damping was implemented over the uppermost 15 km of the 30 km vertical computational domain. Model integrations were carried out using a third-order Runge-Kutta scheme and time steps of 10 s.

The terrain was represented as a 2D bell-shaped symmetric mountain with height h and half-width a placed in the center of the 800 km-wide computational domain. The geometry of the Oregon Cascades within the IMPROVE-2 study regions was approximated by mountain parameters $h = 1.9$ km and $a = 32$ km, while the European Alps in the Lago Maggiore region were represented by setting $h = 3.1$ km and $a = 44$ km. For graphical clarity, the results discussed in this chapter are shown windowed over a mountain-centered subset of the computational domain and after 30 hours of integration. Since our focus is on the structure of the flow over the relatively small spatial domain located directly above the steep terrain, the resulting time

scales are small compared to the inertial period, leading to relatively large Rossby number values (between 2 and 9, see Table 5.1). This limited domain supports simplifying the problem by neglecting rotational effects, hence the Coriolis force was not included in our simulations. The atmospheric environment used to initialize the suite of simulations was characterized by saturated profiles with vertically uniform moist Brunt-Väisälä frequency (N_m), with ${N_m}^2$ varying over the range of $0.03\text{x}10^{-4}$ to $1.0\text{x}10^{-4}$ s^{-2}. The temperature profile was prescribed by a fixed surface temperature (T_s) and a tropopause at 200 mb with isothermal conditions above[1].

5.2   Test of model by comparing Type A and Type B cases

To establish that the numerical model can reproduce the orographic cross-barrier flow patterns identified in this study, we conducted simulations using upstream conditions similar to those observed during two widely studied storms, MAP IOP2b (Type A) and MAP IOP8 (Type B). These simulations included surface friction. IOP2b was characterized by a nearly neutral to slightly unstable upstream flow and wind component normal to the barrier exhibiting a low-level jet (black dots in Figs. 3.13d and 3.14c, respectively). In the corresponding idealized simulation, upstream conditions were specified using a simplified wind profile (characterized by uniform 10 $m\,s^{-1}$ wind with a superposed 2 km-deep jet exhibiting peak speeds of 20 $m\,s^{-1}$ centered at 1 km, with linear shear above and below the jet core) and vertically uniform nearly neutral stable stratification (${N_m}^2 = 0.03\text{x}10^{-4}$ s^{-2})[2].

In the simulation of IOP2b, the low-level jet rose over the windward terrain slope (Fig. 5.1a), in a manner similar to the observed time-mean cross-barrier airflow (Fig. 3.7a). Simulated flow in the lee of the Alpine-like barrier includes enhanced downslope winds that exhibit some aspects of mountain wave behavior. No corresponding

---

[1]The simulation shown in sec. 5.4 used different initial conditions, which are described in that section.

[2]The use of a nearly neutral, yet slightly stable stratification avoided the undesirable complication of convective overturning.

detailed observations are readily available with which to verify this leeside feature. In contrast to the IOP2b, the IOP8 case had a profoundly stable low-level flow (black dots in Fig. 3.16d). The simulation of IOP8 (Fig. 5.1b) was initialized with vertically uniform wind speed (10 m s^{-1}) and stability ($N_m{}^2 = 1.0$x10^{-4} s^{-2}). The contours of the wind normal to the barrier in the simulation show strong low-level flow retardation culminating in reversal of the near-surface wind over the windward slopes at the lower levels. This structure is consistent with the observed cross-barrier mean pattern for IOP8 (Fig. 3.9a). Strong downslope flow in the lee of the Alps conforms to the notion of a rearward tilted wave response to the barrier. The similarities between the simulated patterns depicted in Fig. 5.1 and extensive Doppler radar observations obtained during MAP IOP2b and IOP8 suggest that the model is capturing the orographically-modified flow in a sufficiently realistic way to merit its further use as a tool for exploring some of the controlling parameters of the cross-barrier flow features.

5.3 Sensitivity of terrain modified cross-barrier flow to stability

In this section we explore whether the wind fields observed by Doppler radar in stable MAP and IMPROVE-2 cases are a characteristic response of the flow to terrain forcing, as opposed to simply being some pre-existing inherent property of the baroclinic storm systems. First, a series of experiments initialized with vertically uniform wind speed will be presented. The atmospheric environment used to initialize these idealized simulations was characterized by saturated profiles with vertically uniform moist static stability varying over a range of 0.03x10^{-4} s$^{-2} < N_m{}^2 < 1.0$x10^{-4} s^{-2}, vertically uniform horizontal winds speeds of 10 m s^{-1}, and a fixed surface temperature of $T_s = 283$ K. This variation of the upstream moist static stability yielded a range of moist flow parameter ν_m (recall Chapter 1, sec. 1.2.1) between 0.3 and 3 (Table 5.1) and associated dynamical behavior. Figure 5.2 shows the horizontal wind speed or cross-barrier wind (color shading) and vertical wind shear (black contours) for a suite of simulations conducted using an Alpine-like barrier. The panels on the left-hand side

of the figure show results for free-slip conditions. Thus, the flow variations depicted in these simulations are entirely due to the presence of the mountain. Under neutral moist static stability conditions, the wind speeds increase monotonically toward the crest, the simulated flow easily surmounts the Alpine-like barrier and the vertical shear over the windward side is small (Fig. 5.2a). As the stability increases, the windward flow below crest level progressively slows down and the vertical shear over the windward slopes increases (Fig. 5.2c,e). The experiment based upon the most stable upstream profile exhibits an elevated layer of vertical shear that tilts upward over the windward slope (Fig. 5.2e). The negative wind speeds below 1 km indicate the presence of a deep layer of blocked low-level flow (Fig. 5.2e), reminiscent of the observations made during IOP8 (Figs. 3.9a and 3.10a). The set of experiments shown in Fig. 5.2(a), (c), and (e) indicate that the shear layer over the windward slope can emerge as a result of statically stable flow interacting with the terrain (even in the absence of surface friction).

However, the choice of free-slip lower boundary condition may not produce realistic near-surface flow over mountainous terrain. Therefore, additional simulations were conducted incorporating friction at the land surface. These results are shown in the right-hand side of Fig. 5.2. For the experiment with the lowest stability values, the inclusion of surface friction produces a substantial increase of the near-surface shear on the wind- and leeward sides of the barrier (cf. Figs. 5.2a and 5.2b). For the intermediate stability case, friction causes the windward low-level flow to decelerate even further and a well-defined shear layer emerges (cf. Figs. 5.2c and Fig. 5.2d). Finally, the effect of friction on the windward side is slight for the most stable simulation (cf. Figs. 5.2e and Fig. 5.2f).

An analogous set of simulations was conducted for a Cascade-like mountain (Fig. 5.3). The simulations conducted with a free-slip lower boundary showed that increased upstream stability results in the production of progressively greater vertical shear over the windward slopes. The intensity and upwind extension of the shear layer as well as

the downstream gravity-wave behavior increase under conditions of greater stability (Fig. 5.3 (a), (c), and (e)). The inclusion of friction at the lower boundary increases the near-surface flow retardation [Fig. 5.3(b), (d), and (f)]. The IMPROVE-2 cases described in Chapter 3 exhibited low-level mean stability of $N_m{}^2 = 0.37\text{x}10^{-4}$ s^{-2} ($0.71\text{x}10^{-4}$ s^{-2}) and low-level mean wind speed of 22.5 m s^{-1} (21.5 m s^{-1}) (see Table 3.1). To compare these cases with simulations shown in Fig. 5.3 it is useful to think in terms of ν_m values. The observed cases have $\nu_m =$1.9 (1.3) (see Table 3.1), which is an intermediate state between that represented by panels a-b ($\nu_m = 3$) and c-d ($\nu_m = 1$) in Fig. 5.3 (Table 5.1). In this ν_m regime, the shear layer does not convincingly appear in the absence of friction (Fig. 5.3a,c). Surface friction does, however, lead to a slightly elevated layer of maximum shear, particularly in situations of intermediate stability (Fig. 5.3d). Although the idealized simulation shown in Fig. 5.3e suggest that a robust shear layer could develop over a Cascade-like barrier as a result of stability alone, such strong stratification (accompanied by weak cross-barrier winds) was not observed in the IMPROVE-2 cases. Thus, for the cases described in Chapter 3, the Cascade-modified flow appears to differ from that over the Alps, where large stability and terrain-flow interactions alone may be sufficient to produce strong shear. In the Cascades case, the shear layer is apparently produced primarily by friction with stability playing a lesser role.

5.4   Simulation of IMPROVE-2 Case 11 (13-14 December 2001)

This section explores more realistic simulations using upstream wind and stability profiles that are based on the observations collected during 13-14 December 2001 and are therefore not vertically uniform. To initialize this simulation, a simplified version of the upstream sounding released at 2356 UTC 13 December 2001 was used (solid lines in Fig. 5.4). The sounding contained a shear layer between the surface and 3 km of $\sim$12 m s^{-1} km^{-1}. This sounding was applied at the upstream lateral boundary of the model domain (that is, at a distance of 400 km from the mountain crest) and

the simulation was conducted including surface friction (see sec. 5.1).

The structure of the simulated cross-barrier flow (Fig. 5.5a) is similar to that depicted in the observations (Fig. 3.10b). The isotachs in the simulation bend up over the windward slope as in the observations, and there is flow retardation at low levels. A thin near-surface layer of reversed (downslope) flow appears, but most of the airflow surmounts the barrier (after passing through a windward zone of flow deceleration and lifting). The flow contours reach peak heights (denoting maximum flow deceleration at any given level) near the crest (Fig. 5.5a). Immediately downstream of the crest, the flow contours drop rapidly, denoting downward momentum transport. This pattern is consistent with mountain-induced gravity wave behavior, which has been the subject of many previous simulations focusing on the lee-side flow behavior (e.g., Durran and Klemp 1983). Figure 5.5b shows that the flow response formed a slightly elevated layer of enhanced shear exceeding 17.5 $\mathrm{m\,s^{-1}\,km^{-1}}$ that tilts upward over the windward slopes and extends up and over the crest. This simulation suggests that the shear increase is an inherent feature of the flow over mountainous terrain. While moderate stability contributes somewhat to the development of the shear layer, the assistance of friction is fundamental in enhancing pre-existing vertical gradients in the upstream wind profile in the IMPROVE-2 Type B storms.

Table 5.1: Rossby radius of deformation $(L_r)^a$, Rossby number $(Ro)^b$, flow parameter $(\nu_m)^c$ and relevant parameters associated with WRF simulations of Chapter 5.

Figure	$N_m{}^2$ (10^{-4} s^{-2})	$U_\perp$ (m s^{-1})	h (km)	a (km)	L_R (km)	Ro	ν_m
5.1a	0.03	12.5^d	3.1	44	54	2.8	2.3
5.1b	1.0	10	3.1	44	310	2.3	0.3
5.2a-b	0.03	10	3.1	44	54	2.3	1.9
5.2c-d	0.30	10	3.1	44	170	2.3	0.6
5.2e-f	1.0	10	3.1	44	310	2.3	0.3
5.3a-b	0.03	10	1.9	32	33	3.1	3.0
5.3c-d	0.30	10	1.9	32	104	3.1	1.0
5.3e-f	1.0	10	1.9	32	190	3.1	0.5
5.5	0.37^d	20^d	1.9	32	116	6.2	1.7

[a] $L_R = \frac{N_m h}{f}$; N_m = Moist Brunt-Väisälä frequency; h = Mountain height; f = Corolis parameter

[b] $Ro = \frac{U_\perp}{fa}$; $U_\perp$ = Cross-barrier wind; a = Mountain half-width

[c] $\nu_m = \frac{U_\perp}{N_m h}$

[d] Vertically averaged over the lowest 3 km
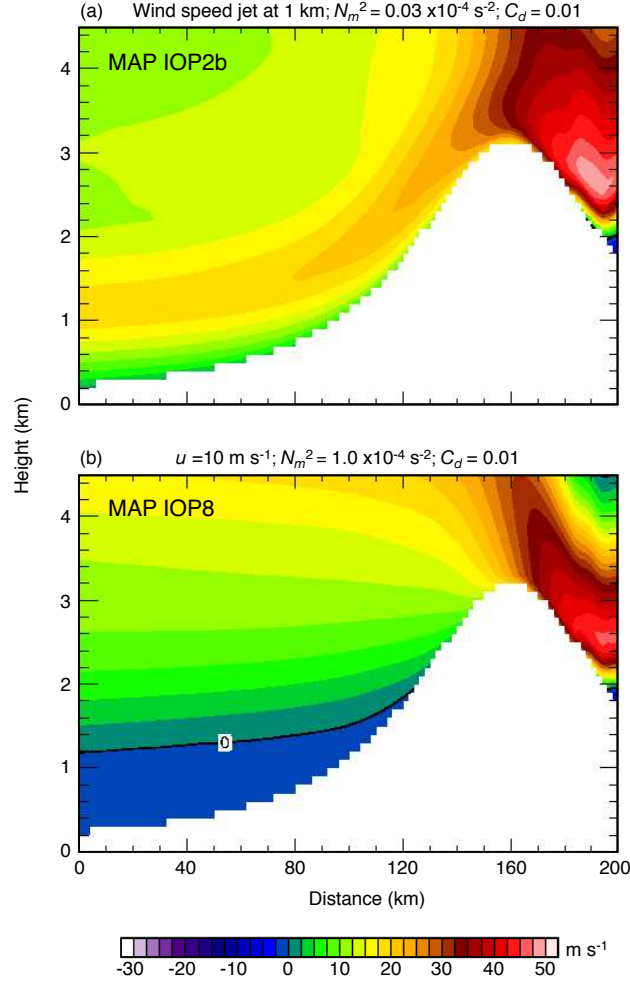
Figure 5.1: Vertical cross section of WRF-simulated moist flow past a 2D bell-shaped mountain with $h = 3.1$ km and $a = 44$ km (representing the European Alps) after 30 h of integration. Horizontal wind speed is shown in color, with positive values denoting flow from left to right and 0 m s^{-1} indicated by the black contour. Horizontal distance is label from the left edge of the display domain, which is a subset of the computational domain (see text). Panel (a) depicts a model run initialized with a saturated atmosphere with $T_s = 293$ K and vertically uniform static stability ($N_m^2 = 0.03 \times 10^{-4}$ s^{-2}). The wind speed profile was vertically uniform (10 m s^{-1}) everywhere except for a layer between the surface and 2 km, where the speeds increased linearly to reach a peak value of 20 m s^{-1} at an altitude of 1 km. Panel (b) was initialized with a saturated atmosphere with $T_s = 283$ K, vertically uniform static stability ($N_m^2 = 1.0 \times 10^{-4}$ s^{-2}) and wind speed (10 m s^{-1}). The initial wind direction from all simulations is from left to right. Both runs were obtained using surface non-dimensional drag coefficient $C_d = 0.01$. From Medina et al. (2005) and provided by Matthias Steiner.
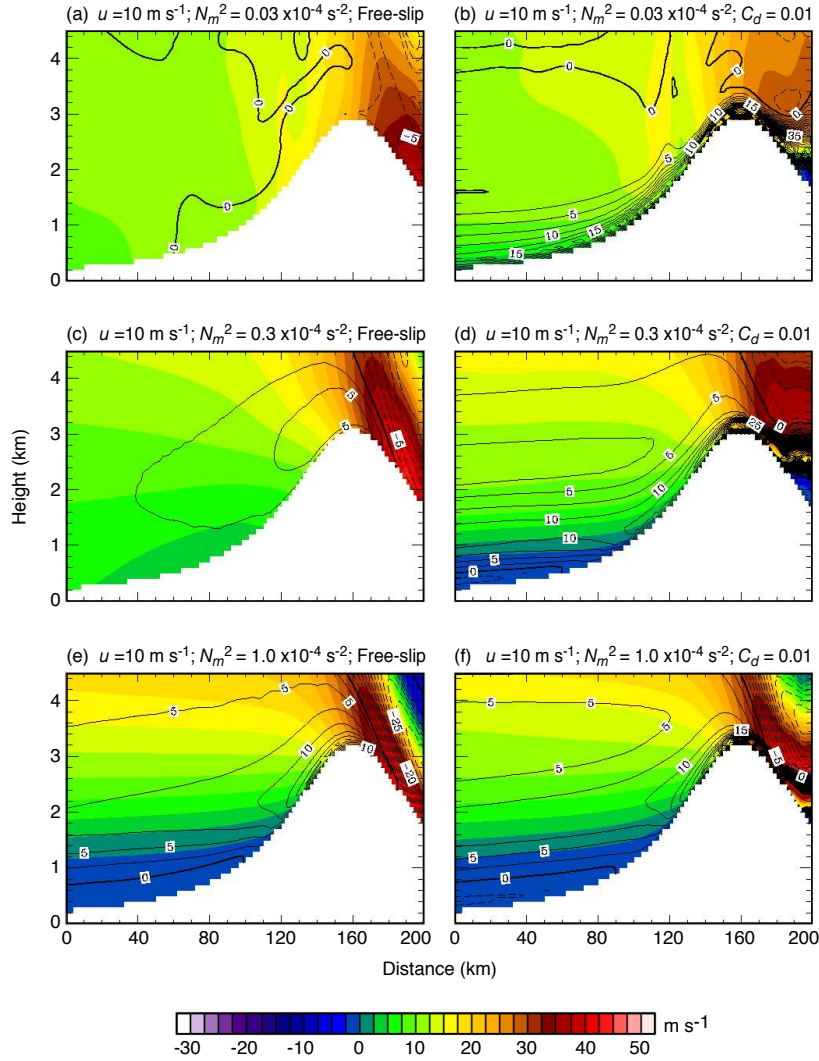
Figure 5.2: Vertical cross section of WRF-simulated moist flow past a 2D bell-shaped mountain with $h = 3.1$ km and $a = 44$ km (representing the European Alps) after 30 h of integration. Horizontal wind speed is shown in color, with positive values denoting flow from left to right. Vertical shear ($\frac{du}{dz}$, where u is the wind speed and z is the vertical coordinate) is shown by black contours at 2.5 m s^{-1} km^{-1} intervals. Horizontal distance is label from the left edge of the display domain, which is a subset of the computational domain (see text). Runs were initialized with a saturated atmosphere, $T_s = 283$ K, vertically uniform wind speed (10 m s^{-1}) and static stability with values of (a)-(b) $N_m^2 = 0.03$ x 10^{-4} s^{-2}; (c)-(d) $N_m^2 = 0.3$ x 10^{-4} s^{-2}; and (e)-(f) $N_m^2 = 1.0$ x 10^{-4} s^{-2}. The initial wind direction from all simulations is from left to right. Model runs depicted in the left column assumed a frictionless land surface, while those on the right were obtained using $C_d = 0.01$. From Medina et al. (2005) and provided by Matthias Steiner.
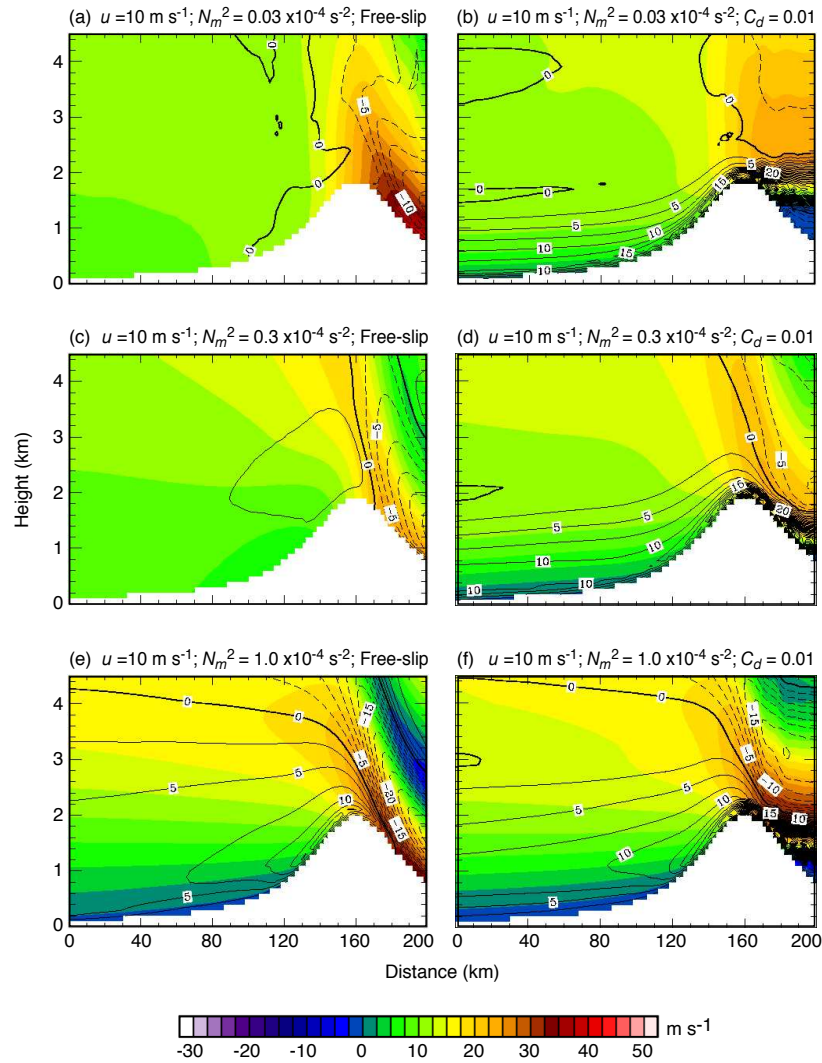
Figure 5.3: As in Fig. 5.2, but using a 2D bell-shaped mountain with $h = 1.9$ km and $a = 32$ km, representing the Cascade Range. From Medina et al. (2005) and provided by Matthias Steiner.

108
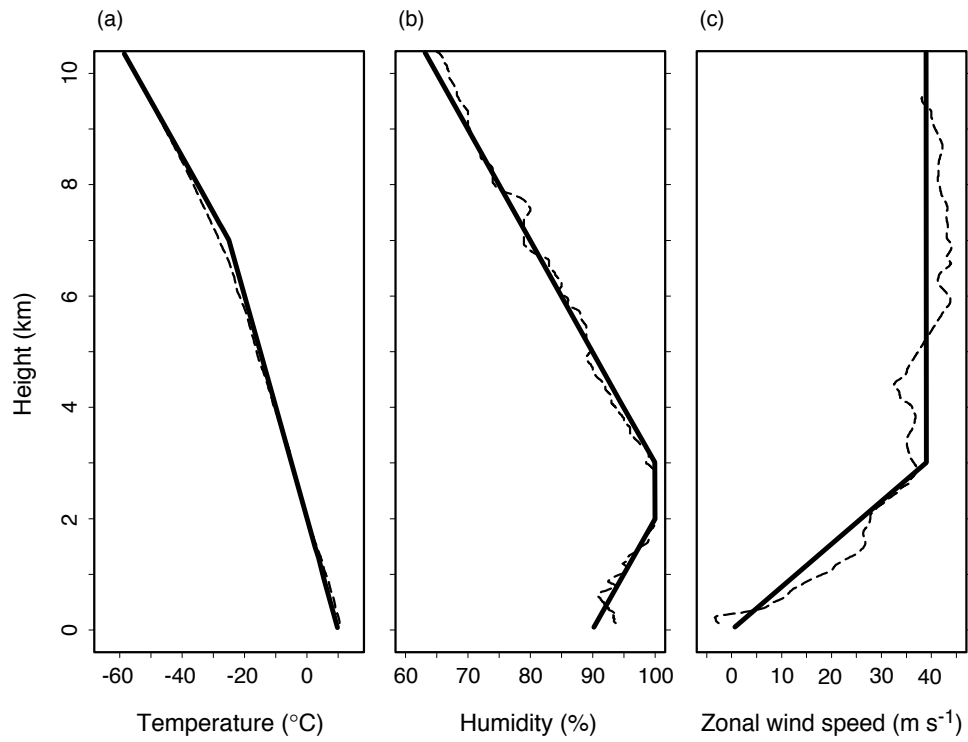
Figure 5.4: Sounding collected at 2356 UTC 13 December 2001 at UW location (Fig. 1.3). Dashed lines indicate observed quantities, while solid lines depict simplified profiles used to initialize the idealized simulations shown in Fig. 5.5. From Medina et al. (2005) and provided by Matthias Steiner.
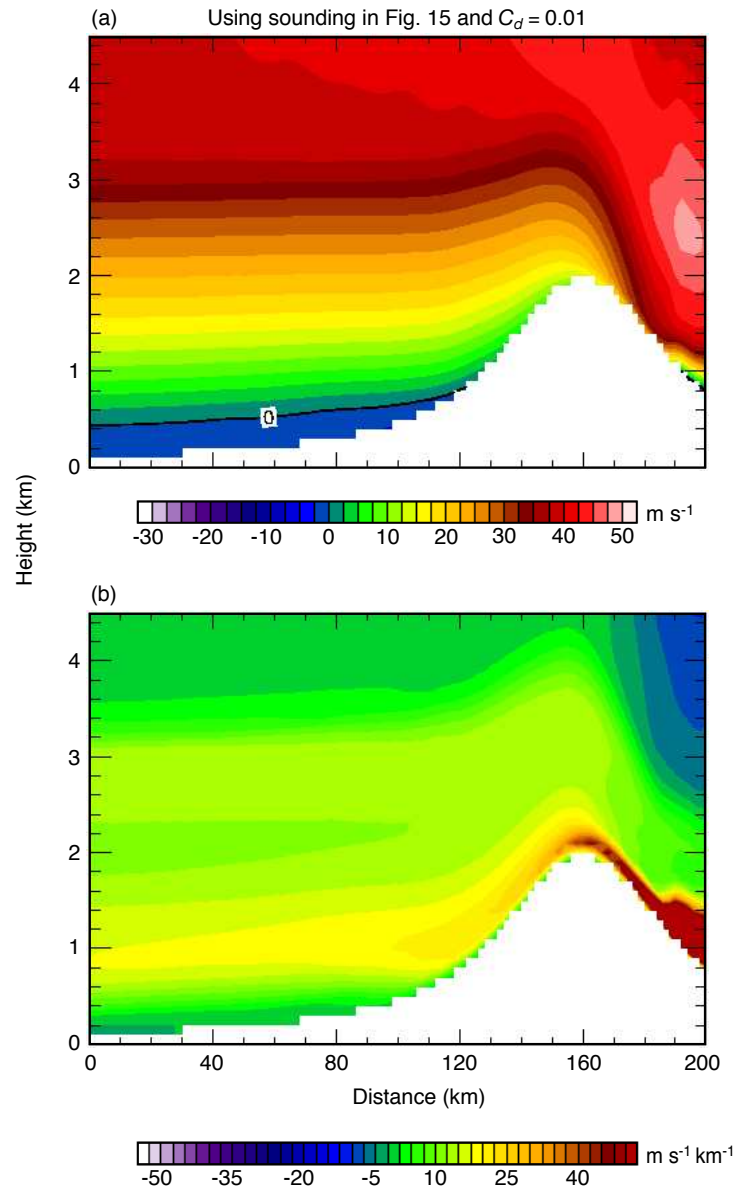
Figure 5.5: As in Fig. 5.3, but initialized using a simplified version of an observed sounding (Fig. 5.4). Panel (a) shows the horizontal wind speed, with $0 \, \mathrm{m \, s^{-1}}$ indicated by the black contour, while panel (b) shows the vertical wind shear. From Medina et al. (2005) and provided by Matthias Steiner.

Chapter 6

HYDROMETEOR DISTRIBUTION AND MICROPHYSICAL PROCESSES OF PRECIPITATION GROWTH IN MESOSCALE MODEL SIMULATIONS OF ALPINE STORMS

In collaboration with Nicole Asencio from the Centre National de Recherches Meteorologiques of Météo-France, a study of mesoscale numerical model simulations of orographically modified storms was conducted. The storms considered are MAP IOP2b (Type A) and IOP8 (Type B). The output from the simulations is analyzed mainly over the Lago Maggiore (LM) region, where most of the data were collected –in particular by the radar network (Fig. 1.11). First, the thermodynamic and kinematic characteristics of the simulations is evaluated. Then the simulated hydrometeor classes and their spatial distribution is compared with the observations. The ultimate goal is to analyze simulated orographically modified flows and embedded microphysical processes responsible for precipitation growth to test and refine the observationally-based conceptual models of orographic precipitation (sec. 4.3).

6.1   Meso-NH model description

The storm simulations were performed with the Meso-NH model, which is an anelastic non-hydrostatic mesoscale atmospheric model (Lafore et al. 1998). The IOP2b and IOP8 simulations are described in detail in Asencio et al. (2003) and Asencio and Stein (2005), respectively. An overview of the most relevant aspects of the simulations is given below. Two nested model domains are used, with horizontal resolutions of 10 km (200 points x 160 points) and 2.5 km (260 points x 170 points). The simulations were conducted using a two-way interactive grid nesting method. The nests have

the same vertical resolution (Stein et al. 2000). The vertical grid contains 50 points with resolution of 60 m at the ground and 800 m in the stratosphere. The top of the model is at an altitude of 18 km. Lateral boundary conditions are given by large-scale operational analyses for the outermost model and they are provided at every time step by the outer model to the inner model. The initial and lateral boundary conditions are given by the French operational analysis [Action de Recherche Petite Echelle et Grande Echelle (ARPEGE) described by Thépaut et al. 1998] and linearly interpolated in time between 6-hourly large-scale analyses. For the 10 km horizontal grid, the subgrid-scale convection is parameterized by a mass-flux convection scheme (Bechtold et al. 2001). For the 2.5 km horizontal grid, the convection is explicitly resolved. The microphysical scheme includes vapor, cloud water, rain, cloud ice, snow, and graupel (Pinty and Jabouille 1998). The spatial and temporal discretizations are second-order accurate and explicit. The orography is included using the Gal-Chen and Sommerville (1975) coordinate transformation. The turbulence parameterization is a 1.5-order closure (Cuxart et al. 2000). The Interactions between Soil Biosphere and Atmosphere (ISBA; Noilhan and Planton 1989) surface scheme is used, with the radiation scheme of Morcrette (1991). The IOP2b (IOP8) simulation starts at 0000 UTC on 19 September (20 October) 1999 and last 54 hours.

This study compares the output from the 2.5 km domain with the observations. For the purposes of this comparison and owing to the large volume of the model output, the vertical resolution of the simulations was reduced to 0.1 km from the surface to 2 km and to 1 km above this level. Instantaneous output of variables such as temperature, relative humidity, hydrometeor mixing ratios, etc., was obtained once an hour over the domain shown in Fig. 6.1a. Figure 6.1 displays the model's representation of the orography and relevant observational sites. Additionally, microphysical outputs (i.e., hydrometeor mixing ratios and conversion/generation rates corresponding to active microphysical processes) were obtained within a subdomain of the 2.5-km resolution domain (Fig. 6.1b) as hourly output consisting of 1-h means.

6.2 MAP-IOP2b (19-20 September 1999)

6.2.1 Validation of simulation on the Alpine scale

Asencio et al. (2003) evaluated the large- and regional-scale aspects of the IOP2b simulation. Here we present a summary of their most important findings regarding validation. They analyzed time series of observed mean sea level pressure (MSLP) over stations near the Alps and compared with the model simulation. They concluded that the quantitative evolution of MSLP was well simulated during this event. They used wind profiler data collected at Lonate (Fig. 6.1b) to evaluate the vertical structure of the simulated winds. The simulated maximum wind speed (located around 10 km altitude) was overestimated by 12 $m\,s^{-1}$. Characteristic flow features (such as an upper-level jet) were misplaced some 100 km toward the east around 1200 UTC 20 September 1999, suggesting that the timing of the simulated baroclinic trough passage was slightly ahead of the actual conditions. To evaluate precipitation, Asencio et al. (2003) compared model outputs with 24-h accumulated rain-gauge data over the whole Alpine domain. The correlation coefficient between observations and simulations was 0.75 (0.80) for 19 September (20 September) 1999. The model overestimated (underestimated) the precipitation by 4% (12%) on 19 September (20 September) 1999. Asencio et al. (2003) concluded that the spatial distribution of rainfall on the southern slopes of the Alps was well captured in the simulation.

6.2.2 Validation of simulation over the Lago Maggiore area

Thermodynamics and airflow from Milan soundings

Milan soundings (Fig. 6.1b) data, collected every 6 h, were used to validate the simulation's thermodynamic structure and low-level flow. Figures 6.2 and 6.3 show time-height plots of the temperature, vapor mixing ratio and winds at Milan as observed (left-hand side) and simulated (right-hand side). The observed and simulated

temperature and vapor mixing ratio structures are similar, although the model predicted slightly cooler conditions (cf. 6.2a and b) and a shallower moist layer from 0600 and 1200 UTC 20 September 1999 (cf. 6.2c and d). The wind speed was overestimated in the simulation at elevations ∼4-6 km from 0000 to 1200 UTC 20 September 1999 (cf. Fig. 6.2e,f). The observed low-level winds from 1800 UTC 19 September to 1800 UTC 20 September 1999 were characterized by easterly flow below ∼0.5 km altitude, then veered to southeasterly at an altitude of 1.0 km and continued to veer at higher levels (Fig. 6.3a). As described in sec. 3.3, a low-level jet was present between 0.5 and 1.0 km altitude. The simulation also produced a low-level jet located at ∼0.5 km, slightly lower than was observed (cf. 6.3a and b). The winds in the simulation are stronger with a southerly component larger than observed between 0000 to 1200 UTC 20 September 1999 (cf. 6.3a and b).

Accumulated rain and mean airflow

During MAP, rain[1] accumulation maps were calculated from radar data by Dr. Jothiram Vivekanandan of NCAR. These estimates were produced using the K_{DP} polarimetric variable measured by the S-Pol radar (Appendix A). Observed wind fields were obtained by synthesizing radial velocity data from the Monte Lema and RONSARD Doppler radars (Fig. 6.1b). Figure 6.4a shows a map of rain accumulated during 20 September 1999 based on the S-Pol 2.5° elevation scan. Ideally, we would like to look at the mean wind field for the same 24 h interval, however these data are not available. The mean wind field at 1.5 km altitude averaged over a shorter interval of 11 h (from 1900 UTC 19 September to 0600 UTC 20 September 1999) is displayed in Fig. 6.4b. At this level the prevailing winds were from the south with a slight easterly component, representing strong cross-barrier flow. Well-defined areas of maximum rain accumulation were located either on top (cells 1, 3, and 5) or on the windward

---

[1]While "precipitation" refers to liquid or solid particles falling to the surface, "rain" refers only to the liquid phase.

slope (cell 2) of the first peaks of the terrain encountered by the upslope flow (Fig. 6.4a, which also displays the 1.3 km terrain-height contour). Cell 6 was apparently not produced by orographic ascent as it tracked over a valley. Cells 1 and 2 extend upstream, while cells 3-5 were more localized over the peaks. The Milan sounding at 0900 UTC 20 September 1999 indicates LCL=0.4 km and LFC=2.1 km (Table 3.1). However, the mean LCL and LFC for the Milan sounding collected at 0000, 0600, 1200, and 1800 UTC 20 September 1999 were 0.4 km and 1.3 km, respectively. These levels are consistent with the rain accumulation pattern to the northwest of S-Pol, which shows that the rain enhancement starts at terrain elevations $\sim$0.4 km (the 0.3 km terrain-height contour is shown in Fig. 6.4c) and that the maxima in rain accumulation occur around terrain heights of 1.3 km. At ranges beyond $\sim$60 km, the rain decreases dramatically according the S-Pol estimation, which is likely a reflection of the radar's limitations associated with beam blocking and broadening at farther ranges.

Figure 6.4c-d shows the model's representation of the observed parameters described above. The simulated mean wind at 1.5 km has an easterly component stronger than observed, particularly over the higher terrain (Fig. 6.4d)[2]. The simulated accumulated rain depicts cells 1-5 at similar locations in relation to the model's orography as was observed (cf. Fig. 6.4a,c)[3], i.e., either on the windward slope or on top of the first peak that the airflow encounters (Fig. 6.4d). Model terrain contours of 0.3, 1.3, 2.3 and 3.3 km are shown in Fig. 6.4c. The highest terrain in the domain displayed in Fig. 6.4 is found along a southwest-northeast oriented ridge located to the northwest of the S-Pol radar and at ranges of $\sim$80 km. The simulation pro-

---

[2]Simulated airflow was available as an instantaneous snapshot once every 60 min. Monte Lema PPI data were available every $\sim$5 min, while RONSARD PPI data were available $\sim$15-60 min. Therefore the observed wind field was obtained by averaging fields obtained every $\sim$15-60 min.

[3]The position of cells 4 and 5 is the model's representation is slightly offset from the observations relative to the radar's grid. However their location in relation to the orography is similar to that observed.

duced local rain maxima on the windward slope of this range, which we will call the "secondary ridge". This feature is consistent with the results from the observational study of orographic precipitation over the coastal mountains of California conducted by James and Houze (2005), where reflectivity maxima were found on top of the first and second major peaks of the terrain. The high peaks ~80 km to the west-northwest of the radar (with elevations > 3.3 km) extended into the layer of subzero temperatures (mean simulated 0°C level is 3.1 km, Fig. 6.2) and hence experienced low rain accumulations (Fig. 6.4c). The mean simulated vertical velocity at 2.5 km exhibits updrafts ($\sim$1-1.5 m s^{-1}) approximately collocated with cells 1-5 and shows the upstream extension of updrafts associated with cells 1 and 2 (Fig. 6.4e). Downdrafts occurred to the lee of the peaks adjacent to cells 1 and 2; the vertical velocity became positive again over the windward slope of subsequent peaks farther to the north and had negative values to the lee of the secondary ridge (Fig. 6.4e).

Mean (1900 UTC 19 September to 0600 UTC 20 September 1999) radial velocity observations (top row) and simulation (bottom row) are shown in Fig. 6.5, along with the 1.3 km orographic contour. Green and blue (yellow and brown) shading indicates flow toward (away from) the radar. The observed 0.5 km RONSARD radar radial velocity pattern (Fig. 6.5a) indicates flow perpendicular to the terrain, i.e., upslope. The corresponding simulated field has a slightly stronger easterly component (cf. Fig. 6.5a,c). At 2.0 km, the Monte Lema radar observations show strong cross-barrier flow (Fig. 6.5b), exemplifying what Peterson et al. (1991) called "coupled flow" and Medina and Houze (2003a) and Buzzi et al. (1998) have termed a high Froude Number, unblocked or flow-over regime, where both the low-level and the higher-level flow rise over the terrain. The model's representation of the 2.0 km Monte Lema radial velocity was also cross-barrier, with its intensity overestimated (as reported by Asencio et al. 2003) by ~4 m s^{-1}(Fig. 6.5d).

Since the representation of the terrain-modified flow in the simulation is in reasonable agreement with the observations, the simulated 3D wind field and accompanying

microphysical processes will be explored further. Figure 6.6 shows a vertical cross along the red line in Fig. 6.1a. This direction is nearly parallel to the mean winds at 1 km and approximately perpendicular to the local terrain to the west of the Lago Maggiore. The wind parameters were averaged over 4 h during IOP2b (0900-1300 UTC 20 September 1999). The wind in the direction of this cross section (i.e., the cross-barrier component) suggests that the low-level jet documented in sec. 3.2.1 and 3.3 extended well upstream of the Alpine slopes, over most of the width of the Po Valley (Fig. 6.6a). The jet rose over the first peaks of the terrain, similar to the observations (Fig. 3.7a). The flow component in the direction normal to the cross section (i.e., along-barrier) showed easterly flow $\sim$10 m s^{-1} near the floor of the Po Valley (Fig. 6.6b), consistent with the Milan sounding observations (Fig. 6.3a). The mean vertical velocity tended to be weak over the Po Valley and positive (negative) over the windward (leeward) slopes of individual Alpine peaks. The mean updrafts over the terrain reached values $\sim$1.5 m s^{-1} or higher, consistent with the VP radar instantaneous observations (sec. 4.1.2).

In the simulations, hydrometeors are described by their corresponding mixing ratios. The vertical cross section plots in Fig. 6.6d-f show time-mean patterns (0900-1300 UTC 20 September 1999) of snow, graupel and rain mixing ratio, respectively, associated with the 3D wind fields just described. The black line in Fig. 6.6d-f denotes the mean 0°C level. The model-derived hydrometeors signatures are qualitatively similar those observed (Fig. 3.7g), showing graupel and snow content maximized atop the first major peak of the terrain, with rain below. Further detailed comparisons between these observed and simulated hydrometeor distributions is conducted in the next section.

Distribution of hydrometeors

A comparison between observed and simulated hydrometeor patterns was conducted by accumulating S-Pol radar particle identification fields during IOP2b (1500 UTC

19 September to 0600 UTC 20 September 1999) to produce a 3D matrix of frequency of occurrence for each hydrometeor. Most of the S-Pol radar data during IOP2b was collected in the northwest sector of radar coverage; therefore, the comparison is restricted to this area. In addition, only points at less than 60 km range from the radar were used since beyond that range the polarimetric parameters are less precise. Information from the 3D matrix is shown in Fig. 6.7. In the left-hand side of the figure, all points located in a given vertical column have been averaged to produce a mean observed frequency of occurrence for each hydrometeor at that horizontal location. In these panels the S-Pol radar is located at (x,y)=(0,0) km. For reference, the 1.3 km orographic contour is also shown. In the right-hand side of the figure all the grid points at the same altitude have been averaged to produce a vertical profile of mean observed frequency of occurrence for each hydrometeor. Figure 6.7a shows the horizontal distribution of the frequency of occurrence of dry snow, which was fairly uniform, with a maximum over higher terrain found in the southwest corner of the domain (Fig. 6.7a)[4]. Wet snow was most frequenct at far ranges from the radar (Fig. 6.7c). The occurrence of graupel was low, indicating that its presence was intermittent; graupel tended to occur most frequently either at the top or over the windward slopes of the lowest peaks (Fig. 6.7e). Light rain was maximized upstream of the lower peaks of the terrain (Fig. 6.7g). Figure 6.7i shows the horizontal distribution of moderate rain. The maximum frequency of occurrence of moderate rain can be identified either directly atop or over the windward slopes of the first peaks of the terrain, apparently corresponding to cells 1-3 identified in Fig. 6.4a. Orographically generated maxima, not so apparent in the 24 h rain accumulation map, are seen at x=-5 km, y=45 km and x=-40 km, y=15 km.

The vertical structure of the hydrometeors consisted of and dry snow at high levels

---

[4]The S-Pol radar data was complied from RHI scans that extended from an elevation of 0° to 20°. Therefore at close ranges from the radar (< 15 km) there are too few data points in a vertical column to construct a mean.

(maximum ~3.8 km, Fig. 6.7b) and intermittent graupel below (maximum ~3.3 km, Fig. 6.7f). Both were melting to form wet snow (maximum ~2.8 km, Fig. 6.7d). Below the 0°C level, light (Fig. 6.7h) and moderate (Fig. 6.7j) rain maximized at ~1.8 km.

Figure 6.8a shows the distribution of the accumulated precipitation (1500 UTC 19 September to 0600 UTC 20 September 1999) to the northwest of the S-Pol radar [located at (x,y)=(0,0)] in relation to the model's orography (indicated by terrain contours of 1.3, 2.3, and 3.3 km). The greatest precipitation accumulation tended to occur over the first peaks of the terrain encountered by the flow; these cells were located approximately along a line extending from x=-60 km, y=0 km to x=-20 km, y=60 km. An exception to this distribution was the maximum at x=-30 km, y=35 km, located inside the Toce River Valley. Precipitation accumulations were also large over the windward slopes of the secondary ridge of the terrain, as identified earlier in this section. To aid in the analysis of the simulated hydrometeors that contributed to the pattern seen in Fig. 6.8a, the mean temperature profile over the horizontal domain outlined in Fig. 6.8c was calculated (Fig. 6.8b). The simulated mean 0°C level was 3.1 km, compared to an mean observed value in a similar time interval of 3.3 km (Fig. 6.2a). For each simulated hydrometeor type, a time-mean mixing ratio for each model grid point was calculated. The data in this 3D matrix were averaged in the vertical and in the horizontal[5]. The horizontal distribution of simulated mixing ratio values of snow and graupel (Fig. 6.8c,e, respectively) show maxima on the windward

---

[5]There is a slight difference in the regions used in calculating the data displayed in Figs. 6.7 and 6.8. In the observations, the radar data was collected at a maximum elevation angle of 20°, therefore at close range from the radar few high altitude observations were available. Hence only observations at ranges > 15 km are shown. For the simulations, data at all grid points was available. We constructed vertically averaged of simulated output for elevations < 20° (not shown) and compared them to simulated data without this restriction (Fig. 6.8). Some differences occur at near ranges from the radar (< 15 km), where the number of grid points used is smaller when an elevation threshold is used. The simulation output is presented for ranges out to 85 km to capture the secondary ridge in the terrain, whereas the observations were used only within 60 km radius of S-Pol.

slopes of the highest peaks (around Monte Rosa [located at x=-70 km, y=25km] and Dom [located at x=-65 km and y=40 km]), where the precipitation is large but not maximized (Fig. 6.8a). There are secondary maxima of snow and graupel above the peaks of the first ridge (Fig. 6.8c,e, respectively). The largest simulated rain mixing ratio consist of maxima slightly upstream of the largest surface precipitation (cf. Fig. 6.8a,g). There is a secondary maximum of rain mixing ratio on the windward slopes of the subsequent ridge. The mixing ratio of rain is near zero over the peaks with elevations > 3.3 km; i.e., over Monte Rosa and Dom. These peaks were above the mean 0°C level ($\sim$3.1 km, Fig. 6.8b).

The vertical layering of the simulated hydrometeors resembles that evident in the observations. The simulated snow and graupel maxima occur at 4 km and 3.5 km, respectively (Fig. 6.8d,f), as in the observations (Fig. 6.7b,f, respectively). The rain signature is maximum near $\sim$2 km and is nearly null at $\sim$4 km (cf. Figs. 6.7h and 6.8h). In the observations, the frequency of occurrence of graupel (Fig. 6.7f) is almost negligible compared to the frequency of occurrence of both dry and wet snow (Fig. 6.7b,d). In the simulation graupel dominates over snow for altitudes between $\sim$2.5 and 5.5 km (Figs. 6.8f,d), suggesting that the simulation may be overproducing graupel. Given the intermittency of graupel in the observations and its persistence in the simulations, it is also possible that the hydrometeor that the model designates as graupel has different characteristics from the hydrometeor that is identified as graupel by the polarimetric radar algorithm. The algorithm identifies the dominant hydrometeor type as graupel if the radar echo is characterized by low ZDR and high reflectivity (Table A.1). In the model, graupel arises when large snow aggregates (diameters > 7mm) collect cloud water droplets and large raindrops. Additionally, in the model the melting of the snow is conducted by converting it into graupel, which is a source of graupel that does not have a counterpart in the observations. Ideally, melting snow should be converted into a different category characterized by an appropriate density and fall speed larger than that of dry snow. However, such

a category does not exist in the microphysical parameterization of the Meso-NH, therefore converting the melting snow to graupel is a shortcut way to assign to the melting snow a more appropriate fallspeed (i.e., that of graupel). This mechanism obviously focuses on depicting the fallspeeds of the hydrometeors correctly and not on their formation mechanisms (Walko et al. 1995). While in the simulation both snow and "graupel" contribute considerably to the precipitation at temperatures less than 0°C (Figs. 6.8d,f), in the observations the signal is dominated by the snow (Figs. 6.7b).

In Fig. 6.9b the simulated precipitating hydrometeors that occur above the 0°C level have been combined (blue line) to compare with the dominant snow (dry) in the observations (blue line in 6.9a). This figure suggests that even though what the model calls "graupel" (snow) does not compare well with the observations of graupel (snow), the combined behavior of snow and graupel is comparable in observations and simulation, as the height of the maximum and vertical distribution are similar. Hence the partitioning of water substance between these two categories appears somewhat problematic in Meso-NH, while their summed total agree more clearly with available observations. Therefore the signals of "graupel" and snow will be added up in what will be termed "cold hydrometeors". The cold hydrometeor signal is, however deeper in the simulations than in the observations (cf. blue lines in Fig. 6.9a,b). The rain signal in both observations and simulation exhibits a similar distribution, with the simulated maximum slightly higher (cf. red lines in Fig. 6.9a,b).

6.2.3   Simulated microphysical growth mechanisms in orographic precipitation

Since it has been established that the Meso-NH hydrometeor fields were comparable with the S-Pol radar observations (subject to the caveats discussed in sec. 6.2.2), we now trun to the microphysical processes as represented in the simulation to test for consistency with our conceptual model (sec. 4.3) and to quantify the magnitude of each individual process. Thirty microphysical processes are included in the Meso-NH

bulk microphysical parameterization scheme. These processes were averaged in time (1500 UTC 19 September to 0600 UTC 20 September 1999) and space.

The main processes that contributed to precipitation growth during IOP2b are presented in Fig. 6.10. The main mechanism that created cloud water was condensation, which was large generally over all the windward slopes and is slightly negative (indicating evaporation) over the leeward slopes (Fig. 6.10a). The absolute maximum occurred on the windward slopes of Monte Rosa, with the largest evaporation rates to the lee of the secondary ridge (Fig. 6.10a). Graupel was created (and cloud water and snow lost) by snow collecting cloud water (Fig. 6.10f, which gives the rate of cloud water loss in this process, hence the negative sign). Graupel grew by collecting cloud water, cloud ice, rain and snow (Fig. 6.10e). Both graupel creation and growth are maximum on the windward slope of the tallest ridge, with a secondary maximum over the lower peaks of the terrain (Fig. 6.10e,f). Rain was created when "graupel" and snow melted, a process that was particularly effective over the secondary ridge of the terrain, i.e. over the orography with elevation near (but below) the 0°C level (Fig. 6.10c). Below the 0°C level, rain grew by collecting cloud water preferentially over the windward slopes (Fig. 6.10b). The highest peaks had near-zero rates of rain-collecting-cloud water as they extended to subfreezing heights. The locations of large graupel melting rates were also the areas when rain was lost due to fallout (Fig. 6.10d).

The largest simulated rates of "graupel" generation and growth occur on the windward slopes of the highest peaks (i.e., Monte Rosa and Dom indicated by dot dashed orographic contour of 3.3 km in Fig. 6.10f,e). Due to the mean 0°C level during this event (3.1 km), melting did not occur over these peaks (Fig. 6.10c), nor did accretion of cloud water by rain (Fig. 6.10b). Therefore, the precipitation at these higher elevations was produced entirely by microphysical processes active at subzero temperatures. The precipitation accumulation on the windward slopes of these peaks was large (Fig. 6.8a), but not as great as over other regions where the orographic

enhancement of precipitation was produced by processes both above and below the 0°C level (e.g., over the lowest peaks of the terrain in Fig. 6.8a). This is significant considering that the condensation rates (Fig. 6.10a) and mixing ratio of snow and "graupel" (Fig. 6.8c,e) show absolute maxima over the near the highest terrain.

The vertical distribution of these processes is shown in Fig. 6.11. Cloud water formation through condensation occured over a wide range of altitudes, with a maximum at about 3 km (black line in Fig. 6.11). Above the 0°C level (~3 km) cloud water was lost to riming by snow to form "graupel" (blue line in Fig. 6.11). "Graupel" grew by collecting cloud ice, cloud water, rain and snow (green line in Fig. 6.11); the collection of cloud water was the largest single contributor to "graupel" growth (not shown). Rain was primarily created by melting of cold hydrometeors, with the highest melting rates were narrowly distributed around the 0°C level (cyan line in Fig. 6.11)[6]. From the surface up to ~3.5 km, rain grew by collecting cloud water (i.e., coalescence, red line in Fig. 6.11). The rate of autoconversion[7] (cloud water droplets coalescing with each other to produce rain droplets) was small[8], suggesting that most of the rain formed by other processes (i.e., melting); however once melting occurred and rain was formed, the rain grew further by collecting cloud water droplets. According to the mean vertical profiles shown in Fig. 6.11, the maximum rate of rain formation by melting was ~4 times larger than that by which rain grew by collection of cloud water (cf. cyan and red lines in Fig. 6.11), however the rates averaged over the whole 3D volume (not shown) were comparable. Rain was lost by fallout, which was the maximum around the 0°C level (magenta line in Fig. 6.11).

---

[6]The process shown by the cyan line in Fig. 6.11 is the creation of rain by melting of graupel. The BMP melting of snow is done by converting it to graupel, therefore the melting of graupel effectively includes the melting of snow.

[7]Based on Kessler (1969), the rate to autoconvert cloud into rain ($CAUTR$) increases linearly with cloud water content, but does not occur below a threshold value. $CAUTR = k_{cr} Max(0, r_c - r_c^*)$, where r_c = cloud water mixing ratio, r_c^* = threshold cloud water mixing ratio, $k_{cr} = 10^{-3}$ s^{-1} and $q_c^* = r_c^*/\rho_{dref} = 0.5 \times 10^{-3}$ kg m^{-3}; ρ_{dref} = density of dry air fraction at the reference state.

[8]Analyzed over a particular hour, the local maximum of autoconversion is about an order of magnitude smaller than the accretion local maxima.

These profiles are consistent with the 1D model calculations conducted by Yuter and Houze (2003) using vertically pointing OPRA radar data collected during IOP2b as input. The rates shown in Fig. 6.11 are of the same order as those calculated by Yuter and Houze (2003) by assuming vertical velocities ~ 2 m s^{-1}, an updraft speed that is consistent with the Meso-NH simulated values over individual peaks (Fig. 6.6c). Therefore, it is suggested that the growth precipitation mechanisms at work over the OPRA site (Fig. 1.11) are representative of processes active on the windward slopes in general.

6.3 MAP-IOP8 (20-21 October 1999)

6.3.1 Validation of simulation on the Alpine scale

Asencio and Stein (2005) have described the IOP8 simulation explored in this study. They compared simulated precipitation with 24-h accumulated rain-gauge data over the Alpine domain and found correlation coefficients between observations and simulation of 0.75 (0.58) for 20 (21) October 1999. Since their analysis was focused on the description and origins of the down-valley flow observed during this case (Steiner et al. 2003), an evaluation of this feature of the wind was also performed. They found that the winds averaged from the surface up to 0.5 km at a location inside the Toce River Valley had an evolution and intensity comparable with the observations of Steiner et al. (2003), and concluded that the down-valley flow was well captured in the model simulation.

6.3.2 Validation of simulation over the Lago Maggiore area

Thermodynamics and airflow from Milan soundings

Figures 6.12 and 6.13 show time-height plots of temperature, vapor mixing ratio and winds at Milan (Fig. 6.1b) as observed (left-hand column) and simulated (right-hand column). The model simulation captures the double 0°C level observed at 1200-1800

UTC 20 October 1999 (black line in Fig. 6.12a,b). This structure is associated with the existence of a mass of cold air over the west end of the Po Valley prior to the event. As was described by (Bousquet and Smull 2003a), this airmass was eventually eroded away as warm southerly incoming air entered the western edge of the Po Basin. Associated with this temperature profile is a double maximum in vapor mixing ratio, which was also depicted by the simulation (Fig. 6.12c,d). The simulated wind speed is in agreement with the observation at early times (1200 UTC 20 October - 0000 UTC 21 October 1999) but some overestimation occurred around 0600 UTC 21 October 1999 (Fig. 6.12e,f). The low-level winds clearly showed blocked flow below $\sim$1 km and a jet above the low-level blocked air (between 1.5 and 2.0 km) between 0000-1200 UTC 21 October 1999 (Fig. 6.13a). In the simulation the blocked air was shallower and the jet overriding it was located at a lower elevation ($\sim$1 km) at 0600 UTC 21 October 1999 (Fig. 6.13b). Both representations exhibit a dramatic transition from easterly flow near $\sim$1 km to southerly flow at $\sim$2.5 km [i.e., exhibiting characteristic of what Peterson et al. (1991) called decoupled flow].

Mean airflow

During IOP8, the 0°C level was lower than during IOP2b (cf. Figs. 6.2a and 6.12a), therefore the polarimetric-based calculation of accumulated rain was contaminated by the radar bright band and is not presented. The simulated accumulated precipitation is shown in Fig. 6.19a and discussed later in this section. Ground-based multiple-Doppler wind fields at 1.0 km averaged from 0500-1500 UTC 21 October 1999 are shown in Fig. 6.14a. The simulated wind vectors show that the easterly flow south of the S-Pol radar gradually decreases in magnitude farther to the west and turns to become northerly at the west end of the domain, where it follows the curving orography (Fig. 6.14b), and is similar generally to the observations in the region of overlap (Fig. 6.14a). The northerly flow was located outside the domain observed the ground-based radars, however Bousquet and Smull (2003a,b) have used airborne

radar analysis to document this feature with great detail [e.g., Fig. 1b in Bousquet and Smull (2005)]. The mean radial velocity at 0.5 km from the RONSARD radar shows that in both the observations and the simulation the flow is easterly south of RONSARD radar but deflected so as to be parallel to the orography to the northwest of the radar (Fig. 6.15a,c). At the 2.0 km level, the flow was southeasterly and cross-barrier, as seen in the Monte Lema radar observations and corresponding simulated pattern (Fig. 6.15b,d).

A vertical cross section in Fig. 6.16 extends from the Alpine peaks to the Po Valley, in a direction nearly parallel to the 1.0 km mean flow. The simulated cross-barrier flow (Fig. 6.16a) shows reversed flow (away from the Alps) at low levels, indicated by green shading, and a shear layer is depicted rising over the terrain, similarly to what was seen in the observations (Fig. 3.9a). The shear layer is consistent with that seen in airborne Doppler radar analysis (Fig. 3.10a), soundings (Fig 3.17a,d), and idealized model simulations (Fig. 5.2e,f). The mean equivalent potential temperature (θ_e) contours (black lines in Fig. 6.16a) give an indication of the pronounced stability of the blocked flow. The cross-barrier flow and θ_e contours illustrate how the air above $\sim$1 km was rising over the low θ_e ($<$ 307 K) air that characterized the shear layer and the reversed flow (Fig. 6.16a). This case constitutes an example of the effective mountain effect (documented in this area by Rotunno and Ferretti 2001), where low θ_e air "blanketing" the Alpine slopes effectively serves as an extension of the actual orography. In these instances, the upstream flow encounters an obstacle formed by the actual terrain and the low θ_e air banked against the slopes. Lin et al. (2005) used a mesoscale numerical simulation to document this phenomenon during IOP8. The cross section of mean vertical velocity presents further evidence of the effective mountain (Fig. 6.16c). The area of orographic lifting does not follow the lower Alpine slopes but instead starts over the Po Valley, well ahead of the elevated terrain and seems to follow the $\theta_e = 307$ K contour (Fig. 6.16c). The updrafts are disconnected or detached from the terrain, a feature recognized and documented by

Rotunno and Ferretti (2001) as indicative of an effective mountain. The individual maxima in vertical velocity coincide with regions where both the cross-barrier wind and the θ_e contours bulge upward (Fig. 6.16a,c). Updrafts are also observed in the Po Valley, both near the surface and between 3-6 km altitudes (Fig. 6.16c). The simulated flow in the direction of the cross section shows an elevated along-barrier jet over the Po Valley (Fig. 6.16b), as was documented by Bousquet and Smull (2003a) by airborne Doppler radar data.

A brief description of the simulated hydrometeor patterns associated with this 3D flow structure is given below. Mean fields of mixing ratio of snow and "graupel" are maximized over the tallest terrain (Fig. 6.16d,e), where the vertical velocity is maximum (Fig. 6.16c). As opposed to IOP2b, where the hydrometeor signature was nearly entirely constrained over the high terrain (Fig. 6.6d-f), large values of snow and "graupel" are also seen inside the Po Valley during IOP8 (Fig. 6.16d,e). Values of rain mixing ratio are nearly uniform along the valley (Fig. 6.16f). The mean 0°C level is lower adjacent to the slopes (black line in 6.16d-f), which is reflected in a decrease in the maximum height of the rain mixing ratio contours and a corresponding increase of subzero hydrometeors minimum height of contours (Fig. 6.16d-f). This feature was noted in observed reflectivity data by Bousquet and Smull (2003a) and Medina et al. (2005). In the next section a comparison between observed and simulated hydrometeors is conducted.

Distribution of hydrometeors

During IOP8 precipitation extended broadly to cover regions both to the northwest (Fig. 6.17, representing a 10 h mean) and to the south (Fig. 6.18, representing a 1 h mean) of the S-Pol radar, located at (x,y)=(0,0). Therefore we will analyze the observed hydrometeors over both areas. The mean frequency of dry snow exhibited a sharp gradient along x = 15 km in Fig. 6.18a, with smaller values observed to the west of this line. Graupel and/or dry aggregates (Ch. 4, sec. 4.2.1) was more

frequent to the south of the S-Pol radar (cf. Figs. 6.17e and 6.18e; and cf. Figs. 6.17f and 6.18f). The vertical layering of hydrometeors over both regions consisted of dry snow aloft, with a maximum near $\sim$2.8 km (cf. Figs. 6.17b and 6.18b), graupel/dry aggregates below, with larger frequencies over the southern domain, were it reached a maximum at $\sim$2.3 km (Fig. 6.18f). The maximum in wet snow occurred at $\sim$1.8 km ($\sim$2.3 km) in the region to the north (south) of the radar. Light rain was frequent at low levels, with maximum values $\sim$1 km (Figs. 6.17h and 6.18h).

The simulated accumulated precipitation from 0500-1500 UTC 21 October 1999 is shown in Fig. 6.19a over areas within 90 km from the S-Pol radar. Maxima are observed on the secondary ridge to the northwest of the S-Pol radar (located at [x,y]=[0,0]), inside the Toce River Valley and over the first peaks to the northeast of the S-Pol radar. A local maximum of precipitation also occurs upstream of the terrain, to the east of the S-Pol (Fig. 6.19a). The upstream area of precipitation coincided with large simulated rain mixing ratio, as did the Toce Valley feature (Fig. 6.19g). Both snow and "graupel" mixing ratios displayed maxima over the terrain slopes, with secondary maxima coinciding with the upstream area of enhanced precipitation (Fig. 6.19c,e). The vertical layering of the simulated hydrometeors consisted of maxima of snow ($\sim$4 km), "graupel" ($\sim$3 km), and rain ($\sim$1 km) (Fig. 6.19d, f, and h). The signals of the simulated cold hydrometeors (snow and "graupel" combined) peaked at altitudes similar to the polarimetric-derived profiles of dry snow (blue lines in Fig. 6.20a,b). Overall, the snow extended through a deeper layer in the model simulation. The vertical distribution of rain was similar in observations and simulation (red lines in Fig. 6.20a,b).

6.3.3   Simulated microphysical growth mechanisms in orographic precipitation

Cloud water grew by condensation in all the areas where the precipitation accumulation was large (cf. Fig. 6.19a and 6.21a). An exception is the Toce River Valley, where the rain was the result mainly of melting (Fig. 6.21c). This result is consistent

with the findings of Steiner et al. (2003) and Asencio and Stein (2005) regarding the dominant role of melting inside the Toce River Valley (and its role in the formation of down-valley winds). The regions of high simulated precipitation accumulation (Fig. 6.19a) coincided with regions of "graupel" generation and growth (Fig. 6.21f,g; the negative sign in panel (f) arises because this process indicated the loss of cloud water). Melting (Fig. 6.21c) only occurs over low-lying terrain or on the slopes in the eastern side of the domain, where the temperature was warm enough, as mean temperatures were lower on the western side of the domain than over the eastern side (Fig. 6.22). Over the western slopes of the terrain, rain could not be formed by melting and it could not grow by collecting cloud water. Rain formation through melting has the potential to produce large raindrops that efficiently collect the readily available cloud water formed by condensation (Fig. 6.21a). Over the western slopes of the domain, the lack of melting (Fig. 6.21c) resulted in lower precipitation accumulations compared to the eastern slopes (Fig. 6.19a), where rain formation by melting and rain growth by cloud water accretion both occurred.

6.4 Summary of IOP2b and IOP8

6.4.1 IOP2b

During IOP2b, the observed rain accumulation pattern consisted of maxima on top of the first peak of the terrain encounter by the flow. The horizontal scale of the rain maxima were on the order of 10-20 km. The Meso-NH simulation captured the distribution and accumulation accurately down to this 10-20 km horizontal scale. The 24 h accumulations of precipitation were locally as high as 300 mm, which were observed at terrain elevations where ascending air reached its LFC. Evidence of upslope enhancement of precipitation was seen at elevations coinciding with the flow LCL, suggesting that forced orographic lifting below the LFC and release of convective instability above this level both contribute to the observed precipitation pattern. The

simulation showed that the windward slopes of the subsequent terrain peaks were also subject to orographic enhancement of precipitation, in an area that was outside the view of the S-Pol radar.

In agreement with the observations, the simulated cross-barrier flow consisted of a low-level jet rising over the terrain. The model simulation documented the existence of this jet well ahead of the Alpine terrain, over the Po valley. The simulation showed strong updrafts on the windward slope of the individual peaks of the terrain. The maxima in precipitation accumulation coincided with updrafts of $\sim$1-1.5 m s^{-1}(or higher).

It was found that simulated "graupel" category is a misnomer, as it includes melting of snow, which is clearly not a riming process. Even when the cold hydrometeors are combined, the signal is deeper than seen in the observations. However, the vertical structure and maximum height of rain and cold precipitating hydrometeors is similar in the observations and simulation. The horizontal distribution of hydrometeors in observations and simulations showed that the ice precipitating hydrometeors are maximized on top of the first peaks of the terrain, while rain is the largest over the windward slopes.

The analysis of the simulated microphysical processes confirm the inferences made based on polarimetric and vertically pointing radar observations and on the analysis of Yuter and Houze (2003), who concluded that riming occurs above the 0°C level with coalescence growth dominating below. The role of riming is two-fold: it creates large heavy particles that fall out quickly, and when they melt they form large raindrops that efficiently collect cloud water that was formed by condensation on the windward slopes.

6.4.2 IOP8

Compared to IOP2b, IOP8 was characterized by colder, more stable conditions. The low-level flow did not rise over the terrain but it was reversed, i.e., away from the

Alps. The flow above 2.0 km was not unlike that seen in IOP2b, i.e., cross-barrier. Decoupled flow was then observed, where the low-level flow direction was distinctly different from that above. A shear layer formed between these flows. The Meso-NH simulation indicated that low equivalent potential temperature air at low-levels effectively modified and "extended" the actual orography, resulting in orographic lifting that was elevated, detached from the terrain and that started not where the terrain ascended but when the equivalent potential temperature contours first sloped upward (over the Po Valley). Small-scale perturbations in the sheared, stable cross-barrier flow were observed. The flow disturbances coincided with equivalent potential temperature perturbations and vertical velocity updrafts. Precipitation occurred as result of lifting over the low equivalent potential temperature air, which started upstream from the Alps. Several mechanisms have been identified that may be responsible for the precipitation enhancement. Dynamical instability associated with strong shear in stable flow can occur and may lead to turbulent overturning, as has been documented in this study. The precipitation enhancement could also be produced by upstream convergence of reversed stable flow with incoming air. A closely related mechanism, put forward by Bousquet and Smull (2005), consists of widespread ascent associated with the large airmass inflow (via the Po Valley) into the nearly enclosed region formed by the Alps and the Apennines.

During both IO2b and 8, the precipitation enhancement is more pronounced when the 0°C level intersects or is not too far above the terrain. Riming occurs above 0°C level. When the rimed hydrometeors melt, they produce large raindrops that can collect the cloud liquid water that is readily available on the windward slopes.
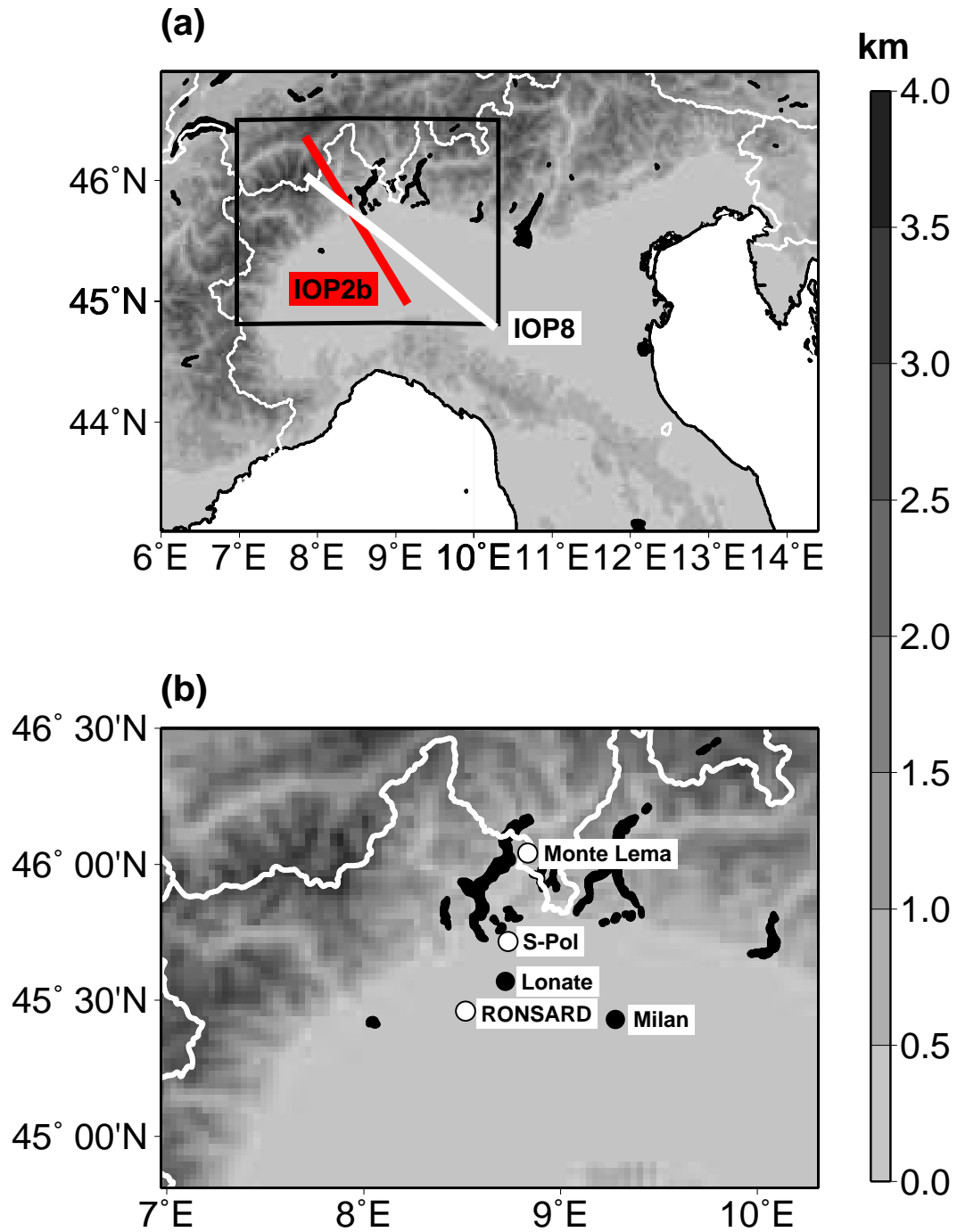
Figure 6.1: Meso-NH resolved orography. (a) Domain of simulated meteorological output (available once an hour as an instantaneous snapshot). The inset displayed in (b) shows the domain of simulated microphysical output (available once per hour as an hourly mean). The relevant observational sites are also shown.
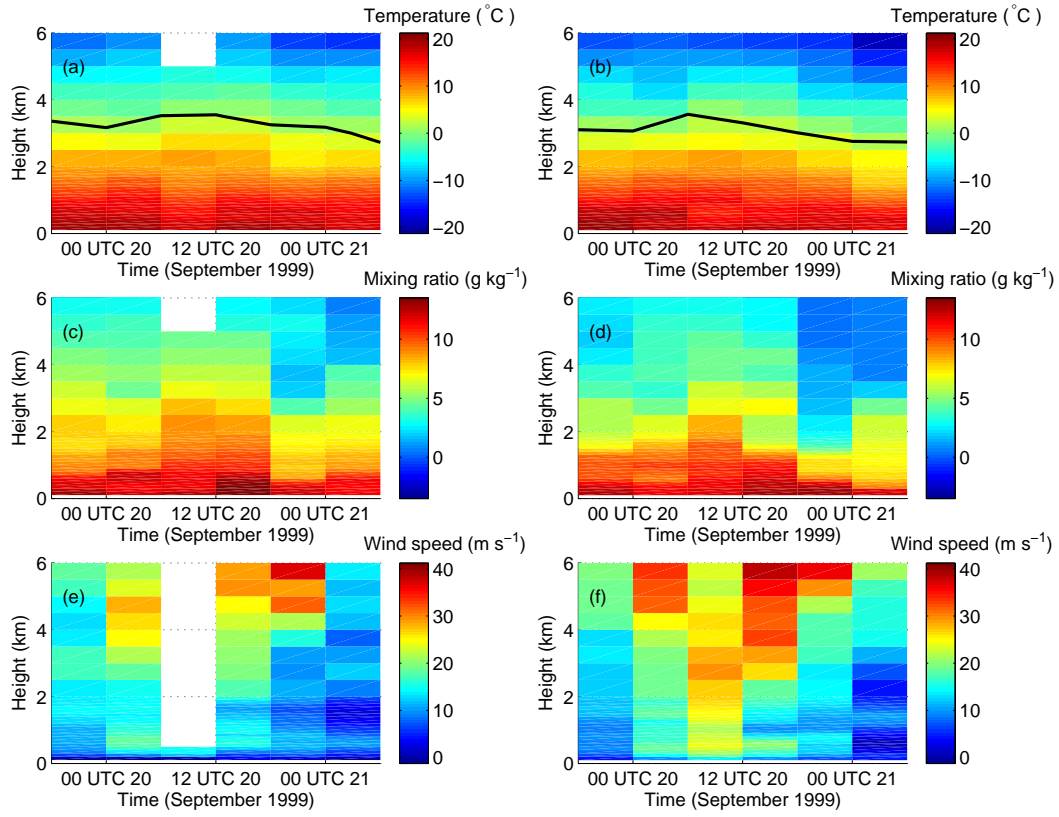
Figure 6.2: IOP2b time-height cross sections of (a)-(b) temperature, (c)-(d) water vapor mixing ratio, and (e)-(f) wind speed as observed by Milan soundings (left-hand column) and as simulated by Meso-NH at Milan's location (right-hand column). The black contour in (a)-(b) indicates the 0°C level.
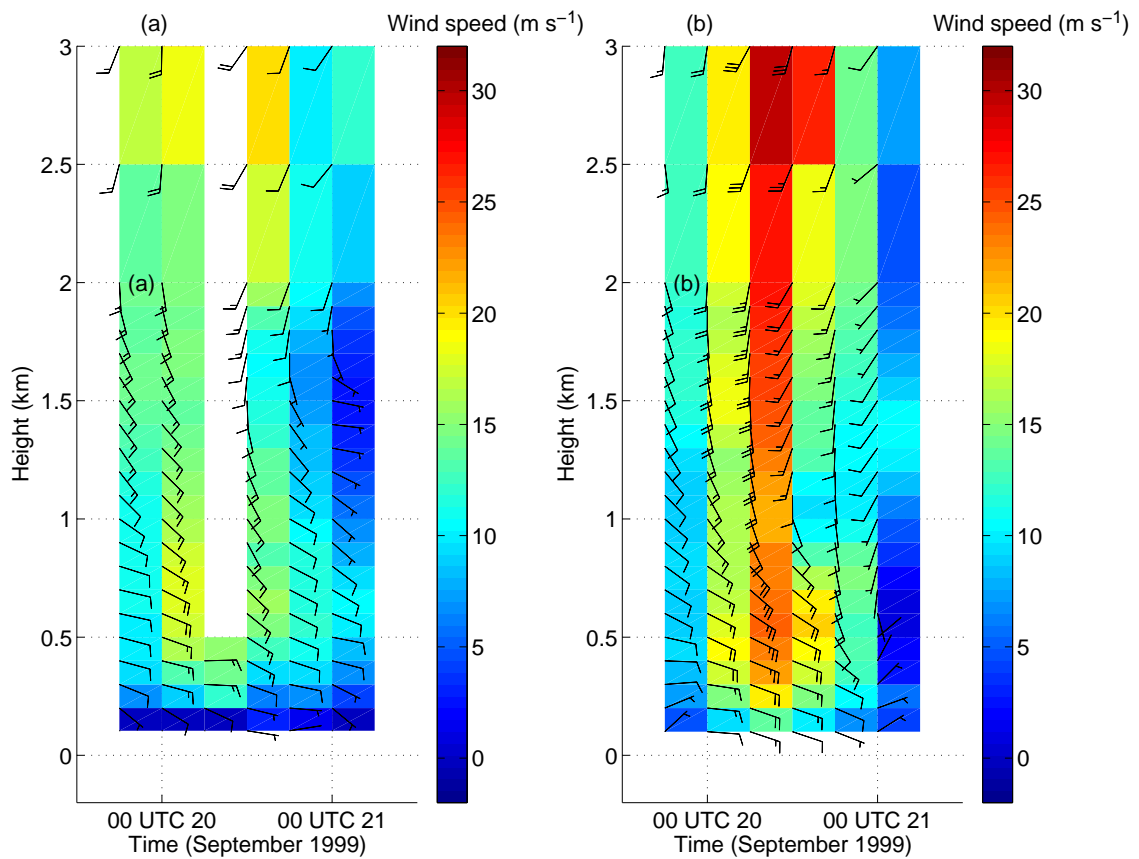
Figure 6.3: IOP2b time-height cross sections of low-level wind speed and wind direction (a) as observed by Milan soundings and (b) model simulated at Milan location.

(a)

(b)

(c)

(d)

(e)
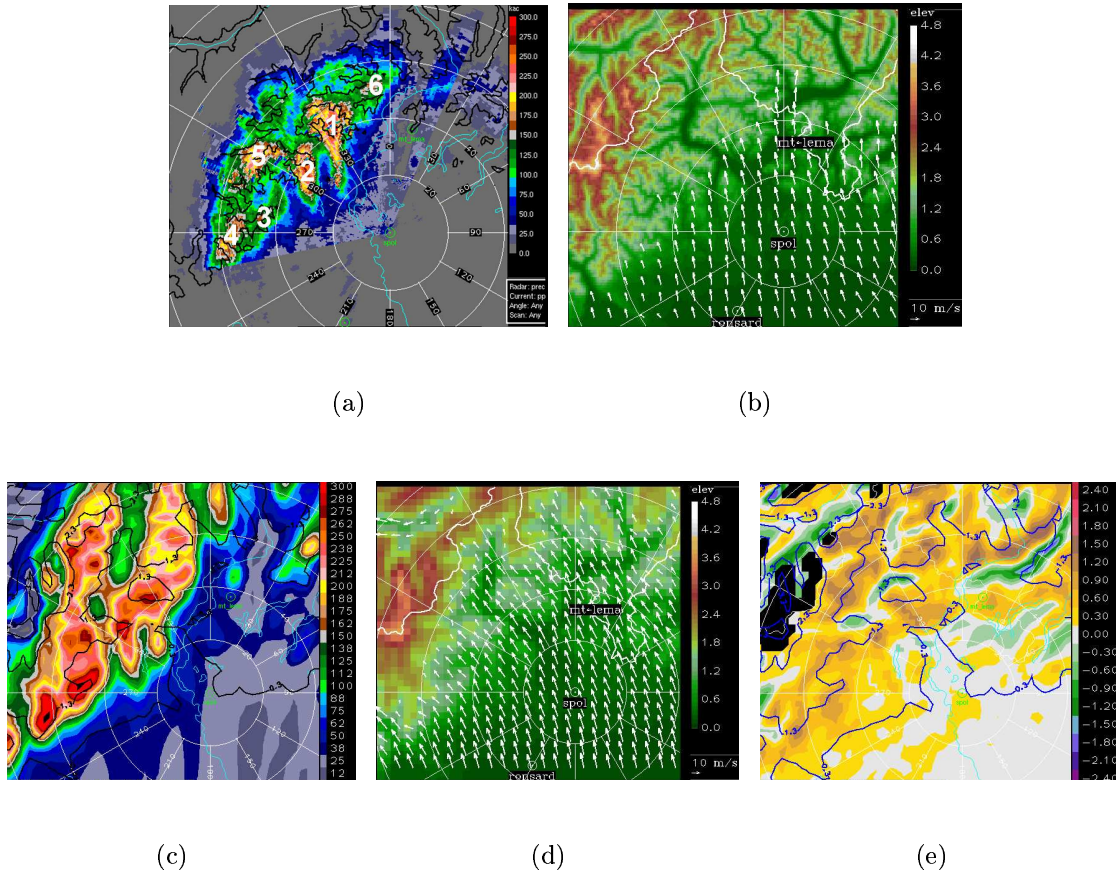
Figure 6.4: Observed (a-b) and simulated (c-e) parameters during IOP2b showing (a) and (c) rain accumulation (mm); (b) and (d) mean winds at 1.5 km and orography. The rain was accumulated during 20 September 1999 (24 h) while the winds fields were averaged from 19 UTC 19 September to 06 UTC 20 September 1999 (11 h). (e) Simulated mean (20 September 1999, 24 h) vertical velocity at 2.50 km (m s^{-1}). The 1.3 km terrain contour is shown in (a). In (c) and (e) the 1.3, 2.3, and 3.3 km terrain contours as represented in the mesoscale model are also displayed. Range-ring spacing is 20 km, centered on the S-Pol radar.

(a)   (b)

(c)   (d)
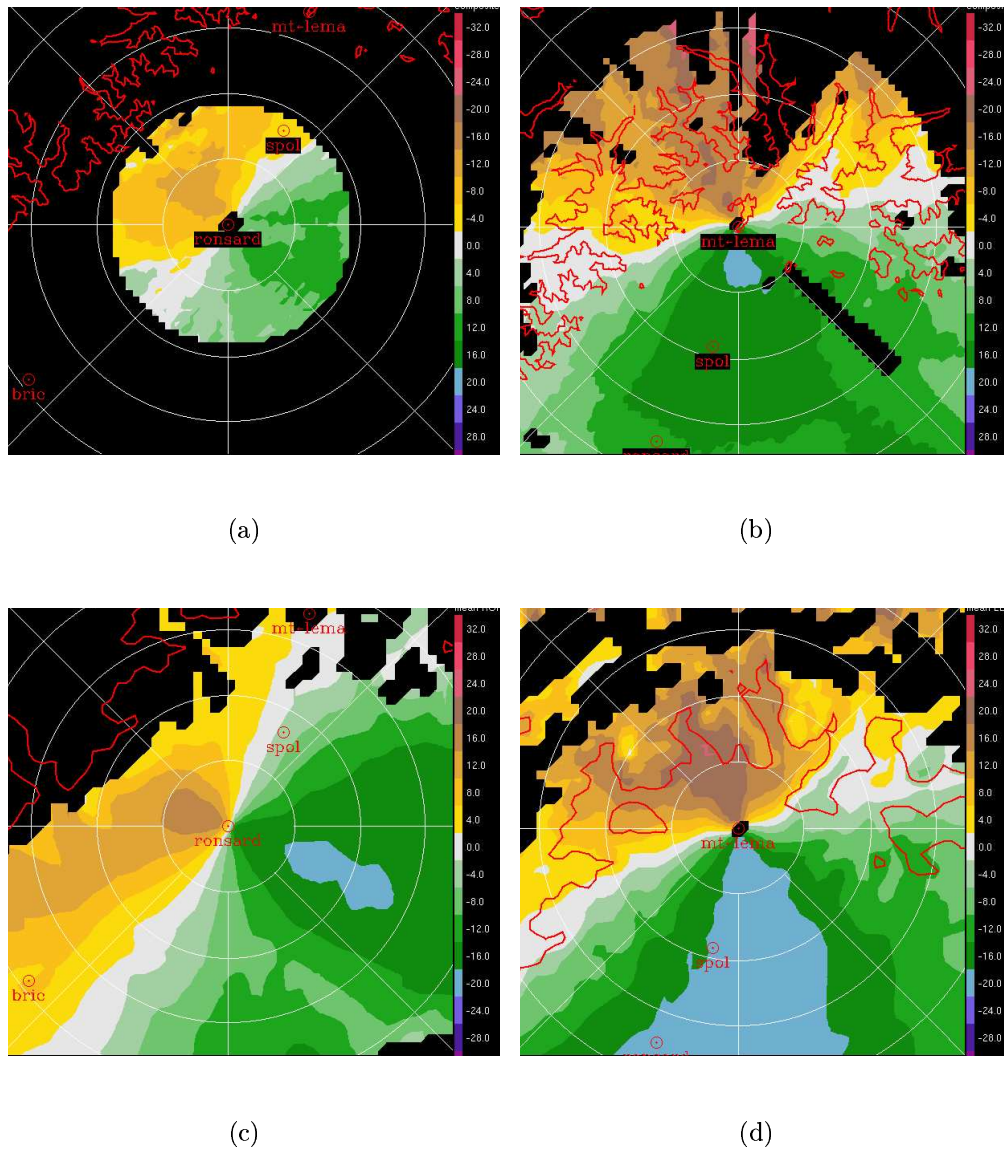
Figure 6.5: Observed (top row) and simulated (bottom row) mean radial velocity fields for IOP2b (m s^{-1}) showing (a) and (c) RONSARD radar mean at 0.5 km. (b) and (d) Monte Lema radar mean at 2.0 km. The fields were averaged from 19 UTC 19 September to 06 UTC 20 September 1999 (11 h). The 1.3 km terrain contour is also shown. Range-ring spacing is 20 km, centered on the S-Pol radar.

(a)

(b)

(c)

(d)

(e)

(f)
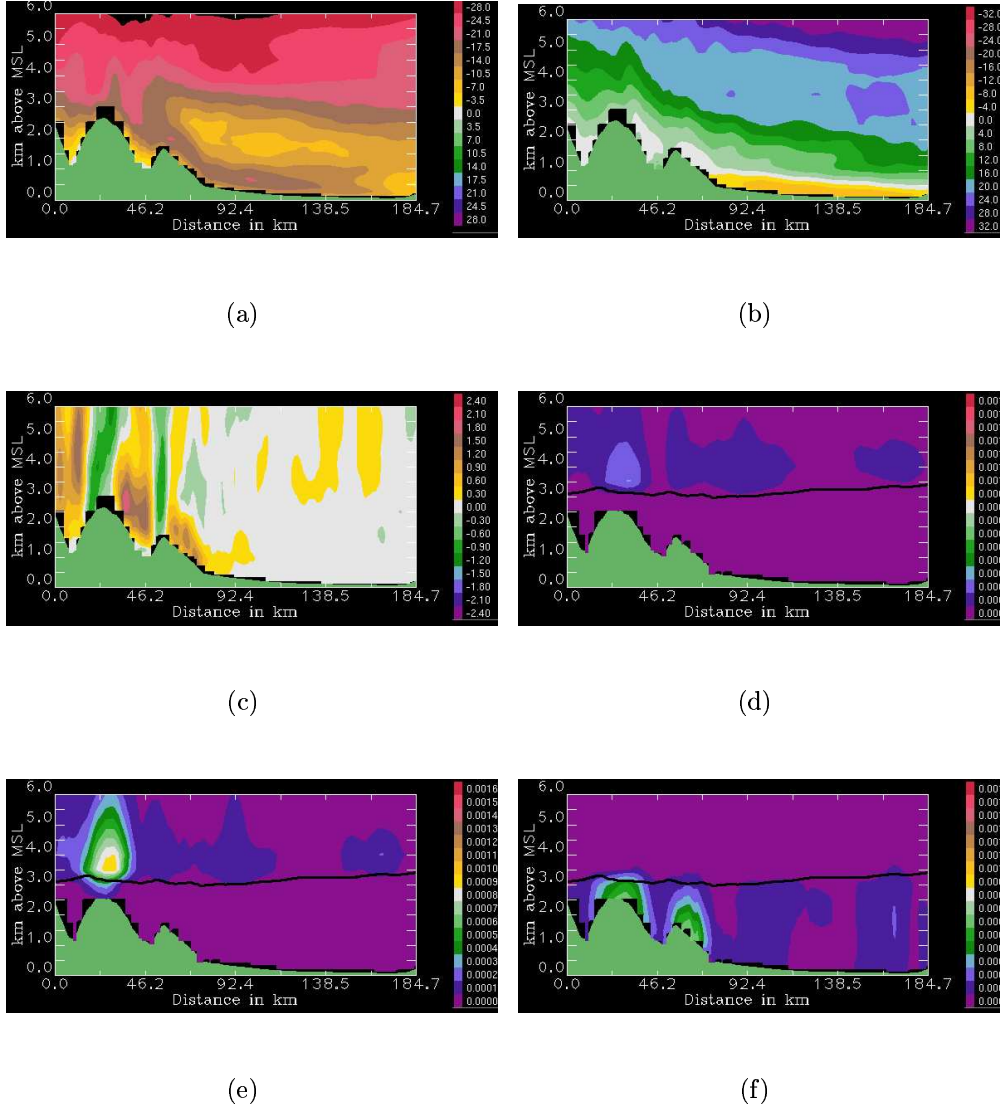
Figure 6.6: Vertical cross-sections of simulated mean (0900-1300 UTC 20 September 1999) fields during IOP2b. (a) Wind component in the plane of the cross section (m s^{-1}), (b) wind component normal to the plane of the cross section wind (m s^{-1}), (c) vertical velocity (m s^{-1}), (d) snow mixing ratio (g kg^{-1}), (e) "graupel" mixing ratio (g kg^{-1}), and (f) rain mixing ratio (g kg^{-1}). The black line in (d)-(f) indicates the mean height of the 0°C level. The location of the cross section is indicated in Fig. 6.1a by the red line.
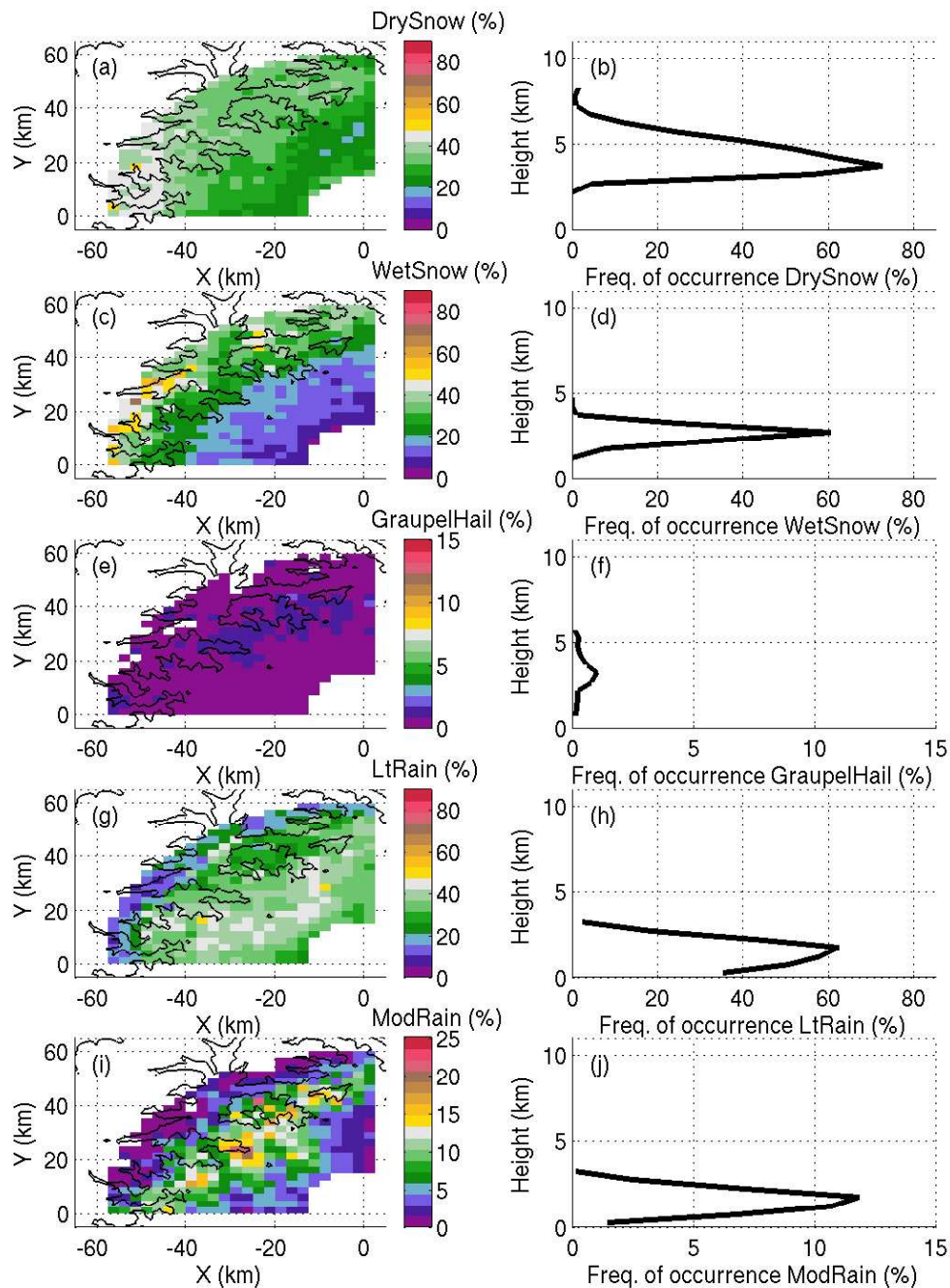
Figure 6.7: Vertically- (left-hand column) and horizontally-averaged (right-hand column) observed frequency of occurrence (%) of hydrometeors accumulated from 1500 UTC 19 September to 0600 UTC 20 September 1999, during IOP2b. (a)-(b) Dry snow, (c)-(d) wet snow, (e)-(f) graupel, (g)-(h) light rain, and (i)-(j) moderate rain. In left-hand column the S-Pol radar is located at (x,y)=(0,0). The terrain contour of 1.3 km is also shown.
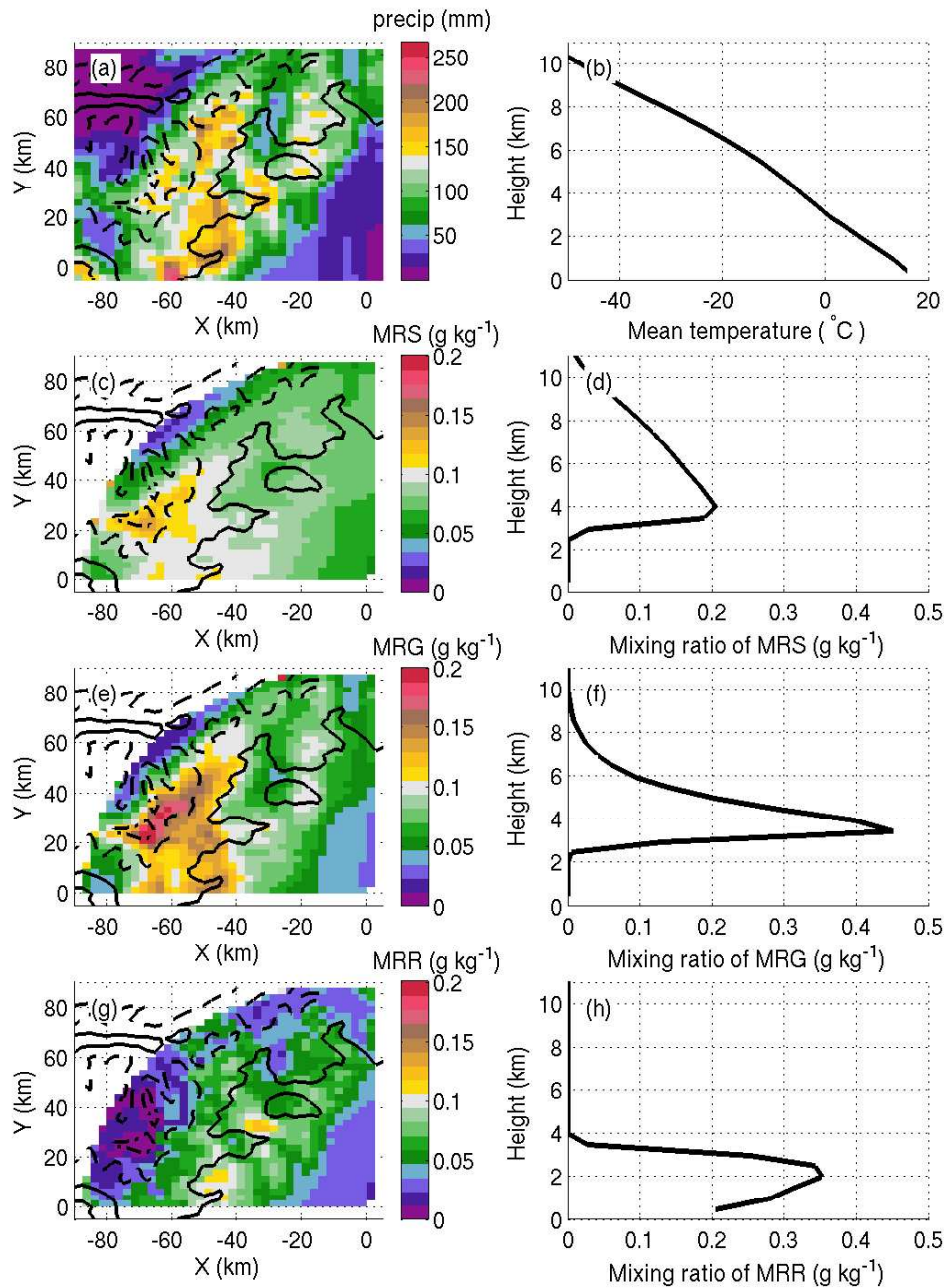
Figure 6.8: Mean or accumulated simulated fields from 1500 UTC 19 September to 0600 UTC 20 September 1999, during IOP2b. (a) Accumulated precipitation distribution, (b) mean vertical profile of temperature. (c) Vertically- and (d) horizontally-averaged snow mixing ratio (MRS). (e) Vertically- and (f) horizontally-averaged "graupel" mixing ratio (MRG). (g) Vertically- and (h) horizontally-averaged rain mixing ratio (MRR). The horizontal distribution panels show the model's terrain contours of 1.3, 2.3 and 3.3 km.
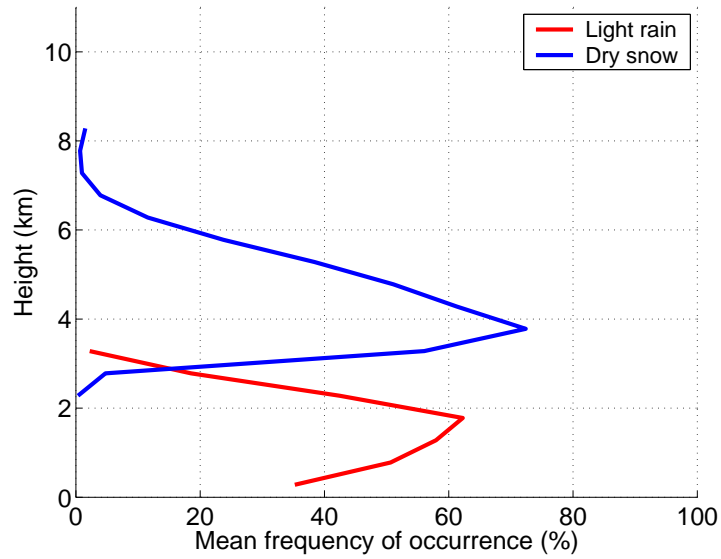
(a)
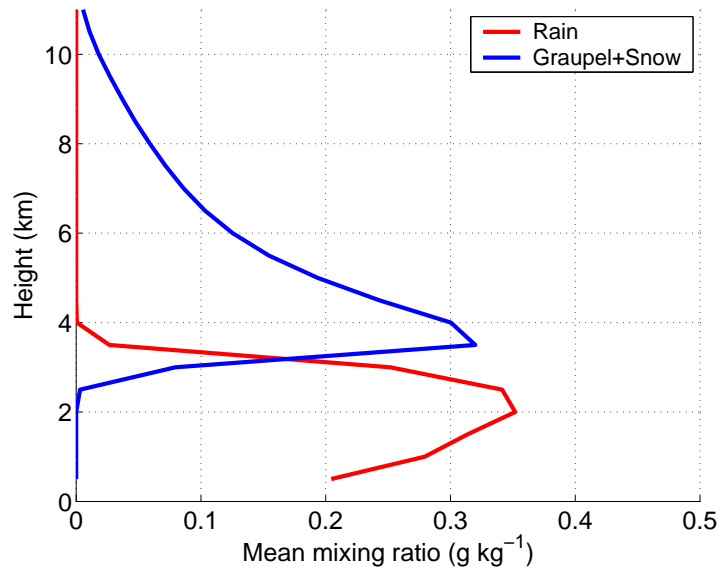
(b)

Figure 6.9: (a) Observed vertical profiles of frequency of occurrence of dry snow (blue line) and light rain (red line) during IOP2b (from data shown in Fig. 6.7). (b) Simulated vertical profiles of mean mixing ratio of snow and "graupel" combined (blue line) and rain (red line) during IOP2b (from data shown in Fig. 6.8).

140
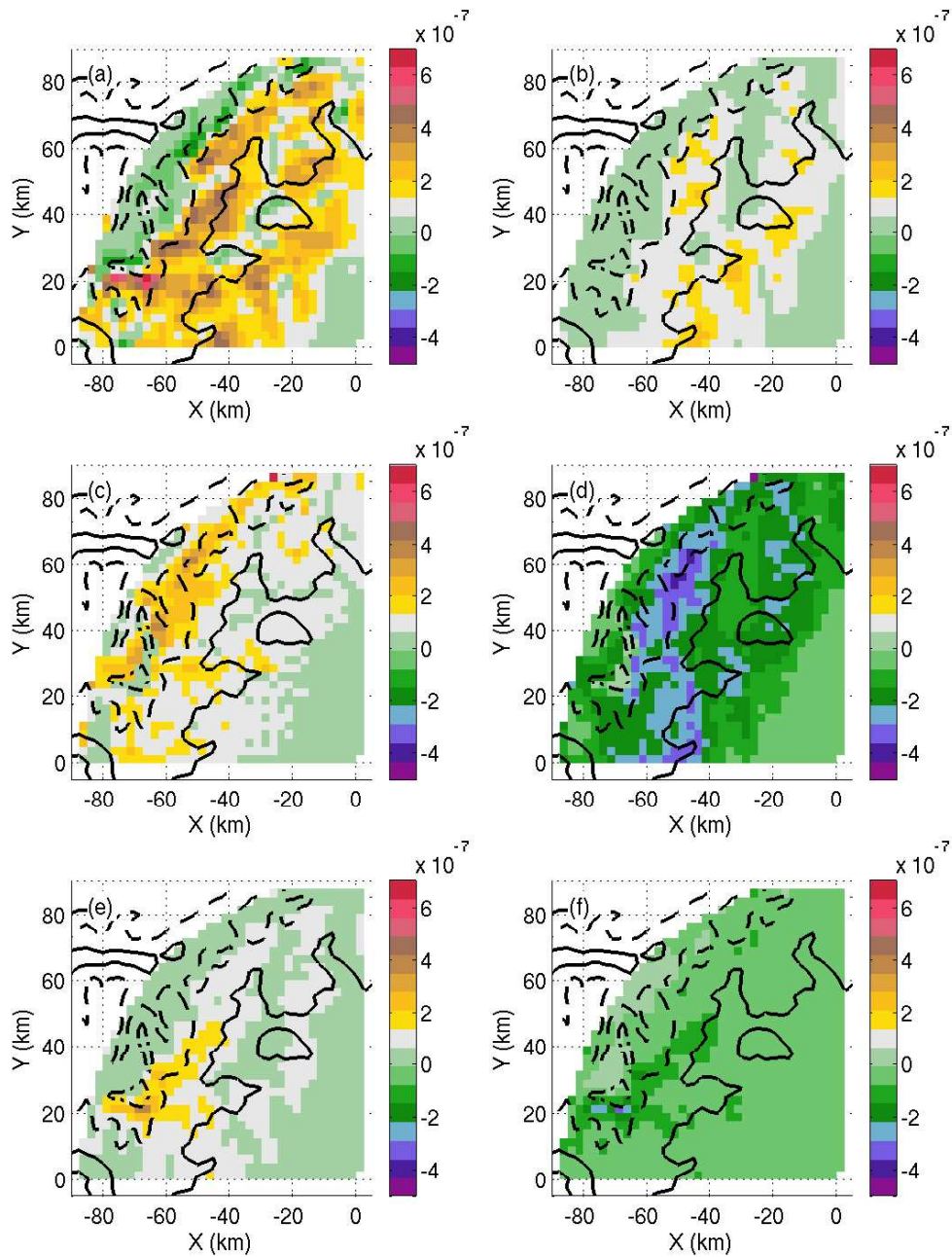
Figure 6.10: Vertically-averaged simulated microphysical processes rates from 1500 UTC 19 September to 0600 UTC 20 September 1999, during IOP2b. (a) Vapor condensation (converts vapor into cloud), (b) accretion of cloud (grows rain by collecting cloud), (c) melting (converts graupel and snow into rain), (d) sedimentation of rain (rain fallout), (e) graupel growth (by collecting cloud, ice, rain and snow), and (f) loss of cloud due to riming by snow to form graupel. The units of the conversion rates are s^{-1}. The model's terrain contours of 1.3, 2.3 and 3.3 km are also shown.
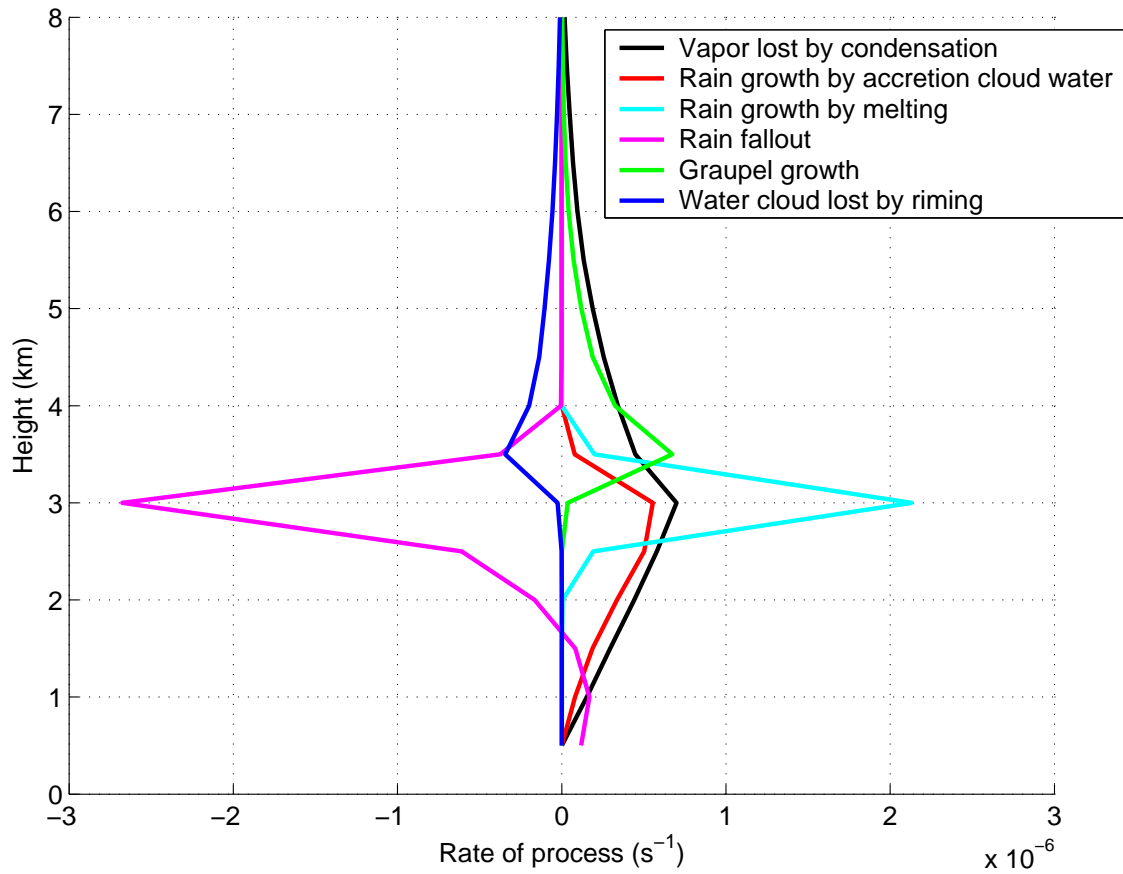
Figure 6.11: Horizontally averaged simulated microphysical processes rates from 1500 UTC 19 September to 0600 UTC 20 September 1999, during IOP2b showing: vapor condensation (converts vapor into cloud; black line), accretion of cloud (grows rain by collecting cloud; red line), melting (converts graupel and snow into rain; cyan line), sedimentation of rain (rain fallout; magenta line), graupel growth (by collecting cloud, ice, rain and snow; green line), and loss of cloud (due to riming by snow to form graupel; blue line).
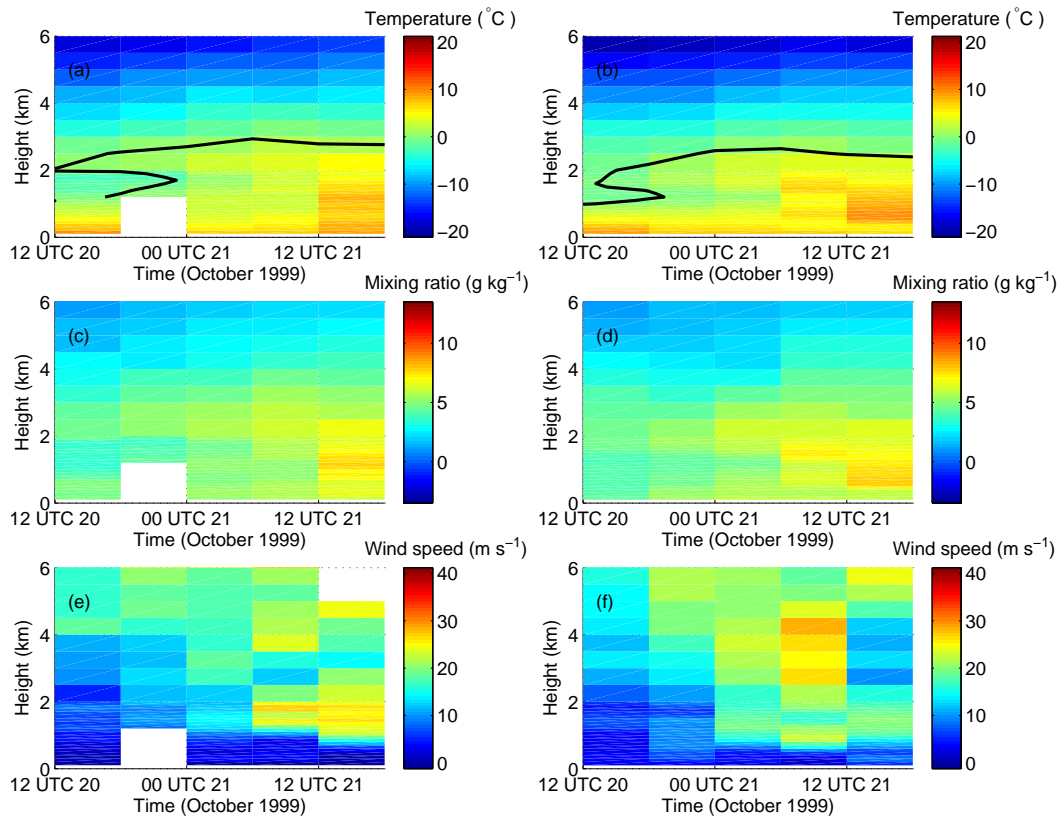
Figure 6.12: IOP8 time-height cross sections of (a)-(b) temperature, (c)-(d) water vapor mixing ratio, and (e)-(f) wind speed as observed by Milan soundings (left-hand column) and as simulated by Meso-NH at Milan's location (right-hand column). The black contour in (a)-(b) indicates the 0°C level.
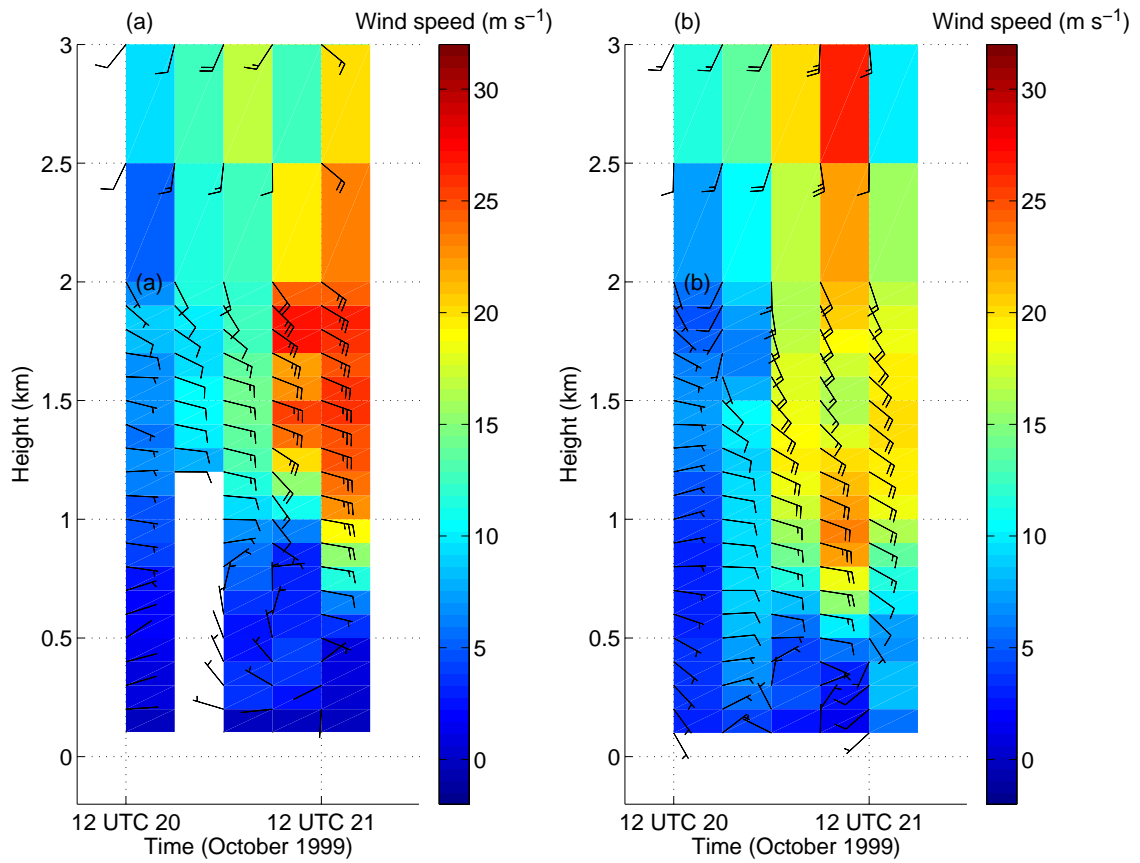
Figure 6.13: IOP8 time-height cross sections of low-level wind speed and wind direction (a) as observed by Milan soundings and (b) model simulated at Milan location.
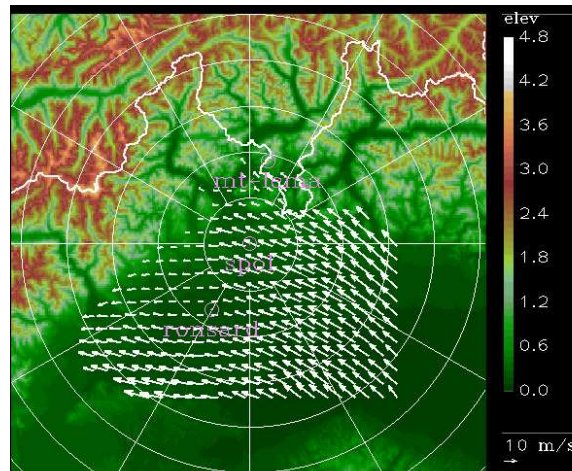
(a)
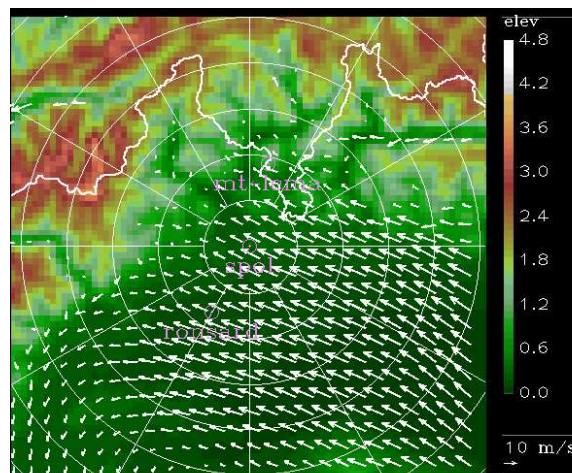
(b)

Figure 6.14: (a) Observed and (b) simulated mean wind field at 1.0 km during IOP8. The winds were averaged from 04-15 UTC 21 October 1999 (11 h). The 1.3 km terrain contour is shown. Range-ring spacing is 20 km, centered on the S-Pol radar.

(a)

(b)

(c)

(d)
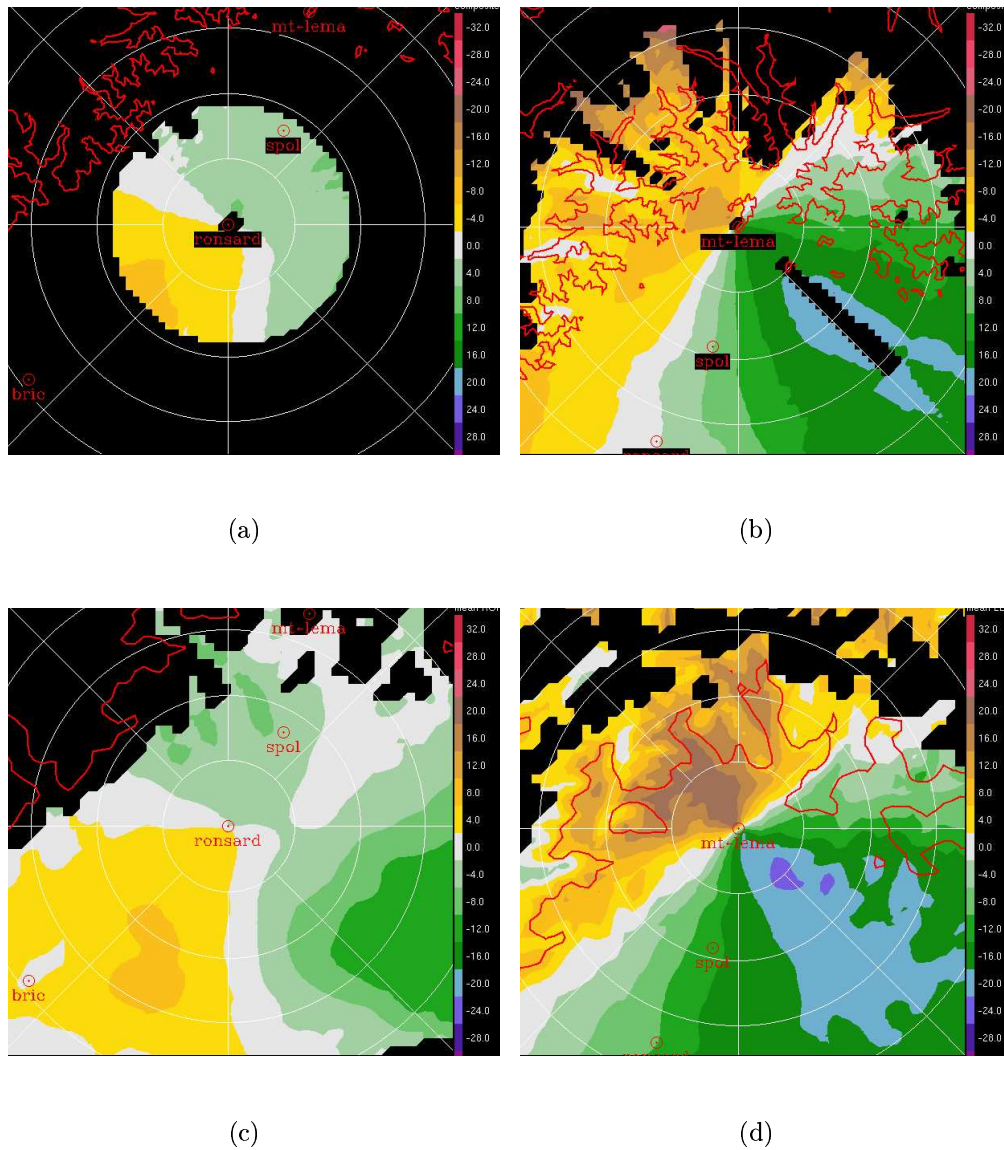
Figure 6.15: Observed (top row) and simulated (bottom row) mean radial velocity fields for IOP8 (m s^{-1}). (a) and (c) RONSARD radar mean at 0.5 km. (b) and (d) Monte Lema radar mean at 2.0 km. The fields were averaged from 04-15 UTC 21 October 1999 (11 h). The 1.3 km terrain contour is also shown. Range-ring spacing is 20 km, centered on the S-Pol radar.

(a)

(b)

(c)

(d)

(e)

(f)
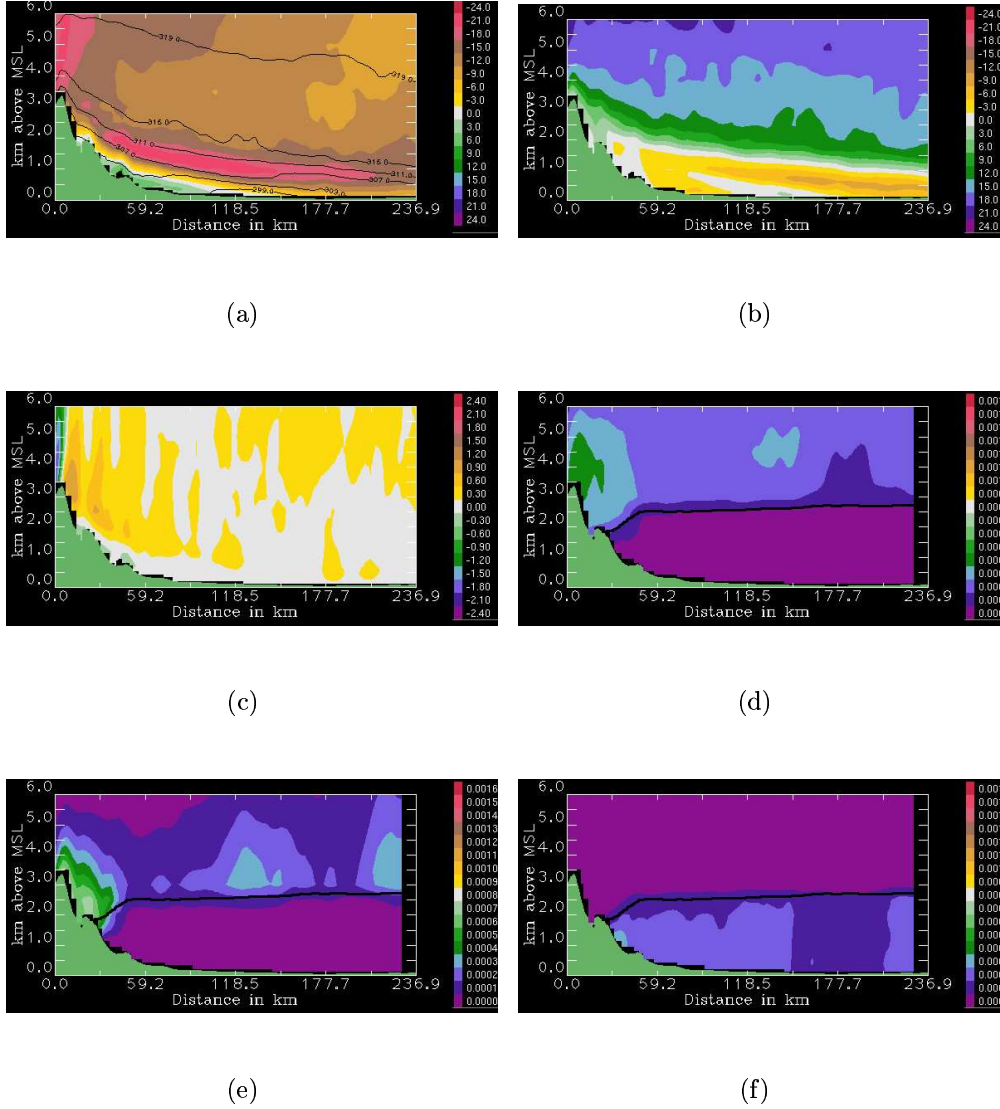
Figure 6.16: Vertical cross-sections of simulated mean (0500-1500 UTC 21 October 1999) fields during IOP8. (a) Wind component in the plane of the cross section (m s^{-1}) and equivalent potential temperature (K), (b) wind component normal to the plane of the cross section wind (m s^{-1}), (c) vertical velocity (m s^{-1}), (d) snow mixing ratio (g kg^{-1}), (e) "graupel" mixing ratio (g kg^{-1}), and (f) rain mixing ratio (g kg^{-1}). The black line in (d)-(f) indicates the mean height of the 0°C level. The location of the cross section is indicated in Fig. 6.1a by the white line.
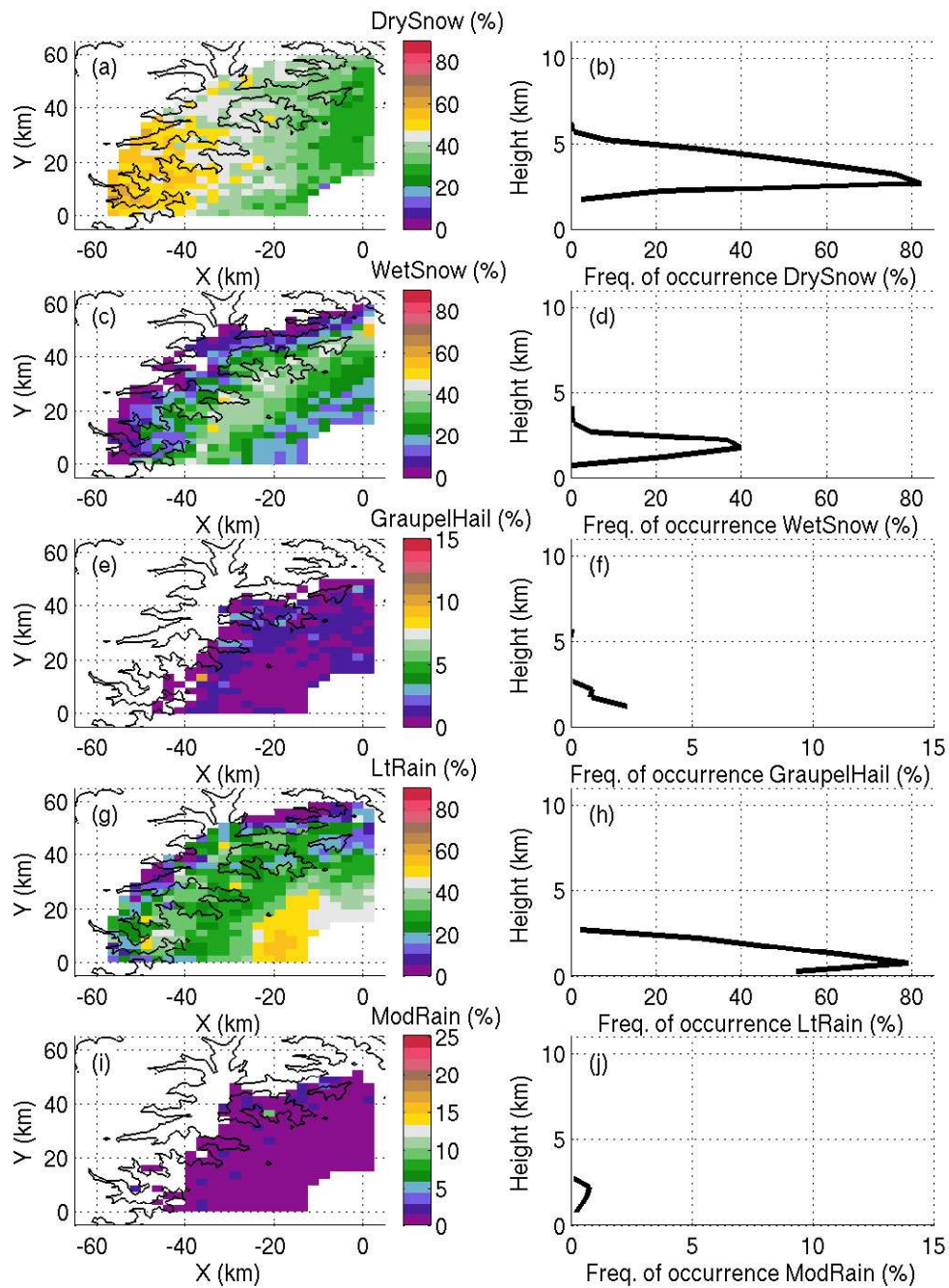
Figure 6.17: Vertically- (left-hand column) and horizontally-averaged (right-hand column) observed frequency of occurrence (%) of hydrometeors accumulated from 0500-1500 UTC 21 October 1999, during IOP8. (a)-(b) Dry snow, (c)-(d) wet snow, (e)-(f) graupel/dry aggreates, (g)-(h) light rain, and (i)-(j) moderate rain. In left-hand column the S-Pol radar is located at (x,y)=(0,0). The terrain contour of 1.3 km is also shown.

Figure 6.18: Vertically- (left-hand column) and horizontally-averaged (right-hand column) observed frequency of occurrence (%) of hydrometeors accumulated from 1000-1100 UTC 21 October 1999, during IOP8. (a)-(b) Dry snow, (c)-(d) wet snow, (e)-(f) graupel/dry aggregates, (g)-(h) light rain, and (i)-(j) moderate rain. In left-hand column the S-Pol radar is located at (x,y)=(0,0). The terrain contour of 0.3 km is also shown.
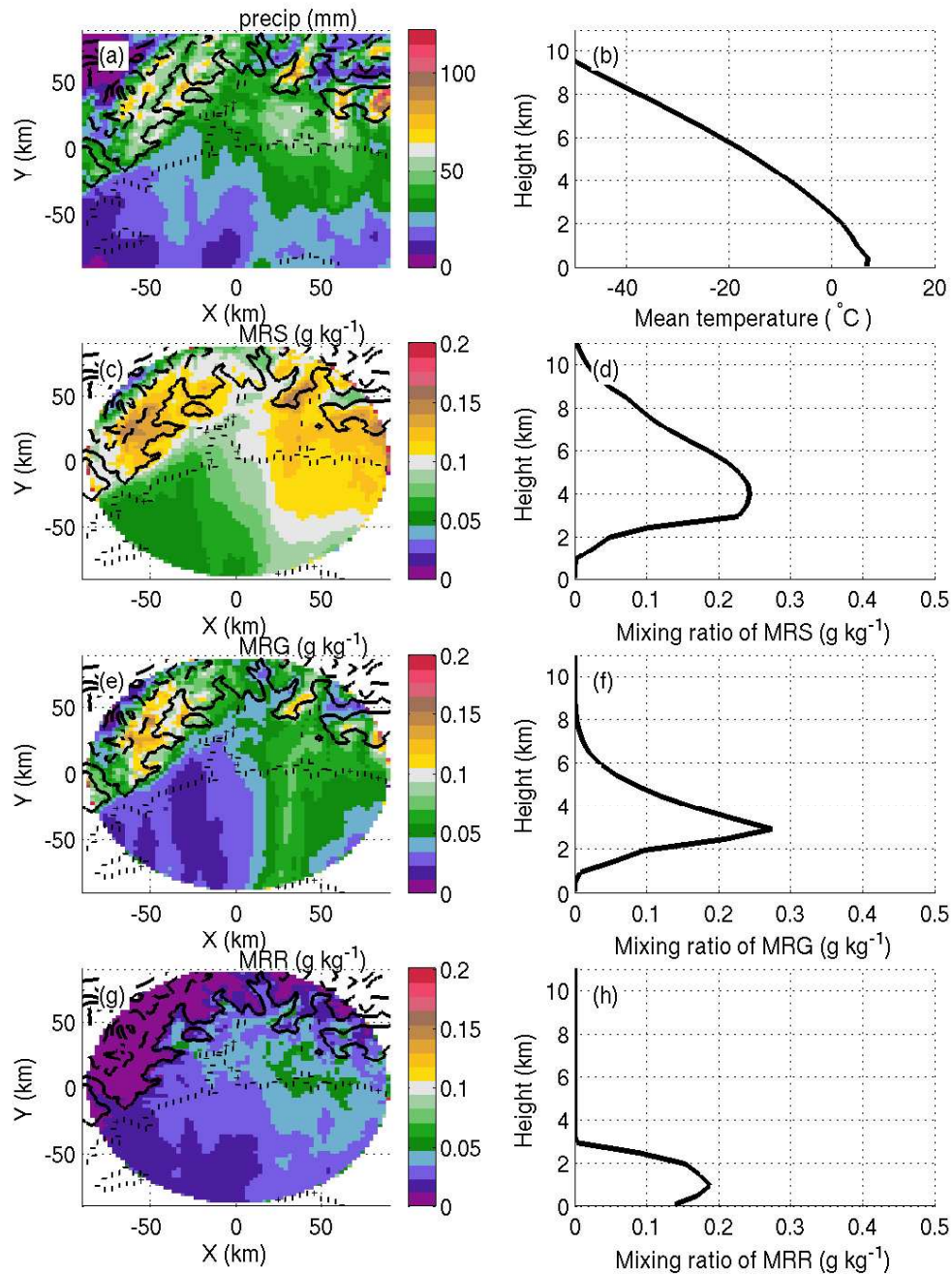
Figure 6.19: Mean or accumulated simulated fields from 0500-1500 UTC 21 October 1999, during IOP8. (a) Accumulated precipitation distribution, (b) mean vertical profile of temperature. (c) Vertically- and (d) horizontally-averaged snow mixing ratio (MRS). (e) Vertically- and (f) horizontally-averaged "graupel" mixing ratio (MRG). (g) Vertically- and (h) horizontally-averaged rain mixing ratio (MRR). The horizontal distribution panels show the model's terrain contours of 0.3, 1.3, 2.3 and 3.3 km.
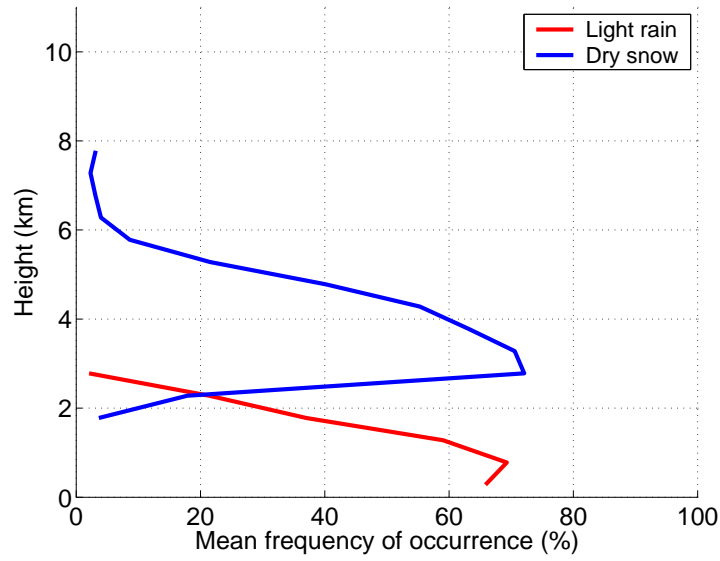
(a)
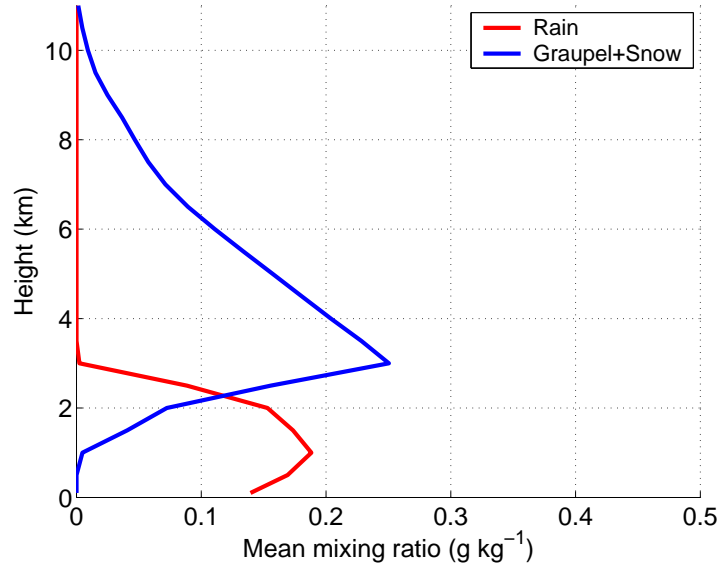
(b)

Figure 6.20: (a) Observed vertical profiles of frequency of occurrence of dry snow (blue line) and light rain (red line) during IOP8 (from data shown in Figs. 6.17 and 6.18). (b) Simulated vertical profiles of mean mixing ratio of snow and "graupel" combined (blue line) and rain (red line) during IOP2b (from data shown in Fig. 6.19).
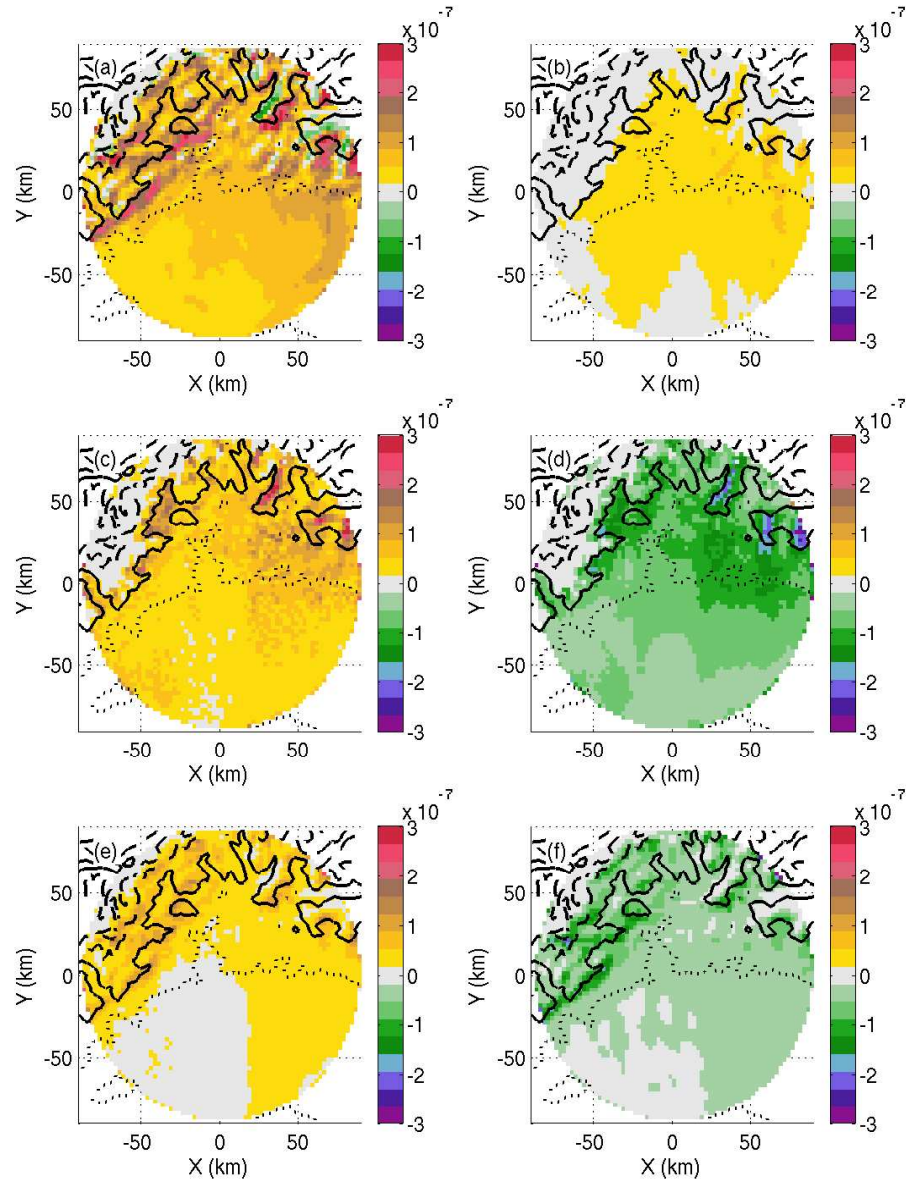
Figure 6.21: Vertically-averaged simulated microphysical processes rates from 0500-1500 UTC 21 October 1999, during IOP8. (a) Vapor condensation (converts vapor into cloud), (b) accretion of cloud (grows rain by collecting cloud), (c) melting (converts graupel and snow into rain), (d) sedimentation of rain (rain fallout), (e) graupel growth (by collecting cloud, ice, rain and snow), and (f) loss of cloud due to riming by snow to form graupel. The units of the conversion rates are s^{-1}. The model's terrain contours of 0.3, 1.3, 2.3 and 3.3 km are also shown.
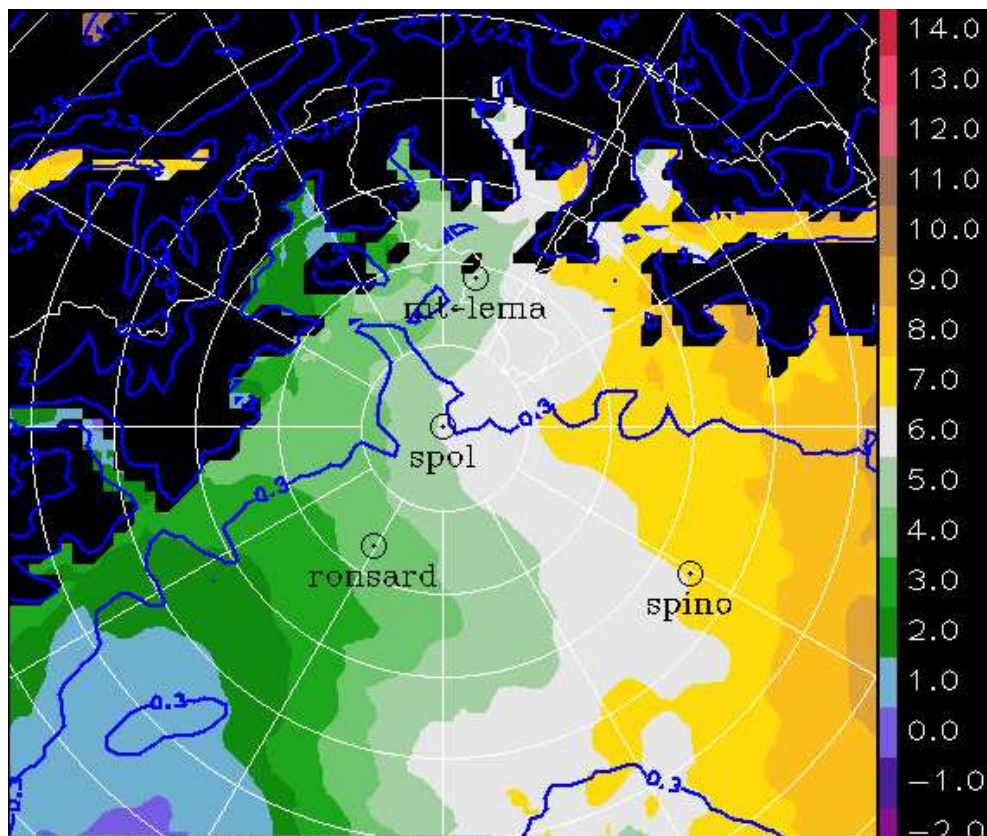
Figure 6.22: Simulated mean IOP8 (0500-1500 UTC 21 October 1999) temperature (°C) at 1.1 km.

Chapter 7

CONCLUSIONS

This study has investigated the orographic enhancement of precipitation that occurs when a mid-latitude cyclone moves over the windward side of a mountain range. High-resolution ground-based and airborne radar data obtained during the MAP and IMPROVE-2 field projects was used to identify and document two distinct terrain-modified low-level flow patterns (termed Type A and B). For each flow pattern, conceptual models of orographic precipitation were derived. The capability of numerical mesoscale models to reproduce observed orographically modified flows and precipitation growth processes was evaluated via idealized/case study simulations, which helped to further test and refine the conceptual models.

These distinct flow patterns occur as baroclinic systems and their associated clouds move over the windward slopes of mountain ranges and provide a background of stratiform precipitation. Type A storms are characterized by a low-level flow that rises easily and abruptly over the first peaks of terrain, often in the form of a jet. The upstream flow favors flow-over regime since it has low stability and strong cross-barrier flow, often characterized by a low-level jet. The lifting of the moisture-laden low-level air produces high liquid water content over the first peaks of the terrain. High liquid water content favors growth of pre-existing precipitation particles by coalescence below the $0°C$ level and by riming above. The rapid fallout of graupel and coalescence-produced raindrops favor locally enhanced precipitation over the first major rise of the terrain encountered by the upstream flow. In addition, if the upstream flow is potentially unstable, convective cells will be triggered in the sudden upslope ascent. These cells produce pockets of especially high concentration of cloud liquid

water. The embedded buoyant convective cells thus accentuate the coalescence and riming processes. The precipitation enhancement starts at elevations similar to the flow LCL, however the maximum in precipitation accumulation seem to be associated with release of instability, as it occurs near the terrain with elevations near the LFC of the flow.

The analysis of a Meso-NH numerical simulation of a flow-over or Type A case suggests that mesoscale models are generally able to reproduce the terrain-modified flow and orographic enhancement of precipitation documented by radar. The largest simulated orographic precipitation enhancement occurred over the first peak of the terrain, as was observed. The numerical simulations suggest that for flow-over conditions the second or higher ridges encountered by the flow, an area that was not well sampled by the ground-based polarimetric radar, may also experience some degree of orographic enhancement of precipitation. The location of model-simulated hydrometeors with relation to the terrain and to the 0°C level was similar to the distribution of radar observations. The microphysical processes of precipitation growth as represented in the model simulation are consistent with the polarimetric radar data (Medina and Houze 2003a) and with simple microphysical calculations (Yuter and Houze 2003). The microphysical processes responsible for precipitation enhancement occur preferentially either over individual peaks or more generally over the windward slopes of the terrain. The largest conversion rate is the generation of cloud water droplets by vapor condensation. Graupel is generated by riming of cloud water droplets onto snow and grows mainly by collecting cloud water droplets. The main mechanism to generate rain is the melting of graupel (and snow). Once rain is created in this manner, it grows below the 0°C by collecting cloud water droplets (coalescence) and is lost by fall out.

The other characteristic flow pattern identified in this study (Type B) exhibits a shear layer on the windward slope. The low-level flow is weak while the flow at higher levels is strong and easily crosses the mountain barrier. A sheared layer is

thus formed above the slow-moving low-level air. The shear layer slopes upward, following the general slope of the terrain. The combination of high shear and static stability produces conditions that support dynamical instability (Ri < 0.25) that is manifested in the form of Kevin-Helmholtz billows and turbulent overturning. The strong updrafts observed within these cells helps concentrate the condensate produced by orographic lifting into pockets of high liquid water content. The small-scale cells within the stable shear layer are embedded in a deep broad precipitating cloud of the large-scale baroclinic system. Aggregation of ice particles falling from the frontal cloud into the layer of cells is aided by the turbulent air motions within the cells. The aggregate snowflakes are large targets for riming by collection and accretion of supercooled cloud drops when located within the cellular pockets of high cloud liquid water content. The aggregates and other ice particles thus acquire greater mass and fall out quickly. In this way the condensate produced by orographic lifting can quickly reach the ground on the lower windward slopes. Without the aid of the cells, the condensate may be carried farther downstream. Since the sloped shear layer may cross the 0°C level, the accretion may take the form of coalescence, as the melted snow from above falls through the cells of enhanced liquid water content.

Idealized numerical simulations were used to explore the issue of whether the windward shear layer was a pre-existing feature of the baroclinic system or a characteristic feature of terrain-modified stable flow. Simulations conducted with uniform upstream air suggested that Type B low-level flow, characterized by a windward shear layer, will develop under sufficiently large static stability conditions. The simulations also indicated that under the strong static stability conditions that prevailed during the Alpine storm IOP8, the windward shear layer appears as a response to stability alone, even in the absence of surface friction. For the moderate statically stable conditions that prevailed during the analyzed IMPROVE-2 cases, the numerical simulations suggest that the assistance of surface friction is fundamental to produce a windward shear layer under uniform upstream flow profile conditions. If the upstream

conditions contain pre-existing shear, the surface friction enhances the shear further over the windward slope. The basic Type B flow was simulated in the Meso-NH for the MAP IOP8 case, which indicated that precipitation enhancement occurred when the flow rose over the "effective mountain", represented by a cool, stable low-level airmass and the actual terrain.

Our results indicate that during mid-latitude cyclone passage over mountain ranges, precipitation is locally enhanced over the windward slopes by small-scale cellularity regardless of the character or regime of the low-level flow. In Type A storms buoyant instability is responsible for the updraft generation versus dynamic instability in Type B cases. Regardless of the overturning mechanism, the updrafts produced in both scenarios are strong enough to activate accretion growth processes (coalescence, aggregation, and riming), which are capable of producing large particles that fallout rapidly on the windward side of the terrain.

BIBLIOGRAPHY

Asencio, N. and J. Stein, 2005: Origins of the reversed flow over the windward Alpine foothills of the MAP IOP3 and IOP8. Quart. J. R. Met. Soc., p. submitted.

Asencio, N., J. Stein, M. Chong and F. Gheusi, 2003: Analysis and simulation of local and regional conditions for the rainfall over the Lago Maggiore target area during MAP IOP 2b. Quart. J. R. Met. Soc., 129, 565–586.

Atlas, D., J. I. Metcalf, J. H. Richter and E. E. Gossard, 1970: The birth of "CAT" and microscale turbulence. J. Atmos. Sci., 27, 903–913.

Baines, P. G., 1995: Topographic effects in stratified flows. Cambridge University Press, p. 482 pp.

Baines, P. G. and R. B. Smith, 1993: Upstream stagnation points in stratified flow past obstacles. Dyn. Atmos. Oceans, 18, 105–113.

Bargen, D. W. and R. C. Brown, 1980: Interactive radar velocity unfolding. Preprints, 19th Conf. on Radar Meteor., pp. Miami Beach, FL, Amer. Meteor. Soc., 278–283.

Baschek, B., R. Schefold and E. Barthazy, 2003: Influence of embedded convection on microphysics of snowfall. Preprints, 31th Conf. on Radar Meteor., pp. Seattle, WA, Amer. Meteor. Soc.

Baschek, B., R. Schefold, M. . Wüest and E. Barthazy, 2002: Influence of embedded convection on microphysics of precipitation. Preprints, 11th Conf. on Could Physics, pp. Ogden, UT, Amer. Meteor. Soc.

Battan, L. J., 1973: Radar observations of the atmosphere. University of Chicago Press, p. 324 pp.

Bechtold, P., E. Bazile, P. Mascart and E. Richard, 2001: A mass flux convection scheme for regional and global models. Quart. J. R. Met. Soc., 127, 869–886.

Bougeault, P., P. Binder, A. Buzzi, R. Dirks, R. Houze, J. Kuettner, R. B. Smith, R. Stienacker and H. Volkert, 2001: The MAP Special Observing Period. Bull. Amer. Meteorol. Soc., 82(3), 433–462.

Bousquet, O. and M. Chong, 1998: A multiple-Doppler synthesis and continuity adjustment technique (MUSCAT) to recover wind components from Doppler radar measurements. J. Atmos. Ocean. Tech., 15, 343–359.

Bousquet, O. and B. F. Smull, 2003a: Airflow and precipitation fields within deep Alpine valleys observed by airborne Doppler radar. J. Appl. Meteor., 42, 1497–1513.

Bousquet, O. and B. F. Smull, 2003b: Observations and impacts of upstream blocking during a widespread orographic precipitation event. Quart. J. R. Met. Soc., special MAP issue, 129, 391–409.

Bousquet, O. and B. F. Smull, 2005: Multiple expression of upstream blocking during MAP IOP8. Quart. J. R. Met. Soc., p. Submitted.

Browning, K. A., 1971: Structure of the atmosphere in the vicinity of large-amplitude Kevin-Helmholtz billows. Quart. J. R. Met. Soc., 97, 283–299.

Browning, K. A. and C. D. Watkins, 1970: Observations of clear-air turbulence by high-power radar. Nature, 227, 260–263.

Buzzi, A., N. Tartaglione and P. Malguzzi, 1998: Numerical simulations of the 1994 Piedmont flood: Role of orography and moist processes. Mon. Wea. Rev., 126, 2369–2383.

Caracena, F., R. A. Maddox, L. R. Hoxit and C. F. Chappell, 1979: Mesoanalysis of the Big Thompson storm. Mon. Wea. Rev., 107, 1–17.

Chapman, D. and K. A. Browning, 1997: Radar observations of wind-shear splitting within evolving atmospheric Kevin-Helmholtz billows. Quart. J. R. Met. Soc., 123, 1433–1439.

Chapman, D. and K. A. Browning, 1999: Release of potential shearing instability in warm frontal zones. Quart. J. R. Met. Soc., 125, 2265–2289.

Chong, M. and S. Cosma, 2000: A formulation of the continuity equation of MUSCAT for either flat or complex terrain. J. Atmos. Ocean. Tech., 17, 1556–1565.

Colle, B. A., 2004: Sensitivity of orographic precipitation to changing ambient conditions and terrain geometries: An idealized modeling perspective. J. Atmos. Sci., 61, 588–606.

Colle, B. A. and C. F. Mass, 1996: An observational and modeling study of the interacion of low-level southwesterly flow with the Olympic Mountains during COAST IOP 4. Mon. Wea. Rev., 124, 2152–2175.

Colle, B. A., C. F. Mass and B. F. Smull, 1999: An observational and numerical study of a cold front interacting with the Olympic Mountains during COAST IOP 5. Mon. Wea. Rev., 127, 1310–1334.

Colle, B. A. and Y. Zeng, 2004: Bulk microphysical sensitivities within the MM5 for orographic precipitation. Part I: The Sierra 1986 event. Mon. Wea. Rev., 132, 2780–2801.

Cox, J. A. W., W. J. Steenburgh, D. E. Kingsmill, J. C. Shafer, B. A. Colle, O. Bousquet, B. F. Smull and H. Cai, 2005: The kinematic structure of a Wasatch Mountain winter storm during IPEX IOP3. Mon. Wea. Rev., 133, 521–542.

Cuxart, J., P. Bougeault and J.-L. Redelsperger, 2000: A turbulence scheme allowing for mesoscale and large-eddy simulations. Quart. J. R. Met. Soc., 126, 1–30.

Ding, L., R. J. Calhoun and R. Street, 2003: Numerical simulation of strongly stratified flow over a three-dimensional hill. Bound.-Layer Meteor., 107, 81–114.

Doviak, R. J. and D. S. Zrnič, 1993: Doppler radar and weather observations. Academic Press, p. 562 pp.

Doyle, J. D., 1997: The influence of mesoscale orography on a coastal jet and rainband. Mon. Wea. Rev., 125, 1465–1488.

Durran, D. R. and J. B. Klemp, 1982: On the effects of moisture on the brunt-väisälä frequency. J. Atmos. Sci., 39, 2152–2158.

Durran, D. R. and J. B. Klemp, 1983: A compressible model for the simulation of moist mountain waves. Mon. Wea. Rev., 111, 2341–2363.

Frei, C. and C. Schär, 1998: A precipitation climatology of the Alps from high-resolution rain-gauge observations. Int. J. Climatol., 18, 873–900.

Gal-Chen, T. and R. Sommerville, 1975: On the use of a coordinate transformation for the solution of the Navier-Stokes equations. J. Comput. Phys., 17, 209–228.

Garvert, M. F., B. A. Colle and C. F. Mass, 2005: The 13-14 December 2001 IMPROVE-2 Event. Part I: synoptic and mesoscale evolution and comparison with a mesoscale model simulation. J. Atmos. Sci., special IMPROVE issue, 62, 3474–3492.

Garvert, M. F., B. F. Smull and C. F. Mass, 2006: Multiscale mountain waves influencing a major orographic precipitation event. J. Atmos. Sci., submitted.

Georgis, J.-F., F. Roux, M. Chong and S. Pradier, 2003: Tripple-Doppler radar analysis of the heavy rain event observed in the Lago Maggiore region during MAP IOP 2b. Quart. J. R. Met. Soc., special MAP issue, 129, 495–522.

160

Grossman, R. L. and D. R. Durran, 1984: Interaction of low-level flow wih the western Ghat mountains and offshore convection in the summer monsoon. Mon. Wea. Rev., 112, 652–672.

Herzegh, P. H. and A. R. Jameson, 1992: Observing precipitation through Dual-polarization radar measurements. Bull. Amer. Meteorol. Soc., 73, 1356–1374.

Hobbs, P. V., 1974: Ice Physics. Oxford Press, Bristol, p. 837 pp.

Hobbs, P. V., 1975: The nature of winter clouds and precipitation in the Cascade Mountains and their modification by artificial seeding. Part I: Natural conditions. J. Appl. Meteor., 14, 783–804.

Hobbs, P. V., R. C. Easter and A. B. Fraser, 1973: A theoretical study of the flow of air and fallout of solid precipitation over mountainous terrain. Part II: Microphysics. J. Atmos. Sci., 30, 813–823.

Hobbs, P. V., R. A. Houze and T. J. Matejka, 1975: The dynamical and microphysical structure of an occluded frontal system and its modificaton by orography. J. Atmos. Sci., 32, 1542–1562.

Hobbs, P. V., R. A. Houze, T. J. Matejka, L. F. Radke, D. G. Atkinson and R. R. Weiss, 1974: The dynamical and microphysical structure of an occluded frontal system and its modificaton by orography. University of Washington, p. Research Report IX.

Houze, Jr., R. A., 1993: Clouds Dynamics. Academic Press, p. 573 pp.

Houze, Jr., R. A., C. N. James and S. Medina, 2001: Radar observations of precipitation and airflow on the Mediterranean side of the Alps: Autumn 1998 and 1999. Quart. J. R. Met. Soc., 127, 2537–2558.

Houze, Jr., R. A. and S. Medina, 2005: Turbulence as a mechanism for orographic precipitation enhancement. J. Atmos. Sci., special IMPROVE issue, 62, 3599–3623.

James, C. N. and R. A. Houze, Jr., 2005: Modification of precipitation by coastal orography in storms crossing northern California. Mon. Wea. Rev., p. In press.

Jameson, A. R., 1983: Microphysical interpretation of multi-parameter radar measurements in rain. Part II: Estimation of raindrop distribution parameters by combined dual-wavelength and polarization measurements. J. Atmos. Sci., 40, 1803–1814.

Jiang, Q., 2003: Moist dynamics and orographic precipitation. Tellus, 55A, 301–316.

Jiang, Q. and R. B. Smith, 2003: Cloud timescales and orographic precipitation. J. Atmos. Sci., 60, 1543–1559.

Jorgensen, D. P., T. Matejka and J. D. DuGranrut, 1996: Multi-beam techniques for deriving wind fields from airborne Doppler radars. Meteorol. Atmos. Phys., 59, 83–104.

Kessler, E., 1969: On the distribution and continuity of water substance in atmospheric circulations. Meteor. Monogr., 10, 84 pp.

Kirshbaum, D. J. and D. R. Durran, 2004: Factors governing cellular convection in orographic precipitation. J. Atmos. Sci., 61, 682–698.

Lafore, J. P., J. Stein, N. Asencio, P. Bougeault, V. Ducrocq, J. Duron, C. Fischer, P. Héreil, P. Mascart, J. L. Redelsperger, E. Richard and J. Vilà-Guerau de Arellano, 1998: The Meso-NH atmosphere simulation system. Part I: Adiabatic formulation and control simulation. Ann. Geophys., 16, 90–109.

Lin, Y.-L., R. D. Farley and H. D. Orville, 1983: Bulk parameterizaton of the snow field in a cloud model. J. Appl. Meteor., 22, 1065–1092.

Lin, Y.-L., H. D. Reeves, S.-Y. Chen and S. Chiao, 2005: Formation mechanism for convection over the Ligurian Sea during MAP IOP-8. Mon. Wea. Rev., 133, 2227–2245.

Locatelli, J. D. and P. V. Hobbs, 1974: Fall speeds and masses of solid precipitation particles. J. Geophys. Res., 79, 2185–2197.

Marwitz, J. D., 1983: The kinematics of orographic airflow during Sierra storms. J. Atmos. Sci., 40, 1218–1227.

Marwitz, J. D., 1987: Deep orographic storms over the Sierra Nevada. Part I: Thermodynamic and kinematic structure. J. Atmos. Sci., 44, 159–173.

Mass, C. F. and G. K. Ferber, 1990: Surface pressure perturbations produced by an isolated mesoscale topographic barrier. Part I: General characteristics and dynamics. Mon. Wea. Rev., 118, 2579–2596.

Medina, S. and R. A. Houze, Jr., 2003a: Air motions and precipitation growth in alpine storms. Quart. J. R. Met. Soc., special MAP issue, 129, 345–371.

Medina, S. and R. A. Houze, Jr., 2003b: Orographic precipitation in potentially unstable Alpine storms. Preprints, ICAM and MAP Meeting, pp. Brig, Switzerland.

Medina, S., B. F. Smull, R. A. Houze, Jr. and M. Steiner, 2005: Cross-barrier flow during orographic precipitation events: Results from MAP and IMPROVE. J. Atmos. Sci., special IMPROVE issue, 62, 3580–3598.

Michalakes, J., S. Chen, J. Dudhia, L. Hart, J. Klemp, J. Middlecoff and W. Skamarock, 2001: Development of a next-generation regional weather research and forecasting model. Developments in Teracomputing: Proceedings of the 9th ECMWF workshop on the use of high performance computing in meteorology, pp. W. Zwieflhofer and N. Kreitz, Eds., World Scientific, 269–276.

Morcrette, J.-J., 1991: Radiation and cloud radiative properties in the European Centre for Medium-Range Weather Forecasts forecasting system. J. Geophys. Res., 96, 9121–9132.

Neiman, P. J., F. M. Ralph, A. B. White, D. E. Kingsmill and P. O. G. Persson, 2002: The statistical relationship between upslope flow and rainfall in Clifornia's Coastal Mountains: Observations during CALJET. Mon. Wea. Rev., 130, 1468–1492.

Newson, R. K. and R. M. Banta, 2003: Shear-flow instability in the stable nocturnal boundary layer as observed by Doppler lidar during CASES-99. J. Atmos. Sci., 60, 16–33.

Noilhan, J. and S. Planton, 1989: A simple parameterization of land surface processes for meteolorogical models. Mon. Wea. Rev., 117, 536–549.

Overland, J. E. and N. A. Bond, 1995: Observations and scale analysis of coastal wind jets. Mon. Wea. Rev., 123, 2934–2941.

Peterson, T. C., L. O. Grant, W. R. Cotton and D. C. Rogers, 1991: The effect of decoupled low-level flow on winter orographic clouds and precipitation in the Yampa River Valley. J. Appl. Meteor., 30, 368–386.

Pierrehumbert, R. T. and B. Wyman, 1985: Upstream effects of mesoscale mountains. J. Atmos. Sci., 41, 977–1003.

Pinty, J.-P. and P. Jabouille, 1998: A mixed-phase cloud parameterization for use in mesoscale non-hydrostatic models: Simulations of a squall-line and orographic precipitation. Preprints, Conf. on Cloud Physics, pp. Everett, WA, Amer. Meteor. Soc., 217–220.

Rotunno, R. and R. Ferretti, 2001: Mechanisms of intense Alpine rainfall. J. Atmos. Sci., 58, 1732–1749.

Rotunno, R. and R. Ferretti, 2003: Orographic effects on rainfall in MAP cases IOP 2b and IOP 8. Quart. J. R. Met. Soc., special MAP issue, 129, 373–390.

Ryzhkov, A. V., T. J. Schuur, D. W. Burgess, P. L. Heinselman, S. E. Giangrande and D. S. Zrnić, 2005: The Joint Polarization Experiment: Polarimetric rainfall measurements and hydrometeor classification. Bull. Amer. Meteorol. Soc., 86, 809–824.

Sheppard, P. A., 1956: Airflow over mountains. Quart. J. R. Met. Soc., 82, 528–529.

Skamarock, W. C., J. B. Klemp and J. Dudhia, 2001: Prototypes for the WRF (Weather Research and Forecasting) model. Prerints, 9th Conf. on Mesoscale Processes, pp. Fort Lauderdale, FL, Amer. Meteor. Soc., J11–J15.

Smith, R. B., 1979: The influence of mountains on the atmosphere. Advances in Geophysics, 21, Academic Press, 87–230.

Smith, R. B., 1980: Linear theory of stratified hydrostatic flow past an isolated mountain. Tellus, 32, 348–364.

Smith, R. B., 1988: Linear theory of hydrostatic flow over an isolated mountain in isosteric coordinates. J. Atmos. Sci., 45, 3889–3896.

Smith, R. B., 1989: Mountain induced stagnation points in hydrostatic flows. Tellus, 41A, 270–274.

Smith, R. B., I. Barstad and L. Bonneau, 2005: Orographic precipitation and Orengon's climate transition. J. Atmos. Sci., 62, 177–191.

Smith, R. B. and S. Grønås, 1993: Stagnation points and bifurcation in 3-D mountain airflow. Tellus, 45A, 28–43.

Smith, R. B. and B. I., 2004: A linear theory of orographic precipitation. J. Atmos. Sci., 61, 1377–1391.

Smith, R. B., Q. Jiang, M. G. Fearon, P. Tabary, M. Dorninger, J. D. Doyle and R. Benoit, 2003: Orographic precipitation and air mass transformation: An Alpine example. Quart. J. R. Met. Soc., special MAP issue, 129, 433–454.

Smolarkiewicz, P. K. and R. Rotunno, 1989: Low Froude number flow past three-dimensional obstacles. Part I: Baroclinically generated lee vortices. J. Atmos. Sci., 46, 1154–1164.

Smolarkiewicz, P. K. and R. Rotunno, 1990: Low Froude number flow past three-dimensional obstacles. Part II: Upwind flow reversal zone. J. Atmos. Sci., 47, 1498–1511.

164

Stein, J., E. Richard, J. P. Lafore, J. P. Pinty, N. Asencio and S. Cosma, 2000: High-resolution non-hydrostatic simulations of flash-flood episodes with grid-nesting and ice-phase parameterization. Meteorol. Atmos. Phys., 72, 203–221.

Steiner, M., O. Bousquet, R. A. Houze, B. F. Smull and M. Mancini, 2003: Airflow within major Alpine valleys under heavy rainfall. Quart. J. R. Met. Soc., special MAP issue, 129, 411–431.

Stoelinga, M. T., P. V. Hobbs, C. F. Mass, J. D. Locatelli, B. A. Colle, R. A. Houze, A. L. Rangno, N. A. Bond, B. F. Smull, R. M. Rasmussen, G. Thompson and B. R. Colman, 2003: Improvement of Microphysical Parameterization through Observational Verification Experiment. Bull. Amer. Meteorol. Soc., 84, 1807–1826.

Straka, J. M., D. S. Zrnić and A. V. Ryzhkov, 2000: Bulk hydrometeor classification and quantification using polarimetric radar data: Synthesis of relations. J. Appl. Meteor., 39, 1341–1372.

Thépaut, J. N., P. Alary, P. Caille, V. Cassé, J. F. Geleyn, P. Moll, J. Pailleux, J. M. Piriou, D. Puech and F. Taillefer, 1998: The operational global data assimilation system at météo-france. Proceedings of the HIRLAM 4 workshop on variational analysis in limited area models, Toulouse, France, pp. 25–31.

Vivekanandan, J., V. N. Bringi, M. Hagen and P. Meischner, 1994: Polarimetric radar studies of atmospheric ice particles. IEEE Trans. Geosci. Remote Sens., 32, 1–10.

Vivekanandan, J., D. S. Zrnić, S. M. Ellis, R. Oye, A. V. Ryzhkov and J. M. Straka, 1999: Cloud microphysics retrieval using S-band dual-polarization radar measurements. Bull. Amer. Meteorol. Soc., 80, 381–388.

Walko, R. L., W. R. Cotton, M. P. Meyers and J. Y. Harrington, 1995: New RAMS cloud microphysics parameterization Part I: The single-moment scheme. Atmos. Res., 38, 29–62.

Weiss, R. R. and P. V. Hobbs, 1975: The use of a vertically pointing pulsed Doppler radar in cloud physics and weather modification studies. J. Appl. Meteor., 14, 222–231.

White, A. B., J. R. Jordan, B. E. Martner, F. M. Ralph and B. W. Bartram, 2000: Extending the dynamic range of an S-band radar for cloud and precipitation studies. J. Atmos. Ocean. Tech., 17, 1226–1234.

Woods, C. P., M. T. Stoelinga, J. D. Locatelli and P. V. Hobbs, 2005: Microphysical processes and synergistic interaction between frontal and orographic forcing of precipitation during the 13 December 2001 IMPROVE-2 event over the Oregon Cascades. J. Atmos. Sci., special IMPROVE issue, 62, 3493–3519.

Yu, C.-K. and B. F. Smull, 2000: Airborne Doppler observations of a landfalling cold front upstream of steep coastal orography. Mon. Wea. Rev., 128, 1577–1603.

Yuter, S. E. and R. A. Houze, Jr., 2003: Microphysical modes of precipitation growth determined by S-band vertically pointing radar in orographic precipitation during MAP. Quart. J. R. Met. Soc., special MAP issue, 129, 455–476.

Zeng, Z., S. E. Yuter, R. A. Houze and D. E. Kingsmill, 2001: Microphysics of the rapid development of heavy convective precipitation. Mon. Wea. Rev., 129, 1882–1904.

Zrnić, D. S., N. Balakrishnan, C. L. Ziegler, V. N. Bringi, K. Aydin and T. Matejka, 1993: Polarimetric signatures in the stratiform region of a mesoscale convective system. J. Appl. Meteor., 32, 678–69693.

Appendix A

POLARIMETRIC VARIABLES AND PARTICLE IDENTIFICATION (PID) ALGORITHM

A.1 Polarimetric variables

In this study we are concerned with data collected with dual linearly polarized radar. The reflectivity factor (Z_H) is proportional to the horizontally transmitted/horizontally received fields, denoted by S_{HH} where the first (second) index refers to the transmitted (received) polarization. Electromagnetic waves transmitted and received with the same polarization (such as S_{HH}) constitute what is known as a co-polar measurement. The shapes and orientations of hydrometeors induce some of the wave transmitted at one polarization to return to the radar with the orthogonal polarization (Herzegh and Jameson 1992). This type of variable constitutes a cross-polar measurement (e.g., the horizontally transmitted/vertically received reflectivity factor, denoted by S_{HV}). A dual-polarimetric radar transmits and receives horizontally and vertically polarized waves. Some of the relevant parameters obtained from dual-polarimetric radar measurements (besides reflectivity factor Z_H) are: differential reflectivity (ZDR), linear depolarization ratio (LDR), specific differential propagation phase (K_{DP}), and correlation coefficient between co-polar returns at zero lag (ρ_{HV}), which are given by:

$$Z_H = (4\lambda^4/\pi^4|K_w|^2\langle|S_{HH}|^2\rangle \tag{A.1}$$

$$ZDR = 10\,log_{10}\left(\frac{\langle|S_{HH}|^2\rangle}{\langle|S_{VV}|^2\rangle}\right) \tag{A.2}$$

$$LDR = 10 \, log_{10} \left(\frac{\langle |S_{HV}|^2 \rangle}{\langle |S_{HH}|^2 \rangle} \right) \tag{A.3}$$

$$K_{DP} = \frac{\Phi_{DP}(r_2) - \Phi_{DP}(r_1)}{2(r_2 - r_1)} \tag{A.4}$$

$$\Phi_{DP} = \Phi_{HH} - \Phi_{VV} \tag{A.5}$$

$$\rho_{HV} = \frac{\langle S_{VV} \, S_{HH}{}^* \rangle}{\langle S_{HH}{}^2 \rangle^{1/2} \langle S_{VV}{}^2 \rangle^{1/2}} \tag{A.6}$$

Φ_{DP} is called the differential propagation phase shift (i.e. the difference between the propagation phase shift of the radar wave at horizontal and vertical polarization during two way propagation), where Φ_{VV} and Φ_{HH} are the phases of the horizontally polarized and vertically polarized waves; and r is range from the radar. The correlation coefficient is defined as the covariance between two variables, divided by the products of the standard deviation of each variable, where S_{ij} is the backscattering matrix element of a hydrometeor. The i (j) subscript refers to the polarization of the incident field (backscattering field). The brackets are statistical expectations. $K_w = (\epsilon_w - 1)/(\epsilon_w + 2)$ is a factor related to the dielectric constant of water; ϵ_w is the dielectric constant; λ is the radar's wavelength (Straka et al. 2000).

As the polarimetric variables are influenced by the size, shape, thermodynamic phase, bulk density, and spatial orientation of the scattering hydrometeors, they may be used in to infer some of the hydrometeor characteristics. A summary of the most relevant particle signatures in each polarimetric variable is described below.

- dBZ: Depends on number concentration and particle diameter to the sixth power. Hence the larger particles (e.g. hailstones) produce the stronger signals.

- ZDR: It helps differentiate rain from solid precipitation and identifies hail near the surface (Herzegh and Jameson 1992). It is useful in identifying raindrops,

which when falling are deformed into oblate spheroids with their major axis oriented horizontally. Since the larger drops suffer a higher degree of deformation when falling, ZDR can be interpreted as the reflectivity weighted mean-axis ratio of the backscattering particles (Jameson 1983). Its signal is proportional to the raindrops size. Wet snow produces a strong return. Hail produces low values due to its tumbling when falling and sphericity. Dry snow give low values due to its low dielectric constant.

- LDR: A pulse emitted in the horizontal direction impinging over a spherical particle will excite a response in all directions, however if a particle is symmetric, the vertical responses will cancel each other producing near zero Z_{HV} values and LDR values approaching negative infinity. If the particle does not have an axis of symmetry in the vertical direction (for example a titled column-shaped ice crystal), the vertical responses excited by the horizontal pulse will not cancel each other and LDR will have a value different from negative infinity. LDR is useful in identifying different ice-particle shapes, orientation and particle phase. It is particularly useful in identifying mixed-phase areas (such as the melting region), which are characterized by relatively high LDR values (Herzegh and Jameson 1992). LDR tends to have small values above the 0°C level if there is no mixed-phase precipitation. Rain has symmetric shapes and small canting angles which gives low LDR values. Dry snow also produces small values since it has a low dielectric constant. Irregular graupel and hail have a strong LDR signature, as well as wet snow due to its outer water layer.

- K_{DP}: In a volume filled with horizontally oriented hydrometeors (e.g. rain), a horizontally polarized wave has larger phase shifts (per unit length) and propagates more slowly than a vertically polarized wave (the opposite holds for a vertically oriented hydrometeor) (Straka et al. 2000). K_{DP} measures the difference between propagation constants for horizontally and vertically polarized

waves. Hence, it can discern between statistically isotropic and anisotropic hydrometeors. Isotropic hydrometeors produce similar phase shifts for horizontally and vertically polarized waves. In general the magnitude of K_{DP} increases with oblateness and with dielectric constant. K_{DP} has a strong signal when statistically anisotropic hydrometeors like rain are larger than 1 mm. It is used to identify non-spherical particles such as ice crystals and raindrops (Vivekanandan et al. 1999).

- ρ_{HV}: The degree of decorrelation between horizontally and vertically polarized echoes depends on the variability in the horizontal and vertical sizes of hydrometeors. Model and observations have shown that $|\rho_{HV}|$ decreases with increasing diversity of hydrometeor orientation and shapes. Decorrelation is also significant when particles are wet or when they are large and irregular in shape. Values of ρ are close to unity in regions populated by single type of relatively smooth, small hydrometeors (such as rain and pure ice crystals, Zrnic et al. 1993). Scatters with various sizes, axial ratios, mixed phases (or melting), and distribution of canting angles produce values < 1 (Zrnic et al. 1993).

A.2 Particle identification (PID) algorithm

Using as a basis comparisons of radar measurements with in situ aircraft and ground-based observation as well as model computations, the relationships described above have been summarized in tables that give typical values of polarimetric observables for various precipitation types (e.g. Doviak and Zrnic 1993, Staka et al. 2000). An example for the particle types relevant to this study is shown in Table A.1. Different particle types may have a similar backscatter signature in one or more polarimetric variables (Table A.1), which complicates the problem of particle identification (PID). However, the join interpretation of several polarimetric variables has proven to be effective in identifying particle types (e.g., Herzegh and Jameson 1992). The analysis of

several polarimetric observables to deduce particle type requires careful examination and can be time consuming. A recent challenge of the polarimetric radar community has been to develop algorithms that can automatically perform the identification. These algorithms will be particularly useful when polarimetric capabilities are added to the existing US nationwide radar network (Ryzhkov et al. 2005). Several particle identification or classification algorithms have been developed by considering multiple polarimetric variables at once, then they output the hydrometeor type that is consistent with the polarimetric signals. One approach as been to use hard boundaries or thresholds based on the known ranges of polarimetric observations for each particle type (e.g., Zeng et al. 2001).

The PID algorithm used in this study is based on a fuzzy logic approach (Vivekanandan et al. 1999), a technique that takes in consideration that the intersection of a set and its complement is not necessarily empty (e.g., the intersection between "rain" and "no rain" regions is not necessarily empty, as there could be a region of mixed phase particles). In fuzzy logic approach there is a smooth transition in polarimetric observation boundaries among precipitation types (Vivekanandan et al. 1999). The core of this algorithm is formed by the membership functions, which based on the known ranges of the polarimetric observables for particle types, describe the degree to which a particular observation belongs to each particle type. Fig. A.1 shows the membership function for moderate rain as a function of reflectivity. The membership function assigns to each reflectivity value an interest value between 0 and 1. A reflectivity observation that under the membership function shown in Fig. A.1 has an interest value close to unity, implies that the degree to which the observation in question belongs to the moderate rain category is high. Likewise, a value close to zero implies that the degree to which the observations belongs to the moderate rain category is low. However, a radar data point is described not only by it reflectivity but by a whole suite of polarimetric variables, therefore all of them need to be taken into account. For the sake of simplicity, we will assume that a radar observation

is characterized by two polarimetic variables: reflectivity and differential reflectivity, which have specific values Z_0 and ZDR_0, respectively. Based on the reflectivity membership function of particle type i, denoted by f_i (e.g., Fig. A.1), it is possible to determine the value $f_i(Z_0)$, which is called the membership value. In the same way, there is a membership function g_i of differential reflectivity for particle type i. Then the observation ZDR_0 has a membership value $g_i(ZDR_0)$. The membership values $f_i(Z_0)$ and $g_i(ZDR_0)$ are added to give an aggregation value (Q_i), which determines the degree to which the radar observables Z_0 and ZDR_0 belong to particle type i. The same operation is performed for all the particle types (each of which has its own membership functions), producing n aggregation values, where n is the number of predetermined particle categories.

The final step is to assign to the radar observables Z_0 and ZDR_0 the particle type that has the maximum aggregation value. In this example only two polarimetric observables were used, however in the actual algorithm five polarimetric observables (described above) plus a vertical profile of temperature (given by a nearby sounding) are provided as input to the algorithm[12]. However, not all the input variables have the same weight. When determining the aggregation value (Q_i), the membership values obtained from reflectivity, differential reflectivity, and temperature weight twice as much as the rest of the polarimetric variables. According to Vivekanandan et al. (1999), this assignment of weights is based on the usefulness of the variables for particle classification and on the measurement accuracy of the input variables.

---

[1]The standard deviation of ZDR, Φ, and radial velocity are also considered. However the only function of these variables is to identify ground clutter contamination, which is characterized by large reflectivity values and noisy ZDR, Φ, and radial velocity fields i.e., large standard deviations.

[2]The membership functions for ZDR, LDR, K_{DP}, and ρ_{HV} also depend on reflectivity, therefore they are two-dimensional functions

Table A.1: Polarimetric Radar Variables

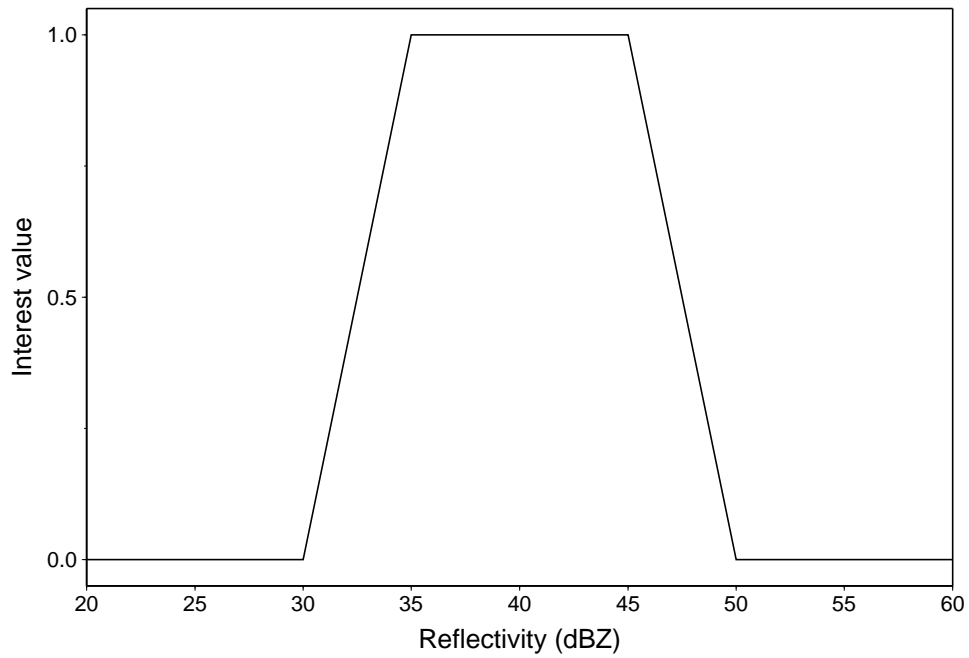| Hydrometeor	dBZ (dBZ)	ZDR (dB)	LDR (dB)	K_{DP} ($^\circ$km^{-1})	ρ_{HV}	T^a ($^\circ$C)
Light rain	13 to 40	> -0.3	< -25	-0.05 to 0.3	> 0.97	> -1
Heavy rain	40 to 60	$> \sim 0.2$	~ -31 to -24	0.07 to 15	> 0.97	> -1
Graupel and/or dry aggregates	35 to 55	-0.3 to ~ 1.9	-29 to -18	0.0 to ~ 2.5	0.85 to ~ 1.0	-30 to 30
Dry snow	10 to 35	-1 to 1.4	-28 to -21	-0.05 to ~ 0.2	> 0.97	-52 to 1
Wet snow	20 to 50	> 0.3	-24 to ~ -17	-0.05 to 1.2	0.7 to 0.98	-8 to 8

^{a} Temperature

Figure A.1: Membership function of reflectivity for moderate rain.

Appendix B

QUALITY CONTROL OF POLARIMETRIC S-POL RADAR DATA

B.1   PID algorithm with high temporal resolution temperature information

As seen in the previous section, the PID algorithm applied to S-Pol polarimetric data requires a vertical profile of temperature. Consequently, the results obtained are sensitive to this input, particularly to the 0°C level. Real-time PID calculations were obtained during MAP and IMPROVE II, however the temperature information was updated only when upper air soundings were available. Our first goal in post processing the radar data was to apply the PID algorithm using high temporal resolution 0°C level as input. This was done by perusing the S-Pol radar reflectivity data to obtain 0°C level data based on the identification and location of the reflectivity bright band. Additionally, 0°C level data was extracted from all the available upper air observations. For IMPROVE-2, this information was heavily complemented with vertically pointing NOAA/ETL S-band radar, which provided high time resolution reflectivity data. The 0°C level information from different sources was integrated into one time series, which was used to run the PID algorithm on the data of interest[1].

B.2   Removing ground clutter

During MAP and IMPROVE II, the S-Pol radar scanned over mountain ranges (Figs. 1.11 and 1.3) and was subject to contamination by returns from the terrain or ground clutter. The radar pixels close to the ground affected by ground clutter exhibit high reflectivity values at the ranges where a radar beam intersects a peak. For example in Fig. B.1c several areas close to the surface were affected by ground clutter (radar

---

[1]This was done for the MAP storms of interest and for the whole IMPROVE-2 dataset.

pixels with reflectivity values greater than approximately 45 dBZ). The radial velocity is also affected by ground clutter, producing values with a large standard deviation and a mean close to zero (Fig. B.1d). Ground clutter contamination was removed from the S-Pol IMPROVE II data by a two-step process:

- 1. Time-independent part: A clutter map was constructed by finding clear air scans (i.e. scans when the S-Pol radar collected data but no meteorological echo was present), an example for the 87° azimuth is shown in Fig. B.1a. Then it was assumed that all the reflectivity echoes greater than a threshold were due to the terrain. A threshold of −6 dBZ was found to be a reasonable value.

- 2. Time-dependent part: The amount of ground clutter is sensitive to changes on the index of refraction of the atmosphere therefore it changes with time. Ground clutter is one of the "particle types" produced by the PID algorithm of Vivekanandan et al.'s (1999). Its identification is based on the radar signature of ground clutter, which consist of large reflectivity values and noisy ZDR, Φ, and radial velocity fields. The noisy spatial characteristics are reflected in large standard deviation values. An example of PID output during a period of heavy rain is shown in Fig. B.1b.

If an individual pixel was collocated with a pixel in the clutter map described above or if it was identified as ground clutter by the PID algorithm, then this pixel was considered to be ground clutter and eliminated. Additionally, when a ground clutter pixel was found, all the data at farther ranges form the radar in that beam was also removed. This was only done for low elevation angles (less than 1° or 2° of elevation). Fig. B.1e shows an example of a reflectivity RHI obtained once the ground clutter was removed.

B.3 Removing aliasing in radial velocity data

A radar sampling in a discontinuous way measures radial velocity with some ambiguity, as it will always lie within the radar's Nyquist velocity (v_n) interval. v_n depends on the radar's pulse repetition frequency and wavelength, for S-Pol it is $+/-$ 22.4 $\mathrm{m\,s^{-1}}$. The measured radial velocity (v_m) is related to the actual radial velocity (v) by:

$$v = v_m + 2nv_n \qquad\qquad (B.1)$$

where n is an unknown integer. Actual radial velocities outside the $+/-v_n$ interval will be aliased or folded into this interval. For example, for S-Pol, an actual radial velocity of 22.5 $\mathrm{m\,s^{-1}}$ will be measured by the radar as -22.3 $\mathrm{m\,s^{-1}}$. Obviously, there may also be actual observations with a value of -22.3 $\mathrm{m\,s^{-1}}$. Folding problems are normally easily identified by visual inspection, however correcting the data manually can be tedious and slow. For this study, the radial velocity was unfolded using NCAR's SOLO software implementation of the Bargen and Brown (1980) algorithm. The algorithm looks along a fixed radar beam (described by its azimuth and elevation) and it tries to reduce discontinuities in the radial velocity if they exist. To evaluate continuity, the mean radial velocity of k number of radar pixels or gates is calculated. The difference between the mean radial velocity and the radial velocity of the gate $k+1$ is calculated and a decision is made regarding what n integer minimizes this difference. Once the gate $k+1$ is either verified to be correct or corrected, the next gate in the beam ($k+2$) is evaluated based on the mean of the previous k gates and so forth. This algorithm does not perform well when the data is patchy, noisy or when there is a large number of missing gates. Therefore, the data has to be checked and corrected manually, which is very labor extensive. Only selected time intervals were unfolded. An example of an "uncluttered" and unfolded radial velocity field is given in Fig. B.1f.
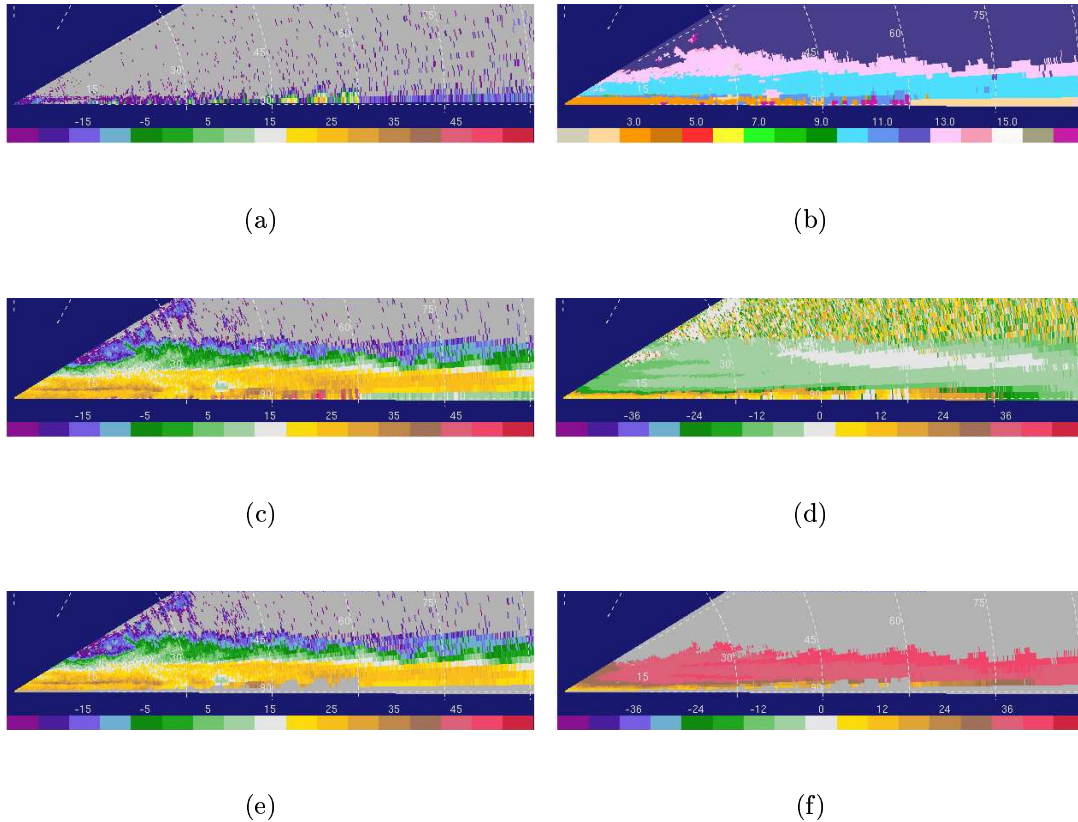
(a)

(b)

(c)

(d)

(e)

(f)

Figure B.1: Example of a 87° azimuth RHI showing (a) clutter map (i.e., reflectivity during a period with no meterological echo). Panels (b)-(f) show radar variables measured during a time of heavy precipitation (2310 UTC 13 December 2001). (b) PID output (magenta pixels denote ground clutter, the particle type that corresponds to each color is shown in Fig. 4.2a). Panels (c) and (d) show raw reflectivity and radial velocity, respectively. Quality controled (e) reflectivity (with ground clutter removed or uncluttered) and (f) radial velocity (uncluttered and unfolded).

VITA

María del Socorro Medina Valles was born in Cd. Juárez, in the state of Chihuahua, México, in 1972. She graduated in 1997 from Mexico City's Universidad Nacional Autónoma de México (UNAM) with a Bachelor degree in Physics. She received Masters in Science in 1999 from UNAM (Atmospheric Physics) and in 2002 from the University of Washington (Atmospheric Sciences).